Controlling the spectral properties of quantum light sources based on a quantum dot in a nanowire

Saptarshi Kotal

Université Grenoble Alpes

THÈSE

Pour obtenir le grade de

DOCTEUR DE L'UNIVERSITÉ GRENOBLE ALPES

Spécialité : **Physique de la Matière Condensée et du Rayonnement**

Arrêté ministériel : 25 mai 2016

Présentée par

Saptarshi KOTAL

Thèse dirigée par **Julien CLAUDON**, Chercheur CEA, Université Grenoble Alpes
et codirigée par **Jean-Michel GÉRARD**, Chercheur CEA, Université Grenoble Alpes

préparée au sein du **Laboratoire PHotonique, ELectronique et Ingéniérie QuantiqueS**
dans **l'École Doctorale Physique**

Contrôle des propriétés spectrales de sources de lumière quantique basées sur une boîte quantique dans un nanofil

Controlling the spectral properties of quantum light sources based on a quantum dot in a nanowire

Thèse soutenue publiquement le **17 juin 2021**,
devant le jury composé de :

Armando RASTELLI
Professor, Johannes Kepler University, Linz (Austria), Rapporteur
Isabelle ROBERT-PHILIP
Directrice de Recherche CNRS, Montpellier (France), Rapporteur
Christophe COUTEAU
Professeur, Université de Technologie de Troyes, Troyes (France), Examinateur
Angela VELLA
Professeure, Université de Rouen, Rouen (France), Examinatrice
Maxime RICHARD
Directeur de Recherche CNRS, Grenoble (France), Président

Résumé

Ce travail vise à contrôler les propriétés spectrales des photons émis par une boîte quantique semiconductrice intégrée dans une antenne à fil photonique. Dans une étude théorique, nous dévoilons tout d'abord un nouveau mécanisme de décohérence dans ce système. Même à température cryogénique, les vibrations thermiques du nanofil induisent un très fort élargissement spectral qui interdit l'émission de photons indiscernables. Nous proposons trois approches qui suppriment efficacement ce canal de décohérence en exploitant une ingénierie des propriétés mécaniques du nanofil. Ensuite, nous introduisons une nanocavité optique à nanofil qui offre une accélération de l'émission spontanée très prononcée (facteur de Purcell théorique de 6.3) sur une large gamme spectrale (30 nm à mi-hauteur). Nous avons fabriqué une nanocavité en GaAs qui contient des boîtes quantiques auto-assemblées en InAs. Les mesures révèlent une accélération de l'émission spontanée par un facteur 5.6 et une efficacité de collection de 0.35 au niveau de la première lentille. Enfin, nous proposons une stratégie pour accorder la longueur d'onde d'émission d'une boîte quantique intégrée dans une antenne à nanofil. Deux électrodes sur puce génèrent une force électrostatique qui plie le nanofil. La déformation résultante module l'énergie de bande interdite de la boîte quantique. Nous avons réalisé ces dispositifs et discutons les premières mesures démontrant l'accordabilité spectrale. Globalement, ces résultats ouvrent des perspectives prometteuses pour les technologies photoniques quantiques, en particulier pour la réalisation de sources avancées d'états quantiques de la lumière.

Abstract

This work aims at controlling the spectral properties of photons that are emitted by a semiconductor quantum dot (QD) embedded in a photonic nanowire antenna. First, we conduct a theoretical study which unveils a new decoherence mechanism in this system. We show that, even at cryogenic temperature, the thermal vibrations of the nanowire induce a large spectral broadening that prevents the emission of indistinguishable photons. We propose three designs that suppress this decoherence channel thanks to an engineering of the mechanical properties of the nanowire. Next we introduce a nanowire optical nanocavity which offers a large acceleration of spontaneous emission (predicted Purcell factor of 6.3) that is maintained over a 30-nm-wide operation bandwidth. We fabricate a GaAs nanocavity which embeds InAs self-assembled QDs. Single QD spectroscopy reveals a maximal acceleration of spontaneous emission by a factor as large as 5.6 and a first lens collection efficiency of 0.35. Finally, we propose a strategy to tune the emission wavelength of a QD embedded in a nanowire antenna. On-chip electrodes generate an electrostatic force that bends the nanowire. The resulting strain modulates the QD bandgap energy. We realise a first generation of devices and discuss preliminary wavelength tuning measurements. Overall, these results open promising perspectives for photonic quantum technologies, in particular for the realisation of advanced sources of quantum light.

Acknowledgements

Having successfully defended my PhD thesis, and looking back upon this experience, I can't help but feel amazed at how swiftly the last four years swept by. Indeed what a memorable journey this has been, with some ecstatic highs, as well as some crushing lows. Regardless the turn of the tides, I have never been alone to brave the waves. These years of my doctoral research have helped me learn and grow significantly, not just by achieving magnificent scientific results that are highlighted in this work, but also on a personal and psychological front. I owe it to a bunch of wonderful people who have been part of this journey, making it this opportunity for self-development one that I will cherish for a long time to come.

I couldn't have realised my project with as much success if it weren't for the able guidance of my supervisor, Julien Claudon. From very early on you provided me with a scope to work independently, while always being available and easily accessible to clarify concepts, to interpret bewildering results, and to discuss plans of action. You instilled in me the importance of distilling the essential information from any topic to first gain a realistic feel for the physical phenomenon behind the concept before delving into rigorous derivations of the details. I also owe my style of scientific expression largely to you, because you have helped me improve how I structure and present information in a pertinent and visually coherent manner.

Navigating through my field of research was also made less challenging thanks to my co-supervisor, Jean-Michel Gérard. You are truly a treasure trove when it comes to the physics of quantum dots. You brought a wider dimension to my appreciation of the project, helping me put my work in context of relevant advances in other research groups and similar achievements on different material platforms. Despite your demanding schedule in the beginning of my PhD, and your constraint due to your health towards the end of my project, you have always been forthcoming to remain up-to-date with my progress and provided me with feedback and suggestions.

I feel extremely fortunate to have been under the supervision of Julien and Jean-Michel. You both have welcomed all my questions, however trivial they may have been, and have benevolently taken the time to patiently help me understand the subject. You have always prioritised my comprehension of the subject over the quantity of results I could produce, and you've gone above and beyond to ensure I could succeed, and for that I am truly grateful to you both.

I began my PhD project around the same time Alberto Artioli (post-doc) joined the team. We worked closely on several stages of the project over three years. We bounced ideas off each other, figured new things out together, and kept the morale of one another up when nothing seemed to work. I could become operational at my work much faster and was able to achieve so many major results over such a short span of time thanks to our close collaboration. Thanks to you I didn't have to repeat the same mistakes you had already learned from during your doctoral work. Thank you dearly for all the skills and tricks you passed on to me, not just in the optics lab or the clean room but also through your work ethic and the way you tackled problems.

Despite all the milestones achieved in my project, my PhD journey wasn't devoid of lulls, uncertainties, and obstacles. However, there was never a dull moment in my office, thanks to my wonderful office mate Romain Fons. It was uncanny how similar we were in so many ways and how we complemented each others presence so effortlessly. My first two years in the lab would be unimaginably drab without your cheerful camaraderie. I will forever cherish the laughter, the madness, the banter, and sometimes the profound conversations we shared together. I am also thankful to Matteo Finazzer with whom I shared my office towards the end of my project. It was rewarding to train you on the PL setups, the flip-chip process, and the COMSOL simulations. Although the time we shared was quite short, we formed a genuine and significant connection. Thank you for putting up with my advice from experience (or the lack thereof), for the lengthy discussions on such varied subjects, and for engaging in our series of politically incorrect jokes.

I'd like to thank Joël Bleuse for training me to operate the micro-PL setup. You were there to help me out whenever I had something I couldn't fix in my experiment. I also value your ability to explain any concept in the most lucid and eloquent manner. You helped me acquire a strong expertise in fine spectroscopy. I thank Yann Genuist for his benevolence and his sustained support with the optimisation of the epitaxial growth process, that enabled him to produce wafers with the exact specifications necessary for our samples. Thank you Yoann Curé for teaching me to run and for helping me troubleshoot my simulations on COMSOL. I am also grateful to all the equipment managers at the PTA cleanrooms (Thierry Chevolleau, Thomas Charvolin, Christophe Lemonias, Marlène Terrier, Frédéric Gustavo, Guillaume Gay, Jean-Luc Thomassin, Christelle Gomez, Delphine Constantin, Eric de la Madeleine, and Nicholas Mollard) for the training of the various nanofabrication techniques and for carrying out certain steps in my sample development process.

Next, I express my gratitude to all the members of my jury for graciously accepting to evaluate my work. I thank my reviewers Armando Rastelli and Isabelle Robert-Philip for their keen interest, as well as their encouraging reports on my thesis. I thank Maxime Richard for having presided over the jury and both Christophe Couteau and Angela Vella for accepting to be my examiners. You all expressed great enthusiasm to discuss my results

and I found it thoroughly fulfilling to answer your stimulating questions. Thank you all for your thoughtful feedback and your hearty appreciation.

More broadly, I'd like to thank the entire NPSC team, of which I was part of. Thank you Bruno Gayral, Régis André, Henri Mariette, Bruno Daudin, Eva Monroy, Christophe Durand, Joël Eymery, Moïra Hocevar, Jean Dussaud, and all the other permanent staff for upholding a truly collaborative and welcoming environment in the lab in which I felt at home from the very first day. I acknowledge the European Union's Horizon 2020 research and innovation program under Marie Skłodowska-Curie Grant Agreement No. 754303 and the French Agence Nationale de la Recherche under the program "Investissements d'avenir" (No. ANR-15-IDEX-02) for funding my PhD project, and the coordinators of the GreQuE and QuEnG projects, Jean-Philippe Poizat and Alexia Auffèves. I also express my gratitude to Sara Guiza, Christine Habdi-Meunier, Julia Sauret, Sarah Mauduit, and Celine Conche, the Human Resource personnel who helped me navigate through the administrative procedures pertaining to my work contract and access to the CEA campus.

My PhD project has been far from an individual undertaking and I owe some parts of my results and experience to my external collaborators. In particular, I am grateful to Niels Gregersen, Yujing Wang, and Andreas Dyhl Osterkryger from the DTU Fotonik Group in Copenhagen for their contribution to the numerical simulations and modelling of the nanowire nanocavity. I also thank Val Zwiller, Mattias Hammar, Katharina Zeuner, Ali Elshaari, Samuel Gyger, Klaus Jöns, Marijn Versteegh, Stephan Steinhauer, Lucas Schweickert, and everyone else from the QNP group at KTH Stockholm for hosting me for two months in team to work on SPSs emitting in the telecom range.

If I look back fondly at my PhD journey today, it is not just because of the skills I have acquired or the scientific results I have produced, but it is as much thanks to the wonderful companionship I have enjoyed with my fellow PhD students, post-docs, and interns of the lab. I will deeply cherish and dearly miss our lunches at H2, the ski-trips, the hikes, the game nights, the drinks after work, and the crazy parties. For all the laughter, madness, and memories I thank you, from the bottom of my heart, all of you 'H2 Kids' and 'H2 Beasts': Akhil Ajay, Alexandra-Madalina Siladie, Marion Gruart, Akanksha Kapoor, Nathaniel Feldberg, Guilherme Torelly, Anjali Harikumar, Alexandre Concordel, Vincent Grenier, Ioanna Dimkou, Houssaine Machhadani, An-Hsi Chen, Rémy Vermeersch, Sergi Cuesta, Saransh Gosain, Saranath Seshadri, Maria Spies, Raouia Rhazi, Fabien Jourdan, Sylvain Perret, Thibaut Jousseaume, Ali Jaffal, Alice Bernard, Camille Barbier, Balakumar Baskaran, Anh Quach, Daniel Montero, Rodrigo Blasco Chicano. Beyond my workplace colleagues I am deeply grateful to Namrata Patel for facilitating my transition into my new environment in Grenoble. Thank you for helping me sort the practical challenges of settling down, for welcoming me to outdoor activities with your friends, and for simply checking in on me, once in a while, to ensure I was coping well with my PhD project. I'd also like to

thank Aniket Rath for being present and for assisting me to overcome a challenging period in my health.

My path leading up to being conferred with my doctorate hasn't been the most straightforward. There has been some trial and error, some honest effort, and some amount of chance along the way, but during the trying times, I'm thankful to have always found support, from all my friends, mentors, and well-wishers in Pondicherry, Dijon, and Grenoble. In particular, thank you so very much Ahana, for your loving company all along the way, albeit the distance. You have dealt with me at my lowest and helped me find my way forward. You have forever unequivocally rooted for my success and I am truly thankful to have you by me. Finally I express my heartfelt gratitude to my dear parents for their constant support on every step of this wonderful journey. You have provided me with a nurturing and encouraging environment to help me grow to be the best of myself. You have always entrusted me with the freedom to find my passion and to define my own path. I owe it to you both for making me who I am today. Thank you for everything.

List of Acronyms & Symbols

Al	Aluminum
AlGaAs	Aluminum Gallium Arsenide
APD	Avalanche PhotoDiode
Ar	Argon
As	Arsenic
Au	Gold
β	Beta Factor
BCl_3	Boron Trichloride
$^{\circ}$C	Degrees Celcius
CCP	Capacitively Coupled Plasma
CH_2F_2	Difluoromethane
$C_6H_8O_7$	Citric Acid
CCD	Charge Coupled Device
CEA	Commissariat à l'Énergie Atomique et aux Énergies Alternatives (French Alternative Energies and Atomic Energy Commission)
Cl	Chlorine
CW	Continuous Wave
DBR	Distributed Bragg Reflector
DTU	Danmarks Tekniske Universitet (Technical University of Denmark), Copenhagen
ε	Collection efficiency
EBL	Electron Beam Lithography
eV/meV/μeV	Electronvolt/Mili-Electronvolt/Micro-Electronvolt
FDTD	Finite-Difference Time Domain
FEM	Finite Element Method

F_P	Purcell Factor
FSR	Free Spectral Range
FSS	Fine Structure Splitting
FWHM	Full Width at Half Maximum
γ	Spontaneous emission rate in radiatiave modes
Γ	Spontaneous emission rate in mode of interest
Ga	Gallium
GaAs	Gallium Arsenide
GHz/MHz	GigaHertz/MegaHertz
GreQuE	Grenoble Quantum Engineering - PhD funding programme
H_2O_2	Hydrogen Peroxide
He	Helium
HE_{11}	Fundamental guided mode in our waveguides
HF	Hydrofluoric Acid
HNO_3	Nitric Acid
ICP	Inductively Coupled Plasma
In	Indium
InAs	Indium Arsenide
IPA	Isopropyl Alcohol
IR	Infra Red
IRF	Instrument Response Function
I_{sat}	Saturation Intensity
K	Kelvin
KTH	Kungliga Tekniska Högskolan (Royal Institute of Technology), Stockholm
λ	Wavelength
Leti	Laboratoire d'Électronique des Technologies de l'Information (Industrial cleanroom facilities at CEA)
LED	Light Emitting Diode
μm/nm	Micrometre/Nanometre
MBE	Molecular Beam Epitaxy

micro-PL	Micro-PhotoLuminescence
$n/n_{eff}/n_g$	Refractive index/Effective refractive index/Group refractive index
$\mathbf{N}_2$	Nitrogen Gas
NA	Numerical Aperture
Nd-YAG	Neodymium-Doped Yttrium Aluminium Garnet
$\mathbf{NH}_3$	Ammonia
Ni	Nickel
NPSC	NanoPhysique et SemiConducteur laboratory
oFMM	Open-geometry Fourier Modal Method
$\mathbf{P}_{exc}/\mathbf{P}_{sat}$	Excitation Power/Saturation Power
PL	Photo-Luminescence
PML	Perfectly Matched Layer
PMMA	Poly(MethylMethAcrylate) - A photoresist
PSB	Phonon Side Band
PTA	Plateforme Technologique Amont (Upstream Technological Platform - academic cleanroom facilities at CEA)
Q	Quality Factor
QD	Quantum Dot
QNP	Quantum NanoPhotonics Group at KTH Stockholm
QuEnG	Quantum Engineering Grenoble - PhD funding programme
r_b/r_t	Modal Reflectivity of top facet/bottom mirror in the nanocavity
RIE	Reactive Ion Etching
$\mathbf{SF}_6$	Sulfur Hexafluoride
$\mathbf{S(NH_4)_2}$	Ammonium Sulfide
Sccm	Standard cubic centimetres per minute
SE	Spontaneous Emission
SEM	Scanning Electron Microscope
$\mathbf{SiCl}_4$	Silicon Tetrachloride
$\mathbf{Si_3N_4}$	Silicon Nitride
$\mathbf{SiO}_2$	Silicon Dioxide
SK	Stranski-Krastanov

SPS	Single-Photon Source
TCSPC	Time-Correlated Single Photon Counting
TE/TM	Transverse Electric/Transverse Magnetic
TEM	Transmission Electron Microscope
Ti	Titanium
Ti:Sa	Titanium Sapphire
TDC	Time to Digital Converter
TM	Transverse Magnetic
TPI	Two-Photon Indistinguishability
V	Volt
W	Watt
X/X*/XX	Neutral Exciton/Charged Exciton/Biexciton
ZPF	Zero Point Fluctuation
ZPL	Zero Phonon Line

Table of contents

List of figures

List of tables

Introduction

For centuries laws of classical physics have described phenomena in the physical world, until the late 19th century, when a few discoveries would necessitate the redefinition of fundamental rules that govern all material existence, and thus *quantum mechanics* was born. Quantum mechanics introduced concepts such as discrete energies, and wave-particle duality, which provided a clearer understanding of the atomic and subatomic worlds. Knowledge of the *'quantum'* nature of matter enabled new technologies such as transistors, lasers, the GPS, and solar cells, thus ushering the *first quantum revolution*. We often hear that we could be on the verge of a *second quantum revolution*, which is associated with technologies that directly exploit the *'strange'* properties of a quantum system, in particular *superposition* and *entanglement*.

Such a quest is driven by prospective applications in four main domains. Quantum communications enable the sharing of secret keys for data encryption with an intrinsic degree of security that is guaranteed by the laws of physics [1]. Quantum sensing and metrology aim at exploiting quantum systems to make high-resolution and highly sensitive measurements that surpass the capabilities of classical techniques [2, 3]. Quantum simulation focuses on studying large and complex real quantum systems, by drawing insights from simulations of the quantum effects of a controllable model systems [4]. Quantum computing exploits the quantum nature of physical systems to perform computations, whereby a general quantum computer could exponentially outperform a classical processor on certain kinds of calculations. [5].

At a fundamental level, quantum information can be encoded on the state of ensembles of two-level quantum systems, referred to as *quantum bits* (or simply *'qubits'*). Some popular examples of material systems used to define qubits are atoms [6], trapped ions [7], molecules [8, 9] and superconducting Josephson junctions [10]. Generally speaking, matter qubits are particularly well suited to realise quantum simulators or processors.

Alternatively, quantum information can also be stored on a single-photon (for example on the polarisation degree of freedom), thus creating a flying qubit that interacts weakly with its environment and offers a long coherence time. Photons can be transmitted over long distances with minimal losses, either in free space or through fibre-optic cables. As such, they constitute a system of choice for quantum communications. Quantum key distribution has been demonstrated with single photons and entangled photon pairs [11, 12]. Quantum

teleportation paves the way towards a *'quantum internet'* [13, 14], and enables photons to mediate interactions between distant matter qubits [15, 16]. In quantum metrology, entangled photons have enabled high-precision measurements with a sensitivity attaining the fundamental Heisenberg limit [17, 18]. Such quantum-enhanced sensing has been demonstrated in phase-contrast microscopy [19], low energy probing of a sensitive atomic spin ensembles [20], and for measuring the concentration of biological molecules [21]. Photonic quantum computing has witnessed encouraging results with the demonstration of several single-qubit [22] and multi-qubit [23, 24] gates, that have enabled several quantum computing tasks [25–27]. Photonic logic gate architectures have been implemented to perform several quantum simulation tasks [28–31], in particular in Boson sampling experiments [32]. Apart from computations based on uncorrelated photons, entangled multi-photon cluster states [33] have emerged as realistic platforms for scalable photonic quantum computing [34].

Most of the above-mentioned applications rely on the efficient generation of quantum states of light, of which the simplest, yet crucial, is a single-photon state. An ideal single-photon source must be capable of generating exactly one photon on demand, which is identical to photons emitted before it, and to those emitted by a different source. Despite impressive progress in the last decades, there is still a large global effort in research towards improving the performance of single-photon sources. Such sources broadly fall into two categories. Probabilistic sources exploit non-linear processes to generate photons in pairs [35–38]. One photon of the pair is then used to herald the emission of the other photon. In contrast, deterministic sources can generate single photons on demand. They are based on single quantum emitters, such as single atoms [39], single ions [40], single molecules [41], colour centers [42–44] and semiconductor quantum dots [45].

A quantum dot (QD) is a nanometric semiconductor *'island'* embedded in a semiconductor matrix of a higher bandgap. This bandgap contrast allows the QD to trap charge carriers (electrons and holes) in the three directions of space, which leads to discrete electronic states, much like a real atom. Direct bandgap semiconductors are of particular interest since they present optically active transitions between these states. There exists several methods to produce self-assembled QDs [46], of which some examples include chemical synthesis [47], Stranski-Krastanov (SK) epitaxy [48], droplet epitaxy [49], and nanowire epitaxy [50]. We focus here on SK epitaxial self-assembled QDs in the InAs/GaAs material system as emitters of non-classical states of light [51]. These emitters offer a fast and stable emission, without any blinking and photo-bleaching, attaining a near-unity radiative yield [52, 53]. Single photons can be generated by spectrally filtering the emission from the recombination of an exciton (electron-hole bound state) [54–56]. Additionally in an ideal QD, the emissions associated with the radiative cascade of a biexciton (doubly-bound pair of electron-hole state) generate a pair of polarisation-entangled photons [57–59]. Finally, cluster states of entangled photons have also been generated with QDs [60].

The practical implementation of self-assembled QDs as photon emitters raises several challenges. Since the QD is enclosed in a material of high refractive index (GaAs in our case, $n = 3.5$), most of the emitted light undergoes internal reflections, letting only $\sim$2% of the light escape [61]. A QD is also susceptible to interact with various sources of decoherence, which broaden the spectrum of the emitted photons. These include acoustic phonons [62–65], fluctuating charges trapped in the QD surroundings [66, 67] and nuclear spins which overlap with the trapped carrier wavefunction [67]. Finally, self-assembled QDs display a dispersion in emission energy due to their individually differing morphology [68]. Such a dispersion is a particular hindrance towards applications that require the interference of identical photons emanating from different sources.

State-of-the-art QD devices generally employ a photonic structure that defines a controlled electromagnetic environment around the emitter. The first major objective is to funnel the QD spontaneous emission (SE) into a controlled channel (a free-space output beam or a guided mode in the case of integrated optics). Among the various approaches investigated so far, one can cite two families of structures: optical microcavities and waveguides. A microcavity exploits the Purcell effect to selectively accelerate SE into the cavity mode. With a large acceleration, the cavity mode becomes the dominant SE channel [69]. Accelerating SE also makes the radiative recombination less sensitive to decoherence, thus considerably facilitating the generation of indistinguishable photons [70–73]. While very successful, this approach is however intrinsically limited to the narrow operation bandwidth defined by the microcavity mode. Waveguides on the other hand rely on the preferential coupling of the emission to a guided mode, by suppressing the emission into all other "unwanted" modes [52, 74–76]. The main advantage of waveguides over microcavities is their wide operation bandwidth. The latter is a key asset to realise wavelength-tunable single-photon sources or to simultaneously collect several detuned QD transitions. However, waveguides generally lack any significant SE acceleration, making the emission of indistinguishable photons more challenging.

The research team at CEA Grenoble, in which this work was carried out, has pioneered the development of photonic nanowire antennas embedding QDs [75]. The antenna is based on a waveguide made of a dielectric material with a large refractive index n. A diameter of the order of λ/n (λ is the free-space operation wavelength) offers optimal lateral confinement of the fundamental guided mode. At the same time, SE into the other free-space modes is strongly inhibited thanks to a dielectric screening effect [52]. As a result, the fundamental guided mode is the preferential emission channel for the QD. To optimise the collection of the guided photons in the far-field, the nanowire stands on a planar mirror and its top extremity is tapered. This taper can either have a needle-like shape [77] or an inverted cone shape, nicknamed 'a photonic trumpet' [78]. Both structures offer a large collection efficiency (predicted value above 0.9), a Gaussian output beam, and a broad operation bandwidth.

Using this approach, bright and pure single-photon sources have been demonstrated [77, 79, 78, 50]. The broad operation bandwidth of the antenna has been exploited to realise wavelength-tunable single-photon sources [80, 81]. It was also key to demonstrate sources of entangled photon pairs [82, 83], and triply correlated photons [84]. Beyond quantum light sources, the QD-antenna system can also be used to enhance optical nonlinearities. For example, giant two-mode nonlinearity was demonstrated in Ref. [85]. Such a system can also enhance the four-wave mixing signal generated by a single QD by several orders of magnitude [86].

Despite all these promising results, the emission of indistinguishable photons with a QD-nanowire system is still to be demonstrated. At a temperature of 4 K and under resonant excitation, the spectral linewidth of the excitonic emission was measured to be around 5 μeV in the best case [87]. This value is around 10 times higher than the radiatively-limited linewidth (0.7 μeV for an excitonic lifetime of 1 ns). Interestingly, the noise spectroscopy conducted in Ref. [87] also showed that the first few thermally-excited low-frequency vibration modes of the nanowire have a significant impact on the QD linewidth. The large coupling to vibrations is a clear asset in the context of hybrid nanomechanics [81, 88–90]. However, it is a nuisance for applications in quantum photonics.

My PhD project aimed at controlling the spectral properties of the photons that are emitted by a semiconductor QD embedded in a photonic nanowire antenna. The results of this manuscript tackle this challenge along three main directions.

- First, we conduct a theoretical study that unveils a decoherence mechanism, specific to nanowire systems. We show that, even at cryogenic temperature, the thermal vibrations of the nanowire induce a large spectral broadening that prevents the emission of indistinguishable photons. We propose three designs that suppress this decoherence channel thanks to an engineering of the nanowire mechanical properties. These results have been published in *Phys. Rev. Lett.* [A.1].

- Next we introduce a new type of optical nanocavity which is based on a nanowire segment. Despite its simplicity, the device offers a large acceleration of spontaneous emission (predicted Purcell factor of 6.3) that is maintained over a 30-nm-wide operation bandwidth. The photonic design was conducted in collaboration with the group of Niels Gregersen (DTU Fotonik, Denmark). We fabricate a GaAs nanocavity that embeds InAs self-assembled QDs. Single QD spectroscopy reveals a maximal acceleration of spontaneous emission by a factor as large as 5.6 and a first lens collection efficiency of 0.35. A large SE rate is indeed an advantage for emitting indistinguishable photons. The broad operation bandwidth is compatible with QD wavelength tuning and with the collection of several detuned transitions. These results have been published in *Appl. Phys. Lett.* [A.2].

- Finally, we propose a strategy to tune the emission wavelength of a QD embedded in a nanowire antenna. On-chip electrodes generate an electrostatic force that bends the nanowire and the resulting strain modulates the QD bandgap energy. We realise a first generation of devices and discuss preliminary wavelength tuning measurements. Such tuning is interesting for applications involving several resonant sources, or for the investigation of collective effects (which involve several emitters) such as superradiance.

In the course of my PhD project, I have been responsible for various tasks. I ran finite element simulations using the COMSOL Multiphysics software to model the vibration modes of nanowire devices. I then programmed a routine on MATLAB to determine the impact of these thermally-driven vibrations on the optical properties of the embedded QD. COMSOL simulations were also employed for the design of strain-tunable photonic trumpets. I participated in the cleanroom processing of nanocavities and strain-tunable trumpets. In particular, together with Alberto Artioli (postdoc in the team), we improved the flip-chip process and developed a new inductively coupled plasma etching recipe at the PTA cleanroom. Finally, I conducted all the optical experiments on the nanocavity devices (micro-photoluminescence, polarisation analyses, time-resolved measurements). I was also involved in a project that is not detailed in this manuscript, in which we fabricated a first generation of trumpet antennas embedding QDs emitting at telecom wavelengths. I characterised these devices during a two-month stay in the group of Val Zwiller at KTH Stockholm.

This manuscript is organised as follows:

Chapter 1 first introduces the electronic and optical properties of self-assembled quantum dots. Then we discuss two major classes of nanostructures employed to control the spontaneous emission of the QDs, namely microcavities and waveguides. Finally, we elaborate physical and optical properties of photonic wire antennas.

Chapter 2 is centred on the theoretical work which investigates the impact of low-frequency thermal vibrations in QD-nanowire antennas. We begin by reviewing the impact of bulk acoustic phonons on the coherence of QD emission. We take the example of an infinitely-long nanowire to illustrate how a reduction of the dimensionality modifies the QD-phonon interaction. We then discuss the specific case of the discrete vibration modes supported by nanoantennas and present our main results. Importantly, we propose three designs that exploit nanomechanical engineering to suppress this decoherence channel.

Chapter 3 presents the nanowire optical nanocavity, which is designed for free-space emission. We elaborate on the design considerations of the structure and describe the fabrication of an Au-SiO_2-GaAs device embedding isolated self-assembled InAs QDs. We conclude the chapter with the results of optical characterisation experiments.

Chapter 4 proposes a wavelength-tunable single-photon source that is based on a photonic trumpet that can be bent with on-chip electrodes. We describe the tuning mechanism and the design of the device. Then we detail the device fabrication process before presenting preliminary experimental results.

Chapter 1

Self-assembled quantum dots in photonic nanostructures

The objective of this chapter is to lay down the fundamental concepts required to appreciate and understand the studies and results described in the subsequent chapters. The first section presents the electronic and optical properties of self-assembled quantum dots (QDs). A key feature of QDs is that they operate much like artificial atoms. These solid-state nanostructures can thus be employed to emit various non-classical states of light on-demand. However, they are generally embedded in a bulk semiconductor material of a much higher refractive index, which in turn poses a challenge in extracting the emitted photons from the QD. The environment of the QD also introduces sources of noise that can degrade the optical properties of the QD. In the second section, we will discuss ways of engineering the photonic environment of the QD to control its spontaneous emission (SE), as well as collecting it efficiently. We will address two widely implemented families of photonic nanostructures, namely microcavities and waveguides. In the last section, we make a detailed description of photonic wire antennas, a class of waveguide structures designed for photon emission into free space.

1.1 Properties of self-assembled InAs/GaAs quantum dots

1.1.1 Fabrication and morphology

The core goal of my PhD project has been to develop and improve the performance of semiconductor single-photon sources based on photonic nanowires. In the course of this project, the emitters of single-photons that I worked with were self-assembled QDs made of indium arsenide (InAs) and embedded in a gallium arsenide (GaAs) matrix. Both these materials are III-V semiconductors, where Ga and In belong to group III and As belongs to group V of the periodic table.

Table 1.1 Some relevant properties of InAs and GaAs. The data presented here was obtained from Ref. [91].

	InAs	GaAs
Lattice parameter at 300 K (Å)	6.0584	5.6533
Bandgap energy at 300 K (eV)	0.36	1.42
Bandgap energy 4 K (eV)	0.42	1.52

Epitaxial QDs, like the ones I studied, are realised by a self-assembling process during growth by molecular beam epitaxy (MBE). The widely used Stranski-Krastanov (SK) method is employed to grow heterostructures with monolayer (ML) precision under ultra-high vacuum (with pressure around 10^{-12} mbar), to avoid impurities and defects. The SK method relies on a growth mode theorised by I. Stranski et L. Krastanov in 1938 [92] and experimentally demonstrated with InAs/GaAs by L. Goldstein et al. in 1985 [48]. In our case, this entails growing InAs on a planar wafer of GaAs. In practice, a substrate of GaAs is placed within a high vacuum MBE chamber and molecular jets of the materials to be grown (Ga, In, As), which are evaporated in effusion cells, are targeted towards the substrate. The precise control of growth is achieved by adjusting the substrate temperature and the molecular fluxes.

The SK growth is favoured when using materials that present a large lattice mismatch and high interaction strength between adatoms (atoms adsorbed on the surface) and the growth surface. From Table 1.1, we find there is a lattice mismatch of $\sim$7% between GaAs and InAs. Fig. 1.1 illustrates the SK growth mode. In the beginning, the InAs adapts to the substrate forming a uniform planar layer. However beyond a critical thickness of 1.7 ML the elastic energy of the InAs layer, induced by the lattice mismatch is too strong to maintain its planar topology. Therefore the InAs relaxes the elastic energy by nucleating into islands on a 1 ML thick residual 2D layer that is called the wetting layer (WL). The islands are capped with a layer of GaAs, in order to prevent them from oxidising and interacting with surface states. This completes the formation of the self-assembled QDs. While InAs QDs are pyramidal before capping, this encapsulation with GaAs causes a redistribution of In atoms due to surface segregation and some diffusion of Ga into InAs, thus leading to the spherical lens-like shape of QDs. This inhomogeneous distribution of InAs causes a position-dependent strain across the QD.

Fig. 1.2 illustrates a cross-section view of an InAs QD within a GaAs matrix. The image was obtained using a transmission electron microscope (TEM). QDs grown following the method described earlier usually have a height ranging between 1 nm and 5 nm and a diameter ranging between 10 nm and 20 nm. The dimensions of the QDs depend on the specific growth parameters implemented. However, since the QDs form by a self-assembly process, which is stochastic, in addition to a random spatial distribution of QDs, there also

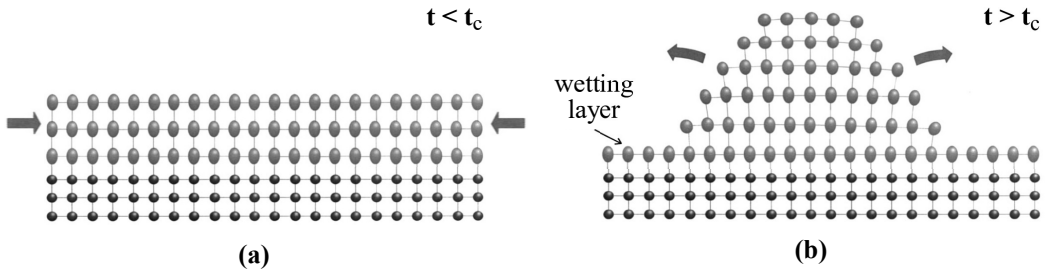

Fig. 1.1 Schematic representation of the Stranski-Krastanov growth mode. The small dark circles represent GaAs, which has a smaller lattice constant, and the large pale circles represent InAs. (a) For InAs layer thickness t, less than the critical thickness t_c, InAs adapts to form a planar layer. The horizontal arrows represent the lateral lattice compression experienced by InAs. (b) The InAs layer clumps to form a small 3D island, elastically relaxing strain (outward arrows) [93].

exists a dispersion in QD dimensions, shape, and composition, across a sample from a single growth. The dispersion in QD size is typically around 10% and the spatial density strongly depends on growth conditions and can vary from as little as 1 QD μm^{-2} to as much as several 100 QDs μm^{-2} [94].

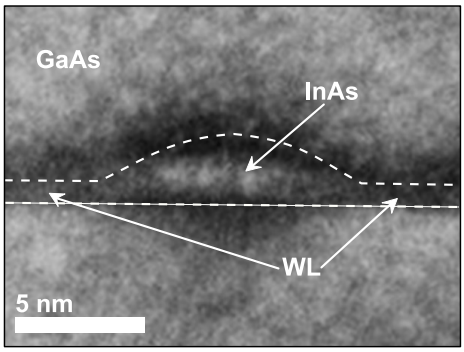

Fig. 1.2 TEM image of an InAs QD cross-section embedded in GaAs. In the image, we can identify a spherical lens-like island which is the QD, with a thin 2D InAs layer on either side representing the WL. The region around the QD is GaAs. This image was obtained from A. Ponchet (CNRS/CEMES) Toulouse, captured on a sample fabricated by J.M. Gérard (France Télécom/CNET, 1993).

1.1.2 Electronic states

1.1.2.a. Electronic states of bulk semiconductor

An individual atom consists of electrons that occupy well-defined discrete energy levels. In the case of two like-atom molecules, the individual atoms form bonds with one another via a hybridisation of orbitals, which lifts the degeneracy of their energy levels and gives rise to additional energy levels. In a crystal lattice, a multipartite interaction gives rise to energy bands separated by forbidden zones. Electrons populate these bands following Fermi-Dirac

statistics. Among the various energy bands, the two that are of particular interest are the conduction band and the valence band. The valence band is the last completely occupied band and the conduction band corresponds to the band where electrons are not bound to any individual atom and can move all across the crystal. The difference in energy between the two bands is known as the energy gap or the bandgap. A semiconductor presents a conduction band that is empty at absolute zero temperature but has a sufficiently narrow bandgap, such that the probability of transferring electrons to the conduction band is non-zero. Electrons in a semiconductor can be excited to a conduction band by optical or thermal excitation.

Due to the periodicity of the crystal, the electrons experience a periodic potential. Therefore, the electronic wavefunctions may be expressed by a Bloch functions of the form,

$$\Psi_{n,\mathbf{k}}(\mathbf{r}) = \exp(i\mathbf{k}\cdot\mathbf{r})u_{n,\mathbf{k}}(\mathbf{r}). \tag{1.1}$$

Thus $\Psi_{n,\mathbf{k}}(\mathbf{r})$ is represented as a plane wave with wavevector $\mathbf{k}$, whose amplitude is modulated by the function $u_{n,\mathbf{k}}(\mathbf{r})$ that has the same periodicity as $V(\mathbf{r})$. There exists several methods to determine the energy band structure of the crystal, which is the evolution of the energy eigenvalues E_n associated to the different Bloch states, as a function of $\mathbf{k}$.

The energy band structure of GaAs, calculated by a local pseudopotential method, can be seen in Fig. 1.3. A point of particular interest on the energy plot is denoted by Γ, which corresponds to the energy at $\mathbf{k} = \mathbf{0}$, (the centre of the first Brillouin zone). The negative energy plots correspond to valence band states and the positive energy plots represent conduction band states. In the case of GaAs, we find that the maximum of the valence band and the minimum of the conduction band coincide at Γ, which shows that GaAs has a direct bandgap.

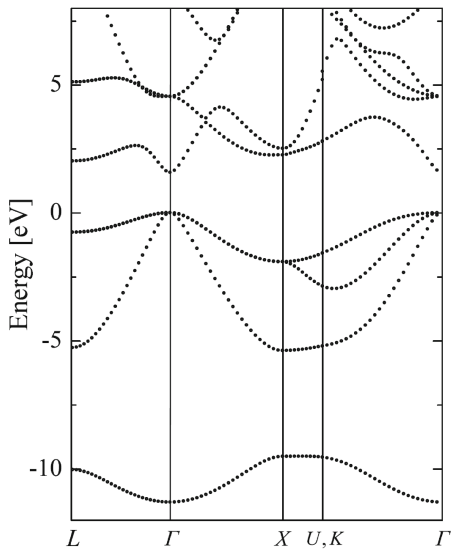

Fig. 1.3 Energy band structure of GaAs obtained from a pseudopotential method [95].

In the case of a direct bandgap semiconductor, which includes all III-V semiconductors, all optical properties can be described from the knowledge of the band structure in the proximity of Γ, the centre of the first Brillouin zone. The band structure around the Γ point can be evaluated using the $\mathbf{k}\cdot\mathbf{p}$ method. The $\mathbf{k}\cdot\mathbf{p}$ method consists in solving the Schrödinger equation for $\mathbf{k}=\mathbf{0}$ to determine $\mathbf{u}_{n,\mathbf{0}}(\mathbf{r})$ and $E_{n,\mathbf{0}}$, then to extrapolate the band structure over the entire Brillouin zone ($\mathbf{k}\neq\mathbf{0}$) by applying perturbation theory. The $\mathbf{k}\cdot\mathbf{p}$ method also makes it possible to obtain analytic expressions for effective mass and band dispersion around points of symmetry [96]. A detailed treatment of this method may be found in Ref. [95].

The energy bands in the vicinity of Γ can be approximated by parabolas, having the form $E_{edge}\pm\hbar^2k^2/2m^*$, where E_{edge} represents the band edge. Electrons occupying these energy bands behave like free-space electrons, as long as the electron energy remains within the range of validity for the parabolic band approximation. The electrons in the energy bands appear to possess a mass, called effective mass (m^*), which is different from the free-space electron mass. This is called the effective mass approximation.

Solving the Schrödinger equation, at the Γ point, yields wavefunctions that are characterised by an orbital angular momentum **L**. In particular, L = 0 for the conduction band and L = 1 for the valence band, where L is the quantum number associated with the eigenvalues L^2 from $\hbar^2L(L+1)$. Disregarding spin-orbit coupling entails a three-fold degeneracy of the valence energy bands with $m_l=0, m_l=\pm1$. The magnetic quantum numbers, m_l are the eigenvalues of L_z which is the z component of **L**. The three degenerate valence band states are known as the light-hole, heavy-hole, and split-off energy bands. It must also be noted that each orbital bands are doubly degenerate in spin.

Taking the spin-orbit interaction into account implies the addition of the spin orbit Hamiltonian to the Schrödinger equation. This interaction term is proportional to $\mathbf{L}\cdot\sigma$. The resulting solutions are eigenstates of the total angular momentum, $\mathbf{J}=\mathbf{L}+\sigma$ and its z component J_z. For L = 1 and $\sigma=1/2$ one obtains J = $3/2, 1/2$, while the eigenvalues j_z of J_z can take any of the $2j+1$ values, $J, J-1, ..., -J+1, -J$. The spin-orbit coupling thus causes the split-off band to shift to a lower energy, thus lifting the otherwise three-fold degenerate valence band. The spin-orbit coupling doesn't affect the conduction band, since its orbital angular momentum is L = 0 [96].

An external biaxial compressive strain exerted on the semiconductor matrix lifts the remaining two-fold degeneracy of the valence band. As a result of this strain, the light-hole band is shifted towards lower energy in the order of several tens of meV [97, 98]. These shifts in energy are sufficiently large to consider only the heavy-hole state as the valence band of the system. This effect is particularly relevant for systems embedded in a host material, such as the InAs wetting layer and QDs in GaAs. The nature of lifting degeneracy between the light-hole and heavy-hole states depends on the geometry and the material composition of the system. In some situations, the energy shift may be reversed, in which

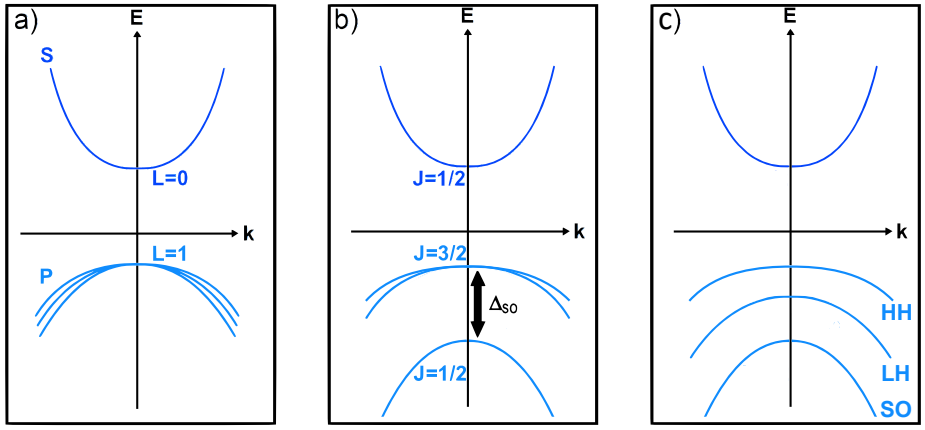

Fig. 1.4 Schematic representation of energy band structure near Γ of direct gap semiconductors, (a) not considering spin-orbit coupling, (b) taking spin-orbit coupling into account, (c) including effects of biaxial compressive strain experienced by the QD from the surrounding semiconductor matrix. Δ_{SO} denotes the energy difference between the $J = 3/2$ and $J = 1/2$ valence bands.

case the valence band would be simplified to only the light-hole state. These scenarios are dealt with in more depth in Ref. [97]. Fig. 1.4 depicts the conduction and valence bands of a direct gap semiconductor in the vicinity of Γ for all the situations discussed above.

The description so far of the band structure has addressed 3D bulk semiconductors. The effects of external strain were invoked only to present the lifting of degeneracy in the valence band. However, once we begin to deal with structures of reduced dimensionalities, the electron (hole) wavefunction gets confined leading to a progressive quantisation of quantum numbers in the direction of confinement. This confinement in turn affects the density of states (DOS) until for a 0D structure, such as a QD, the DOS spectrum is completely discretised, much like an atom. This outcome gives the QD its nickname of "artificial atom". Fig. 1.5 summarises the effects of confinement on the energy DOS. In practice, such confinement is achieved by introducing a semiconductor with a small bandgap into a surrounding semiconductor matrix with a larger bandgap. This difference in bandgap produces a potential barrier that allows trapping of charge carriers.

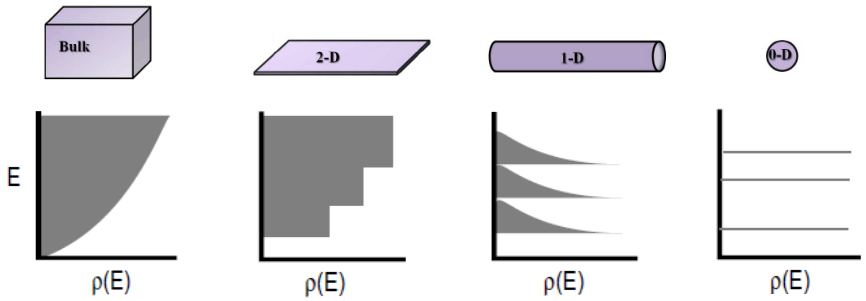

Fig. 1.5 Density of states corresponding to various degrees of spatial confinement.

1.1.2.b. Electronic states of the wetting layer

Having presented the electronic states in a 3D bulk semiconductor, we consider the electronic states of our system of interest, namely the QD and the WL. As presented in Sec. 1.1.1, in our case, the WL is a 2D layer of InAs on which the QDs are scattered. This 2D layer represents a quantum well that confines carriers only in the growth (z) direction, while the carriers are free to move in the (x,y) plane. The electronic states of the WL may be determined following an envelope function formalism[98], which consists in describing the wavefunctions of the carriers by Bloch functions of the form,

$$\Psi_{j,\mathbf{k}}(\mathbf{r}) = \phi_{n,j}(\mathbf{r})u_{j,\mathbf{k}}(\mathbf{r}). \tag{1.2}$$

In the Bloch functions used for the 3D semiconductor case (Eqn. **??**), the plane wave term $e^{i\mathbf{k}\cdot\mathbf{r}}$, characterised the translational invariance in the bulk crystal. Here this term is replaced by the envelope function $\phi_{n,j}$, that varies gradually on the scale of the crystallographic lattice, and arises from the confinement of carriers. This envelope function may be expressed as a product of a plane wave component delocalised in the (x,y) plane and a term corresponding to a localised state in the z direction,

$$\phi_{n,j} = e^{i\mathbf{k}_p\cdot\mathbf{r}_p}\Phi_{n,j}(z), \tag{1.3}$$

where n is the quantum state number localised along z, and j is the band index. Each band corresponds to its energy level $E_{n,j}$ which exhibits a 2D continuum. The density of states, as illustrated in Fig. 1.5, features a step-like trend. In the case of a 1 ML thick InAs quantum well, only the first quantum state ($n = 1$) is confined, thus the DOS presents only one step. In reality, the WL comprises rough step-like layers rather than a uniform 2D layer. These defects behave somewhat like spread-out QDs, thus replacing the 2D quasi-continuum by more-or-less localised states, which has the effect of softening the abrupt step-like features of the DOS to eventually resemble more like Fig. 1.6.

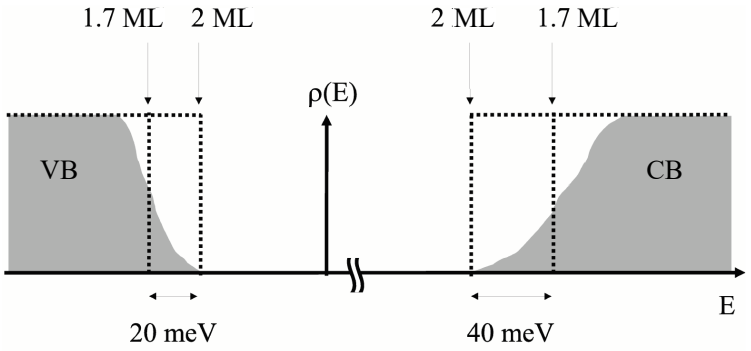

Fig. 1.6 Schematic representation of the density of states of the wetting layer, where ML = monolayer, VB = valence band, and CB = conduction band [99].

1.1.2.c. Electronic states of a quantum dot

A QD is a 0D nanostructure that confines carriers in all three spatial directions, thus giving rise to discrete energy levels, much like an atom. Self-assembled InAs QDs in particular have a lens-like shape, which is flattened in the growth direction (z direction or [001] crystallographic axis). Additionally, such QDs often feature an in-plane ellipticity. The realistic confinement potential of such a system thus doesn't present any symmetries nor is it separable, thus making it impossible to solve the system analytically. In order to describe the physical phenomena of the system, its morphology may be approximated to a flattened cylinder [99, 100]. The confinement potential, in this case, comprises the anisotropy of confinement between the z axis and the (x,y) plane, and the strain experienced by the QD from the surrounding semiconductor matrix. Under the simplified geometry of the QD, the confinement potential now presents a cylindrical symmetry around the z axis. The discrete energy levels arise from the valence (heavy-hole) and conduction bands.

The allowed energy levels may be calculated following an envelope function formalism, using a function similar to Eqn. 1.2. $\phi_{n,j}(\mathbf{r})$, in this case, comprises a product of a term expressing the confinement along the growth direction, and a term that describes the lateral confinement in the (x,y) plane, which also has cylindrical symmetry. This lateral component is expressed in the envelope eigenstate basis $\{|L,m_z\rangle\}$, which are quantum numbers related to the L^2 and L_z operators. Analogous to the WL only the first quantum state ($n=1$) is bound.

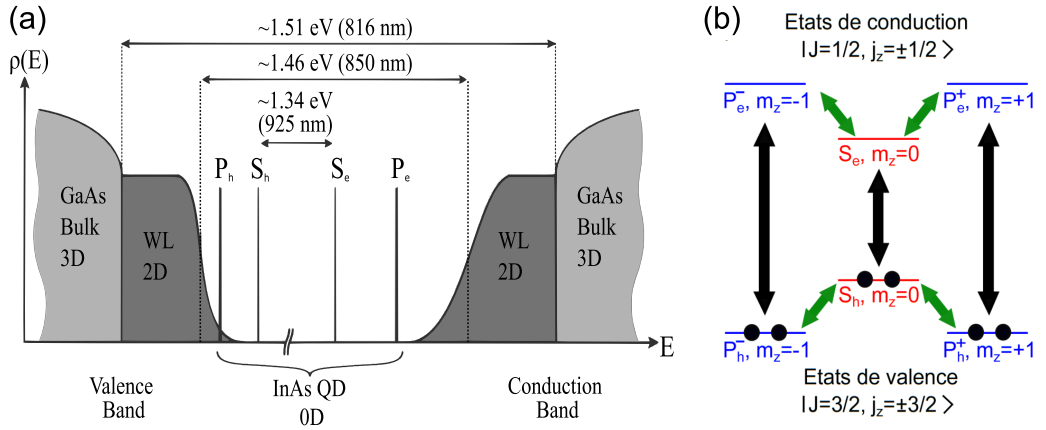

Fig. 1.7 Electronic states of an InAs/GaAs QD. (a) Schematic diagram of the density of states corresponding InAs/GaAs QD system. Values of energy gaps indicated here correspond to typical values at $T \approx 4K$ for QDs used in this work. (b) The ground state of the QD with its valence band completely occupied by electrons, represented by black dots. The arrows correspond to the allowed transitions between the different envelop states. Black arrows represent interband transitions, while green arrows represent intraband transitions. Figures adapted from Ref. [101].

The bandgap difference between InAs QDs and the surrounding GaAs matrix translates into a finite potential well for bound carriers in the QD. This implies that the QD can

possess only a limited number of confined states. For QDs with sub-micron emission wavelength, like the ones used in this work, only the states corresponding to envelope functions with $L = 0$ and $L = 1$ are bound (corresponding to S and P states from an atomic physics analogy). For larger QDs with longer emission wavelengths, D states ($L = 2$) must also be included among bound states. The InAs/GaAs QD system may be completely described with a density of states representation, such as the one in Fig. 1.7 (a). The values presented correspond to typical values for QDs used in this work, at cryogenic temperature ($T \approx 4K$). These values may vary with the morphology and growth condition of the QDs. Let S_e and P_e (S_h and P_h) be the confined states of the conduction band (the valence band), which are the only states available to carriers trapped in a QD. Fig. 1.7 (b) portrays the ground state of a QD, with its valence band completely occupied.

A more realistic QD shape (e.g. lens-shaped) exhibits some qualitative differences from the discussion above. The wavefunctions of the carriers no longer extend until the edges of the QD, thus the lateral confinement effects are stronger. The QD at a constant height has fewer energy states than a cylindrical QD of the same height, and the wavefunction of the first states are localised closer to the centre of the QD [102].

1.1.3 Optical transitions of a quantum dot

1.1.3.a. Optical selection rules

A QD in its fundamental (ground) state features a filled valence band and an empty conduction band. An electron from the valence band may absorb energy from a photon and jump to the conduction band. The initial and final states of the electron may be expressed in terms of an envelope function ϕ and atomic components u as $|\psi_i\rangle = |u_i\rangle|\phi_i\rangle$ and $|\psi_f\rangle = |u_f\rangle|\phi_f\rangle$. The interaction between the electron and the electromagnetic field may be expressed using the dipole approximation as, $H = -\mathbf{D}\cdot\mathbf{E}$, where $\mathbf{D}$ and $\mathbf{E}$ are the electric dipole and electromagnetic field operators, respectively. Higher-order terms are ignored since the QD is much smaller than its emission wavelength.

The transition probability thus depends on the matrix element:

$$\langle\psi_f|H|\psi_i\rangle = -\mathbf{E}\cdot\langle\phi_f|\mathbf{D}|\phi_i\rangle\cdot\langle u_f|u_i\rangle - \mathbf{E}\cdot\langle\phi_f|\phi_i\rangle\cdot\langle u_f|\mathbf{D}|u_i\rangle. \tag{1.4}$$

The first term is non-zero only if $|u_f\rangle = |u_i\rangle$: it corresponds to intraband transitions (see Fig. 1.7). In addition, $\langle\phi_f|\mathbf{D}|\phi_i\rangle$ must be non-zero for permissible transitions. This requirement leads to the selection rule for the z-projection of the total angular momentum of the envelope function, $\Delta m_z = \pm 1$. Intraband transitions generally occur between P_e and S_e. The size and shape of the QD stongly influence the energy spacing, which for InAs QDs has been measured between a few tens to a few hundreds of meV [103, 104]. The second term in the transition probability equation describes the interband transition:

$\langle u_f|\mathbf{D}|u_i\rangle$ is non-zero for $|u_f\rangle \neq |u_i\rangle$. In addition, allowed interband transitions conserve the envelope state, i.e. $|\phi_f\rangle = |\phi_i\rangle$ ($S_e \leftrightarrow S_h, P_e \leftrightarrow P_h$). This condition is satisfied for transitions presenting a variation of the z-projection of the total angular momentum, of $\Delta j_z = \pm 1$. In this work, we focus on the interband transitions.

1.1.3.b. Bright and dark excitons

When an electron from the valence band makes an interband transition to the conduction band, it leaves a vacancy in the valence band. This absence of an electron is treated as a positive pseudo particle, called a "hole", which has the same characteristics as an electron, except having the opposite sign. An attractive Coulombic interaction between the electron and the hole leads to the formation of the bound state, known as an "exciton" (X), which lowers the overall energy of the system. Spontaneous emission (SE) results from the radiative recombination between an electron and a hole.

The ground states of an electron in the conduction band S_e are,

$$|e\uparrow\rangle = |J = 1/2, j_z^e = +1/2\rangle, \qquad |e\downarrow\rangle = |J = 1/2, j_z^e = -1/2\rangle, \tag{1.5}$$

and those of a hole in the heavy-hole valence band S_h are,

$$|h\Uparrow\rangle = |J = 3/2, j_z^h = +3/2\rangle, \qquad |h\Downarrow\rangle = |J = 3/2, j_z^h = -3/2\rangle. \tag{1.6}$$

From these states we can envisage a total of four separate electron-hole pair bound states, or exciton states. We only consider electron-hole bound states constructed with S envelop states because only the S_eS_h transition exists well isolated spectrally, while the P_eP_h transition overlaps a spectral quasi-continuum due to the QD-WL crossed transitions. These exciton states can be identified by the sum of the z-projection of the total angular momentum as follows,

$$\begin{aligned}
|e\downarrow, h\Downarrow\rangle &= |\downarrow\Downarrow\rangle \equiv |j_z^{eh} = -2\rangle,\\
|e\uparrow, h\Downarrow\rangle &= |\uparrow\Downarrow\rangle \equiv |j_z^{eh} = -1\rangle,\\
|e\downarrow, h\Uparrow\rangle &= |\downarrow\Uparrow\rangle \equiv |j_z^{eh} = +1\rangle,\\
|e\uparrow, h\Uparrow\rangle &= |\uparrow\Uparrow\rangle \equiv |j_z^{eh} = +2\rangle.
\end{aligned}$$

Only two of the four exciton states obey the selection rule for optical interband transitions and thus only $|\uparrow\Downarrow\rangle$ and $|\downarrow\Uparrow\rangle$ are optically active. They are referred to as bright excitons. They emit left (σ^-) and right (σ^+) circular-polarised photons, respectively. The states $|\downarrow\Downarrow\rangle$ and $|\uparrow\Uparrow\rangle$, on the other hand, are not optically active and are known as dark excitons. Some mechanisms can flip the spin of a hole or an electron, thereby converting

a dark exciton into a bright one, the latter in turn may recombine radiatively and emit a photon.

1.1.3.c. Photoluminescence of a quantum dot

In a typical non-resonant photoluminescence (PL) experiment (Fig. 1.8), the excitation energy of the laser is set higher than the GaAs bandgap. This results in the generation of carriers in the bulk material, which diffuses through the WL before randomly being captured by the QD, hence occupying its various energy levels. The radiative recombination of these carriers would produce several emission lines in the luminescence spectrum, corresponding to the various optical transitions. Individual lines can be filtered spectrally and their corresponding transitions be determined by methods such as power dependence of the emission intensity [105], correlation measurements, [106] and analysis of the fine structure in the presence of a magnetic field [107].

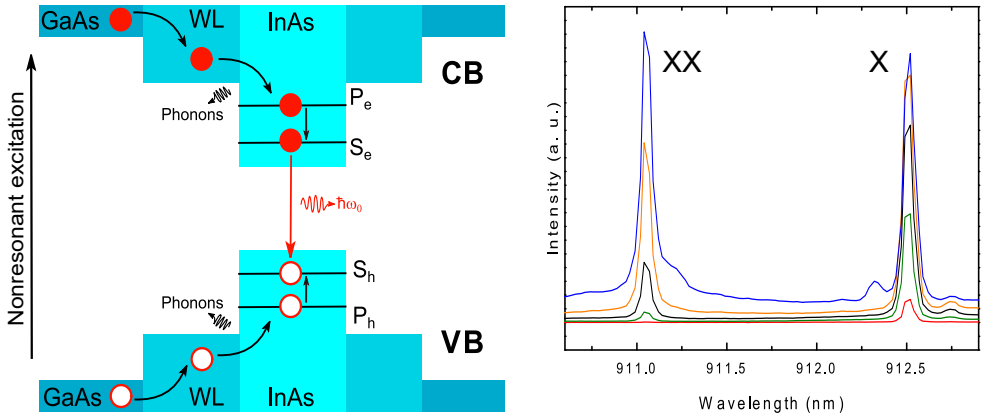

Fig. 1.8 QD photoluminescence. For non-resonant excitation, the laser generates free carriers in the semiconductor surrounding the QD. These free carriers diffuse through the WL to be captured by the QD, where they recombine to emit photons. The right panel shows a sample micro-PL spectrum of an exciton (X) and the corresponding biexciton (XX) at different excitation power.

Similarly, a single optical transition may be selectively probed via resonant photoluminescence. This is achieved by tuning the central energy of the laser excitation to match the desired optical transition. This method of excitation ensures little energy is injected into the QD environment, thus preventing incoherent processes from influencing the spontaneous emission[108].

1.1.3.d. Fine structure of a neutral exciton

As introduced in Sec. 1.1.3.b., an electron-hole pair, or a neutral exciton, features four distinct quantum states. Two of these states are coupled to light while the other two are not, known as the bright and dark excitonic states respectively. Coulomb interactions between

the electron and hole lift this degeneracy. The Coulomb interaction consists of two terms, one a direct attractive interaction, and a second exchange term. The exchange interaction term is responsible for the coupling of spins of the electron and hole, which results in the lifting of degeneracy between the bright and dark exciton states.

Let σ_e and σ_h be the spin of an electron and a hole respectively. The short-range part of the exchange interaction of the electron-hole pair may be expressed as [109],

$$H_{exchange} = -\sum_{i=x,y,z} \left(a_i \sigma_{h,i} \cdot \sigma_{e,i} + b_i \sigma_{h,i}^3 \cdot \sigma_{e,i} \right), \tag{1.7}$$

where a_i and b_i are the spin coupling coefficients along every direction, with z corresponding to the growth direction. Using the total angular momentum eigenstates of the exciton $\{|+1\rangle, |-1\rangle, |+2\rangle, |-2\rangle\}$ as a basis, the matrix formulation of $H_{exchange}$ is expressed as [109],

$$H_{exchange} = \frac{1}{2} \begin{pmatrix} \delta_0 & \delta_1 & 0 & 0 \\ \delta_1 & \delta_0 & 0 & 0 \\ 0 & 0 & -\delta_0 & \delta_2 \\ 0 & 0 & \delta_2 & -\delta_0 \end{pmatrix}, \tag{1.8}$$

where $\delta_0 = -3/4(a_z + 9b_z/4)$, $\delta_1 = 3/8(b_x - b_y)$, and $\delta_2 = 3/8(b_x + b_y)$. The block diagonal form of $H_{exchange}$ indicates that the bright exciton states don't mix with the dark exciton states. The bright and dark states are split by an energy δ_0, with the dark states being lower in energy than the bright ones. The typical value of δ_0 is in the order of a few hundreds of μeV [110]. The off-diagonal elements of the subblocks lead to state mixing between the two bright states, and between the two dark states. This in turn results in the lifting of degeneracy of the bright and dark exciton states by δ_1 and δ_2 respectively. Typical values for the two splitting energy are δ_1 in the range of 10 to 100 μeV, and $\delta_2 = 1\mu eV$ [111]. The eigenstates of the exchange Hamiltonian are,

$$|X_H\rangle = (|+1\rangle + |-1\rangle)/\sqrt{2}, \tag{1.9}$$
$$|X_V\rangle = (|+1\rangle - |-1\rangle)/\sqrt{2}, \tag{1.10}$$
$$|D_y\rangle = (|+2\rangle + |-2\rangle)/\sqrt{2}, \tag{1.11}$$
$$|D_x\rangle = (|+2\rangle - |-2\rangle)/\sqrt{2}. \tag{1.12}$$

The two bright exciton eigenstates ($|X_H\rangle, |X_V\rangle$) are split by δ_1, which is referred to as the exciton fine structure splitting (FSS). When these two excitons recombine to return to the ground state they emit a linearly polarised photon each, H and V (see Fig. 1.9).

While the primary outcome of the short-range exchange interaction is to split the exciton quadruplet into bright and dark pair states, the long-range exchange interaction has two effects. It not only adds to the splitting between bright and dark excitons (γ_0), but also

contributes (γ_1) to the splitting of the bright exciton in structures with in-plane asymmetry, into transverse and longitudinal components. The long-range exchange interaction has no impact on the dark exciton states.

The contribution of the long range exchange interaction can be included by simply adding the necessary terms to the bright exciton subblock in Eqn. 1.8, which becomes [110],

$$\begin{pmatrix} \delta_0 + \gamma_0 & \delta_1 + \gamma_1 \\ \delta_1 + \gamma_1 & \delta_0 + \gamma_0 \end{pmatrix}, \tag{1.13}$$

where $\gamma_1 = (\gamma_x - \gamma_y)$, and $\gamma_{x,y}$ are the coupling constants of the long range exchange interaction in the x and y directions. When the QD exhibits in-plane rotational symmetry, $\gamma_x = \gamma_y$ hence $\gamma_1 = 0$. In addition, when the x and y axes are equivalent, $\delta_1 = 3/8(b_x - b_y) = 0$ because $b_x = b_y$, thus resulting in the vanishing of the splitting between the bright exciton states to vanish. Self-assembled QDs tend to have an inherent anisotropic in-plane trapping potential, which may arise from an anisotropy in QD form, in QD composition [112], or in strain [113]. Therefore the ability to restore the degeneracy of the bright exciton states is crucial to produce polarisation entangled photon pairs, for instance. Many techniques have been developed in order to modify the exciton FSS to achieve degeneracy of states, which involve the use of electric fields [114], and strain [115].

1.1.3.e. The neutral biexciton

Just as the exciton is a bound state between an electron in the conduction band and a hole in the valence band of a QD, similarly there exists bound states that consist of multiple carriers. The biexciton (XX) state is one such multiparticle state, that consists of two electrons being bound to two holes in the S-shell of the QD. According to the Pauli exclusion principle, there can be only one configuration of such a state. The biexciton state thus is a singlet state and can be expressed as,

$$|XX\rangle = \frac{1}{\sqrt{2}} \left(\Uparrow\Downarrow\rangle - |\Downarrow\Uparrow\rangle\right) \otimes \left(\uparrow\downarrow\rangle - |\downarrow\uparrow\rangle\right). \tag{1.14}$$

The energy of the biexciton is written, $E_{XX} = 2E_X - E_b$, which may be less or more than the sum of energies of two uncorrelated excitons depending on the sign of E_b. E_b is the binding energy that results from the Coulomb interaction between the carriers. An attractive (repulsive) interaction is characterised by a positive (negative) value of E_b, whose magnitude is a few meV [100]. The nature of Coulomb interaction is dictated by the size of the QD. The QDs we use are small, due to their flash-growth process (more details in Chapter 3), and generally feature a negative binding energy.

When one electron-hole pair in the biexciton state recombines radiatively by emitting a photon, the QD finds itself in a neutral exciton state. The photon emitted by a biexciton

and the photon emitted by an exciton have different energies that are separated by E_b which is of the order of 2 meV for InAs QDs. The difference in energy makes it possible to differentiate the two photons corresponding to each transition spectrally. For a non-symmetric QD, the photon emitted by the biexciton is linearly polarised. The polarisation depends on the bright exciton state to which the biexciton has decayed (Fig. 1.9) (a). The $|XX\rangle \rightarrow |X_H\rangle$ transition generates a photon with H-polarisation, while the $|XX\rangle \rightarrow |X_V\rangle$ transition produces a photon with V-polarisation. When the FSS of the exciton is removed, both possible decay sequences become indistinguishable, and the information on the decay path adopted by the biexciton is lost, thus generating a pair of photons that are entangled in polarisation [58, 116].

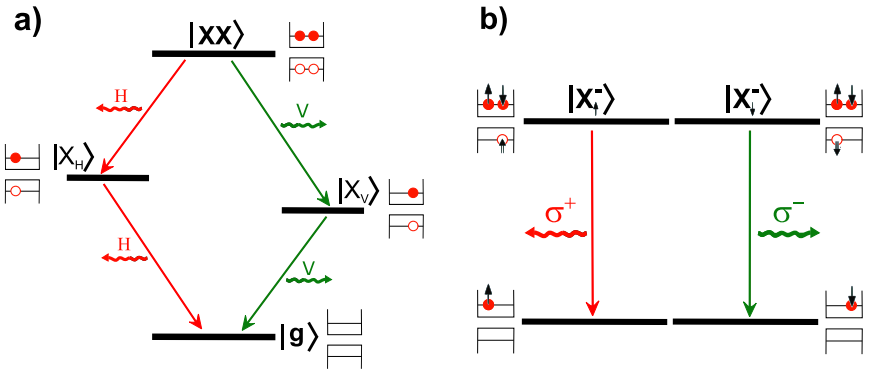

Fig. 1.9 (a) Schematic representation of the possible decay sequences of the $|XX\rangle$ state in cascade via the bright exciton states $|X_H\rangle$ and $|X_V\rangle$, emitting photons polarised horizontally H, and vertically V. The dark exciton states are omitted in order to simplify the representation. (b) Radiative recombination scheme of a negative trion (a positive trion has an equivalent state diagram) [101].

1.1.3.f. The trion

Finally, the bound state formed by a set of three carriers (neutral exciton with an additional carrier), is a charged exciton or trion state. There can be two kinds of trions, namely the positive trion consisting of two holes and one electron, and the negative trion, comprising of two electrons and one hole. Both holes and electrons being Fermions, the two carriers of the same species must have opposite spins, while the single carrier species could have any of the two possible spins making both trion states doubly degenerate. In this case, there is no Coulomb exchange interaction due to Kramers theorem which states that a system consisting of an odd number of Fermions remains at least doubly degenerate in the absence of an external magnetic field [117]. The two states corresponding to the positive trion are

expressed as,

$$|X^{+}_{\Uparrow}\rangle = \frac{1}{\sqrt{2}}\left(|\Uparrow\Downarrow\rangle - |\Downarrow\Uparrow\rangle\right)\otimes|\uparrow\rangle, \tag{1.15}$$

$$|X^{+}_{\Downarrow}\rangle = \frac{1}{\sqrt{2}}\left(|\Uparrow\Downarrow\rangle - |\Downarrow\Uparrow\rangle\right)\otimes|\downarrow\rangle. \tag{1.16}$$

Similarly the two states corresponding to the negative trion can be denoted as,

$$|X^{-}_{\uparrow}\rangle = \frac{1}{\sqrt{2}}|\Uparrow\rangle\otimes\left(|\uparrow\downarrow\rangle - |\downarrow\uparrow\rangle\right), \tag{1.17}$$

$$|X^{-}_{\downarrow}\rangle = \frac{1}{\sqrt{2}}|\Downarrow\rangle\otimes\left(|\uparrow\downarrow\rangle - |\downarrow\uparrow\rangle\right). \tag{1.18}$$

The energy of the trion is different from the sum of the neutral exciton energy and a single carrier energy. This difference depends on the Coulomb interaction, whose sign and magnitude depend on the QD shape and size [100]. Thus the radiative recombination of an electron-hole pair from the trion generates a photon of different energy from that emitted by the neutral exciton decay. Upon radiative recombination, the trion leaves the QD with either a single electron or hole state. The emitted photon is circularly polarised, σ^{+} or σ^{-} depending on the spin of the additional charge carrier.

1.1.4 Decoherence channels

Since QDs are embedded in a solid-state environment, their carrier states inevitably couple to the electromagnetic and mechanical degrees of freedom of the surrounding material. These degrees of freedom include lattice vibrations, charge fluctuations due to lattice defects and impurities, spin fluctuations in the collection of nuclei. They have detrimental effects on the quality of single-photons emitted by the quantum dot, causing dephasing, spin-flip, and non-radiative decay processes (thermal escape of carriers from QD levels to barrier bands). In the absence of these limiting mechanisms, the coherence of the exciton state is only limited by radiative recombination of the trapped carriers. The annihilation of the exciton state leads to the creation of a photon. This process is dictated by the radiative lifetime of the exciton, T_1. In this ideal scenario, T_1 determines the temporal duration and the spectral linewidth of the emitted photon. However, the exciton state may lose its coherence without a decay of its population, which would be an outcome of random interactions of the state with its environment. This channel of decoherence is known as dephasing because the uncontrolled interactions with the environment cause a loss of information on the phase of the exciton state. When the dephasing occurs at a timescale that is faster than the radiative recombination T_1, the linewidth of the photon is described by the coherence time T_2, a timescale over which the coherence of the exciton state phase is preserved. Nonetheless, the temporal duration of the photon is still determined by T_1. The dephasing may be

simply modelled assuming the coupling to a Markovian reservoir, which controls the optical transition state stochastically. The emission spectrum features Lorentzian peaks whose linewidth is defined by the radiative lifetime as follows [111],

$$\frac{1}{T_2} = \frac{1}{2T_1} + \frac{1}{T_2^*}, \quad \text{equivalent to} \quad \gamma = \frac{\gamma_{sp}}{2} + \gamma^*, \tag{1.19}$$

where T_2 is the total coherence time, and T_2^* is the pure dephasing time, γ is the total dephasing rate, γ_{sp} is the SE rate, and γ^* is the pure dephasing rate. From the equation above it is evident that for non-negligible pure dephasing, the coherence decay rate of the excited state is faster than the decay of the population. This implies that the resulting emission linewidth of the excited state would be larger than the expected linewidth limited by the radiative lifetime. In the following, we examine in more detail some of the important decoherence channels.

1.1.4.a. Charge noise

A fluctuating electrostatic environment in the vicinity of a QD generates a local electric field $\mathbf{E}(t)$ that varies in time. This varying field acts on the QD through the confined Stark effect thus resulting in a shift in transition energy of the QDs. These fast fluctuations of the optical transition energy, in turn translate into a significant broadening of the optical linewidth in comparison to the radiatively limited linewidth. This is the principal detrimental effect of charge noise [67]. Charge noise being caused by the charge environment of the QD tends to vary depending on the sample history. Thus while it generally presents low-frequency components (< kHz) [67], it may, under certain conditions, also exhibit high-frequency components [118]

1.1.4.b. Spin noise

Spin noise on the other hand is induced by the fluctuations of the nuclear spins of the QD material. This fluctuation of spins generates a time-varying magnetic field, $\mathbf{B}_N(t)$, which couples to the QD via the hyperfine interaction. Unlike charge noise, which in a given charge environment, has the same effect on both a neutral and charged exciton, spin noise affects them differently. In the case of a neutral exciton with a finite FSS, $\mathbf{B}_N$ tends to shift the optical transition energy, somewhat like charge noise. However in the case of a trion, spin noise induces a Zeeman splitting on the degenerate trion states leading to an altered emission profile associated with two mildly detuned spectral lines. Spin noise interacts with the QD typically in the μs timescale.

1.1.4.c. Phonon dephasing

Another major source of dephasing in QD carrier states is the coupling to lattice vibrations, particularly acoustic phonons. This coupling is unavoidable and exists by the virtue of QDs being embedded in a solid-state material. Two principal effects of this coupling are observed. The first is the apparition of phonon sidebands (PSBs) on either side of the radiatively-limited Lorentzian emission line, also known as the zero phonon line (ZPL) [62, 63]. These phonon sidebands correspond to the emission of a photon, associated with the emission or absorption of a phonon. The second effect leads to the homogeneous broadening of the ZPL linewidth [64]. The resulting emission spectrum is shown in Fig. 1.10. It is strongly temperature-dependent. At low temperature, the broadening of the ZPL is generally negligible. Also, the high energy PSB is absent. However, the low energy PSB, which corresponds to the emission of a phonon, always persists.

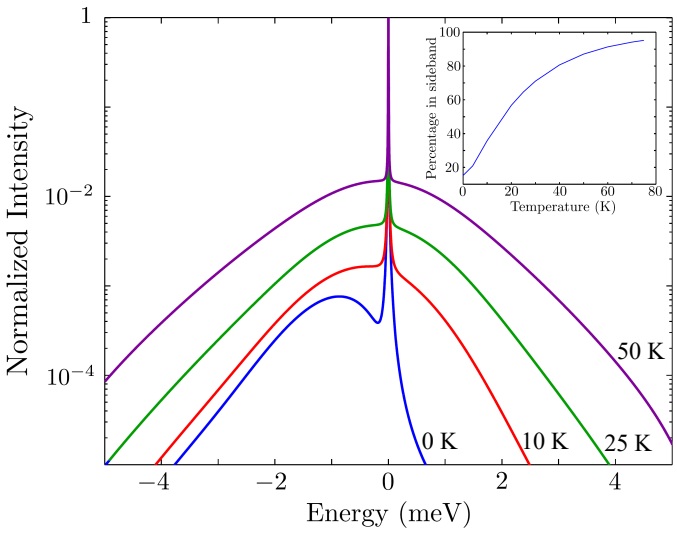

Fig. 1.10 Normalised emission spectrum of a QD coupled to a phonon reservoir at different temperatures. The inset indicates the fraction of total emission accounted for by the PSBs [111].

The coupling of the exciton to a phonon reservoir is a significant and undesirable source of decoherence, which imposes serious limitations in the generation of indistinguishable photons. The mechanism of this coupling will be addressed in more depth in Chapter 2. We will also see that nanowire structures are particularly sensitive to low-frequency phonons, an effect that is absent in the bulk.

1.2 Photonic structures

QDs are appealing emitters for sources of quantum light. InAs QDs are reported to present elevated values of quantum efficiency of the order of 0.9 [53], they offer a stable emission

of photons, and they do not suffer from photobleaching. Despite all these assets, several challenges need to be overcome in order to develop a practical source of quantum light based on QDs. One of these challenges stems from the fact that a QD behaves as a point-like emitter that generates a quasi-isotropic emission pattern within the semiconductor material. Furthermore, because of the large refractive index contrast between the barrier material and air, only a small fraction of light can escape. Thus the collection efficiency of InAs QD in bulk is as low as only 2% [61]. Another challenge is the degradation of the quality of emitted photons due to the QD coupling to various sources of dephasing, discussed in the previous sections. These shortcomings may be vastly improved by specific engineering of the QD electromagnetic environment, to make the QD emission directional, and to increase the QD SE rate so that it is less sensitive to different coherence channels. In the following section, we present some of the photonic structures most widely used to establish sources of quantum light comprising a QD emitter embedded in a higher bandgap semiconductor.

1.2.1 Figures of merit of spontaneous emission control

Before introducing systems used to control the SE in QD emitters, let's take a look at the figures of merit used to characterise the performance of photonic nanostructures. Two widely used indicators are the Purcell factor F_P and the β-factor. The Purcell factor is defined as,

$$F_P = \frac{\Gamma_M}{\Gamma_0}, \tag{1.20}$$

where Γ_M is the SE rate in a mode of interest M, and Γ_0 is the SE rate of the same emitter in an unstructured bulk material, that serves as a reference. The β-factor, on the other hand, is expressed as,

$$\beta = \frac{\Gamma_M}{\Gamma_M + \gamma}, \tag{1.21}$$

with γ denoting the rate of SE coupled to the continuum of all modes other than the mode M.

The Purcell factor was originally introduced to address optical cavities, which present significant acceleration of SE due to a strong spatial and spectral confinement of the optical mode. It is used to characterise other systems too, such as waveguides, in which case it is referred to as a generalised Purcell effect. In contrast, the β-factor is a more general figure of merit. In particular, $\Gamma_M \gg \gamma$ may be achieved either by enhancing the contribution of Γ_M (Purcell effect in cavities), or by suppressing the influence of γ (photonic crystals, or dielectric screening effect in waveguides, to strongly inhibit the emission into undesired modes). In the limit when $\beta = 1$, the corresponding nanostructure is classified to be strictly monomode. The derivations of both these figures of merit will be elaborated for specific systems in subsequent sections.

1.2.2 Optical cavities

In the case of an emitter within a cavity, the density of accessible optical modes for the emitted photons is discretised due to the 3D confinement of light by the cavity. We consider here a single mode of the cavity, with an angular frequency ω_c.

We denote the coupling between the emitter and the cavity by g, which characterises the rate of coherent exchange of energy between the two. A realistic system also exhibits losses. The cavity stores photons during a finite time, and the rate at which it loses them, or the cavity damping rate, is expressed as $\kappa = \omega_c/Q$, where Q is the quality factor of the cavity. The losses of the emitter are given by γ_{sp}, which describes the spontaneous emission into modes other than the cavity mode. Depending on the hierarchy between the coherent coupling and losses, two regimes of interaction emerge: the strong coupling regime ($g \gg (\kappa, \gamma_{sp})$) and the weak coupling regime ($g \ll (\kappa, \gamma_{sp})$).

1.2.2.a. Strong coupling regime

In the strong coupling regime ($g \gg (\kappa, \gamma_{sp})$), the emitter-cavity dynamics are governed by coherent interactions which can be described by the Jaynes-Cummings Hamiltonian,

$$H = \hbar\omega_{em}\hat{\sigma}^\dagger\hat{\sigma} + \hbar\omega_c\hat{a}^\dagger\hat{a} + \hbar g(\hat{\sigma}\hat{a}^\dagger + \hat{\sigma}^\dagger\hat{a}). \tag{1.22}$$

The first term represents the Hamiltonian of the emitter transitioning from ground state $|g\rangle$ to excited state $|e\rangle$ ($\hat{\sigma}^\dagger$) and vice versa ($\hat{\sigma}$). The second term describes the electromagnetic field in terms of the photon creation ($\hat{a}^\dagger$) and annihilation ($\hat{a}$) operators. The interaction term describes the $|g\rangle \rightarrow |e\rangle$ ($|e\rangle \rightarrow |g\rangle$) transition with the simultaneous absorption (emission) of a photon.

The time signature of the emitter-cavity interaction presents an oscillatory behaviour, called Rabi oscillations, which corresponds to the photon emission, then absorption, then remission, and so on. This reversible coherent exchange of energy is a consequence of the strong coupling between the emitter and the cavity. In reality, the cavity isn't ideal and this introduces losses of the emission into the continuum, thus leading to damped oscillations.

1.2.2.b. Weak coupling regime

In the weak coupling regime ($g \ll (\kappa, \gamma_{sp})$) the coupled cavity-continuum system can be described as a mixed quasi-mode having a density of states given by,

$$\rho(\omega) = \frac{2}{\pi\Delta\omega_c}\frac{\Delta\omega_c^2}{4(\omega-\omega_c)^2 + \Delta\omega_c^2}. \tag{1.23}$$

$\rho(\omega)$ has a Lorentzian profile with a FWHM of $\Delta\omega_c = \kappa$, which is the rate at which the cavity mode loses photons.

The SE rate of the emitter into the quasi-continuum mode can be quantified by the Fermi's golden rule,

$$\Gamma = \frac{2\pi}{\hbar^2}|\langle e,0|H_{int}|g,1\rangle|^2\rho(\omega_{em}), \tag{1.24}$$

where $|e,0\rangle$ denotes the emitter in its excited state and no emitted photons in the cavity, and $|g,1\rangle$ denotes the emitter in the ground state, with one photon being emitted in the cavity. $\rho(\omega_{em})$ represents the density of accessible states at the emitter frequency ω_{em}. H_{int} is the interaction Hamiltonian, which under the dipole approximation, is expressed as,

$$H_{int} = -\mathbf{d}\cdot\mathbf{E}(\mathbf{r}_{em}). \tag{1.25}$$

where $\mathbf{E}(\mathbf{r}_{em})$ is the electromagnetic field operator, at the location $\mathbf{r}_{em}$ of the emitter, and $\mathbf{d}$ is the electric dipole operator.

We consider an emitter with a linear optical dipole. The SE into the cavity mode is maximum when the emitter is resonant with the cavity, it is located on the $\mathbf{E}$ field maximum, and it features a dipole oriented along the local polarisation. The SE rate of the emitter in such a case is,

$$\Gamma_{cav}^{max} = \frac{2d_{em}^2 Q}{\hbar\varepsilon_0 n^2 V_{eff}}. \tag{1.26}$$

Here $d_{em}^2 = |\langle e|\mathbf{d}|g\rangle|^2$, and V_{eff} is the effective quasi-mode volume denoted by,

$$V_{eff} = \frac{\iiint n^2(\mathbf{r})|\mathbf{E}(\mathbf{r})|^2 d^3\mathbf{r}}{n^2 max(|\mathbf{E}(\mathbf{r})|^2)}, \tag{1.27}$$

and n is the refractive index of the quasi-mode at the emitter location.

The SE rate of an emitter embedded within a linear, homogeneous, isotropic dielectric material of refractive index n is,

$$\Gamma_0 = \frac{d_{em}^2\omega_{em}^3 n}{3\pi\hbar\varepsilon_0 c^3}. \tag{1.28}$$

We can now calculate the Purcell factor F_P in the cavity mode, which is defined as the ratio between the SE rate Γ_M in a mode of interest M and the SE rate Γ_0 of the emitter in an unstructured semiconductor environment of refractive index n, which serves as a reference. Thus we have,

$$F_P = \frac{\Gamma_{cav}^{max}}{\Gamma_0} = \frac{3}{4\pi^2}\frac{Q}{V_{eff}}\left(\frac{\lambda_c}{n}\right)^3. \tag{1.29}$$

From Eqn. 1.29 we find that to increase the Purcell factor, and hence accelerate the SE rate, we can either increase the quality factor of the cavity or reduce the effective volume of the confined mode. In the following section, we will review some popular examples of optical cavities that exploit this effect.

1.2.2.c. Examples of photonic cavities

In the course of the last couple of decades, several approaches have been adopted to develop dielectric photonic cavities. Out of these, the primary cavity systems are portrayed in Fig. 1.11.

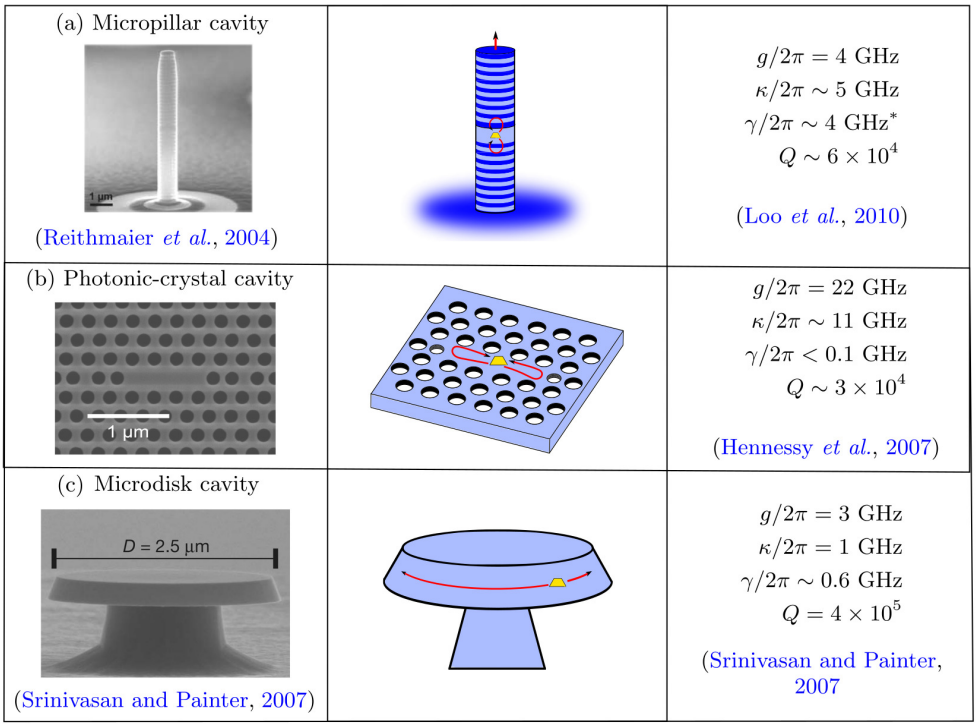

Fig. 1.11 Examples of microcavities. Images correspond to real structures and are captured with a SEM. The operation principle of the coupling of the emitter to the cavity is illustrated in the diagrams. (a) Micropillar cavity embedding an InAs QD. The emission is confined by the AlGaAs/GaAs Bragg mirrors on either side of the QD. (b) Photonic crystal cavity on a 2D membrane, embedding a QD in the middle of the zone without holes. (c) Microdisk cavity with a layer of embedded QDs that couple to the gallery modes of the cavity. [111].

Micropillar cavities. A micropillar cavity, as represented in Fig. 1.11 (a), consists of two Bragg mirrors. These mirrors consist of alternating layers of materials with different refractive indices (say, n_1 and n_2). These layers are grown by MBE and have a thickness of $\lambda/4n_i$, where λ is the emission wavelength of the emitter resonant to the cavity. The micropillar is etched by a top-down approach. The emitter is carefully positioned at the very centre of a layer whose thickness is λ/n_1, in between the Bragg mirrors. This zone confines the cavity mode. When InAs QDs are used as emitters, GaAs and AlGaAs are often employed to define the Bragg mirrors. The reflectivity of the mirrors is controlled by the number of interchanging layers that are defined. This allows obtaining an almost perfectly reflecting bottom mirror. The top mirror is intentionally created with a slightly lower reflectivity than the lower one. While this difference in reflectivity degrades the Q

of the cavity, it also permits the preferential upward extraction of light. The diameter of the micropillar is a vital parameter, which must be sufficiently small in order to restrict the lateral expansion of the mode, thus providing a tighter effective volume. However, diameters less than 1-2 μm have been reported to degrade the Q factor of the cavity [119]. In literature, the effective volume generally used tends to be in the order of $V_{eff} \sim 10(\lambda/n)^3$, associated with a quality factor of the order of $Q \sim 5 \times 10^4$. For instance Ref. [120] reports $Q \sim 6.5 \times 10^4$ for a cavity of diameter of 7μm, and Ref. [121], achieved $Q \sim 1.65 \times 10^5$ for a cavity of diameter of 4μm.

Photonic crystal cavities. The control of SE of a QD embedded in a photonic crystal was first demonstrated in 2005 [70, 122]. A photonic crystal cavity is obtained by introducing local defects in a two-dimensional membrane riddled with periodically etched holes. While several kinds of photonic crystal cavities exist, one of the best performing and most popular types consists of eliminating three linearly adjacent holes in a membrane of holes following a triangular periodicity, as shown in Fig. 1.11 (b). Such cavities can achieve an effective volume of the order of $(\lambda/n)^3$ and strongly suppress the emission into free-space modes [123]. Quality factors of $Q = 3 \times 10^4$ was achieved with a GaAs membrane [124], while for Si cavities, with emission around 1.55 μm, $Q = 2 \times 10^6$ has been reported [125].

Microdisk cavities. These cavities comprise a dielectric disk with a diameter in the range of $1 - 10\mu$m, and a thickness of λ/n, pictured in Fig. 1.11 (c). The confinement of light in this system arises from a sequence of total internal reflections producing a mode that is localised on the periphery of the disk. Such a mode is known as a whispering-gallery-mode. First demonstrations of SE acceleration on InAs QDs in a microdisk was made in 2001 [126]. While the effective volume of such a system is much larger than the previous cavities presented, it is compensated by an elevated Q which eventually results in a significant Purcell enhancement of SE. Literature shows that for microdisks of GaAs, $Q = 4 \times 10^5$ [127], and for Si microdisks, $Q = 5 \times 10^6$ [128], have been reported.

1.2.2.d. Assets and limitations of photonic cavities

Tremendous technological progress has been and continues to be made on the acceleration of SE using photonic cavities, to achieve near-unity β. The first demonstration of $F_P \sim 5$ in a micropillar cavity was made in 1998 [69], while in 2018 $F_P \sim 65$ was achieved on a photonic crystal cavity [129]. Although such acceleration of SE has made it possible to emit indistinguishable photons [70, 72], the approach of cavities possesses some limitations. In particular, the necessity of the emitter-cavity resonance condition means that not only the emitted photon must spectrally match the cavity mode, but the emitter must also be spatially located at the electric field maximum within the cavity. Self-assembled QDs following a

Stranski-Krastanov growth method, present a stochastic spatial distribution as well as an inhomogeneous spectral dispersion of ∼20-50 meV. This shortcoming can be overcome using a deterministic in-situ lithography technique [130]. The position and energy of a QD are determined, at $T = 10$ K, by photoluminescence, before a laser exposes a photosensitive resin on the surface of the sample in order to delineate the cavity.

While cavities make it possible to generate single photons at a high quality, the techniques necessary to achieve optimal cavities tend to be technologically demanding. Additionally, such systems need emitters to be monochromatic. While this criterion is satisfied by self-assembled QDs at cryogenic temperatures, it isn't the case for broadband emitters such as nitrogen vacancies in diamond. Finally conceiving applications such as the generation of entangled photon pairs, or feeding a spectrally matched multi-source quantum circuit (e.g. quantum computing) becomes challenging. To realise such systems sources based on waveguides are very appealing, because of their broad operation bandwidth. Control of SE in these systems is described in the next section.

1.2.3 Optical waveguides

Waveguides offer an alternative strategy to control the SE of an embedded emitter. Several kinds of waveguides have emerged in the last couple of decades, among which slow-light photonic crystal waveguides and plasmon waveguides rely on accelerating the emission in a given mode much like a cavity. However, a near-unity β-factor may also be achieved by inhibiting the emission in free-space modes. This approach is adopted by photonic crystal waveguides and photonic nanowires.

1.2.3.a. Controlling spontaneous emission in a guided mode

In a waveguide light can propagate freely along one direction (say, z), while being strongly confined in the two transverse directions. We consider the simplest scenario of a waveguide that supports a single mode. The corresponding electric field, may be expressed as,

$$\mathbf{E}(\mathbf{r},t) = \mathbf{E}(\mathbf{r}_\perp)\exp(i\omega t - k_z z), \tag{1.30}$$

where $\mathbf{E}(\mathbf{r}_\perp)$ represents the transverse field distribution (perpendicular to the propagation direction), ω is the angular frequency and k_z is the propagation constant.

In order to simplify the calculation of the SE rate into the guided mode, the following assumptions are made. The emitter is modelled as a point dipole that emits at a wavelength λ_{em} and the nanowire is considered to have a finite length such that, $L \gg \lambda_{em}$. Applying periodic boundary conditions along z results in a quantisation of k_z with an interval of

$\Delta k_z = 2\pi/L$. The spectral density of states associated with the guided mode is given by,

$$\rho_{1D}(\omega) = \begin{cases} 0 & \text{when } \omega < \omega_{CO} \\ 2\frac{L}{2\pi|v_g(\omega)|} & \text{when } \omega \geq \omega_{CO} \end{cases} \tag{1.31}$$

where $v_g = d\omega/dk_z$ is the group velocity of the desired mode, and ω_{CO} is the cut-off angular frequency above which the guided mode is present. The factor 2 arises from the two guided modes propagating along $+z$ and $-z$.

To compute an expression for the maximum SE rate into the guided mode, the emitter is assumed to be located at a maximum of the electric field and that the emitter dipole is aligned in the direction of the local polarisation of the mode. Substituting the relevant terms in Eqn. 1.24, the maximum SE rate in the guided mode is found to be,

$$\Gamma_{wg}^{max} = \frac{2d_{em}^2\omega_{em}}{\hbar\varepsilon_0 n^2 S_{eff}|v_g(\omega)|}. \tag{1.32}$$

Here n is the refractive index at the emitter location and S_{eff} is the effective surface of the guided mode expressed as,

$$S_{eff} = \frac{\iint n^2(\mathbf{r}_\perp)|\mathbf{E}(\mathbf{r}_\perp)|^2 d^2\mathbf{r}_\perp}{n^2 max(|\mathbf{E}(\mathbf{r}_\perp)|^2)}. \tag{1.33}$$

S_{eff} characterises the transverse confinement of the guided mode.

Analogous to a cavity, the generalised Purcell factor for waveguides may be expressed as,

$$F_{P,wg} = \frac{\Gamma_{wg}^{max}}{\Gamma_0} = \frac{3}{4\pi}\frac{(\lambda_{em}/n)^2}{S_{eff}}\frac{n_g(\omega)}{n}, \tag{1.34}$$

where $n_g(\omega) = c/|v_g(\omega)|$ is the group index of the mode of interest at frequency ω. Comparing Eqn. 1.34 with Eqn. 1.29 reveals an analogy with the cavity Purcell factor, with a correspondence between the spatial mode confinement terms $S_{eff} \leftrightarrow V_{eff}$ and a correspondence between the density of state terms $n_g(\omega)/n \leftrightarrow Q$. It thus becomes evident that in order to maximise $F_{P,wg}$, S_{eff} must be minimised while maximising n_g. In the following section we present some of the principal strategies employed to develop waveguides.

1.2.3.b. Examples of high-β waveguides

Plasmonic waveguides. A plasmonic waveguide comprises a metallic nanowire placed only a few nanometres away from an emitter. The emitted light is therefore coupled to surface plasmons that are guided along the nanowire. The nanowire diameter is generally in the sub-wavelength range, thus offering tight transverse mode confinement by virtue of $S_{eff} \ll (\lambda_{em}/n)^2$. It also supports the coupling over a broad spectral band. A Purcell factor

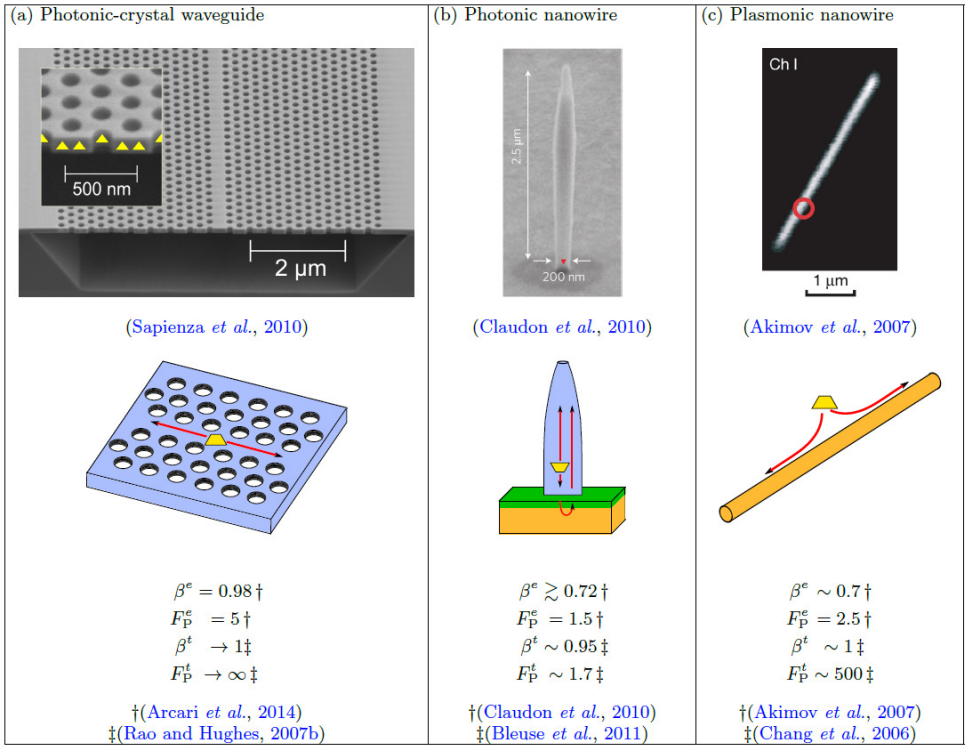

Fig. 1.12 Some examples of photonic waveguides. Each image corresponds to a real structure captured with a SEM. The diagrams illustrate the working principle of the guiding of light emitted by the emitter. (a) Photonic crystal waveguide membrane. A layer of QD is embedded in the middle of the membrane and is indicated by yellow triangles. (b) Photonic nanowire consisting of an InAs QD embedded in a GaAs nanowire. The nanowire sits on a $SiO_2 - Au$ hybrid mirror and the top part is tapered in order to maximise the collection efficiency. (c) Plasmonic wire coupled to a single QD emission via a surface plasmon mode [111].

of over 500 has been predicted in 2006, for such systems under certain circumstances [131]. The first experimental demonstration of the system was made in 2007 with a CdSe colloidal QD as emitter and a silver nanowire, as pictured in Fig. 1.12 (a). The study reported an SE acceleration of $F_{P,wg} = 2.5(\beta \sim 0.7)$ [132]. This approach unfortunately suffers from extreme losses in the metal [131, 133]. Some solutions to overcome these losses include adiabatic coupling of the plasmonic mode to a dielectric guide [131], or to produce the plasmonic mode between two metallic nanowires [134].

Photonic crystal waveguides. As the name suggests such waveguides are embedded into a photonic crystal. Historically such a waveguide was first proposed in 1993 by introducing a line defect in a 3D photonic structure [135]. Near-unity values of β are achievable by reducing, on one hand, the group velocity of the guided mode but also by inhibiting the coupling to the continuum of free-space modes. In practice, these waveguides are often defined on a 2D membrane, covered in holes distributed with a triangular periodicity

(Fig. 1.12 (a)). An emitter is embedded in the middle of the waveguide which is a crystal corridor defined by eliminating a line of holes. When such a waveguide is devoid of any imperfection due to fabrication, it can in theory completely eliminate the coupling to lossy free-space modes, attaining $\beta = 1$, at a single precise wavelength, for planar dipoles [136, 137]. In reality guided modes of such systems present high group dispersion, which means the group refractive index n_g is strongly frequency-dependent. This property may be exploited to selectively accelerate emissions at a given frequency, which leads to slow-light regimes ($v_g \ll c$) over a narrow spectral range. A Purcell factor of $F_P \sim 60$ was obtained from the demonstration of a group index of $n_g \sim 300$ from a Si membrane in 2005 [138]. While this result was promising, it must be noted that generally, a high group index implies a narrow operation band making the waveguide more sensitive to defects arising from fabrication, which in turn enhances the optical losses in transmission [139, 140]. Therefore optimal systems must settle for a moderate group index, which can be adjusted by modifying the geometric parameters of the photonic crystal. The highest value of $\beta = 0.984$ has been demonstrated on a GaAs membrane, with $\beta > 0.9$ over a spectral range of 10 nm in 2014 [74].

Dielectric photonic nanowire waveguides. As shown in Fig. 1.12 (b), these waveguides are made of a dielectric nanowire having a high refractive index (e.g. $n = 3.45$ for GaAs). These cylindrical wires may be developed following an etching (top-down) [77, 78], as well as an epitaxial (bottom-up) [141, 50] process. The strong inhibition of SE into free-space modes is the primary benefit of such a system, which it achieves through a dielectric screening effect on dipoles oriented along the plane perpendicular to the direction of growth (nanowire axis). Unlike in photonic crystal waveguides, guided modes in a dielectric nanowire are weakly dispersive, allowing to maintain their efficiency over a very large spectral range, $\Delta\lambda \sim 100$ nm [142]. The CEA research team I worked in, exploits these structures to realise nanowire antennas, which are optimised for free space operation. The following section discusses the main concepts behind such antennas in more detail.

1.3 Photonic wire antennas

In this section, we will take a closer look at the dynamics of spontaneous emission in a photonic nanowire. Next, we show how to collect the guided photon by discussing the design considerations of a complete nanowire antenna.

1.3.1 Spontaneous emission into guided modes

We begin by considering an infinitely long wire with a circular cross-section of diameter d. The additional effects of a finite length, structured top extremity, and bottom mirror, can be introduced with a Fabry-Pérot model.

1.3.1.a. Guided modes

The wire has a refractive index n ($n = 3.45$ for GaAs used in this work), is oriented along the vertical z direction, and is surrounded by free-space ($n_c = 1$). The guided modes are confined in the (x,y)-plane, and are free to propagate along the z-direction with a scalar propagation constant k_z. The complete derivation of supported modes of the structure is beyond the scope of this work and can be found in [143]. Since the system exhibits a cylindrical symmetry, the electromagnetic field associated to the guided modes can be expressed as,

$$\begin{bmatrix}\mathbf{E}(\mathbf{r},t)\\ \mathbf{H}(\mathbf{r},t)\end{bmatrix} = \begin{bmatrix}\mathbf{E}_{l,m}(r)\\ \mathbf{H}_{l,m}(r)\end{bmatrix} e^{\pm il\theta} e^{i(\omega t - k_z z)}, \quad (l \in \mathbb{N}, m \in \mathbb{N}^*). \tag{1.35}$$

Waveguides such as the one considered here are not restricted to only supporting pure transverse electric, TE ($E_z = 0$), of pure transverse magnetic, TM ($H_z = 0$), fields. Modes with TE or TM symmetry must have $l = 0$ and $m \geq 1$. Waveguides also support hybrid modes that are classified depending on the relative magnitudes of E_z and H_z. If E_z dominates, the corresponding mode is named EH_{lm}, conversely HE_{lm} modes feature a dominant H_z. Figure 1.13 illustrates the dispersion relation of the first few modes of a waveguide. The fundamental guided HE_{11} mode is always supported by the waveguide and doesn't feature any cutoff, unlike the other modes. Every mode, except the ones for which $l = 0$, are two-fold degenerate due to the $e^{il\theta}$ factor in Eqn. 1.35.

Since we are interested in monomode operation, we focus hereafter on the coupling to the fundamental guided mode. In particular, we consider a point-like emitter, featuring a linear transverse optical dipole, with free-space wavelength $\lambda = 950$ nm embedded in the wire. Thus the emitter couples to the in-plane component of the guided mode. From Fig. 1.13 it is evident that the waveguide is monomode as long as its reduced diameter satisfies $d/\lambda < 0.229$. In the particular case of an on-axis emitter, the wire remains monomode until $d/\lambda < 0.366$. Indeed the TE_{01} and TM_{01} modes exhibit a null electric field amplitude at the wire axis [75].

1.3.1.b. Spontaneous emission in the fundamental guided mode (HE_{11})

We have seen in Sec. 1.2.3 that the SE rate into the guided mode depends on the effective surface S_{eff} and on the group index n_g. Fig. 1.14 summarises the effective surface (S_{eff}),

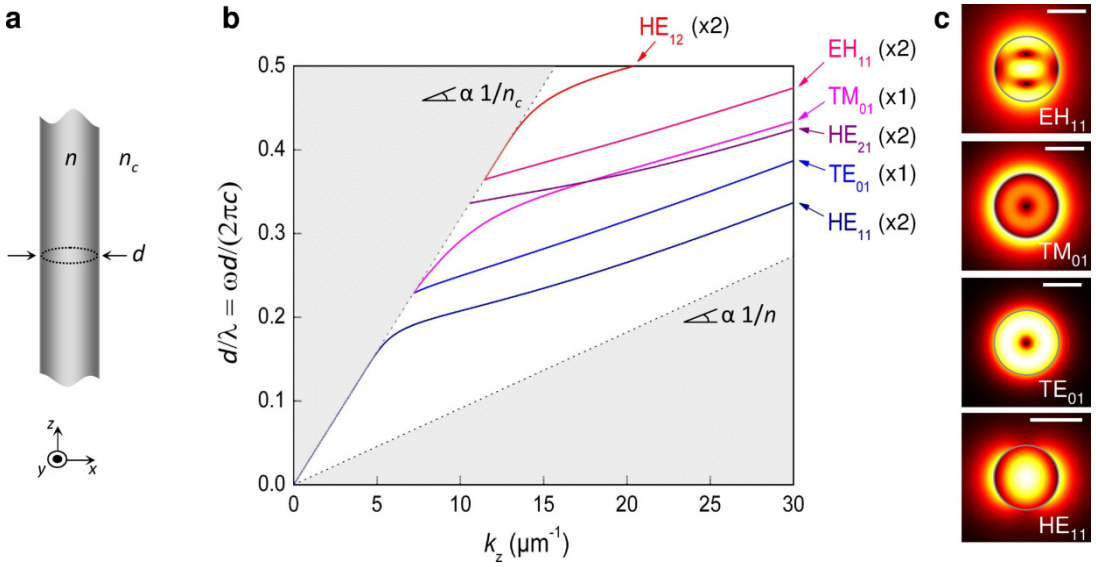

Fig. 1.13 Guided modes of an infinitely long cylindrical GaAs wire. (a) The geometry of the cylindrical waveguide. (b) Dispersion curves of the first guided modes of the wire. $d/\lambda = \omega d/(2\pi c)$ is plotted as a function of the propagation constant k_z. The polarisation degeneracy is indicated within brackets beside the mode label. (c) In-plane electric field amplitude for the first few guided modes. The map of HE_{11} is plotted for $d/\lambda = 0.25$ while the others are plotted for $d/\lambda = 0.37$. The scale bars represent 200 nm. [144].

the group index ($n_g = c(k_z/\omega)$), the effective index ($n_{eff} = c(dk_z/d\omega)$), and the normalised SE rate as a function of the reduced diameter d/λ, for an on-axis emitter.

A closer look at the plots reveals two confinement regimes. For $d/\lambda < 0.17$, n_{eff} approaches n_c. This is indicative of poor lateral confinement of the mode in the waveguide. In other words, the mode is primarily deconfined and spills out into the surrounding outside the waveguide. S_{eff} in this regime increases sharply for decreasing d/λ. Asymptotically the dispersion relation appears to be linear at this scale and corresponds to that of a plane wave propagating in the cladding. For $d \gg \lambda/n$, n_{eff} approaches n, which indicates that the mode is most localised within the wire. For very large diameters, the dispersion relation approaches the one of a plane wave propagating in the bulk material constituting the wire. S_{eff} exhibits an almost quadratic dependence over d, in this regime. The maximum coupling to the HE_{11} mode occurs when $d/\lambda = 0.235$. At this point $S_{eff} = 0.41 \times (\lambda/n)^2$, and $n_g = 1.55 \times n$. The resulting maximum SE rate into HE_{11} is $0.9 \times \Gamma_0$ [75].

1.3.2 Inhibition of spontaneous emission into radiation modes

As briefly mentioned earlier, an emitter can also be coupled to a 3D continuum of free-space modes, which are referred to as radiative modes hereafter. Fig. 1.15, depicts the SE rate γ into non-guided radiative modes. As showcased in the plot, there is a large inhibition of the SE into radiative modes for $d/\lambda < 0.3$ presenting indeed $\gamma < \Gamma_0/10$ in this range [142].

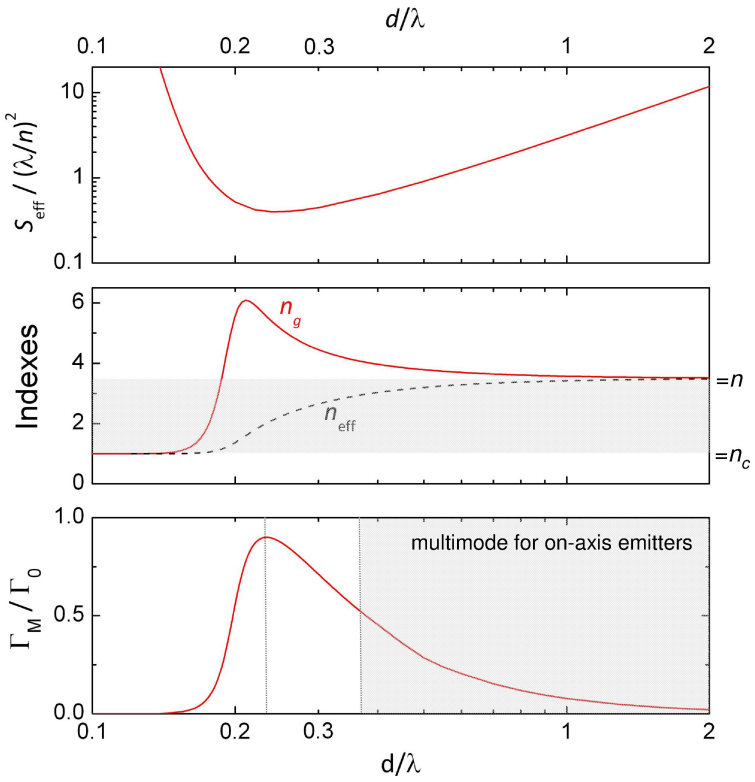

Fig. 1.14 Characteristics of the fundamental guided HE_{11} mode as a function of reduced diameter d/λ, where λ is the free-space wavelength. The horizontal axis is in log scale. (Top panel) Effective mode surface normalised by $(\lambda/n)^2$. Vertical axis is in log scale. (Middle panel) Effective index n_{eff} and group index n_g. (Bottom panel) Normalised SE rate into HE_{11}. The shaded area demarcates the multimode regime for an on-axis emitter. For an off-axis emitter, the multimode regime begins from the dotted line, at a lower wire diameter. [144].

This suppression of coupling to radiative modes due to a dielectric screening effect. In order to gain a simplified appreciation of this effect, we consider below, a very thin wire, whose diameter is small in comparison to the emission wavelength in matter. Under these conditions, the system may be described within the electrostatic approximation.

1.3.2.a. Dielectric screening in the electrostatic approximation

The assumption $d \ll \lambda/n$, renders wave propagation within the wire negligible. We neglect here the spatial dependence of the electromagnetic fields. The dielectric screening effect arises when an electric field $\mathbf{E}_{inc}$ incident on the wire perpendicularly to its axis, polarises the dielectric material, leading to the appearance of surface charges. This effect is illustrated in Fig. 1.16 (a). The distribution of charge generates its own electric field $\mathbf{E}_{dep}$ with an

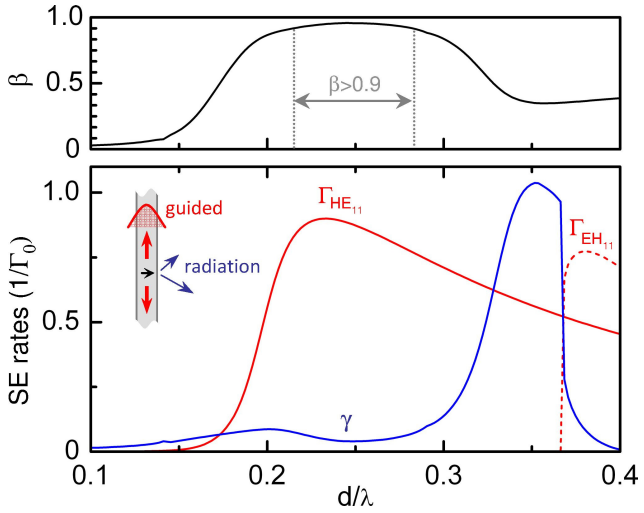

Fig. 1.15 SE dynamics for an on-axis emitter. (Bottom panel) Normalised SE rate into the fundamental HE_{11} mode (red), radiation modes (blue), EH_{11} mode, as a function of d/λ for an on-axis transverse optical dipole with $\lambda = 950$ nm, embedded in an circular, infinitely long wire. (Top panel) The β-factor as a function of d/λ. [75].

opposing orientation to $\mathbf{E}_{inc}$,

$$\mathbf{E}_{dep} = -\frac{\left(\frac{n}{n_c}\right)^2 - 1}{\left(\frac{n}{n_c}\right)^2 - 1 + 2}\mathbf{E}_{inc}. \tag{1.36}$$

For materials presenting a large mismatch in refractive index, $n \gg n_c$, the amplitude of $\mathbf{E}_{dep}$ is almost as large as that of $\mathbf{E}_{inc}$. In this scenario the total electric field in the wire $\mathbf{E}_{inc} + \mathbf{E}_{dep}$ tends towards zero, which leads to a suppression of the zero-point fluctuations (ZPF) of non-guided radiative modes [145]. Invoking Eqn. 1.24 the SE rate γ into radiative modes for a transverse emitter presenting a linear dipole can be expressed as,

$$\gamma \propto \left(\frac{2}{\left(\frac{n}{n_c}\right)^2 - 1 + 2}\right)^2 \rho_{3D}. \tag{1.37}$$

A normalisation by $\Gamma_0 \propto (n/n_c)\rho_{3D}$ leads to,

$$\frac{\gamma}{\Gamma_0} = \frac{2^2}{\frac{n}{n_c}\left[\left(\frac{n}{n_c}\right)^2 - 1 + 2\right]^2}. \tag{1.38}$$

This dielectric screening is valid, under the electrostatic approximation, for any transverse dipole orientation and position (including off-axis). For a GaAs wire, $n/n_c = 3.45$ which results in a strongly inhibited SE of $\gamma/\Gamma_0 = 0.007$. However following analogous

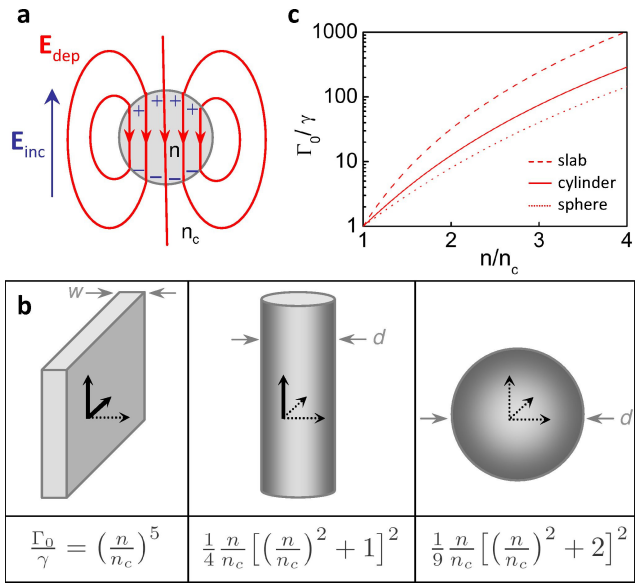

Fig. 1.16 Dielectric screening in the electrostatic approximation. (a) Schematic diagram illustrating the principle of dielectric screening in a cylindrical wire of circular cross section, immersed in a constant electric field $\mathbf{E}_{inc}$. (b) Dielectric screening in an infinite 2D membrane, an infinitely long cylinder, and a sphere. The dipole along the short (finite) axis experiences screening represented by dotted arrows, along with the respective inhibition factor Γ_0/γ. The dipole (solid arrow) along the infinite dimension is not screened. This effect holds under electrostatic approximation valid for $(w,d) \ll \lambda/n$. (c) Plot of inhibition factor, Γ_0/γ as a function of contrast of refractive index between the structure material and its surrounding, n/n_c, for the three geometries. [75].

reasoning on longitudinal dipoles (oriented in the direction of the wire axis) shows they don't experience this dielectric screening, presenting a normalised rate $\gamma/\Gamma_0 = n/n_c$ [146].

Dielectric screening is a general effect, which can be also observed in nanostructures with other dimensionalities, such as membranes [147] and spheres [145]. It must be noted however that only dipoles oriented along the short dimensions of the structures (indicated by dotted arrows in Fig. 1.16) undergo a dielectric screening, while dipoles oriented along the longer or infinite dimensions experience no screening. Fig. 1.16 (c) presents the inhibition factor Γ_0/γ as a function of n/n_c for the three geometries of nanostructures considered. Γ_0/γ varies according to $-p^2(n/n_c)^5$ for high index mismatch, indicative of the scale of suppression of SE into radiative mode achievable from these structures.

1.3.3 Fraction of spontaneous emission into the HE_{11} mode

The fundamental HE_{11} mode family consists of two modes that have orthogonal linear polarisations and obey the same dispersion law. To compute β into the HE_{11} mode, we represent the QD as two orthogonal, linear optical dipoles oriented in the plane perpendicular to the wire axis. We assume that the two dipoles possess the same oscillator strength. When considering a QD situated on the axis of a wire, due to the symmetry of the situation, it may

be treated as a single linear dipole. The β-factor of such a dipole is thus,

$$\beta = \frac{\Gamma_{HE_{11}}}{\Gamma_{HE_{11}} + \Gamma_g + \gamma}, \tag{1.39}$$

where the denominator is a sum of the SE rates into HE_{11}, other guided modes, and radiation modes, respectively. From Fig. 1.15, we find $\beta_{max} = 0.95$ for $d/\lambda = 0.24$, which is characteristic of an almost pure monomodal emission. Such a result can be attributed, on one hand, to a large coupling to the fundamental mode ($\Gamma_{HE_{11}} \sim \Gamma_0$), but also to a strong inhibition of SE into free-space modes. It is also noteworthy that $\beta > 0.9$ for d/λ in the range of 0.21 to 0.28. This makes the wire more tolerant toward fabrication variations and offers a broad operation bandwidth $\Delta\lambda/\lambda = 0.26$ [75]. β degrades significantly for an emitter located further off from the wire axis. This degradation is due to a decrease in the coupling to HE_{11}, combined with a higher SE rate into higher order guided modes [75].

1.3.4 Photonic wire antennas

All the SE of a QD embedded in an infinitely-long nanowire is funnelled into the fundamental guided mode. However, a realistic nanowire has a finite length. The nanowires we use are generally propped vertically on a planar substrate. The integrated QD can emit photons that propagate upward or downward. Since only the upward propagating photons are collected, half of the photons would be lost into the substrate. In order to recover the downward propagating photons, a mirror with a strong modal reflectivity for the fundamental guided mode is introduced between the substrate and the bottom facet of the nanowire. Additionally in the range of diameters considered for the wires, the HE_{11} mode is strongly confined within the wire and presents a lateral extension ($\sim \lambda/n$) that is much smaller than the free-space wavelength (λ). As a consequence, photons exit the structure with large divergent angles therefore limiting the collection of photons in the far-field [148]. To overcome this problem the top end of the nanowire is deliberately shaped to achieve a more directional emission. In the following, we introduce a Fabry-Pérot model which provides simple analytical formulas that are very useful to determine the design of the wire.

1.3.4.a. Fabry-Pérot model

We summarise here the main results of the Fabry-Perot model developed in Ref. [142]. The model supposes that the reflections at the wire facets modify only the coupling to guided modes, leaving the coupling to radiation modes unchanged. Therefore the emission rate of the emitter and the collection efficiency of the system can be determined from information about the reflectivity of the facets and the position of the emitter. For now we assume the top facet reflectivity $r_t = 0$. The bottom mirror reflects the downward emitted photons back towards the top of the wire. The emission rate and subsequently the collection efficiency are

maximised when the reflected beam interferes constructively with the upward propagating beam, in other words, the reflected beam must acquire a phase of $2\pi m$. This condition of phase imposes only a discrete set of optimal vertical positions h_m for the emitter. All vertical positions h_m are equivalent in terms of SE ratio into HE_{11} and lead to,

$$\Gamma_{HE_{11}} = \Gamma^{\infty}_{HE_{11}}(1+|r_b|), \tag{1.40}$$

where $\Gamma^{\infty}_{HE_{11}}$ is the emission rate into HE_{11} for an infinite wire. For a perfect mirror (r_b = 1), we have $\Gamma_{HE_{11}}/\Gamma_0$ = 1.8.

The collection efficiency may be expressed as,

$$\varepsilon(\theta) = \frac{1}{2}\beta^{\infty}\frac{(1+|r_b|)^2}{1+\beta^{\infty}|r_b|}T_{\alpha}(sin\theta), \tag{1.41}$$

where $T_{\alpha}(sin\theta)$ is defined as the taper transmission into a cone of numerical aperture $NA = sin\theta$, β^{∞} is the SE coupling factor for an infinite wire. To obtain an optimal extraction efficiency the only parameters that must be tweaked are therefore the reflectivity of the bottom mirror, and the transmission through the tapered top. In the best case scenario ($|r_b| = 1$ and $T_{\alpha}(sin\theta) = 1$), $\varepsilon = 2\beta^{\infty}/(1+\beta^{\infty}) = 0.98$.

1.3.4.b. Bottom mirror

The primary objective of the bottom mirror, situated between the substrate and the nanowire, is to offer near unity reflectivity for the mode of interest, over a large spectral range, so as to prevent the loss of photons coupled to the downward propagating fundamental mode. The solution retained to overcome this problem, has been to implement a metallic mirror made of gold. Such a mirror is convenient to integrate and provides a large reflectivity over a broad spectral range. The reflectivity plummets to almost zero around the diameter range of interest ($d/\lambda \sim 0.23$). This effect is suspected to be caused by the coupling to surface plasmon modes [149]. Fortunately the addition of a thin (9-11 nm) silica layer between the gold and the nanowire restores $|r_b|^2 > 0.9$ over the entire desirable diameter range.

1.3.4.c. Needle and trumpet top tapers

The objective of engineering the top end of the nanowire is two-fold. On one hand, it must annul the modal reflectivity associated with HE_{11}, while on the other it must allow for efficient collection in the far-field by a commercial microscope objective. Both these requirements were satisfied by gradually tapering the top end of the nanowire. We discuss in the following, two taper geometries.

The first solution is to gradually decrease the wire diameter, to end up with a needle-like configuration with an angle α (Fig. 1.17 (a)). The progressive decline in diameter

reduces n_{eff} of HE_{11} gradually such that the mode is less confined by the nanowire until for $d/\lambda \leq 0.15$ the mode is completely deconfined in the surrounding vacuum [150]. This expansion allows to eliminate the reflection from the top facet and leads to a directive emission. The angle α of the taper must be $< 2^\circ$ to ensure an adiabatic expansion of the mode.

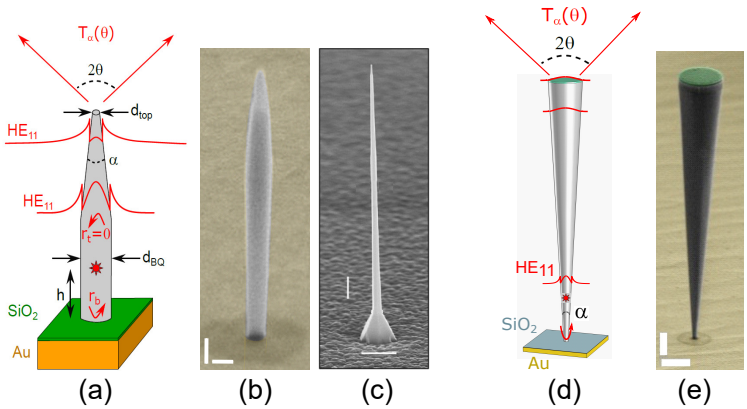

Fig. 1.17 (a) Diagram of a photonic nanowire antenna on an Au-SiO_2 mirror. The top end of the wire is tapered to form a needle. This taper allows the guided HE_{11} mode to extend outside the wire, to achieve a directional far-field emission. (b) SEM image of an example of a needle antenna fabricated by a top-down process [77]. Vertical and horizontal scale bar: 0.2 μm. (c) SEM image of an example of a needled antenna fabricated by a bottom-up process needle antenna [50]. Vertical and horizontal scale bar: 1 μm. (d)Schematic diagram of a trumpet nanowire antenna set on an Au-SiO_2 mirror. The HE_{11} mode is adiabatically expanded within the taper. (e) SEM image of trumpet nanowire antenna fabricated with a top-down process. [78]. Vertical and horizontal scale bar: 1 μm.

An alternate nanowire configuration to expand the HE_{11} mode adiabatically, is an inverted conical taper, or as we call it, a 'photonic trumpet'. The HE_{11} mode is expanded by gradually increasing the wire diameter. In doing so the mode remains well confined within the wire rather than progressively extending into the surrounding. The reflection of the top facet is suppressed with an antireflection coating [151].

Comparing the performance of a trumpet taper to that of a needle taper, we find that both geometries offer near-unity transmission into a Gaussian mode. However nearly perfect adiabatic expansion of HE_{11} is achieved for $\alpha < 15^\circ$, for a trumpet, while the needle suffers strong non-adiabatic losses for $\alpha > 2^\circ$ [78]. Such a strict constraint on taper angle makes needle nanowires challenging to realise by top-down fabrication, however, they have enabled the generation of high-performance devices fabricated by bottom-up techniques [50]. In contrast, by virtue of its tolerant performance over a large range of α, trumpet taper nanowires proved to be less technologically challenging and more reproducible in terms of top-down fabrication. They are also considerably promising and versatile to be implemented in free-space and fibre-coupled optics applications [152]. In

Chapter 4 we will elaborate a complete fabrication process to develop these structures as well as introduce strategies to exploit them for tunable sources of quantum light.

1.3.4.d. Examples of devices based on photonic wire antennas

Over the last couple of decades, QDs embedded in such nanowire antennas with a needle or trumpet top-taper, have been implemented in several applications. They have enabled the development of bright single-photon sources, demonstrating high photon purity [50, 77–79], as well as sources of entangled photon pairs [82, 83], and correlated photon triplets [84]. Wavelength-tunable single-photon sources have been produced on these systems [80, 81], thanks to their large operating bandwidth. This same asset coupled to the 'atom-like' nature of a QD led to the exploitation of giant optical nonlinear interactions at a single-photon scale [85]. Finally, such QD in nanowire antenna systems aided the amplification of signal in a four-wave mixing experiment on individual QDs [86]

1.4 Conclusion

In this chapter, first we have presented the general electronic properties of semiconductor self-assembled QDs, focusing particularly on flattened lens-shaped InAs/GaAs QDs. The strong confinement, in all three spatial directions, of charge carriers in a QD, results in discrete energy levels. We then discussed the various excitonic complexes associated with the S states, namely the neutral exciton, the biexciton, and the two trions, and we addressed their fine structure splitting in the absence of a magnetic field. The QD solid-state environment leads to some inevitable dephasing of its excitonic complex states. The principal sources of dephasing are related to the coupling to phonons, electric charges, and nuclear spins, all hindering the generation of indistinguishable single-photons.

The second part of the chapter was dedicated to photonic structures, designed to enhance the light collection efficiency and in some cases to accelerate the SE rate. This control can be achieved via precise engineering of the electromagnetic environment of the QD. We reviewed two main classes of structures: resonant optical cavities and photonic waveguides. Optical cavities accelerate the SE into the resonant mode of the cavity, through the Purcell effect, thus making the radiative recombination process insensitive to dephasing mechanisms. Microcavities achieve high Purcell enhancement of SE with a combination of an elevated quality factor Q, and a small mode volume. The high Q in turn entails stringent limitations on the operation bandwidth of the device. Waveguides on the other hand, generally lead to single-mode emission by inhibiting the emission into all other modes. Even though they generally provide a modest acceleration of SE, they feature a broad operation bandwidth.

In the third part, we focused on the nanowire antenna and detailed SE control in these structures. The Purcell factor can be slightly increased (≈ 1.8) by introducing a gold mirror on one end of the wire. The other end can be tapered in order to achieve highly directive emission, ensuring an excellent collection efficiency in the far-field. The emitted mode couples almost perfectly to a Gaussian free-space mode, making these systems promising for free-space as well as fibre-coupled optics. Besides, nanowire antennas sustain such high performance over a wide spectral range.

A challenge with nanowire antennas however is the coupling of the optical transitions to acoustic phonons, arising from thermally induced mechanical vibrations of the wire. Such a coupling causes an undesirable broadening of the emission linewidth of the ZPL. The lack of a significant Purcell acceleration of SE in these systems makes emitters more susceptible to phonon coupling, which poses strong limitations on the generation of indistinguishable photons. This decoherence will be addressed in Chapter 2 along with proposed solutions to suppress it.

In Chapter 3, we will introduce a new photonic nanostructure, which is a cross-over between a nanowire and a microcavity, that conserves the broadband operation from the former, while retaining the Purcell enhancement of SE from the latter. Additionally making the antenna more compact makes it less sensitive to phonon modes.

Finally, the broadband operability makes nanowire antennas appealing components for realising tunable sources of single-photons. A new strategy to tune the spectral properties of a QD in a nanowire antenna is presented in Chapter 4.

Chapter 2

Decoherence from low-frequency thermal vibrations in nanowire single-photon sources

Bright sources of indistinguishable photons are key resources for photonic quantum information technologies [18]. In this context, self-assembled semiconductor quantum dots (QDs) offer important assets to realise practical devices. However, their solid-state environment also raises significant challenges, since the coupling of the QD to uncontrolled degrees of freedom may degrade the spectral purity of the emitted photons [67]. Despite impressive progresses in the last years [72, 108, 153–156], it remains very important to understand QD decoherence processes. As briefly discussed in Chapter 1, these degrees of freedom comprise three decoherence processes: the charge fluctuation in the electrostatic environment of the QD, the coupling to nuclear spins of the host material, and the coupling to acoustic phonons. These processes influence the QD at different timescales, in particular, the first two are slow processes, where the interactions generally occur in the μs scale. Charge noise can be curbed using electrically contacted structures. Spin noise is more difficult to control but is also much weaker than charge noise.

The last source of decoherence is the unavoidable coupling to lattice vibrations. Owing to an interaction in the ps to ns timescale, which is comparable to or faster than the SE rate of a QD, dephasing due to acoustic phonon proves to be a fundamental limiting factor of the degree of indistinguishability of a source. The dephasing due to the coupling to lattice vibrations has been intensively studied, and the impact of bulk acoustic phonons is now well understood [62–64, 157–162]. Yet, modern quantum light sources are often based on a photonic nanostructure that defines a controlled electromagnetic environment around the QD [111], giving rise to a discrete set of low-frequency mechanical resonances. While a few theoretical works have investigated the decoherence of a QD coupled to phonon continua

of reduced dimension [65, 163], the impact of the *discrete* phonon resonances hosted by realistic nanowire structures remains to be explored.

In this chapter, we will introduce the theory used to describe the exciton-phonon interaction in bulk, before extending it to nanostructures of reduced dimensions. The structuration of the QD surrounding necessarily reshapes the phonon landscape and gives rise to a discrete set of low-frequency mechanical resonances, which confine elastic energy in tiny volumes. Even at cryogenic temperature, the thermal excitation of a single mechanical mode can then have a sizeable influence on the QD optical linewidth. This was demonstrated on a QD embedded in a nanowire antenna [87], a system widely employed to realise bright sources of quantum light [50, 77, 78, 80, 82–84]. A comprehensive theoretical analysis reveals that the QD spectral broadening is dominated by the contribution of a finite set of low-frequency mechanical modes, and strongly depends on the QD location within the nanowire section. To overcome this fundamental limitation, we will present several proposed designs based on the engineering of the nanomechanical properties, which may play a key role in the development of other high-performance light-matter interfaces based on nanostructures. This chapter is adapted from Ref. [164].

2.1 Phonon decoherence for a QD in bulk

In this section, we examine decoherence due to acoustic phonon modes for a QD embedded in a bulk environment. The coupling between the QD and phonon modes arise because the strain associated with the phonon modes modifies the QD emission energy via the deformation potentials. This coupling modifies the QD emission lineshape. The phonon-induced decoherence of the radiative emission of a QD leads to the apparition of broad sideband peaks on either side of its emission spectrum, as well as a broadening of the central emission peak (zero phonon line, ZPL). This phenomenon occurs somewhat universally across QD systems. It was initially observed on II-VI CdTe/ZnTe QDs [62], but subsequently also evidenced in other QD systems, such as InAs/GaAs [63], GaAs/AlAs [165], and GaN/AlN [166].

2.1.1 Exciton-phonon Hamiltonian

According to the description developed in Chapter 1, a QD may be modelled as a two level system, consisting of a ground state $|0\rangle$ and an excited state $|1\rangle$. The phonon environment is described as a set of independent harmonic oscillators. The interaction between an exciton and an acoustic phonon may be addressed by considering transitions between eigenstates that emerge from a mixing of a discrete excitonic state with a continuum of acoustic phonon modes. The theory used to quantify the exciton-phonon interaction is based on the localised electron-phonon interaction [167]. The complete Hamiltonian of the system, following the

formalism developed in Refs. [64, 65, 168], may be expressed as,

$$H = H_{QD} + H_{ph} + H_{in}, \tag{2.1}$$

$$H_{QD} = \hbar\omega_{01}|1\rangle\langle 1|, \tag{2.2}$$

$$H_{ph} = \sum_{\mathbf{q}} \hbar\omega_{\mathbf{q}} a_m^\dagger a_m, \tag{2.3}$$

$$H_{in} = (V_L + V_Q)|1\rangle\langle 1|, \tag{2.4}$$

where H_{QD} is the 2-level QD Hamiltonian with transition energy $\hbar\omega_{01}$. H_{ph} is the phonon Hamiltonian with $\hbar\omega_{\mathbf{q}}$ the energy of the phonon mode with momentum $\mathbf{q}$, and $a_{\mathbf{q}}^\dagger$ ($a_{\mathbf{q}}$) the associated phonon creation (annihilation) operator. H_{in} is the QD-phonon interaction Hamiltonian, which consists of two terms: one linear in phonon displacement (V_L) and one quadratic in phonon displacement (V_Q).

The linear interaction term V_L is expressed as,

$$V_L = \sum_{\mathbf{q}} L_{\mathbf{q}}(a_{\mathbf{q}} + a_{\mathbf{q}}^\dagger), \tag{2.5}$$

with $L_{\mathbf{q}}$ representing the linear coupling strength,

$$L_{\mathbf{q}} = M_{\mathbf{q}e}^{11} - M_{\mathbf{q}h}^{11}. \tag{2.6}$$

In this equation $M_{\mathbf{q}b}^{mn}$ is the matrix element representing a transition of an electron, denoted by replacing the subscript b by e (and a hole, by replacing b by h) between two electronic states m and n induced by a phonon mode with a momentum $\mathbf{q}$, when the phonon dephasing of a QD occurs predominantly by deformation potential coupling [62]. $M_{\mathbf{q}b}^{mn}$ can be written as,

$$M_{\mathbf{q}b}^{mn} = D_b\langle\psi_b^m(\mathbf{r})|\nabla\cdot\mathbf{u}_{\mathbf{q}}(\mathbf{r})|\psi_b^n(\mathbf{r})\rangle, \tag{2.7}$$

where $\nabla\cdot\mathbf{u}_{\mathbf{q}}(\mathbf{r})$ is the volumetric strain at a generalised coordinate $\mathbf{r}$, and $\mathbf{u}_{\mathbf{q}}$ is the phonon displacement.

$$\nabla\cdot\mathbf{u}_{\mathbf{q}}(\mathbf{r}) = \sqrt{\frac{\hbar\omega_{\mathbf{q}}}{2\rho_M u_s^2 \mathscr{V}}}\exp(i\mathbf{q}\cdot\mathbf{r}), \tag{2.8}$$

with ρ_M is the mass density, u_s is the velocity of sound in the material, D_b is the deformation potential, which characterises the changes strain causes to band structures, for the electron band, denoted by replacing the subscript b by e, and for the hole band, obtained by replacing b by h, $\mathscr{V}$ is the phonon quantisation volume, and $\psi_b^m(\mathbf{r})$ is the confined wavefunction of the m-th state. The phonon modes are considered to be plane waves represented by $\exp(i\mathbf{q}\cdot\mathbf{r})$ in Eqn. 2.8. For an InAs QD, $D_e = -5.08\ eV$, $D_h = -1\ eV$, $\rho_M = 5.67\ g/cm^3$, and $u_s \approx 4000\ m/s$ [63].

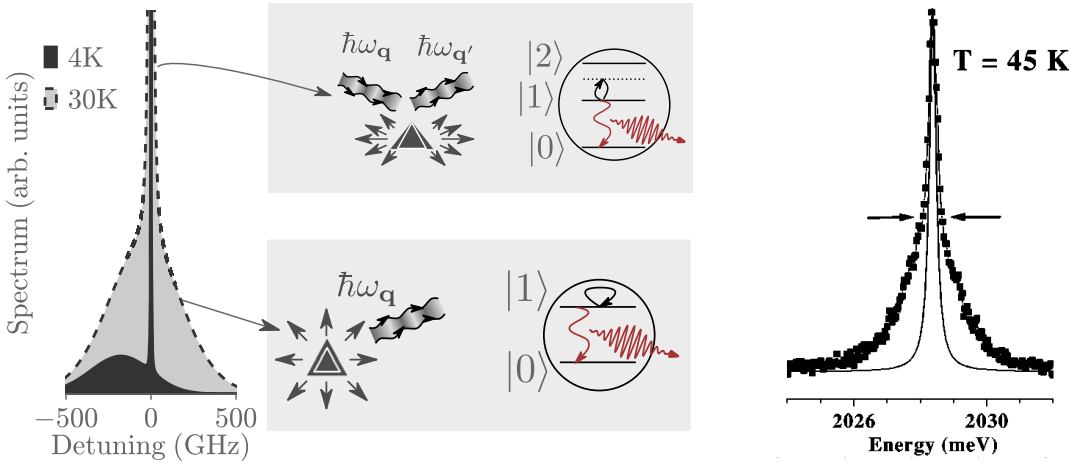

Fig. 2.1 (Left) Dephasing of QD emission spectrum due to phonons. The emission spectrum consists of a zero phonon line (ZPL) surrounded by broad phonon sidebands (PSBs). The spectrally thin ZPL is broadened due to a quadratic coupling characterised by the scattering of phonons through virtual excitation of the exciton to higher states. The broad PSBs arise from a linear coupling to phonons. They correspond to the emission of a photon assisted by the emission or absorption of a phonon. [65]. (Right) PL line shape of a CdTe QD at T = 45 K. The lineshape can no longer be described by a Lorentzian profile, due to the PSBs on either side of the ZPL. Figure adapted from Ref. [62]

The quadratic interaction term $Q^m_{\mathbf{q}b}$ is represented as follows,

$$V_Q = \sum_{b,m} \left[\sum_{\mathbf{q}} Q^m_{\mathbf{q}b} (a_{\mathbf{q}} + a^\dagger_{\mathbf{q}}) \right]^2, \tag{2.9}$$

$$Q^m_{\mathbf{q}b} = \frac{M^{1m}_{\mathbf{q}b}}{\sqrt{\Delta_m}}, \tag{2.10}$$

where Δ_m is the energy difference between the first excited state, $|1\rangle$ and the m-th state of the QD, with $m \geq 2$.

2.1.2 Emission lineshape of QD in bulk

After exciting a QD from its ground state $|0\rangle$ to its excited state $|1\rangle$, with a delta-pulse at time $t = 0$, the evolution of the QD coherence at $t > 0$ can be computed from the dipole correlation function, expressed as [64, 65, 168, 169],

$$P(t) = \langle \sigma^-(t)\sigma^+(0) \rangle$$

with σ^+ and σ^+ representing the off-diagonal elements of the two-level QD density matrix. σ^+ (σ^+) represents the transition between $|0\rangle$ to $|1\rangle$ ($|1\rangle$ to $|0\rangle$). The evolution of $P(t)$ due

to the coupling to phonons is described by,

$$P(t) = \left\langle \mathscr{T} \exp\left[-\frac{i}{\hbar}\int_0^t \mathrm{d}\tau (V_L + V_Q)\right]\right\rangle$$

where $\mathscr{T}$ is the time ordering operator, V_L and V_Q the coupling terms in the interaction picture. The complete mathematical treatment of this expression is rather complex, and we discuss below the final result. The interested reader may find more details and the derivations in Ref. [168]. The contributions of linear and quadratic couplings can be separated according to,

$$P(t) = \exp[-i\mu_F t + K_L(t) + K_Q(t)], \tag{2.11}$$

where K_L (K_Q) represents the contribution from the linear (quadratic) interaction, and is composed of the phonon Green's function. The term $i\mu_F t$ represents a spectral shift, arising due to the quadratic coupling. $i\mu_F t$ has no impact on the coherence of the system, thus it will be ignored hereafter.

Assuming instantaneous excitation in $|1\rangle$, as well as a negligible thermal population of this state, the QD photon emission spectrum $S(\omega)$ can be calculated following Ref. [64],

$$S(\omega) = \mathrm{Re}\int_0^\infty \mathrm{d}t e^{-\Gamma t/2} P(t) e^{-i\omega t}. \tag{2.12}$$

The interaction of the QD with electromagnetic modes is treated as a Markovian decay channel. It is introduced phenomenologically through the decay factor denoted by $\exp[-(\Gamma/2)t]$. The corresponding spontaneous emission decay rate Γ is determined by applying the Fermi golden rule to the photonic environment. In Eqn. 2.12, the dephasing associated with spontaneous emission is introduced as a multiplicative term, which is equivalent to factorising the phonon interaction by the electromagnetic mode interaction. These two interactions can be treated separately when the respective correlation functions act on very different timescales. We will see in the next section that, InAs QDs exhibit a coupling cutoff to phonons with energies greater than ~ 1 meV, which entails that the phonon interactions occur in the range of a few picoseconds. The interaction between a QD in bulk and electromagnetic modes is observed in the order of the optical period, which for an InAs QD exhibiting a 1 eV energy split between $|0\rangle$ and $|1\rangle$, leads to a timescale in the femtosecond range. This large mismatch in timescale means that the phonon interaction can be considered almost constant over the optical interaction timescale. In other words, this factorisation holds as long as the density of optical states does not vary significantly over a spectral range which includes relevant phonon modes [170].

In the following sections, we take a closer look at the expressions for K_L and K_Q, as well as discuss the various impacts of linear and quadratic QD-phonon coupling. The

expressions are obtained by performing a suitable mathematical development of Eqn. 2.11. The complete derivation and justification of K_L and K_Q remain out of the scope of the current work. Interested readers may find the necessary details in Ref. [64, 168].

2.1.2.a. Impact of linear coupling: acoustic phonon sidebands

According to Ref. [65], the linear interaction between a QD and phonons in bulk can be expressed as,

$$K_L(t) = -\frac{1}{2\hbar^2}\sum_{\mathbf{q}}|L_{\mathbf{q}}|^2\left[(2N_{\mathbf{q}}+1)\left(\frac{\sin\frac{\omega_{\mathbf{q}}}{2}}{\frac{\omega_{\mathbf{q}}}{2}}\right)+\frac{2i}{\omega_{\mathbf{q}}^2}(\sin\omega_{\mathbf{q}}t-\omega_{\mathbf{q}}t)\right], \tag{2.13}$$

where $\omega_{\mathbf{q}}$ is the frequency of the phonon mode with momentum $\mathbf{q}$, $N_{\mathbf{q}}$ is phonon occupation number given by a Bose-Einstein distribution, $N_{\mathbf{q}} = 1/[\exp(\hbar\omega_{\mathbf{q}}/k_BT)-1]$. The other terms have been defined in Eqns. 2.6, and 2.7.

In the limit where the thermal energy, k_BT is sufficiently lower than the spacing between two excited states of the exciton, higher excited states may be neglected limiting the discussion to a single excited state. In this situation, the coupling of an exciton with every phonon mode alters the equilibrium position of the lattice and an exciton energy shift. The shift in exciton energy, known as the polaron energy, is temperature-independent and denoted by $\Delta_{\mathbf{q}}$ in Fig. 2.2. The shift in the lattice equilibrium position, on the other hand, changes the overlap between wave-functions having different phonon states, thus resulting in the apparition of transitions between different phonon occupation states during the excitonic recombination. In other words, the exciton can not only recombine with no phonon contribution, but it may relax to the ground state by emitting or absorbing a phonon as well, as pictured in the inset of Fig. 2.2 [62].

While the linear coupling to phonons doesn't affect the width of the ZPL, it modifies the QD emission spectrum by generating phonon sidebands (PSBs). These PSBs are a result of phonon-assisted recombination of the exciton. Specifically, the ZPL corresponds to QD emission with zero phonon contribution. Exciton recombination assisted by phonon emission appears as a sideband red-shifted in energy from the ZPL, while contributions to QD emission from phonon absorption emerges as a sideband that is blue-shifted in energy. Emission into the sidebands can be strongly suppressed by reducing the temperature whereby freezing phonons, however, it isn't possible to eliminate the lower energy sideband, since phonon emission prevails even at absolute zero temperature. Thus at low temperature, the emission spectrum of a QD presents asymmetric sidebands.

The phonon sidebands have a finite spectral extension. It can be estimated in the simple case of a spherical QD with parabolic confinement potentials. The wave function of its lowest confined states would have an isotropic Gaussian distribution with a variance of L. This length L characterises the extent of localisation of the exciton within the QD,

which varies based on QD lateral size corresponding approximately to $2L\sqrt{2ln2}$ [62]. The dephasing associated to a mode $\mathbf{q}$ is determined by the square of the coupling strength, $|L_{\mathbf{q}}|^2$ (see Eqn. 2.13, which scales as $(M^{11}_{\mathbf{q}b})^2 \propto q\ \exp[-(qL)^2/2]$. This in turn defines a cutoff in phonon energy, expressed as $\hbar u_s/L$ [64]. In particular, for the InAs QDs we use, L is estimated to be around 5 nm [171]. Phonons with energies two times greater than this cutoff ($\approx 1\ meV$ for InAs QDs), have little impact on the dephasing of the exciton in the linear regime, i.e. these phonons don't contribute to the PSBs. Fig. 2.2 illustrates the coupling constant as a function of phonon energy for different values of L for II-VI semiconductor QDs [62].

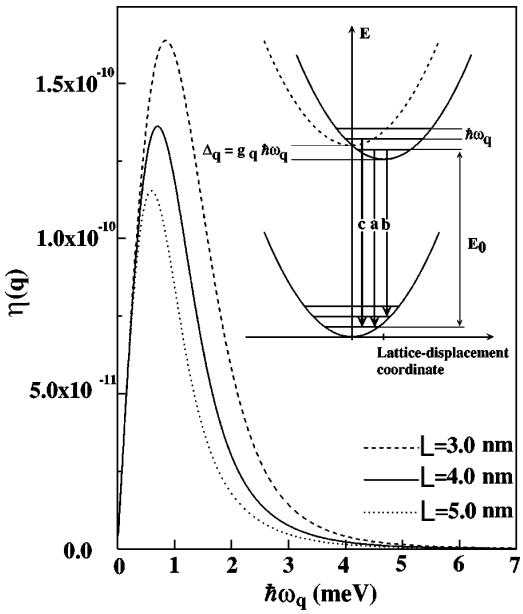

Fig. 2.2 The exciton-phonon coupling constant $\eta(q)$ as a function of phonon energy $\hbar\omega_q$. Each phonon mode $\mathbf{q}$ is characterised by the modulus of its wave vector q, $\eta(q)$ is integrated over all directions of $\mathbf{q}$, and is expressed as $\eta^2(q) = \rho(q)(L_q/\hbar\omega_q)^2$. The inset illustrates the energy of the exciton-phonon system for a phonon mode m. The lattice harmonic potentials of the initial and final states are represented as parabolas, where the dotted on is in the presence of phonon coupling, while the coupling is neglected in the solid one. The labelled vertical arrows represent optical transitions, namely the recombination without phonon interaction (a), the emission of a phonon (b), and the absorption of a phonon (c). Figure adapted from [62].

2.1.2.b. Impact of quadratic coupling: homogeneous broadening of the zero-phonon line

The quadratic coupling of a QD to phonon leads to the elastic scattering of phonons by a QD, mediated by virtual transitions of the QD from its first excited state to other excited states. A complete mathematical description of the quadratic coupling is rather cumbersome since it involves transitions between many QD states, arising from multiple interactions between

a phonon and the QD. However, some hypotheses may help to simplify the description. The first approximation consists in considering transitions only between the excited states $|1\rangle$ and $|2\rangle$ of the exciton, which is justified because the strength of the quadratic interaction scales as $1/\Delta_m^2$, where Δ_m is the energy spacing between state $|1\rangle$ and state $|m\rangle$, $m \geq 2$. Next, due to a "weak" interaction between a QD and a phonon, it is assumed that a phonon, while being elastically scattered from a QD, interacts only once with the latter. Further justification for these assumptions is presented in Ref. [168].

Under these simplifying hypotheses, one finds that in the long-time limit, the quadratic exciton-phonon interaction, leads to a Markovian dephasing and is represented as an exponential decay,

$$K_Q(t) = -\Gamma_{3D} t, \tag{2.14}$$

where Γ_{3D} is the dephasing rate in bulk and is expressed as,

$$\Gamma_{3D} = 3\pi \frac{u_s}{L} C_Q^2 \int_0^\infty \mathrm{d}(qL)(qL)^{10} e^{-(qL)^2} N_q(N_q+1), \tag{2.15}$$

with L representing the QD wavefunction radius, q the phonon wave number, and N_Q is the phonon occupation number. The dimensionless constant C_Q is defined as,

$$C_Q = \frac{D_e^2/\Delta_e + D_h^2/\Delta_h}{3(2\pi)^2 \rho_M u_s^2 L^3}. \tag{2.16}$$

where u_s represents the speed of sound, ρ_M is the mass density, D_e (D_h) denotes the deformation potential of the electron (hole), and Δ_e (Δ_h) corresponds to the energy spacing between excited states of the electron (hole).

Upon inspecting Eqn. 2.15, we see that the bulk dephasing rate Γ_{3D} experiences two cut-offs. These cut-offs are, $q_L = 1/L$, which is a limit defined by the QD size, and $q_T = k_B T/\hbar u_s$, which is imposed by the thermal population of modes. By equating both the limits $q_L = q_T$, allows to identify a critical temperature $T_c = \hbar u_s/k_B L$. This leads to the emergence of two operation temperature regimes. From Eqn. 2.15 we find at $T < T_c$, the cut-off in wave vector $\mathbf{q}$ is set by the temperature. Γ_{3D} thus scales as $(T/T_c)^{11}$, which leads to a rapid collapse of the quadratic interaction due to the freezing of phonons. In particular for $T \leq 5K$ decoherence due to quadratic coupling can be completely neglected [65]. At higher temperature $T > T_c$, the cut-off is set by the QD size. We thus have $N_q(N_q+1) = (k_B T/\hbar\omega_{\mathbf{q}})^2$, which leads to Γ_{3D} scaling as $(T/T_c)^2$.

2.2 Phonon decoherence in an infinite nanowire

The discussion so far was focused on the impact of the interaction with acoustic phonons on the exciton coherence of a QD in bulk. In practice, QDs are often integrated into

nanostructures designed to improve the light collection efficiency. Such nanostructures necessarily reshape the phonon environment. As a first illustration of this effect, we present in this section the theoretical results of Ref. [163], which considers an infinitely-long nanowire with a diameter of 50 nm (we note this diameter is typically 4 times smaller than that of photonic wire antennas). Following Ref. [163] we first consider the modification associated with linear coupling. While the phenomenon of QD decoherence due to acoustic phonons in a nanostructure is fundamentally the same as in bulk material, the structuration essentially gives rise to two major differences. These differences, as pictured in Fig. 2.3, are the apparition of satellite peaks on the PSBs, and the broadening of the ZPL.

The lateral confinement of the wire limits the family of guided modes that are supported at low energy, thus altering the density of modes at low-frequency. The wire supports more guided modes as the mode energy increases, as illustrated in Fig. 2.4. Even though similar low-frequency modes are present in bulk, their coupling strength is significantly enhanced in a nanowire (Fig. 2.4). This amplification in coupling may be attributed to the fact that these mechanical modes confine elastic energy in small volumes, within the nanowire. As a result, the linear coupling between the QD and low-frequency phonon modes is altered and manifests itself in the form of distinct satellite peaks in the sidebands of a QD emission spectrum, as shown in Fig. 2.3. Among these low-frequency modes, the nanowire amplifies the coupling strength between a QD and phonons with energy sufficiently small, to produce emission satellites that are spectrally located within the natural linewidth of the ZPL. Thus the ZPL is broadened within the linear interaction regime, and the broadening is only amplified when the system also undergoes quadratic interactions.

The interaction between the QD and an electromagnetic mode can be considered to be uncorrelated to the QD-phonon interaction because they act on largely different timescales, femtoseconds for the former ($\sim$ 1/bandwidth) and picoseconds for the latter. Thus it remains valid to include the QD-electromagnetic mode interaction phenomenologically to the QD-phonon treatment. In the high-energy limit, modes possess wavelengths much smaller than the physical size of the nanowire, causing the latter to appear much like bulk material. Therefore a density of modes similar to bulk is retrieved in the high-frequency limit. Consequently, the quadratic coupling isn't affected by the structuration either, because the phonons responsible for virtual transitions generally possess high frequencies, such that their energy may be comparable to the QD excited states energy difference.

Similar effects, although less pronounced than the infinite nanowire, have been predicted in the case of an infinite 2D membrane in Ref. [65]. In the following section, we focus our attention on a finite nanowire antenna. Under finite dimensions in all 3 dimensions, the nanowire antenna acts as a 0D structure, thus sustaining discrete mechanical resonances. We perform a comprehensive study in order to estimate the impact of these discrete modes on the coherence of a QD emission.

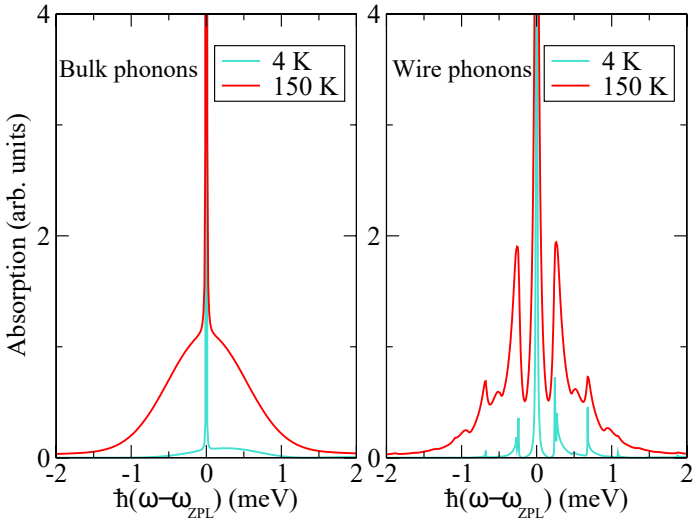

Fig. 2.3 Absorption spectra of a QD in bulk (left) and a QD in a nanowire (right) as a function of energy detuning with respect to the ZPL transition energy ($\hbar\omega_{ZPL}$), at different temperatures [163].

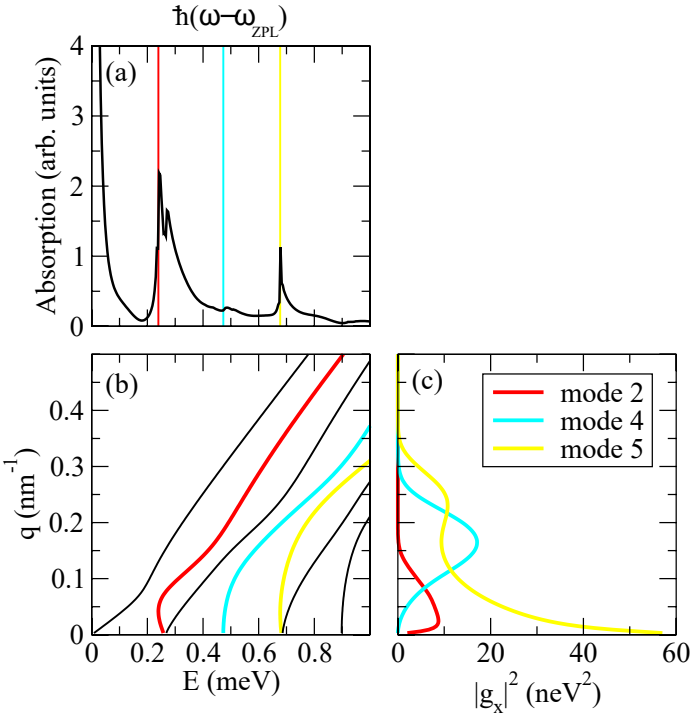

Fig. 2.4 (a) A portion of the absorption spectrum of a QD in an infinite nanowire with a 50*nm* diameter at 40 K. The spectrum is representative of the density of phonon modes as a function of energy. The reference transition energy $\hbar\omega_{ren}$ is the ZPL emission energy. (b) Phonon mode spectrum indicating the families of modes present in the nanowire at different energies. (c) Exciton coupling strength of a few selected phonon modes of the nanowire [163].

2.3 Decoherence due to low-frequency thermal vibrations in nanowire antennas

In previous sections, we have discussed the different regimes of interaction between QD and acoustic phonons, and we have established that low frequency mechanical mode continua are a dominant source of QD decoherence in nanostructures of reduced dimensionality. Compared to the bulk, a realistic nanowire features a set of discrete, low frequency mechanical resonances, typically in the MHz-GHz range. In this section, we focus on the specific impact of these discrete low-frequency mechanical resonances. We bear in mind that the high-frequency part of the phonon environment also contributes to the spectral broadening of the QD emission (through the formation of acoustic phonon sidebands, and the homogeneous broadening of the zero-phonon line [64]). However, we limit our study to the interactions that are linear in phonon displacement. The objective here is not to provide a complete description of phonon dephasing in our nanowire systems, but rather to estimate the impact of low-frequency mechanical resonances on the decoherence of the QD.

2.3.1 Vibration modes of nanowire antennas

Nanowire antenna geometry. Nanowire antennas exploit a tapered dielectric waveguide to shape the emission of a QD into a directive free-space beam [75]. As shown in Fig. 2.5, the nanowire features a diameter $d \sim \lambda/n$ around the QD, where λ is the free-space operation wavelength and n the nanowire refractive index. To optimise light collection efficiency, the nanowire stands on a hybrid dielectric-metallic mirror and is terminated by a top taper, which can feature either a 'needle' (panel (a)) or 'trumpet' shape (panel (b)). Needle antennas can be obtained with top-down [77, 80] or bottom-up [50, 83] fabrication strategies, while photonic trumpets have so far been produced only through top-down processing [78]. In this work, we consider GaAs antennas, either featuring a needle or trumpet top taper, which embed a self-assembled InAs QD ($\lambda = 900\,$nm). The emitter is located on the first antinode of the vertical standing wave pattern generated by the mirror reflection, 100 nm above the bottom mechanical clamping plane. This choice maximizes the optical bandwidth of the antenna, which exceeds 100 nm [142]. In both cases, the bottom part of the antenna is identical ($d = 200\,$nm). At the level of the QD, the wire reduced diameter is $d/\lambda = 0.23$, a choice which leads to an optimal lateral confinement of the guided mode, and thus to a maximal $\Gamma^{\infty}_{\mathrm{HE}_{11}}$ ($\Gamma^{\infty}_{\mathrm{HE}_{11}} = 0.9 \times \Gamma_{\mathrm{bulk}}$ for an on-axis emitter, with Γ_{bulk} the bulk reference SE rate). Both antennas stand on a gold-silica mirror, with a modal energy reflectivity $|r_b|^2 = 0.91$.

The needle antenna (Fig. 2.5(a)), measuring 3 μm in height, is very close to the one investigated in Ref. [77], which was realised with a top-down (etching) process. The needle has a diameter at its base of 200 nm, and a 1.1 μm top taper ending in a top facet of 80 nm in

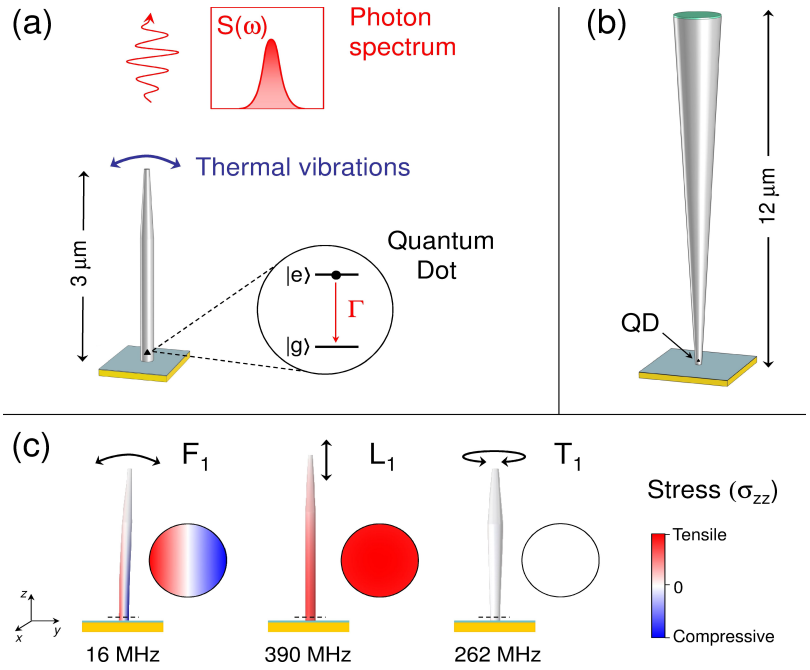

Fig. 2.5 Nanowire antennas with a 'needle' (a) and 'trumpet' (b) top taper. The thermal excitation of nanowire vibration modes generates a fluctuating stress which modulates the QD bandgap energy and thus broadens the spectrum $S(\omega)$ of QD photons. (c) Fundamental flexural (F_1), longitudinal (L_1) and torsional (T_1) vibration modes for the needle antenna shown in (a). The color codes the amplitude of the σ_{zz} stress component.

diameter. It is also representative of the typical dimensions of bottom-up nanowire antennas. While the photonic trumpet (Fig. 2.7(a)) under study is identical to the one investigated in Ref. [78]. It features a height of 12 μm; the top facet is 1.5 μm large, and is covered by a $\lambda/4$ anti-reflection coating (green layer in Fig. 2.7(a)).

For pedagogical purposes, we first detail the case of the GaAs needle antenna shown in Fig. 2.5(a). Its mechanical spectrum is calculated with a finite element software. As schematised in Fig. 2.5(c), the first vibration modes fall into three families, flexural (F), longitudinal (L) and torsional (T). T-modes can be neglected since they essentially generate shear stress, which does not modify the bandgap energy of a self-assembled QD to first order [87, 172]. In contrast, F- and L-modes generate a longitudinal stress σ_{zz} which strongly modulates the QD bandgap energy [172]. For L-modes, σ_{zz} is uniform over horizontal nanowire sections, the coupling strength g_m does not depend on the QD lateral position. For F-modes, σ_{zz} is null on a central neutral axis and increases linearly when approaching the sidewall, g_m is thus strongly position-dependent [88].

2.3.2 Electron-phonon Hamiltonian

The electron-phonon Hamiltonian, after neglecting non-linear intermode couplings [173] for the phonon Hamiltonian, can be expressed as,

$$H = \hbar\omega_{01}|1\rangle\langle 1| + \sum_m \hbar\omega_m a_m^\dagger a_m + \sum_m \hbar g_m (a_m + a_m^\dagger)|1\rangle\langle 1|, \tag{2.17}$$

Here we retain only the linear coupling term in the interaction Hamiltonian. Since the phonon wavelengths vastly exceed the QD size, the latter can be modelled as a point-like structure, leading to the coupling strength [90, 174],

$$g_m = \left(\frac{\partial\omega_{01}}{\partial u_m}\right) u_m^{\mathrm{zpf}}. \tag{2.18}$$

In this expression, u_m is a scalar coordinate which describes the mode displacement, $\left(\frac{\partial\omega_{\mathrm{eg}}}{\partial u_m}\right)$ is the QD spectral shift in response to this displacement. u_m^{zpf} is the rms value of zero-point fluctuations,

$$u_m^{\mathrm{zpf}} = \sqrt{\frac{\hbar}{2m_m^{\mathrm{eff}}\omega_m}}, \tag{2.19}$$

with m_m^{eff} the mode effective mass and ω_m the resonance angular frequency. In practice, $\left(\frac{\partial\omega_{\mathrm{eg}}}{\partial u_m}\right)$ is dominated by the shift of the bandgap of the QD material. For a self-assembled QD, with a large residual bi-axial compressive strain, it reads [172],

$$\hbar\frac{\partial\omega_{\mathrm{eg}}}{\partial u_m} = a\left(\frac{\partial\varepsilon_{\mathrm{h}}}{\partial u_m}\right) + \frac{b}{2}\left(\frac{\partial\varepsilon_{\mathrm{sh}}}{\partial u_m}\right). \tag{2.20}$$

Here, a is the deformation potential associated with the hydrostatic strain $\varepsilon_h = \varepsilon_{xx} + \varepsilon_{yy} + \varepsilon_{zz}$ and b the deformation potential associated with the tetragonal shear strain $\varepsilon_{\mathrm{sh}} = 2\varepsilon_{zz} - \varepsilon_{xx} - \varepsilon_{yy}$ (z is the QD growth axis). We suppose that the QD is composed of an $In_{0.5}Ga_{0.5}As$ alloy and use $a = -7.5\,\mathrm{eV}$ and $b = -1.9\,\mathrm{eV}$ (linear interpolation between the deformation potentials of InAs and GaAs, given in Ref. [175]). The quantities $\left(\frac{\partial\varepsilon_{\mathrm{h}}}{\partial u_m}\right)$, $\left(\frac{\partial\varepsilon_{\mathrm{sh}}}{\partial u_m}\right)$, ω_m and m_m^{eff} are determined from numerical simulation using a finite element software (Comsol Multiphysics). The mode solver provides: (i) ω_m, (ii) the strain tensor at arbitrary location in the structure for a displacement equal to the oscillation amplitude u_m^{max}, which yields the two first derivatives and (iii) the time-averaged total elastic energy $\langle W_{\mathrm{el}}\rangle_t$, from which we deduce the effective mass using:

$$\langle W_{\mathrm{el}}\rangle_t = \frac{1}{4} m_m^{\mathrm{eff}} \omega_m^2 (u_m^{\mathrm{max}})^2. \tag{2.21}$$

2.3.3 Emission lineshape of QD in nanowire antennas

In order to evaluate the phonon dephased lineshape $S(\omega)$ (Eqn. 2.12) of the QD we pursue an approach analogous to the one presented in Sec. 2.1.2. The interaction between QD and electromagnetic modes occurs in the order of the inverse of the bandwidth of the nanostructure, which in our nanowires leads to a timescale in the femtosecond range. This timescale is 3 orders of magnitude smaller than the phonon interaction, which means the density of optical states does not vary significantly over a spectral range including relevant phonon modes. We are thus still justified to treat the interaction between QD and electromagnetic modes phenomenologically. However narrow band photonic structures, which present a spectral bandwidth that is comparable to the phonon spectral band, such as resonant microcavities or slow-light waveguides do not allow for the correlations between phonons and electromagnetic modes to be overlooked. These narrow band systems therefore generally require a more involved treatment to be able to compute the spontaneous decay rate [158, 159, 176]. An alternate timescale mismatch between the phonon and optical interactions could be obtained in a highly spectrally-narrow resonant cavity as in Refs. [72, 159]. The bandwidth of the cavity is significantly narrower than the spectral extent of the PSBs, which if resonantly matched to the ZPL could act as a spectral filter for the PSBs. The cavity promotes the ZPL as a more preferential emission channel, and in the process draws in some emission that would otherwise feed the PSBs back into the ZPL. The decoupling argument between the optical and phononic interaction still holds in this case however the treatment would be slightly different than in broadband nanowires.

Since there is no mode mixing between low-frequency modes at cryogenic temperature, we can rewrite $P(t) = \prod_m P_m(t)$, which describes the time-evolution of dipole-dipole correlations driven by the (uncorrelated) contributions of individual vibration modes from Eqn. 2.11 as,

$$\begin{aligned} P_m(t) &= \exp\left[-\theta_m^2 \sin^2\left(\frac{\omega_m t}{2}\right) - \eta_m^2(1-e^{-i\omega_m t})\right], \\ \text{where } \eta_m^2 &= (g_m/\omega_m)^2 \quad \text{and} \quad \theta_m^2 = 4\eta_m^2 N_m \\ \text{with } N_m &= [\exp(\hbar\omega_m/k_B T) - 1]^{-1}. \end{aligned} \tag{2.22}$$

The argument proportional to η_m^2 accounts for phonon emission in the zero-temperature limit, and the one proportional to θ_m^2, accounts for the thermally-activated absorption and emission of phonons. For simplicity, we have omitted the so-called polaron shift in $P_m(t)$, which simply induces a rigid spectral shift of the QD emission spectrum. $S(\omega)$ can be recast as the convolution product,

$$S(\omega) = S_{\text{rad}}(\omega) * S_1(\omega) * S_2(\omega) * \cdots . \tag{2.23}$$

Here, $S_{rad}(\omega)$ is the radiatively-limited QD emission spectrum,

$$S_{\text{rad}}(\omega) = \frac{\Gamma/2}{\omega^2 + (\Gamma/2)^2}, \tag{2.24}$$

while $S_m(\omega)$ captures the spectral broadening associated with mode m.

$$S_m(\omega) = \int_{-\infty}^{+\infty} \mathrm{d}t P_m(t) \exp(-i\omega t). \tag{2.25}$$

$S_m(\omega)$ consists of spectral lines separated by ω_m, whose relative weights are governed by the parameters θ_m^2 and η_m^2.

Considering a needle antenna cooled down to $T = 4\,\text{K}$, θ_m^2 and η_m^2 are plotted in Fig. 2.6(a) for the first 15 vibration modes. For F-modes, we plot the on-sidewall, maximal values. Both θ_m^2 and η_m^2 decrease as the mechanical frequency increases. For all modes $\eta_m^2 \ll 1$, whereas $\theta_m^2 \gg 1$ for the first harmonics and $\theta_m^2 \ll 1$ in the high-frequency limit. For the first vibration modes ($\theta_m^2 \gg 1 \gg \eta_m^2$), $S_m(\omega)$ is a comb of spectral lines with a Gaussian envelope having a standard deviation $|g_m|\sqrt{2N_m}$ (Fig. 2.6(b)). In this case, the QD experiences a spectral broadening which directly reflects the thermally-driven stress fluctuations, whose rms values are given for a few modes as an inset in Fig. 2.6(a). Since $|g_m|\sqrt{2N_m}$ features a relatively smooth dependence on ω_m, all modes found in this limit significantly contribute to the spectral broadening. The high-frequency limit corresponds to a perturbative regime (η_m^2, $\theta_m^2 \ll 1$). As shown in Fig. 2.6(b), $S_m(\omega)$ is then composed of a central spectral line, flanked by a red and a blue sideband, whose weights are $\eta_m^2(N_m+1)$ and $\eta_m^2 N_m$, respectively. For the considered needle antenna, we compute the mechanical spectrum up to 8 GHz, and the sideband weight for the last modes is below 10^{-4}.

Fig. 2.6(c) shows the calculated QD emission spectrum for on-axis and on-sidewall locations, at $T = 4\,\text{K}$. For reference, we plot as a shaded curve the radiatively-limited spectra. These spectra differ significantly because the local density of optical states varies in the nanowire section [75]. We take here $\Gamma = 1.74 \times \Gamma_{\text{bulk}}$ on the axis, and $\Gamma = 0.33 \times \Gamma_{\text{bulk}}$ on the sidewall [52], with $\Gamma_{\text{bulk}} = (1\,\text{ns})^{-1} = 2\pi \times 160\,\text{MHz}$ the reference decay rate of a typical QD embedded in bulk GaAs. Due to nanowire vibrations, both on-axis and on-sidewall emitters feature a spectrum that differs from the radiatively-limited lineshape. An on-axis emitter is only coupled to L-modes, and the sidebands generated by L_1 (390 MHz) are clearly resolved in the spectrum. On the sidewall, the emitter experiences a strong contribution of low-frequency F-modes. The QD emission is then well approximated by a Voigt profile, which is much broader than the radiatively-limited lineshape.

Similar results are obtained in photonic trumpets (Fig. 2.7), for which QD linewidths have been measured with resonant spectroscopy. At low driving power, the QD investigated in Ref. [87] features a full width at half maximum (FWHM) of 5.1 μeV and a radiatively-limited FWHM of 0.7 μeV. The QD position was determined by strain-gradient

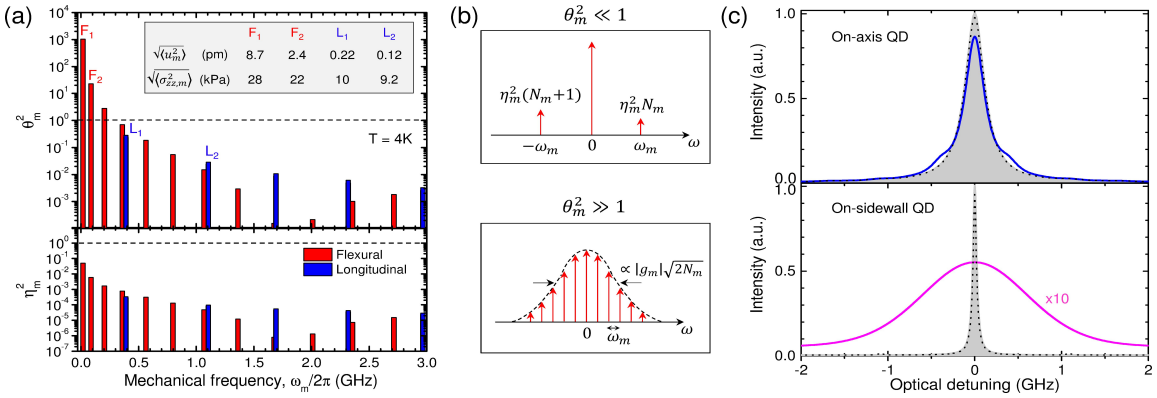

Fig. 2.6 Impact of the thermal vibrations of a needle antenna at $T = 4\,\mathrm{K}$. (a) θ_m^2 and η_m^2 for the first 15 vibration modes. Inset: rms values of the thermal top facet displacement $\langle u_m^2 \rangle^{1/2}$ and of the longitudinal stress $\langle \sigma_{zz,m}^2 \rangle^{1/2}$ for a few modes. For F-modes, we plot the maximum, on-sidewall values. (b) Lineshape $S_m(\omega)$ for $\theta_m^2 \gg 1$ and for $\theta_m^2 \ll 1$ (in both cases $\eta_m^2 \ll 1$). The arrows represent Dirac δ-peaks. (c) Solid line: Calculated QD emission profile, $S(\omega)$. Dotted line: Calculated QD emission profile without the 7 first mechanical modes (6 F-modes and 1 L-mode). Filled curve: Lorentzian, radiatively-limited emission line, $S_{\mathrm{rad}}(\omega)$. Top panel: on-axis QD; Bottom panel: on-sidewall QD.

mapping [88]: the emitter is off-axis by 35 nm (the mean wire radius is 145 nm). Our theory then predicts a FWHM of 2.9 μeV, showing that even for QDs that are relatively close to the nanowire axis, thermal vibrations constitute a major source of decoherence at $T = 4\,\mathrm{K}$.

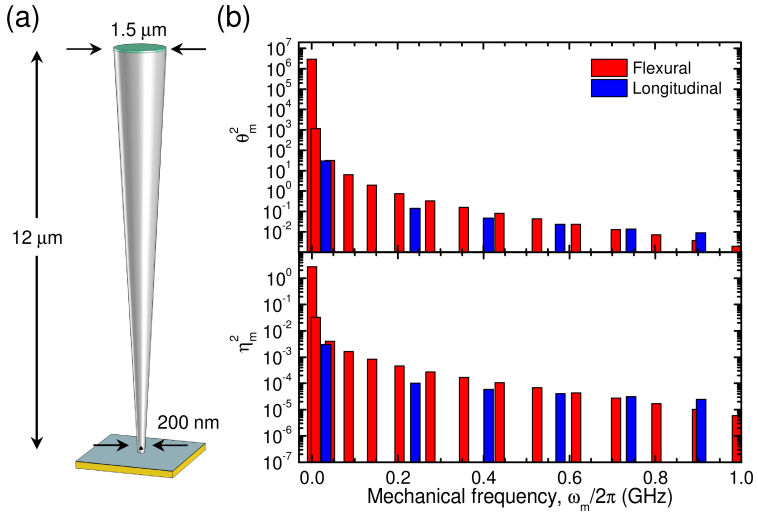

Fig. 2.7 (a) Standard trumpet antenna. (b) θ_m^2 and η_m^2 for the first vibration modes. There are several differences with the needle antenna. The fundamental flexural mode features a very large $\eta_m^2 > 1$. This agrees well with previous optomechanical studies on this system [87, 90]. An on-sidewall QD is in the so-called ultra-strong coupling regime, defined by $\eta_m = g_m/\omega_m > 1$. We note that all the other modes feature $\eta_m^2 \ll 1$. In addition, the fundamental L-mode has a strong contribution ($\theta_m^2 > 1$). This explains why photon indistinguishability is degraded for an on-axis emitter compared to the case of the needle antenna.

Fig. 2.6(c) also demonstrates that the spectral broadening is dominated by the contribution of the first mechanical modes. By suppressing the first 7 modes in a needle antenna, we were able to restore an emission profile that is very close to the radiatively-limited one. This can be directly traced back to the very fast decrease of θ_m^2 and η_m^2 at large mechanical frequency.

For a quantitative analysis, in the subsequent sections, we will consider the photon indistinguishability I, a figure of merit that corresponds to the outcome of a Hong-Ou Mandel two-photon coalescence experiment, a key phenomenon for many quantum information protocols. Assuming a perfectly antibunched photon emission ($g^2(0) = 0$), the degree of indistinguishability can be calculated as [65, 177],

$$I = \Gamma \int_0^\infty \mathrm{d}t e^{-\Gamma t} |P(t)|^2. \tag{2.26}$$

The maximum degree of indistinguishability of emitted photons, for a nanowire single-photon source, is achieved for a QD located on the wire axis. In particular, a nanowire operating at T = 4 K, this maximum values is $I = 0.75$ for a needle and $I = 0.5$ for a trumpet. At just 20 nm off-axis, I drops to around 0.5 for a needle, and 0.4 for a trumpet, until I plummets to almost zero for both in the case of a QD at the wire-edge.

2.3.4 Suppressing decoherence by decreasing operation temperature

To improve I, a first obvious strategy is to reduce the operating temperature. The numbers given in the following include only the effect of nanowire vibrations and exclude all other decoherence channels. Fig. 2.8 confirms that at $T = 4\,\mathrm{K}$, thermal vibrations of needle and trumpet antennas lead to indistinguishability values that are not compatible with the requirements of quantum optics experiments. In a pumped ^{3}He cryostat ($T = 300\,\mathrm{mK}$), a QD located on the axis of a needle antenna features $I = 0.98$ and emitters with a distance to the axis below 20 nm exhibit $I > 0.92$ (Fig. 2.8(a)). However, on-sidewall emitters are still plagued with a poor I. In this situation, accurate emitter positioning in the nanowire section is critical to minimise vibration-induced decoherence. For top-down devices, this could be realized with deterministic lithography techniques [178–180]. Interestingly, the bottom-up fabrication route defines an on-axis QD with an even better accuracy [50]. Operating the source in a dilution fridge ($T = 20\,\mathrm{mK}$) further improves I and the tolerance on the emitter lateral position.

2.4 Mechanically engineered nanowire antennas

Below we explore a different and less expensive path to improve I. We propose to engineer the decoherence channels, bringing all vibration modes deep into the perturbative regime

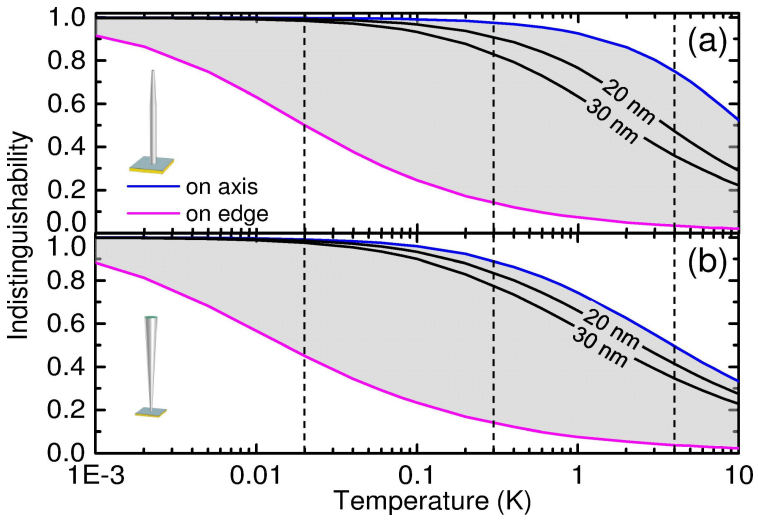

Fig. 2.8 Photon indistinguishability I as a function of the operation temperature T for a typical needle (a) and trumpet (b) nanowire antenna. We consider four transverse QD positions: on-axis, 20 nm off-axis, 30 nm off-axis and on-sidewall. The vertical dashed lines indicate the typical base temperature in a dilution fridge (20 mK), a pumped ^{3}He cryostat (300 mK) and a liquid ^{4}He cryostat (4 K).

(θ_m^2, $\eta_m^2 \ll 1$), for which mechanical sidebands feature a vanishingly small weight. This approach largely suppresses the impact of low-frequency vibrations, restoring photon indistinguishability when the antenna is operated in a standard ^{4}He cryostat. Generally speaking, it is interesting to shift mechanical resonances towards the high-frequency domain, because both N_m and η_m decrease. A second important improvement direction is to locate the emitter as far as possible from high-stress zones. In the following, we propose three designs that exploit separately or combine these ideas. We also present the photonic rationale of the designs, which preserve a large light extraction efficiency ($> 80\%$). Changes in the geometry also imply (small) changes in the QD emission rate Γ, which are taken into account in the calculation of I.

In this section, we present the photonic rationale behind each mechanically engineered antenna, and we also propose a fabrication process for them. More details on the photonic properties of the device are given in Appendix B.

2.4.0.a. Needle antenna covered by a low-index dielectric shell

As illustrated in Fig. 2.9(a), covering the antenna with a conformal dielectric shell made of a low-index material represents a simple yet effective solution to suppress vibration decoherence. We consider here SiO_2, but other materials could be employed as well. The shell can be deposited on a standard needle antenna (optimal $\Gamma^{\infty}_{HE_{11}}$ for $d/\lambda = 0.24$), using a conformal deposition technique, such as Plasma Enhanced Chemical Vapour Deposition. The complete planarisation of the device can be obtained by spin-coating an appropriate polymer (see for example Ref. [181]).

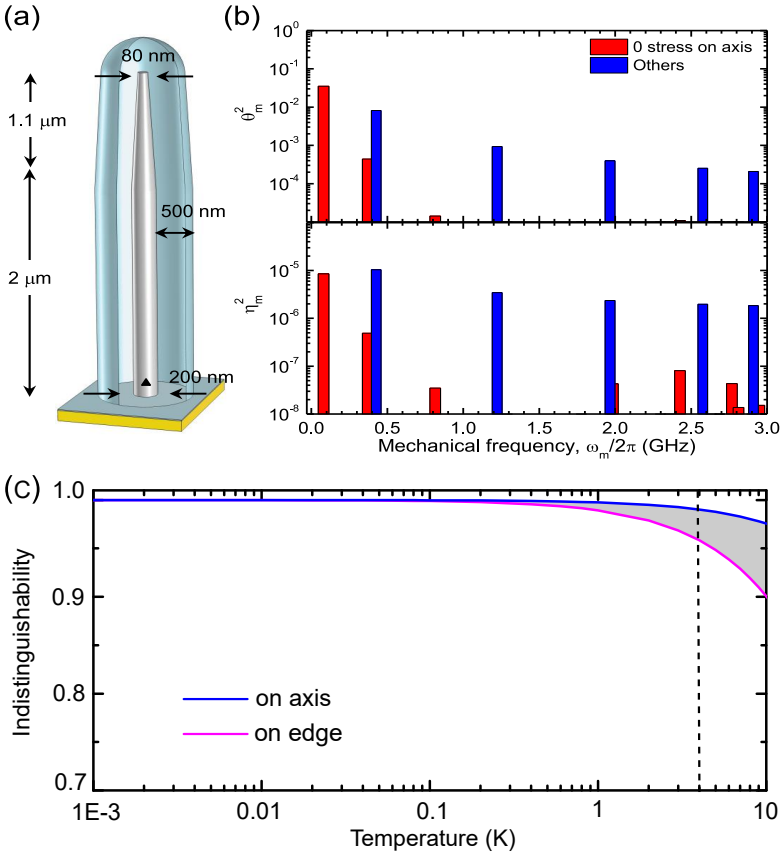

Fig. 2.9 (a) Needle-like antenna covered with a conformal, low-index dielectric shell (thickness of 500 nm). (b) θ_m^2 and η_m^2 for the first vibration modes. Compared to the bare needle antenna, flexural modes resonate at higher frequencies, while longitudinal ones do not experience major frequency shifts. In all cases, θ_m^2 and η_m^2 are strongly reduced, which explains the better indistinguishability. (c) Photon indistinguishability I as a function of the operation temperature T. The dotted vertical line marks $T = 4K$.

A shell with a thickness of just $s = 500\,\text{nm}$ leads to excellent performance at $T = 4\,\text{K}$: An on-axis emitter features $I = 0.99$, and I exceeds 0.96 at any QD lateral positions. The shell largely suppresses the impact of F-modes, because an emitter embedded in the core remains far from the lateral stress maximum, which is located at the external sidewall of the shell. Also, the frequency of F-modes increases with the structure diameter. The impact of L-modes also decreases, essentially because the shell increases the effective mass of the resonator, hence reducing g_m. As s further increases, performance continues to improve, since the phonon environment progressively matches the one of bulk material. From a technological point of view, the limit $s \to \infty$ can be conveniently achieved through a planarisation of the device. This approach also proves to be very efficient when applied to trumpet-like antennas standing on a bottom mirror.

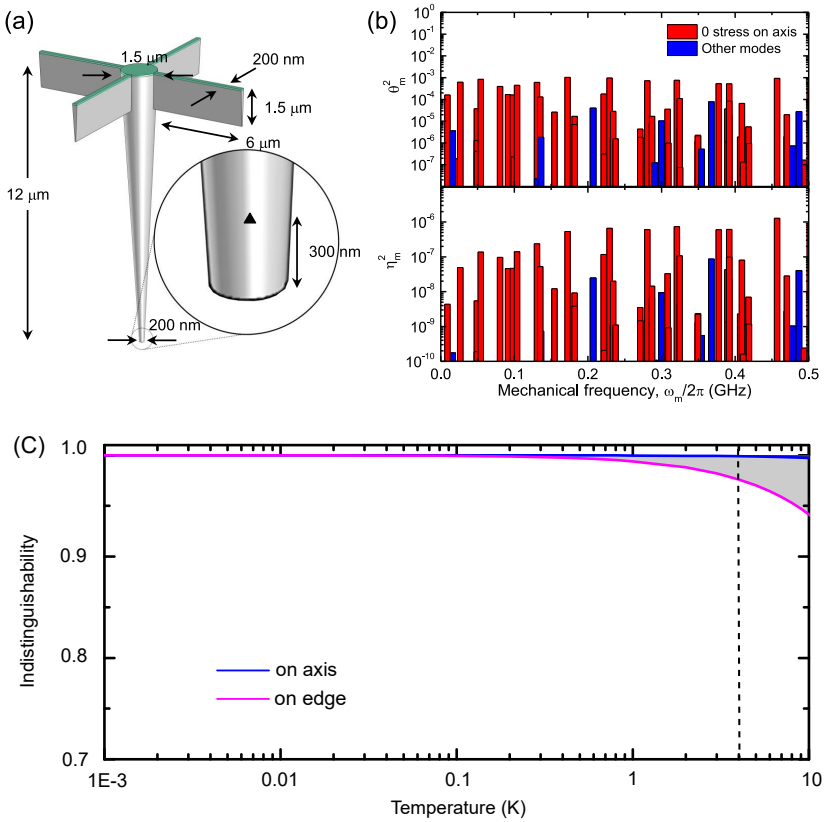

Fig. 2.10 (a) Suspended trumpet taper. The structure is suspended by four arms connected to anchoring pillars (not shown). (b) θ_m^2 and η_m^2 for the first vibration modes. (c) Photon indistinguishability I as a function of the operation temperature T. The dotted vertical line marks $T = 4K$.

2.4.0.b. Suspended photonic trumpet

In standard nanowire antennas, QDs are located close to a longitudinal maximum of the vibration-induced strain. However, the suspended photonic trumpet shown in Fig. 2.10(a) completely reverses this situation. In the proposed device, the top part of the taper is anchored to distant pillars and the QD is located close to the bottom part of the nanowire, which is terminated by a flat facet, used as a mirror. The emitter is thus located close to a free end of the nanowire, which dramatically decreases the coupling strengths and restores excellent spectral properties ($I > 0.98$ for all QD positions).

We keep the taper dimensions of the standard photonic trumpet, and suspend it with anchoring arms (Fig. 2.10(a)). For this device, the bottom, flat dielectric facet is used as a mirror. A reduced diameter $d/\lambda = 0.25$ ensures a good facet modal reflectivity $|r_b|^2 = 0.41$, while preserving a close-to-optimal $\Gamma^{\infty}_{\mathrm{HE}_{11}}$ ($\Gamma^{\infty}_{\mathrm{HE}_{11}} = 0.87 \times \Gamma_{\mathrm{bulk}}$ for an on-axis emitter). The phase acquired upon reflection on the dielectric facet is close to 0. Therefore, the first antinode is located on the facet, and cannot be used. The QD is located on the second antinode, $\sim 300\,\mathrm{nm}$ above the facet.

Ref. [86], shows that it is possible to realise suspended trumpets anchored to pillars in a single dry etching step. In this first realisation, the bottom part of the trumpet was terminated by a conical tip, with a reflectivity close to zero. A flat bottom facet is crucial to achieving a significant reflectivity and thus a large collection efficiency. To define this facet, we propose to integrate a sacrificial AlGaAs layer (typical Al content of 80 %) below the QD layer. An isotropic wet chemical etching will be employed to remove the sacrificial layer, releasing the bottom tip and revealing the desired flat bottom facet. If stopped in due time (etching depth $\sim 100\,\text{nm}$), this wet etching will not compromise the mechanical stability of the anchoring pillars, which are much thicker than the trumpet (pillar bottom diameter $> 2\,\mu\text{m}$, trumpet bottom diameter $\sim 200\,\text{nm}$). Alternatively suspended trumpets could be realised by glueing the top facet of the trumpet on the cleaved end of a single-mode fiber [152].

2.4.0.c. Photonic trumpet with a mechanically-decoupled top taper

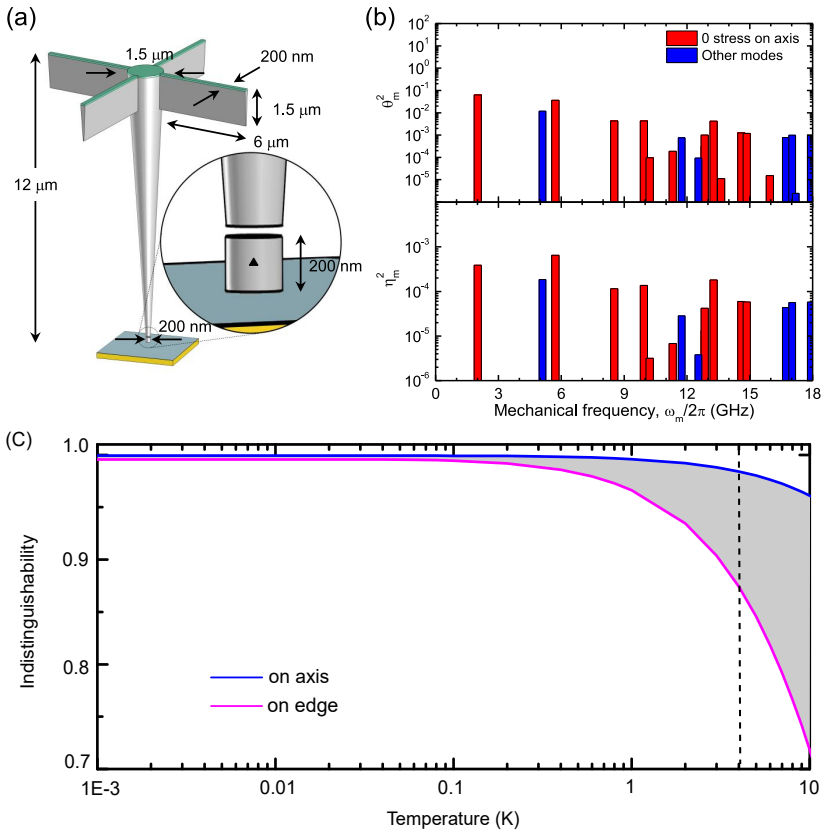

Fig. 2.11 (a) Trumpet antenna with a mechanically-decoupled top taper. The top taper is suspended by four arms connected to anchoring pillars (not shown). (b) θ_m^2 and η_m^2 for the first vibration modes. All mechanical resonances are pushed to very high frequencies (> GHz). (c) Photon indistinguishability I as a function of the operation temperature T for three mechanically-engineered antennas. The dotted vertical line marks $T = 4K$.

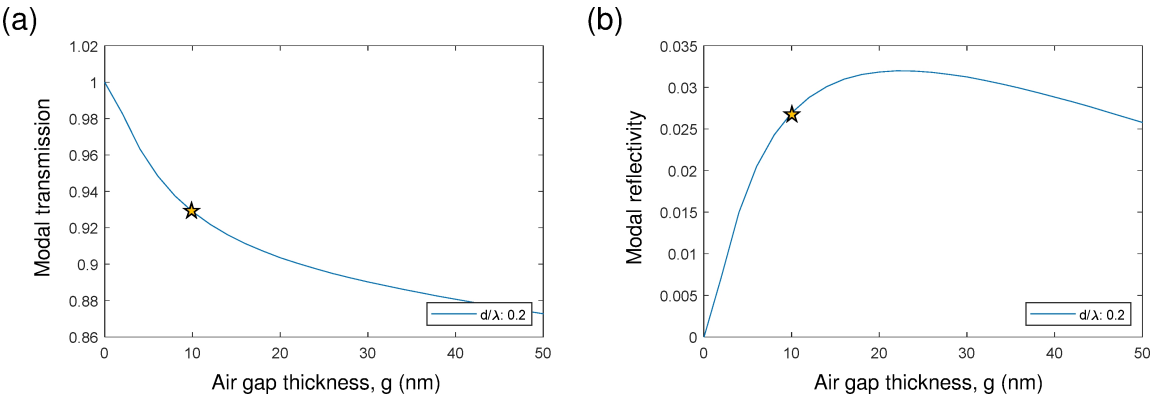

Fig. 2.12 (a) Modal transmission of the fundamental guided mode through the gap section, as a function of the gap opening g. (b) Modal reflectivity as a function of g. We consider a reduced wire diameter $d/\lambda = 0.20$ and a free-space operation wavelength $\lambda = 900\,\text{nm}$. The star indicates the value used in the design ($g = 10\,\text{nm}$).

A last possible strategy is to shift all mechanical resonances to very large (GHz) values. In the device schematised in Fig. 2.11(a), a 10 nm thin air gap is introduced between a 200 nm-high bottom nanowire section and the top taper. The air gap is sufficiently thin to minimise the optical discontinuity, while completely decoupling the bottom part from the taper from a mechanical point of view. Owing to its nanoscale volume, the bottom section exhibits a fundamental resonance frequency as high as 2 GHz, an increase by more than 3 orders of magnitude compared to a standard trumpet. For an on-axis emitter, $I = 0.98$ and $I > 0.87$ for all emitters.

The QD is embedded in a short (200 nm high) nanowire section, which is mechanically decoupled from the top taper by a thin gap of thickness g (Fig. 2.11(a)). The modal transmission T_{gap} of the gap critically depends on the wire diameter. For $d/\lambda = 0.23$, T_{gap} is significantly degraded even for modest gap opening ($T_{\text{gap}} = 0.67$ for $g = 10\,\text{nm}$). To limit the optical discontinuity associated with the gap, it is interesting to decrease d, so that a larger fraction of HE_{11} propagates in air. This is done at the cost of a weaker lateral confinement, and thus a reduced emission rate into HE_{11}. A diameter $d/\lambda = 0.2$ represents a good compromise. As shown in Fig. 2.12, T_{gap} is then as large as 0.93 for $g = 10\,\text{nm}$. In the same time, $\Gamma^{\infty}_{\text{HE}_{11}}$ is still reasonably large ($\Gamma^{\infty}_{\text{HE}_{11}} = 0.54 \times \Gamma_{\text{bulk}}$ for an on-axis emitter). For all considered openings, the modal reflectivity of the gap remains below 3 %. Therefore, it has a minor impact on the total SE rate, which can still be computed with Eqn. C.1.

As a starting point for the fabrication of this structure, we consider a planar epitaxial structure supported by a gold + silica planar mirror (obtained by a flip-chip process). Then a trumpet connected to pillars with anchoring arms is defined. This step is similar to the one employed to fabricate suspended trumpets, however with two differences: i) the etching depth and the trumpet lateral dimensions are now chosen so that the bottom part of the trumpet remains connected to the substrate and ii) the sacrificial layer, whose removal

will define the future gap, is located above the QD layer. Analogous to the suspended trumpets, the sacrificial layer is removed by wet chemical etching. The etching depth ($\sim 100\,\text{nm}$) is large enough to ensure complete removal in the trumpet section and small enough to preserve the mechanical stability of the anchoring pillars. To avoid a collapse of the very thin gap due to capillary forces, the drying of the sample will very likely require supercritical drying.

2.5 Conclusion

In conclusion, in this chapter, we delved into the problem of dephasing in QD emission due to the coupling to acoustic phonons that arise from the deformation of the lattice surrounding the QD. The coupling to phonons happens to be a decoherence channel that influences a QD in a timescale of the order of its radiative lifetime, thus making it rather challenging to exclude completely. The interaction between acoustic phonons and an exciton can be separated into two effects, one with a linear dependence on phonon displacement, and the other varying quadratically with phonon displacement. In a bulk material, the linear interaction is characterised by the recombination of the exciton accompanied by either emission or absorption of a phonon. This gives rise to spectrally broad PSBs on either side of the ZPL. The linear interaction exhibits a coupling cutoff to phonon modes with wavelengths shorter than the order of the exciton confinement dimension. In the case of InAs QDs this cutoff is for phonon modes of energy $> 1\ meV$. On the other hand, the quadratic interaction is driven by the scattering of phonons through virtual transitions of the exciton to higher states. This in turn manifests as a homogeneous spectral broadening of the ZPL. The quadratic interaction is generally negligible at cryogenic temperature (T < 5 K), but becomes important for larger temperatures, on the order of a few tens of Kelvin.

For QDs embedded in nanowire antennas, the decoherence due to phonon interaction is enhanced due to a strong coupling of the QD to discrete low-frequency phonon modes. These modes confine elastic energy into reduced volumes and are sufficiently low in energy to produce a broadening of the ZPL within the linear interaction regime. Therefore we performed a comprehensive study to estimate the degree of dephasing attributed to only mechanical vibrations of nanowire needles and trumpets, within the linear interaction regime. This decoherence depends on the QD position within the nanowire section. It is minimal (but finite) on the axis and increases as the QD approaches the wire sidewalls. We found that these mechanical modes could account for $\sim 60\%$ of the broadening of the QD linewidth measured in a trumpet antenna [87]. We also showed that the detrimental effects of discrete low-frequency modes are dominated by the first vibration modes. In particular, among all the different geometries we considered, only about the first dozen modes seem to have the most influence on the spectral linewidth. This phenomenon is due to both a rapid decline of the parameter $\eta^2 = (g_m/\omega_m)^2$ and also a diminution in their thermal population.

Finally, we proposed several possible solutions to suppress the impact of these first set of mechanical vibration modes of our nanowires. Our solutions exploit nanomechanical engineering of the QD-nanowire environment, which allowed us to successfully regain a photon indistinguishability of over 0.9 in every situation, irrespective of the QD position within the nanowire. Thus we have not only demonstrated that nanowire thermal vibrations constitute a major decoherence channel for an embedded QD, but also that this limitation can be overcome through specific engineering of the mechanical properties of the antenna. Our work establishes such nanomechanical engineering as a crucial part of the design of high-performance light-matter interfaces based on photonic nanostructures. In particular, we anticipate that mechanical vibrations also play an important role in suspended on-chip waveguides [156, 182], a potential building block of integrated quantum photonic circuits.

Finally, another very efficient way to mitigate phonon decoherence is to rely on a photonic structure that accelerates SE. In Chapter 3, we propose and demonstrate a nanowire nanocavity that offers a broadband Purcell effect.

Chapter 3

A nanowire nanocavity for broadband Purcell enhancement

In the previous chapter, we have elaborated the two major categories of photonic nanostructures used to efficiently extract light from embedded quantum dots (QDs). These are namely, microcavities and nanowire waveguides.

In an optical microcavity, an emitter is resonantly coupled to a cavity mode. The emission is selectively accelerated into the coupled mode due to the Purcell effect. When the latter is sufficiently strong, spontaneous emission into the cavity mode becomes the preferential channel of emission. Such an acceleration of spontaneous emission also renders the emission less sensitive to various decoherence channels. However, the requirement of resonance between the emitter mode and the cavity mode places strict constraints on the emission wavelength of the emitter, as well as its position within the microcavity. This extreme selectivity in wavelength makes it difficult to implement any form of tuning system on sources of quantum light based on microcavities. Additionally, deterministic techniques must be used to ensure the optimal position of the emitter in the cavity [124, 130, 183–185].

Dielectric waveguides, on the other hand, rely on extracting light from the emitter by coupling it to a guided mode. The cross-sectional dimensions of the nanowire are in the order of the emission wavelength in matter, to ensure optimal lateral confinement. The major advantages of nanowires are their broad operation bandwidth. This allows for simultaneous coupling to optical transitions of different energies, making nanowires promising candidates to establish tunable sources of quantum light. Nonetheless, these systems generally provide a limited acceleration of spontaneous emission, making the optical recombination more sensitive to decoherence sources in the environment.

Microcavities lack a broadband operation but are resilient to noise due to their high Purcell factors. In contrast, nanowires offer broadband coupling, although they tend to be more sensitive to sources of noise. It would appear then that the ideal single-photon source should have the best of both systems - a high enough Purcell enhancement while retaining

broadband characteristics - in some sense, a love child of the nanowire waveguide and the microcavity.

Nanocavities potentially combine the assets of these two mainstream approaches. Thanks to their ultra-small mode volume, nanocavities indeed provide a large Purcell acceleration with a moderate optical quality factor, which directly translates into a large operating bandwidth. This strategy inspired several proposals [75, 142, 149, 186], but only a few broadband QD nanocavity devices have been demonstrated so far, using photonic crystals [155] or bull's-eye structures [180, 187, 188]

In this chapter, we present a new type of nanocavity based on a nanowire. Despite its simplicity, this structure offers an appealing performance in terms of SE acceleration and light collection efficiency. We begin by briefly introducing the nanocavity and laying out the theoretical methods used to determine its design parameters, then elaborate the fabrication process of the nanocavities, followed by the optical experiments I carried out to characterise them along with the corresponding results.

3.1 Design of a nanowire nanocavity

The geometry of the nanocavity we consider is presented in Fig. 3.1. The nanocavity consists of a gallium arsenide (GaAs) cylinder (truncated nanowire) set on a silica-gold (SiO_2-Au) bottom mirror. The SiO_2 layer acts as a spacer to prevent the coupling to surface plasmon polaritons (SPPs), which causes a strong decrease in modal reflectivity of the guided mode. The reflectivity drops to as little a $\sim$3% for a nanowire with a diameter of the order of λ/n (wavelength in a material of refractive index n) [149]. The GaAs-air interface at the top facet of the nanocavity forms a second mirror with a weaker reflectance, by virtue of the refractive index mismatch. The QD is situated at a height corresponding to the first antinode of the fundamental HE_{11} mode.

To design the nanocavity, we first rely on a single-mode model, which considers the reflection of the fundamental guided mode (HE_{11}) on the nanowire extremities. This simple analytic approach provides physical intuition but fails to completely capture the physics of the device. It will thus be complemented by calculations taking into account more modes and based on an open-geometry Fourier modal method (oFMM) [189]. These calculations were conducted by Andreas Østerkryger, Yujing Whang, and Niels Gregersen at the Technical University of Denmark, Copenhagen. We review the essentials of the methods that were used and the design and performance parameters that were computed, in the sections that follow.

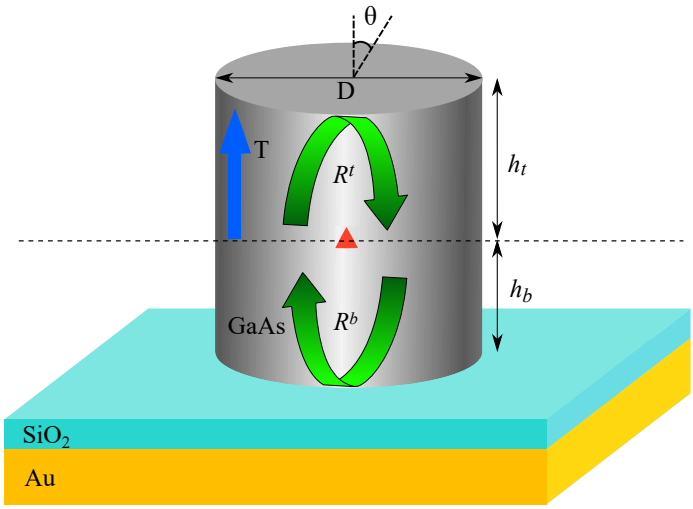

Fig. 3.1 Design of a GaAs nanocavity set on a silica-gold mirror. The distance between the QD (red triangle) and the mirror corresponds to the first antinode of the HE_{11} mode.

3.1.1 Single-mode model

The nanocavity presented in Fig. 3.1 is an example of a finite-length nanowire. In such a case, the spontaneous emission (SE) of the embedded QD is modified by the reflections occurring at the ends of the nanowire. This modification of SE may be calculated by rigorously solving Maxwell's equations of the scattering problem of the complete system. The same could be achieved by implementing finite computational domain methods, such as finite-difference time-domain (FDTD), and finite element method (FEM). However such approaches tend to be tedious and computing-resource hungry and fail to provide much physical insight into the system, and as a consequence prevent the engineering of individual parameters that dictate the overall performance of the device. Instead, we first rely on a single-mode model based on an element-splitting approach [149, 151, 190]. The major assumption made in this method is that the reflections at the top facet and bottom mirror alter only the emission rate into the fundamental guided mode, while the emission rate into the radiation mode continuum remains the same as that of an infinite nanowire.

The model considers the propagation of the fundamental waveguide mode (HE_{11}) in the nanocavity. We denote the spontaneous emission rate into the HE_{11} mode of an infinitely long nanowire by $\Gamma_{HE_{11}}$, and the amplitude coefficients of the fundamental mode propagating upward ($A_\uparrow$) and downward ($A_\downarrow$) with respect to the QD plane by,

$$A_\uparrow = A_s + r_b A_\downarrow, \quad A_\downarrow = A_s + r_t A_\uparrow, \tag{3.1}$$

where r_t and r_b are the complex modal reflection coefficients from the top facet and bottom mirrors respectively, seen from the QD. The phase accumulated over the propagation of HE_{11} starting from the QD layer to and from the bottom mirror (top facet) is included in the coefficients r_b (r_t). A_s is the discontinuity in amplitude induced by the dipole source. In

particular, for a QD in an infinitely long nanowire, we have $A_\uparrow = A_\downarrow = A_s = (\Gamma_{HE_{11}}/2)^{1/2}$. By solving the Eqns. 3.1, we obtain,

$$A_\uparrow = A_s \frac{1+r_b}{1-r_t r_b}, \tag{3.2}$$

$$A_\downarrow = A_s \frac{1+r_t}{1-r_t r_b}. \tag{3.3}$$

The total SE rate Γ_T in the finite nanowire is expressed as,

$$\Gamma_T = (1-|r_t|^2)|A_\uparrow|^2 + (1-|r_b|^2)|A_\downarrow|^2 + \Gamma_{rad}, \tag{3.4}$$

where Γ_{rad} is the SE rate into radiation modes. Γ_{rad} remains unaffected by the reflections induced by ends of the finite nanowires, and remains the same as that in an infinite nanowire.

The rate of SE into the cavity mode Γ_C, depends on the scattering coefficients, and after being normalised by the SE rate in the bulk material Γ_0, we obtain,

$$\frac{\Gamma_C}{\Gamma_0} = \mathrm{Re}\left[\frac{(1-r_t)(1+r_b)}{1-r_t r_b}\right] \frac{\Gamma_{HE_{11}}}{\Gamma_0} \equiv F_P^G. \tag{3.5}$$

Since no assumptions were made on the spectral and spatial location of the QD position with respect to the cavity to derive Eqn. 3.5, it represents the normalised SE rate into HE_{11} at an arbitrary wavelength. Alternatively, the Purcell factor F_P, which also describes the normalised SE rate into the cavity mode, may be written as,

$$F_P = \frac{\Gamma_C}{\Gamma_0} = \frac{3}{4\pi^2}\frac{Q}{V}\left(\frac{\lambda}{n}\right)^3, \tag{3.6}$$

where V represents the mode volume, and Q is the quality factor of the cavity. However the main difference between Eqns. 3.5 and 3.6 is that Eqn. 3.6 holds only when the QD emission is in resonance with the cavity, and the QD is also situated at a field maximum, while Eqn. 3.5 is valid for an emitter situation anywhere within the nanowire, and emitting at any wavelength. Eqn. 3.5 may therefore be considered as a generalised Purcell factor. Finally both Eqns. 3.5 and 3.6 require that the linewidth of the emitter be narrower than the linewidth of the cavity. In the case of the nanocavity, the low quality factor (Q) of the cavity, due to the weakly reflecting top facet, offers a cavity linewidth which is several orders of magnitude larger than that of the InAs QDs, and therefore Eqns. 3.5 and 3.6 are both applicable.

The Q factor of the cavity may be computed as,

$$Q = \frac{-\lambda_c}{2(1-|r_t r_b|)} \frac{\partial}{\partial \lambda} arg(r_t r_b), \tag{3.7}$$

where λ_c is the resonance wavelength such that $\arg(r_t r_b) = 0$.

Finally we define an expression for the extraction efficiency of the nanowire, which we define as the fraction of emitted photons that are collected by a lens over the top facet within a cone spanning a solid angle of $2\pi(1 - cos\theta)$. The number of photons collected may be expressed as $T(\theta)|A_\uparrow|^2$, where $\gamma(\theta)$ is the fraction of photons transmitted into the observed cone, carried by an upward-propagating HE_{11} mode. We thus have,

$$\varepsilon(\theta) = \frac{\gamma(\theta)|A_\uparrow|^2}{\Gamma_T}. \tag{3.8}$$

The scattering coefficients, r_t, r_b, and $\gamma(\theta)$ and the SE rates $\Gamma_{HE_{11}}$, and Γ_{rad} are computed and optimised separately using the oFMM. The oFMM is a numerical technique that is used in modeling open photonic systems that have major properties that depend on radiative losses.

In oFMM, the structure of interest is divided into z-invariant sections (uniform refractive index profile). The total electromagnetic field in these sections is considered to be a superposition of eigenmodes travelling along the $\pm z$ direction. Open boundary conditions are used to simulate the infinite physical space with a finite computation volume. The eigenmodes are expanded over a set of basis functions and plugged into Maxwell's equations. By assuming no free current ($\mathbf{J} = 0$), the equations are solved as an eigenvalue problem, thus allowing to determine the eigenmodes as well as the propagation coefficients. The transmission and reflection matrices between adjacent z-invariant layers are obtained by matching the electromagnetic fields at every interface. Then the scattering at all interfaces is sought, using the scattering matrix formalism [191], which is a cyclic method for calculating the reflection and transmission matrices between any two layers. This allows to access all the modal expansion coefficients in the structure, and hence also the coupling between modes. The oFMM differentiates itself from brute-force methods in terms of the modal description it provides, which offers a more intuitive physical understanding of the system.

3.1.2 The single-mode model applied on the nanowire nanocavity

Before a complete design for the GaAs nanocavity may be obtained, several design parameters must first be optimised. In order to maximise the effects of the cavity, the QD must be placed on an antinode of the cavity mode, which means, $\arg(r_b^{HE_{11}}) = \arg(r_t^{HE_{11}}) = 2\pi n$, where $n = 0, 1, 2,...$ We consider below a cavity mode that features 3 longitudinal antinodes. The QD is located on the nanowire axis, on the first longitudinal antinode (starting from the bottom mirror). We next determine the diameter leading to a large emission rate into the cavity mode. To this end the modal reflectivity at the top facet, as a function of reduced nanowire diameter (D/λ) is plotted in Fig. 3.2. While $|r_b| = \sqrt{0.9}$ does not significantly depend on the diameter D [149], both $|r_t|$ and $\Gamma_{HE_{11}}/\Gamma_{bulk}$ strongly depend

on this parameter. From Fig. 3.2 we find $\Gamma_{HE_{11}}/\Gamma_{bulk}$ is maximum at $D = 0.23\lambda$. For $D = 0.23\lambda$, $|r_t| = \sqrt{0.24}$ [142], however in order to increase $|r_t|$ further, we choose here a slightly larger diameter. The transverse confinement of HE_{11} is degraded a bit in the process, but the top facet reflectivity is significantly increased. For example, $D = 0.26\lambda$ leads to $\Gamma_{HE_{11}}/\Gamma_{bulk} = 0.86$ for an on-axis emitter and $|r_t| = \sqrt{0.43}$, which from Eqn. 3.5 yields a Purcell factor as large as 7.3. At the same time, $|r_t|$ remains small enough to i) ensure a modest optical quality factor (∼30) and thus a large operation bandwidth and ii) keep losses in the bottom mirror at a reasonable level and thus preserve a good collection efficiency.

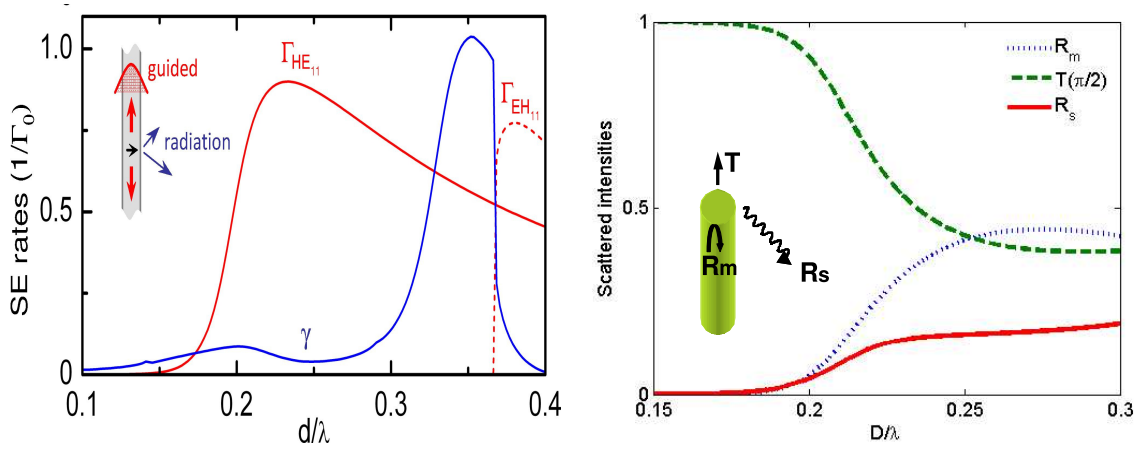

Fig. 3.2 (Left) Normalised SE rates and β-factor for an on-axis emitter in an infinite nanowire [75]. (Right) Modal reflectivity R_m of the top facet as a function of reduced diameter, D/λ for a finite nanowire. $T(\pi/2)$ is the transmission of the fundamental HE_{11} collected through a NA = 1 and R_s is the intensity of the mode reflected into radiation modes. [142].

The next design consideration is the SiO_2 layer thickness in the SiO_2-Au mirror. Since this thickness can be chosen freely, the reflectance of the HE_{11} mode, $R_b = |r_b|^2$, is plotted in Fig. 3.3, as a function of the nanowire diameter, considering different thicknesses for the SiO_2 layer. The optimal thickness varies considerably based on the diameter of the nanowire, however for wire diameter around D = 240 nm ($D/\lambda = 0.26$ for $\lambda = 920nm$), 7 nm is retained as the optimal option. The silica layer is introduced to reduce the reflectance dip of the simple metal mirror, which is caused by the coupling to SPPs.

3.1.3 Beyond the single-mode model

Although the single-mode model is a useful tool to simply and analytically understand the behaviour of a system, in reality, it alone doesn't suffice to describe the nanocavity. The nanocavity mode cannot be solely constructed with HE_{11}, due to a small coupling of HE_{11} to weakly guided or non-guided modes upon reflection on the facets. For instance, the bottom mirror has a reflectivity of $R_{HE_{11}}$ = 0.92 for the HE_{11} mode. The remaining 8%

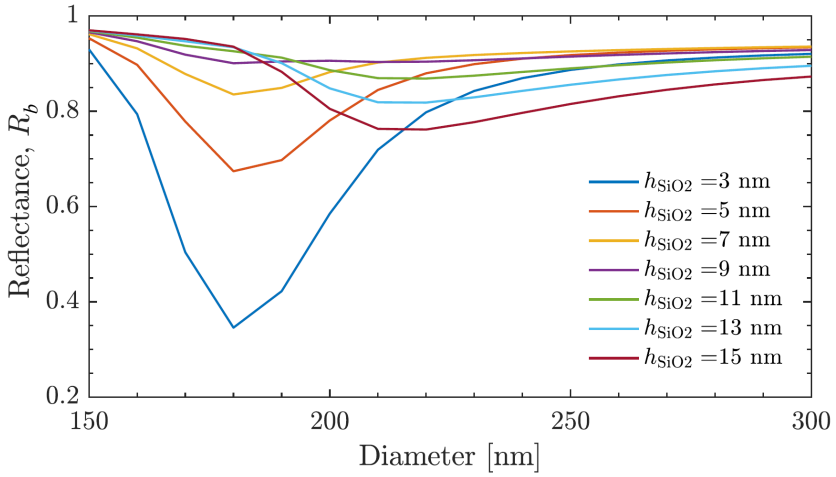

Fig. 3.3 Modal reflectance of the HE_{11} mode as function of the nanowire diameter for various thickness of the SiO_2 layer, calculated for an operation wavelength of 920 nm. [192].

of the power of the HE_{11} mode therefore goes into weakly-guided or non-guided modes. Similar losses also occur at the top facet. Due to the short height of the nanocavity, these non-guided modes can be reflected from the bottom mirror and interfere with the HE_{11} emission, which has interesting consequences on the nanocavity performance. Therefore, the result we present, hereafter are obtained with a Fourier modal method implementing open geometry boundary conditions, which permits to take into account the coupling of the emitter to all relevant modes. The nanocavity geometry used for the simulations had a diameter D = 245 nm. The QD was positioned at h_b = 70nm and h_t = 390 nm. The cavity resonance is found at λ_C = 928 nm.

3.1.3.a. Enhancement of the SE rate

Fig. 3.4 (a) shows the normalised SE rate Γ_C/Γ_0 as a function of $(\lambda - \lambda_c)$. On resonance, $\Gamma_C/\Gamma_0 = 6.3$. This value, though slightly lower than the single-mode prediction, remains remarkably high for such a simple structure. Furthermore, a pronounced SE acceleration is maintained over a 30 nm-large bandwidth (full width at half maximum (FWHM)). Fig. 3.4 (a) also shows γ/Γ_0, the normalised emission rate into the 3D continuum of radiation modes. Thanks to a strong dielectric screening effect [52], $\gamma/\Gamma_0 \ll 1$ over an even larger spectral range. As a result, the fraction $\beta = \Gamma_C/(\Gamma_C + \gamma)$ of SE funnelled into the cavity mode is as high as 0.98 at resonance and exceeds 0.95 over a 100 nm spectral range (Fig. 3.4 (b)).

3.1.3.b. Source efficiency

As evidenced in Fig. 3.4 (b), a broadband β-factor directly translates into a broadband collection efficiency ε. At resonance, one obtains ε as large as 0.54 into a first lens having

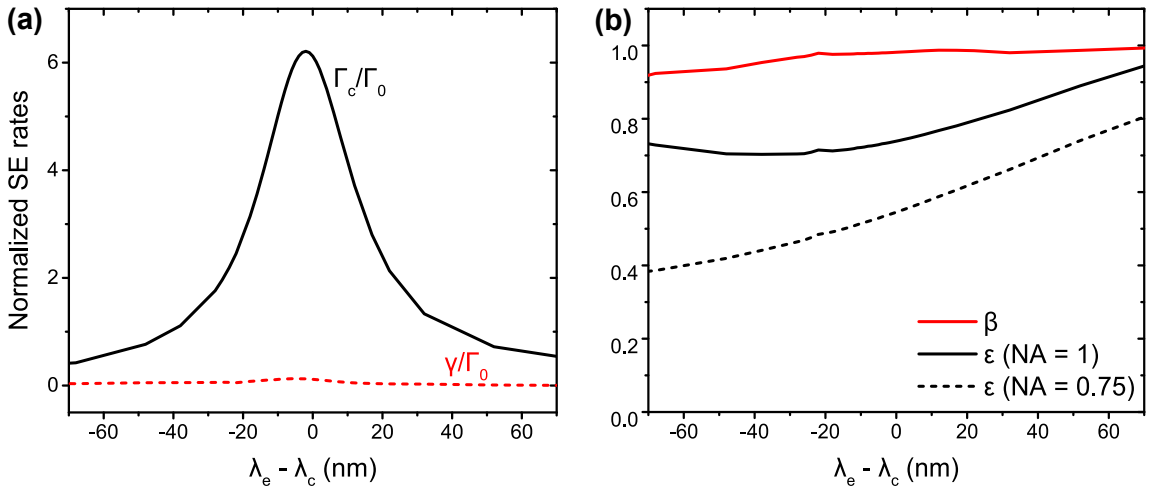

Fig. 3.4 (a) Normalised SE rates into the cavity mode (Γ_c/Γ_0) and into the 3D continuum of radiation modes (γ/Γ_0) calculated as a function of the emitter-cavity wavelength detuning ($\lambda - \lambda_c$). (b) Fraction β of SE funnelled into the cavity mode and first lens collection efficiency ε (for NA = 0.75 and 1), as a function of ($\lambda - \lambda_c$). All calculations are conducted for h_b = 70 nm, h_t = 390nm, and d = 245 nm, which leads to a cavity resonance at λ_c = 928 nm.

a NA = 0.75. To shed light on loss channels, we also plot a calculation of ε for NA = 1. This reveals firstly the limitations set by absorption losses upon reflection on the bottom gold layer. Secondly, a comparison between the two NAs shows that the output beam is directional: more than 70% of the photons emitted upwards can be collected with NA = 0.75.

3.1.3.c. Far-field emission pattern

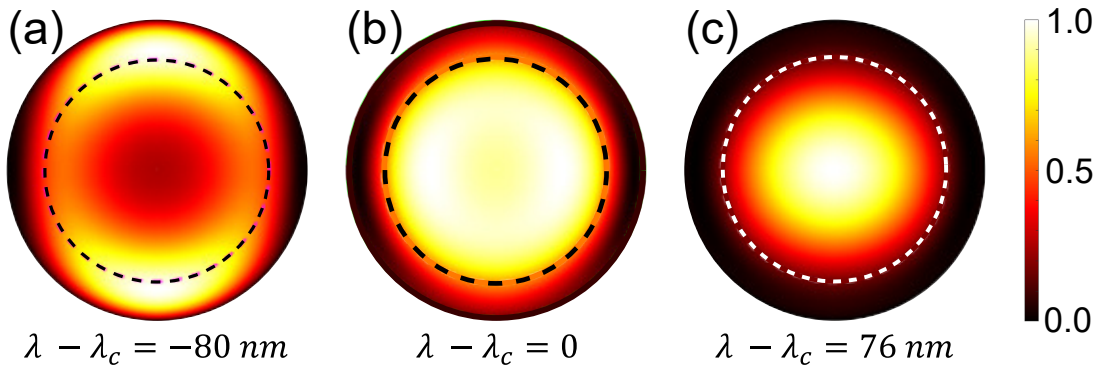

Fig. 3.5 Calculated far-field emission patterns. The far-field patterns correspond to a QD: (a) negatively detuned from cavity mode, (b) on resonance with cavity mode, (c) positively detuned from cavity mode. The dashed circles mark a numerical aperture of 0.75. These calculations are conducted for a linear optical dipole.

The angular profile of the device output beam, pictured in Fig. 3.5 (b) confirms that a realistic microscope lens with NA = 0.75 allows collecting the majority of the emitted photons. We note that this profile results from the subtle interplay between several contributions (scattering and reflection by the top facet) and involves interference associated with the reflection from the bottom mirror. Fig. 3.5 (a) depicts the far-field emission pattern of an emitter detuned by -80 nm with respect to the cavity mode. The emission pattern is anisotropic and more dispersed, with the field maxima being pushed close to the edge. The collection efficiency of a lens with NA = 0.75 now drops to 48%. Lastly, for an emitter with +76 nm detuning, we find in Fig. 3.5 (c), that the far-field emission pattern becomes more focused towards the centre, and presents a circular symmetry. The collection efficiency at NA = 0.75, in this case, increases to 87%. This result is promising because it entails that a detailed optimisation of the design could further increase the beam directionality and in turn the collection efficiency for moderate collection NA. Such an optimisation is ongoing in the group and will be part of a future work.

3.2 Fabrication process

After having discussed the theoretical models used to design the optimal geometry for the nanocavity, in this section, we detail the sample fabrication process. Even though the geometry of the nanocavity appears rather simple it takes a multistage fabrication process to realise a complete sample. The various stages of the fabrication process are summarised as follows:

- Growth of planar sample by molecular beam epitaxy
- Deposition of Au-SiO_2 bottom mirror
- Flip-chip (gluing on a host substrate and removal of the growth wafer)
- Electron beam lithography and lift-off to define a Ni hard mask
- Inductively coupled plasma etching to define the nanocavities

It is critical to execute each step as accurately as possible since defects and deviations could negatively affect the final figures of merit of the nanocavity. The growth stage defines the emission properties of the QDs and the vertical dimensions of the final sample. The flip-chip stage ensures a good adherence between the sample and the new substrate and therefore a good thermalisation with the cryostat. The lithography and etching stages are responsible for delimiting the lateral dimensions of the cavity which determine its Purcell factor.

3.2.1 Growth by molecular beam epitaxy

Growth by molecular beam epitaxy (MBE) is a method producing high-quality semiconductor structures by the deposition of one layer of semiconductor material at a time, on a semiconductor substrate. This method permits to elaborate structures with high precision since their thickness can be controlled at a single atomic layer level.

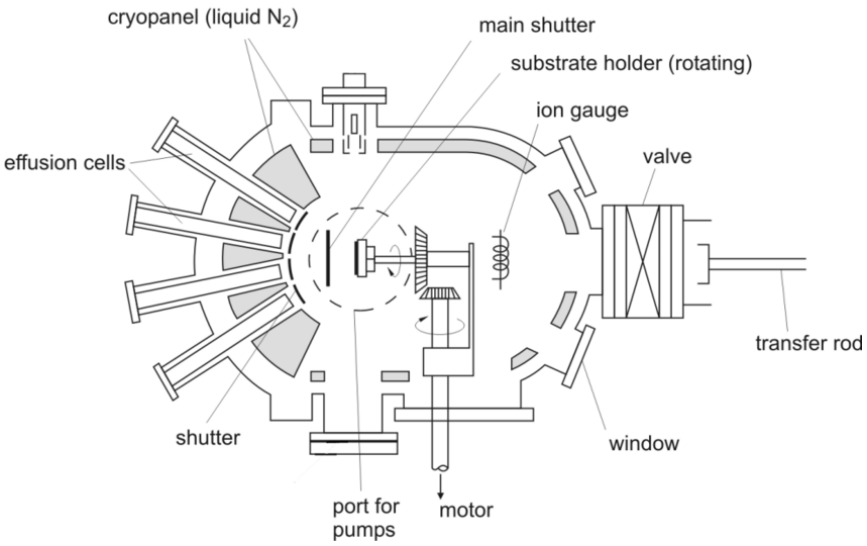

Fig. 3.6 Schematic representation of a MBE chamber.

In this section, we describe successively the growth of samples, executed by Yann Genuist, and their early optical characterisation by macro-PL that I carried out. A MBE chamber schematically resembles Fig. 3.6. The chamber is maintained at ultra-high vacuum ($\approx 10^{-9}$ mbar) to prevent the contamination of the growth sample by impurities. The walls of the epitaxy chamber are also cooled to liquid nitrogen temperature to maintain a high vacuum and to prevent the evaporation of substance that have deposited on them.

The substrate on which the growth is to be performed is mounted on a temperature-controlled holder, by clipping it in a frame. The effusion cells contain the various pure elements that may be used for the growth. The growth rate can be adjusted by varying the flux of the individual elements, which is achieved by finely modulating the temperature of crucibles in which the elements are contained. The emitted flux follows the Arrhenius law: the hotter the crucible, the higher the flux of the element.

The process for developing the nanocavities begins with the growth of planar heterostructures, by MBE on a semi-insulating (001) GaAs wafer. The planar sample consists of a layer of InAs QDs, embedded in a layer of GaAs, which rests on a sacrificial layer of $Al_{0.8}Ga_{0.2}As$. The sample is grown upside down to deposit the bottom mirror on what is the top of the sample after growth. It will be set right side up by a flip-chip process by gluing the mirrored face to a new substrate and then by grinding off the original growth

substrate. The AlGaAs acts as a sacrificial layer that will allow to cleanly expose the actual top face of the sample. These steps of the process will be discussed in more detail later.

The exact geometry of the planar sample is displayed in Fig. 3.7 and the growth parameters are given in Table 3.1. The substrate is heated to a temperature at which the GaAs surface is deoxidised, which provides a reference for the substrate temperature ($T_{de-ox} = 590°C$). The entire growth is carried out in an arsenic-rich environment, where arsenic is constantly introduced into the chamber as As_4 molecules at flux pressure of 1.6×10^{-6} mbar. Without this constant supply of As_4, the As from the heated substrate would evaporate leaving droplets of Ga, which would roughen the surface. In order to get small QDs emitting around 920 nm, we use a method which has been proposed in Ref. [94]. We deposit a quantity of InAs equivalent to around 1.9 monolayers, i.e. slightly larger than the 1.7 monolayers critical thickness for 3D growth of InAs on GaAs. To limit the expansion of the InAs islands after their nucleation, we deposit InAs over a flash lasting one second, which is very fast compared to usual growth rates in MBE. We then immediately cap the InAs islands with GaAs.

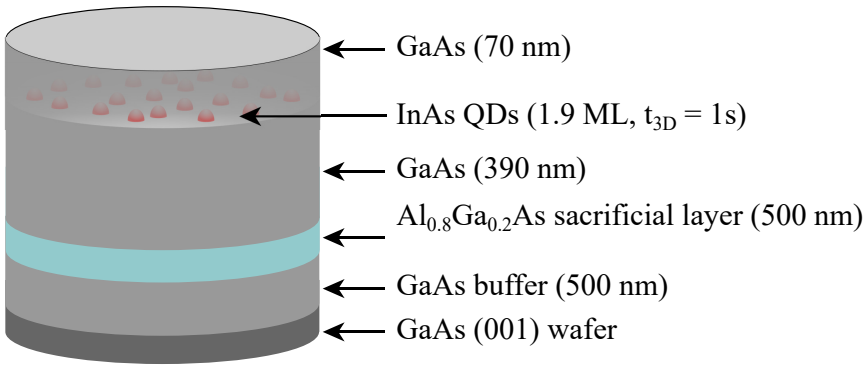

Fig. 3.7 Planar heterostructures used for the fabrication of nanocavities.

Table 3.1 Growth parameters used for planar heterostructures of the nanocavity sample performed in a As-rich environment, where • indicates the shutter of respective cell is closed.

Growth step	Thickness (nm)	Temperature (°C)			
		Al	In	Ga	Substrate
GaAs buffer	500	•	•	920	600
$Al_{0.8}Ga_{0.2}As$	500	1081	•	850	600
GaAs body	390	•	•	920	600
InAs QDs	1.9 monolayers	•	890	•	525
GaAs capping	70	•	•	920	600

3.2.1.a. Feedback on growth quality from photo-luminescence profiles

After the growth of every planar sample that Yann Genuist completed, I optically scanned the 2-inch diameter wafer, one quarter of a wafer at a time, to obtain the bulk photoluminescence (PL) profiles across the sample. A schematic representation of the setup used to characterise the wafers is illustrated in Fig. 3.8.

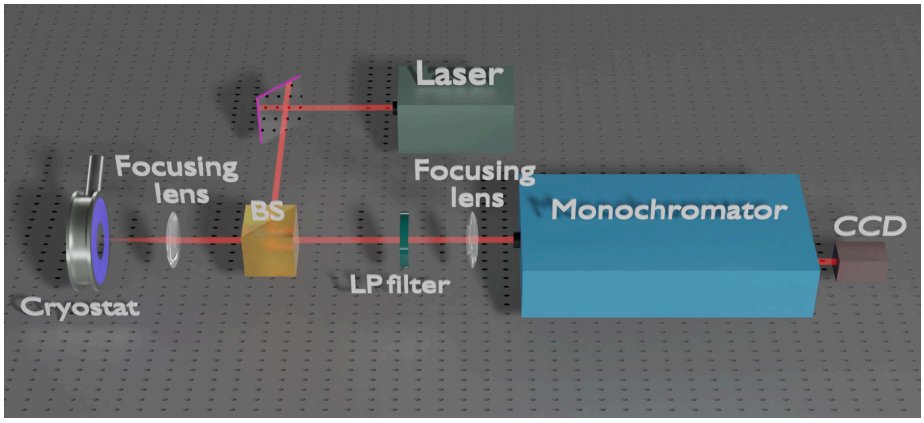

Fig. 3.8 Macro-photoluminescence setup used to characterise bulk emission properties of planar growth samples. The laser wavelength is $\lambda = 780$ nm, the focal length of the lenses is 75 nm, and the wavelength of the LP filter is 800 nm.

An 18 mW, 780 nm diode laser, collimated into a 1 mm^2 spot was used to excite the QDs in the bulk. The photo-luminescence signal is collected in a spectrometer with an entry slit of 0.1mm and resolved using a 600 grooves/mm grating. The photo-luminescence spectrum was obtained by integrating the signal during 0.1 sec. The final planar sample (Ref. No. AS1086) that was used to realise nanocavities, presented a bulk emission centred at 920 nm with a spectral width (FWHM) of $\sim$ 40 nm. The ensemble photoluminescence spectrum of one zone of this wafer is shown in Fig. 3.9

3.2.2 Deposition of the bottom mirror

After the growth of the epitaxial structure, the next step in the process is to deposit the high reflectivity mirror. This mirror, as already presented in Sec. 3.1.2, consists of a combination of metal (Au) and dielectric (SiO_2) layers.

Before making any deposition on the epitaxial sample, its surface must be thoroughly cleaned and treated to ensure a high-quality mirror deposition. Each quarter (cleaved for PL characterisation) piece of the 2-inch epitaxial wafer is deoxidised with diluted ammonia (NH_3), the surface is then passivated with ammonium sulfide ($S(NH_4)_2$). This kind of treatment ensures the wafer surface is devoid of surface oxidisation, particles, or chips of all sizes (residue from cleaving or dust). A 7 nm-layer of SiO_2 is then deposited by electron-beam evaporation. The deposition is performed by Eric Delamadeleine (CEA-IRIG/SINAPS).

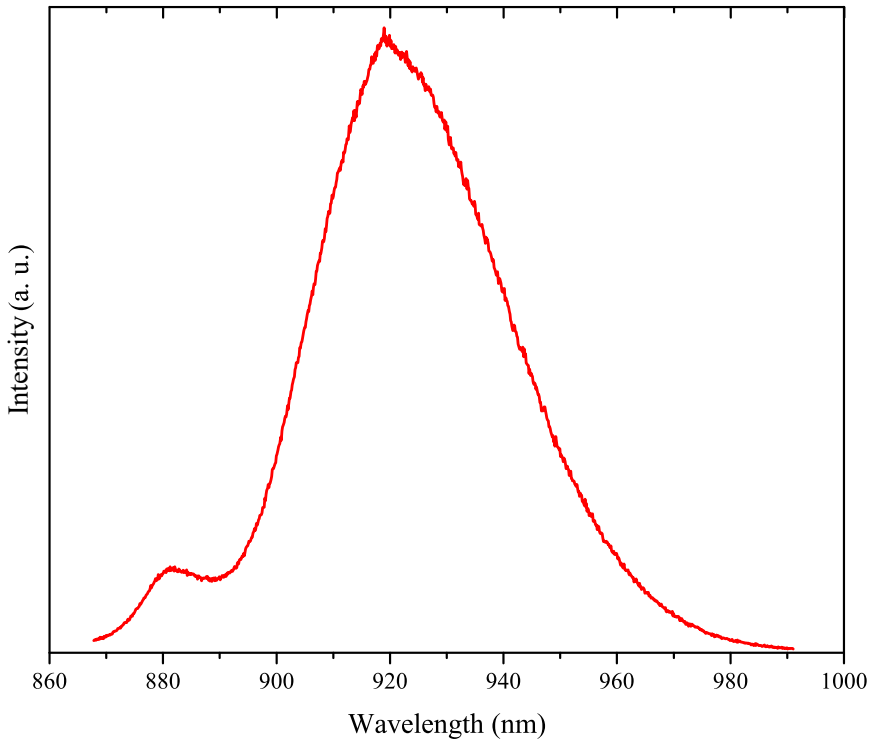

Fig. 3.9 Ensemble photoluminescence spectrum of planar growth sample (Ref. No. AS1086), which was used to realise nanocavities.

Following the SiO_2 layer a 250 nm-thick Au layer is deposited by electron-beam metal evaporation, on a Plassys MEB550, at the Upstream Technological Platform (in French, Plateforme Technologique Amont - PTA). To do this, first hydrocarbon contaminants on the wafer must be cleaned. This cleaning is done by baking the wafer at 100°C on a hotplate for a couple of minutes. Since Au has a poor adherence to SiO_2, a 3 nm layer of Ti is deposited as an adherence layer between the two. Simulations confirm that the impact of this Ti layer on the optical properties of the mirror is negligible.

3.2.3 Flip-chip process

The flip-chip process consists of a sequence of four main steps,

(a) the bonding of the planar sample mirror-side down on a new GaAs substrate using SU-8 2005, an epoxy-based photoresist;

(b) the partial removal of the growth wafer by mechanical polishing over abrasive discs;

(c) the removal of the remainder of the growth wafer to expose the AlGaAs sacrificial layer by chemical etching in a H_2O_2 and $C_6H_8O_7$ solution;

(d) removal of AlGaAs sacrificial layer using HF.

These steps are described briefly hereafter, and elaborated in more detail in Chapter 4, where I present the technological development accomplished during my PhD project. We begin by measuring the thickness of the GaAs growth wafer using a mechanical micrometric probe. Knowing the exact thickness will help us stop the abrasion correctly during the growth substrate removal step later.

- **Wafer bonding.** This consists of gluing the planar sample onto another GaAs wafer substrate with the Au-SiO_2 mirror-side down. The glue used is an epoxy-based negative photoresist, SU-8 2005, widely used to define high-resolution masks for lithography or etching processes. The SU-8 2005 is then annealed with heat on a hotplate for 25 min at 100°C, followed by a post-cure bake for about 30 min at 210°C.

- **Removal of the growth substrate.** The growth substrate is removed by a combination of physical and chemical etching. First, most of the substrate is removed by abrasive polishing until only a layer of about 30 μm of it is left. This layer is then dissolved by submerging the sample in a chemical bath of hydrogen peroxide (H_2O_2) mixed with citric acid ($C_6H_8O_7$) at 35°C until the sacrificial layer is exposed.

- **Chemical etching of sacrificial layer.** The sample is submerged in a 50% hydrofluoric acid bath for a minute or two, to get rid of the AlGaAs sacrificial layer. The sample is then washed in deionised water, before drying off under a clean jet of N_2 gas.

3.2.4 Definition of a hard mask

To be able to elaborate nanostructures from a planar heterostructure using a top-down approach, we need to define a mask that consists of the entire sample design layout. A positive electron-beam resist coat is applied to the top of the sample. This mask pattern will then be defined in the resist using electron-beam lithography. Upon development of the resist the exposed parts are removed leaving a stencil pattern. A layer of nickel (Ni) is deposited. Then the resist is lifted off to leave a hard mask covering only the areas of interest to be protected from the etching. The sample then undergoes dry etching by plasma in order to define the desired nanostructures. Finally, the Ni hard mask is chemically dissolved thus leaving a complete sample ready to be characterised optically. While these steps will be described in more detail, in the following sections, here we address the designing of the hard mask layout.

3.2.4.a. Design of the mask layout

The basic layout of the sample consisted of the pattern illustrated in Fig. 3.10. A 4×10 matrix of circles with diameters ranging from 110 nm to 500 nm (ΔD =10 nm) would allow

defining nanocavities of the respective diameters. I added a series of triangles leading each row and column as directional aids in finding a nanocavity of a specific diameter. I also included a set of coordinate indices to help with positioning during optics measurements. I replicated the basic motif across a 5×5 mm surface, forming a 28×16 matrix.

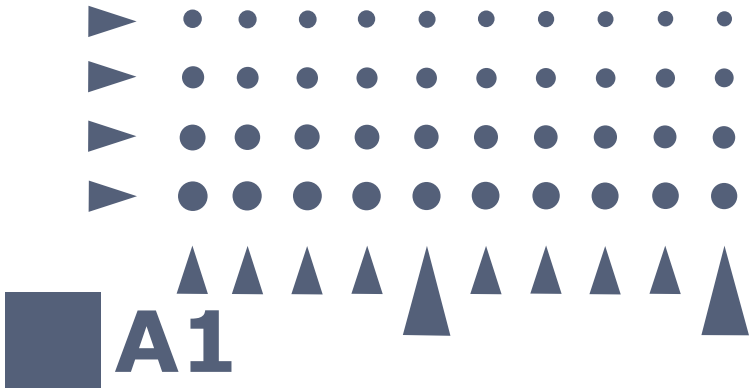

Fig. 3.10 (a) Basic pattern layout for the lithography mask of the nanocavity sample. This pattern is repeated to optimally cover the entire sample surface.

I developed the overall lithography mask in two stages. First I wrote a semi-automated programme on Matlab that defined the coordinates of all the points required to define every shape on the mask. I would have to define the basic layout parameters, such as the bounds of the diameter range, the diameter variation interval, the spacing between features on the basic motif, and total sample size, and the programme would attempt to fit the basic motif as many times possible to optimally cover the complete sample area. The programme would extract the position for each individual feature and save them in data files.

In the second stage of the design, I imported the data file that I generated on Matlab, to a mask editing software called L-Edit from Tanner Tools EDA to draw out the complete mask design. I then exported the design in a format readable by the lithography machine (.gds) and that would conclude the mask design step.

3.2.4.b. Electron beam lithography

Electron beam lithography (EBL) is a method of patterning that consists of exposing a resist by a focused beam of electrons. A thermal field emission electron gun generates a stream of electrons, which passes through a series of apertures, electromagnetic lenses, electrodes, and coils that shape and direct the electrons into a focused beam onto the sample. The beam is electrostatically deflected to scan the surface of the sample.

The EBL system we used for patterning at the PTA was the JEOL 6300 FS. Before exposing the sample under an electron beam, it was coated with the 4% poly(methyl methacrylate) (PMMA) photoresist. The resist was spin-coated on the sample at 4000 rpm for 40 sec with an acceleration of 4000 rpm. It was then baked on a hot plate at 140°C for about 10 min. The sample was exposed with doses in the range of 1000-3000 μC/cm^2.

Because of proximity effects, the exact dose depends on the different sizes of features on the sample. Tests were carried out to optimise the doses.

After the electron beam exposure, the PMMA resist was developed in a 1:3 methyl isobutyl ketone (MIBK) and IPA solution for about 30 sec, before submerging the sample in IPA for about 30 sec to stop the development then drying it under a jet of N_2 gas.

3.2.4.c. Deposition of the metallic mask and lift-off

In this step, we deposit a metallic layer and implement a lift-off procedure to create localised hard masks to be able to etch the various structures in the following step. We deposit a 150 nm thick layer of Ni using Plassys MEB550 electron beam metal evaporation at the PTA. After the deposition, we leave the sample in a bath of acetone for several hours to dissolve all the unexposed PMMA resist along with the deposited Ni over it. The acetone bath must be kept covered, to slow down the evaporation, and checked from time to time to ensure the presence of sufficient acetone. Once all the unexposed PMMA is removed we are left with a sample ready to be etched.

3.2.5 Inductively coupled plasma etching

Etching is a common top-down process, widely used in nanofabrication, to define nanostructures. Etching enables to transfer patterns on a sample by removing all the material that isn't covered by the mask. While several etching techniques exist, we implement inductively coupled plasma (ICP) etching. This method is particularly efficient to produce high aspect ratio nanostructures, like the ones presented in Chapter 4. The etching recipe used to fabricate the nanocavities uses the following gases: silicon tetrachloride ($SiCl_4$), boron trichloride (BCl_3), and argon (Ar). The recipe is adapted from the one used to develop our photonic 'trumpet' sample. I will address the ICP etching technique as well as the elaboration of our etching recipe more in depth in Chapter 4. We tracked the progression of etching with the help of laser interferometry, in order to determine the endpoint. The relative reflectance of the etching surface oscillates due to the phase interference between light reflected from the top and bottom facets. Concretely we can determine the etch endpoint by counting a specific number of oscillations which relates to the etched depth by, $\Delta d = N \times \lambda/2n$, where Δd is the thickness etched, N is the number of oscillations, λ is the laser wavelength, and n is the refractive index of the etched material.

3.2.5.a. Chemical etching of metallic mask

The final step in the fabrication process is the removal of residues of the Ni mask. We perform the chemical etching on our sample with 10% nitric acid (HNO_3). We submerge the sample in the acid for $\sim$ 1.5-2 min and then we withdraw it and wash it with deionised

water, to stop the chemical reaction. That concludes the fabrication process and the nanocavity sample is ready to be optically characterised. Fig. 3.11 depicts SEM images of the nanocavity sample after the fabrication process.

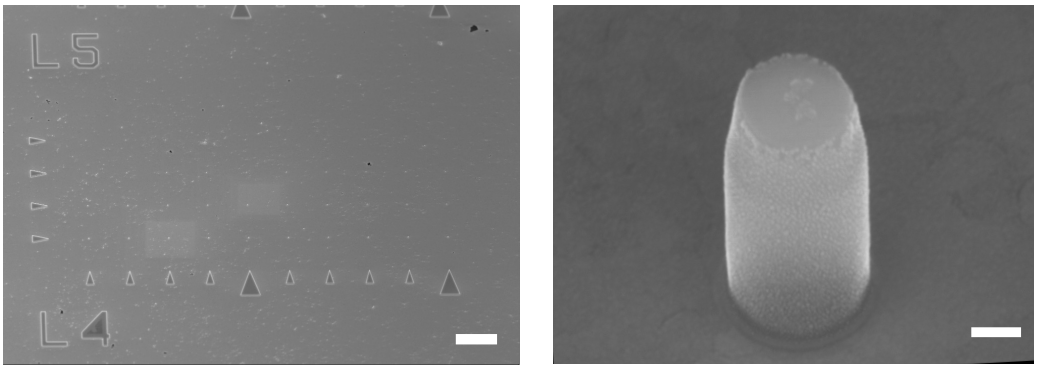

Fig. 3.11 SEM images of the nanocavity sample at the end of its fabrication process. Scale bar: 20 μm (left), 100 nm (right).

3.3 Micro-photoluminescence setup

In this section, we present the optical setup used for the characterisation of the nanocavities. An experimental setup that has simultaneously a high spectral and spatial resolution is mandatory to be able to probe the optical properties of the QDs in the nanocavities. A high spatial resolution is desirable to enable the excitation of only a few QDs at a time, and a high spectral resolution is required to be able to isolate the emissions of each individual QD. Additionally, to study the dynamics of the optical transitions of a QD, the setup must possess a temporal resolution for photon detection faster than the shortest exciton decay time, which in our study is predicted to $\sim$180 ps. The micro-photoluminescence (micro-PL) setup used for these measurements was developed by Joël Bleuse. On this setup, I performed time-integrated spectroscopy of infrared (IR) PL from QDs, as well as time-resolved PL enabling the measurement of the exciton decay time in nanocavities. A simplified schematic representation of the setup is illustrated in Fig. 3.12.

3.3.1 Cryogenics and sample imaging

3.3.1.a. Cold finger cryostat

In order to obtain narrow QD emission lines, the sample should be maintained at ultra-low temperatures ($\sim$ 4 K). We use the MicrostatHe cryostat from Oxford Instruments, which is a helium (He) flow sample-in-vacuum cryostat. The cryostat features an optical window and the sample is attached to a cold finger. An isolation vacuum of around 5×10^{-4} mbar is generated in the cryostat, thanks to a turbopump. The cold finger is cooled down with

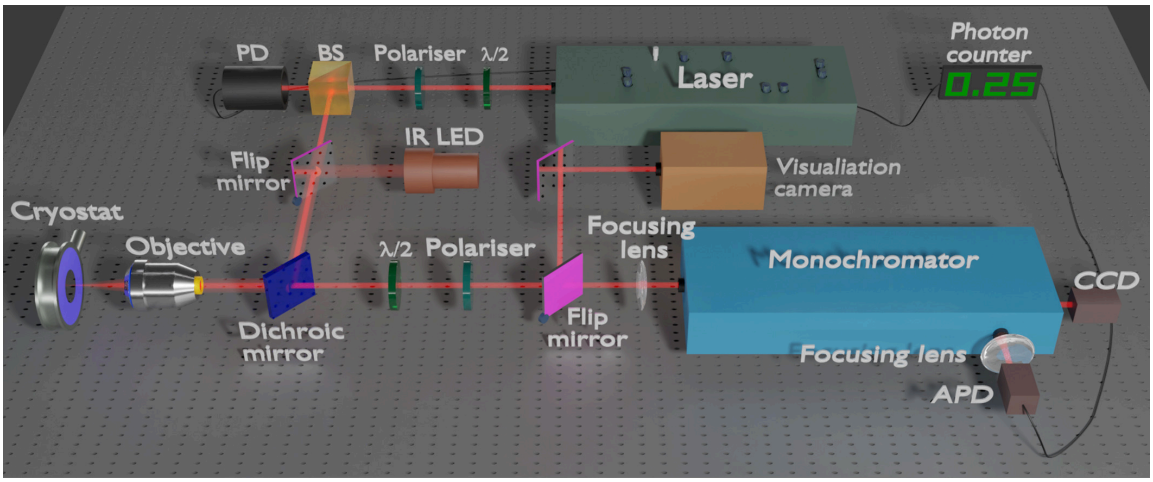

Fig. 3.12 Schematic diagram of the complete experimental setup used to characterise the nanocavities. The setup is optimised to study samples in the IR range, enabling time-resolved micro-PL spectroscopy. The laser wavelength is λ = 820 nm, the focal length of the lenses is f = 75 mm

a flow of gaseous He. The He that exits the cryostat is recovered to be recompressed and liquefied again. The cooling power is controlled by adjusting the pressure of the He flow. The temperature of the sample is monitored with a thermometer and kept steady using a thermocouple in a temperature controller.

3.3.1.b. Imaging systems

We use an IR LED with a collimated beam, to illuminate the sample, through a high-resolution microscope objective from Zeiss (Plan Neofuar NA = 0.75 and magnification of 63×), to visualise the sample and to help us navigate across it. The cryostat containing the sample is securely fixed on the optics table, while the microscope objective is mounted on a chassis whose position along every coordinate axis is controlled with micrometric screws with a resolution of 1/32 μm. The image of the sample is captured on an Andor Luca 604 electron multiplied charge-coupled device (CCD) camera, which has a sensor of 1004 × 1002 pixels, with each pixel measuring 8 μm × 8 μm. The image of the sample is captured on the camera with an intermediate lens implemented to image the back focal plane of the microscope objective.

3.3.2 Infrared spectroscopy

3.3.2.a. Optical excitation

As we have seen in Sec. 3.2.1.a., the QDs luminesce in the near-infrared (IR), in the neighbourhoods of 920 nm. We excite the QDs non-resonantly by pumping the system, with photon energy slightly under the bandgap of GaAs, at 820 nm. We use a titanium:sapphire

(Ti:Sa) solid-state modelocked laser, the Mira 900 model from Coherent, to excite the nanocavities. The cavity of the Ti:Sa laser can be tuned to modulate its wavelength continuously between 730 nm to 960 nm, thanks to a birefringent Lyot filter. The laser can be set to work in both pulsed and continuous (CW) mode. In the former mode, it has a pulse length of 200 fs and a repetition rate of 76 MHz. For all our measurements, we set the Ti:Sa laser in pulsed mode, at 820 nm (just under GaAs bandgap at T = 4 K), for non-resonant excitation. The output power of the laser is $\sim$1 W, which is attenuated by a set of a polariser and a $\lambda/2$-plate. The attenuated power is then focused down to a 1.5 μm-diameter spot onto the sample, using the same Zeiss microscope objective, as mentioned previously.

3.3.2.b. Grating spectrometer

The emitted signal from the sample is focused by a f = 75 mm lens through an adjustable slit of a 640 mm focal length monochromator (Horiba Jobin-Yvon FHR 640), that diffracts the light to spread the different wavelengths out. A reflective diffraction grating of 1200 grooves/mm is used to spread the signal. These spectrally filtered photons can be collected on a CCD camera to observe the intensity as a function of emission wavelength.

The CCD camera we use is the Andor Idus 420, which has a Si sensor, and is cooled by the Peltier effect to -70°C. The sensor has 1024 $\times$ 255 pixels with each pixel measuring 26 μm $\times$ 26 μm. Its quantum yield at -100°C for 920 nm is close to 50%, according to the specification sheet from the supplier.

3.3.2.c. Polarisation analyser

To perform a polarisation analysis, we use a combination of $\lambda/2$ waveplate and a linear polariser. The polariser is aligned along the direction of preferential transmission of the grating (polarisation aligned with the orientation of the grooves). The $\lambda/2$ waveplate is used to rotate the direction of the polarisation of the incident photons. We use this system to evaluate the collection efficiency of nanocavities and to analyse the fine structure splitting of excitons.

3.3.3 Time-resolved photoluminescence

3.3.3.a. Experimental setup

The photons collected from a nanocavity are spectrally resolved with a diffraction grating monochromator. This signal is focused on the sensor of an APD with the help of a suitable set of lenses. A slit at the exit allows to spatially filter the specific transition that we intend to study. In order to perform the time-resolved measurements, we implement an APD from Id-Quantique (Id 100-50 ultra-low noise module). It possesses a highly sensitive 50 μm Si detector, making it desirable to measure the dynamics of emissions coming from individual

transitions. However, although its quantum yield is rather high in the visible range (35%), it drops drastically in the near-IR range, offering only about 4% at 900 nm. Therefore a perfect alignment of the setup is indispensable for a good signal-to-noise ratio, essentially due to dark current. Additionally, longer integration times are also helpful. We integrated the signal over intervals ranging from 100 sec to 20 mins. The detector offers a temporal resolution of around 40 ps and a dead time of 45 ns.

The APD is connected to a Time-Correlated Single Photon Counting (TCSPC) board - Time Harp 260 from PicoQuant, which measures the time interval between two events. In our case, it is set to measure the time interval between a laser pulse, detected by a fast PIN-photodiode, and the corresponding emission of a photon from a QD in a nanocavity, detected using the fast APD. The Time Harp TCSPC board works on a Time to Digital Converter (TDC) circuit, which measures time differences based on delay times of signals in its semiconductor logic gates. TCSPC systems have a TDC connected to each input channel. All TDCs run off the same crystal clock and time differences between the different channels are obtained through arithmetic operations in hardware. The delay time intervals are compiled into time bins (25 ps) to make a histogram that reflects the number of photons detected as a function of detection time. In practice, the photon counter measures the time interval between a detected photon (start of the timer) and the following laser pulse trigger (stop of the timer). This prevents recording instances with no photon emission, or when a photon hits the sensor during the dead interval of the APD.

3.3.3.b. Temporal response of the optical setup

The accuracy of a measurement of decay times of a QD will depend on the cumulative temporal responses of the various optical components in the setup. Therefore before proceeding towards a quantitative determination of lifetimes we must first evaluate the reduction of temporal resolution in the experimental setup, caused primarily by the two photodiodes (that detect the laser pulse and photons from a QD), the photon counter, and the grating. The overall temporal resolution of the setup may be expressed as,

$$\Delta_{setup} = \sqrt{\Delta_{PD}^2 + \Delta_{APD}^2 + \Delta_{count}^2 + \Delta_{grat}^2}, \tag{3.9}$$

where Δ_{PD} is the temporal response of the laser pulse detector, Δ_{APD} is the response of the QD emission photon detector, Δ_{count} is the temporal resolution of the photon counter, and Δ_{grat} is the temporal response of the grating. The values of Δ_{setup} can be calculated using $\Delta_{grat} = (1/c)(2Lsin\alpha)$, where L is the length of the grating, α is the angle of incidence, and c is the speed of light, and the other Δ's obtained from datasheets of the respective component manufacturers.

Experimentally, we can determine the temporal resolution of the experimental setup by reflecting the 200-fs laser pulses (set λ = 920 nm) off a mirrored surface, in place of the

semiconductor sample, and by recording the distribution of the arrival times of reflected photons at the APD. Fig. 3.13 shows the temporal distribution we obtained in both linear and logarithmic scales.

In the linear representation, the distribution presents a FWHM of about 80 ps. The temporal resolution of the setup in turn limits the shortest decay time we could measure. Given that InAs QDs present a radiative lifetime of the order of 1 ns. The limit of 80 ps would correspond to a Purcell factor of $F_P = 12.5$. Since from theoretical calculations we expect our nanocavities to present a maximum $F_P = 6.3$, we can rely on our setup for accurate results. We will however need to deconvolute the setup response time from our experimental data of QD emissions, to obtain the actual decay times.

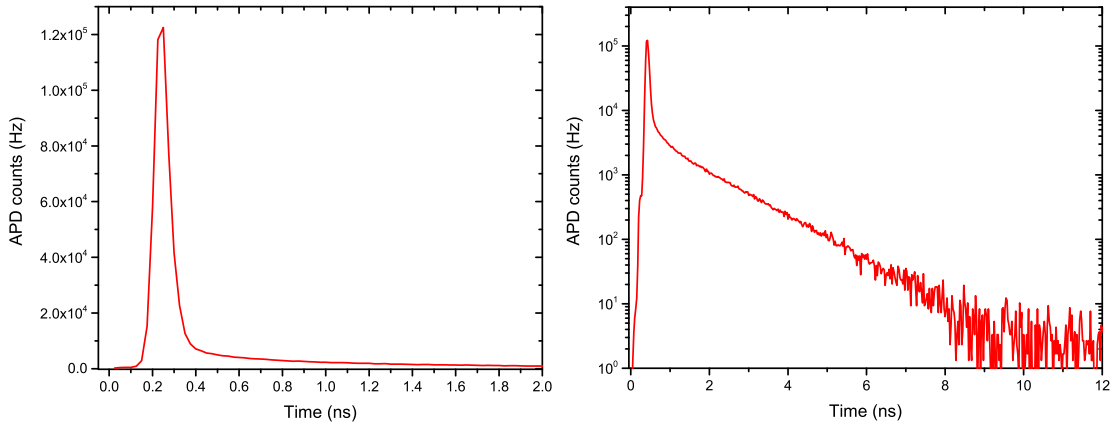

Fig. 3.13 Temporal response distribution of setup, in linear (left) and logarithmic (right) scales, measured for laser pulses with $\lambda = 920$ nm.

We notice also that the temporal distribution isn't symmetrical. Beyond 0.3 ns the photon count decays gradually to zero. This asymmetry is characteristic of a phenomenon that is typical of detectors like the ones we use, which is wavelength dependent, and is known as a "tail of diffusion". The logarithmic representation of the temporal distribution in Fig. 3.13 illustrates the "tail of diffusion" more clearly.

3.3.3.c. Analysis of experimental data

Time-resolved measurements of decay time are inherently limited by the response of the setup. The recorded signal, being a convolution of the photon arrival times with the response of the setup, leads to reported lifetimes that tend to be consistently slightly longer. To extract an accurate value for the radiative rates of QDs in nanocavities, it is important to correct the results from the delay caused by the setup. This may be achieved by performing a deconvolution operation between the setup response, from Fig. 3.13, and each decay time measurement from QDs. In practice however, the deconvolution procedure proved to be rather cumbersome. Therefore we choose to take the inverse approach, which is illustrated below. Let's suppose the experimental decay is governed by a single-rate exponential

process,

$$I(t) = Ae^{-\Gamma t}, \tag{3.10}$$

where A is an arbitrary weight parameter and Γ is the radiative recombination rate.

I employed the following strategy instead of deconvoluting the response of the setup from the experimental data. The case of a fit to a single-exponential decay is explained below:

- Generate $I(t)$ by setting initial values for A, Γ,
- Perform numerical convolution between $I(t)$ and the setup-response curve,
- Compare result of convolution with experimental data using a nonlinear least square method,
- Update values for A, Γ,
- Perform the above steps recursively until the parameters converge.

I coded a Matlab script that performed the above algorithm automatically on multiple decay time data files. The script exported the computed decay times as well as a well-formatted table with the original experimental data and the fitting function data for further analysis. Such an automated evaluation simplified the tedious task of individually fitting large batches of exciton decay time measurements, as well as drastically speeding up the determination of lifetime values for a large number of QDs. A similar method was employed to fit bi-exponential decays, with the fitting function $I(t) = A_1 e^{-\Gamma_1 t} + A_2 e^{-\Gamma_2 t}$, and by optimising the parameters, $A, \Gamma_1,$ and Γ_2.

3.4 Optical characterisation of nanocavities

The process I pursued to characterise the nanocavities, is as follows. I screened nanocavities with diameters in the range between 200 nm to 240 nm, performing polarisation analysis on well isolated and bright lines from their emission spectrum. I identified and selected only the excitonic lines (neutral and charged), on which I carried out time-resolved measurements, to determine the Purcell acceleration of the radiative recombination rate. Finally, I determined the collection efficiency of the sources by measuring the spectrally integrated intensity at saturation I_{sat} for 10 excitonic lines with the fastest recombination rates. Some details on these 10 excitonic lines are provided in Table 3.2.

3.4.1 Micro-photoluminescence spectroscopy

I characterised several devices and first focus on a structure with a nominal diameter of 220 nm, which I denote NC_1 for reference. This structure is chosen because it offers a direct

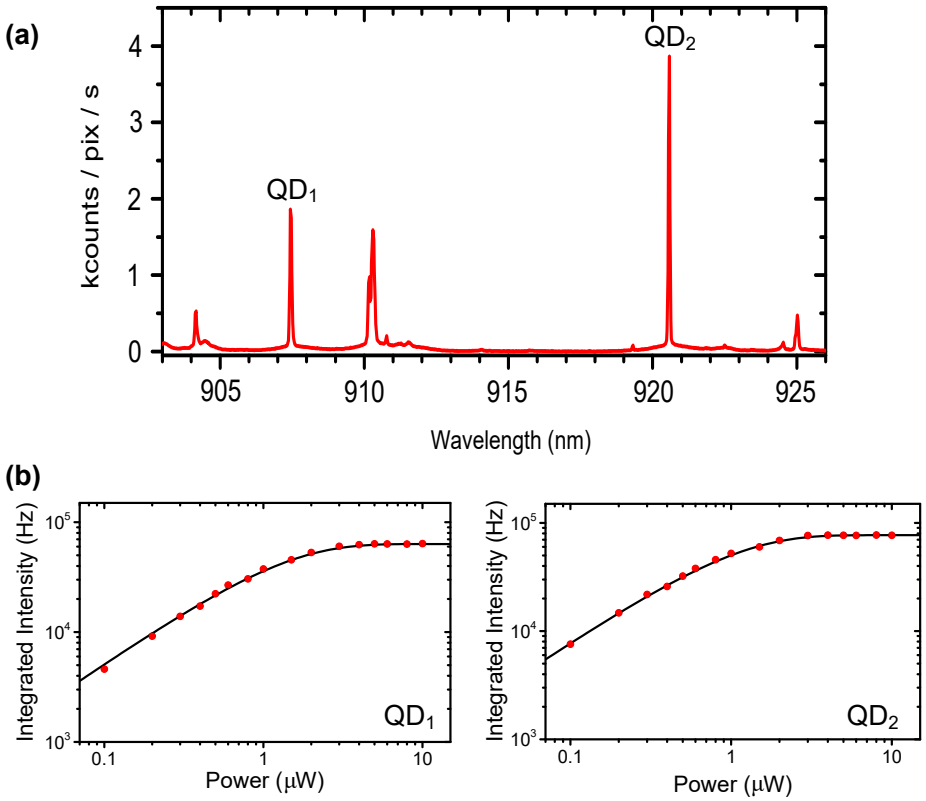

Fig. 3.14 (a) Micro-PL spectrum as measured on the CCD under pulsed excitation (P_{exc} = 300 nW) at T = 4 K. (b) Power-dependent saturation intensity plots of the emission lines marked QD_1 at 907.4 nm, and QD_2 at 920.6 nm.

demonstration of the broad operation bandwidth of the device. The photoluminescence spectrum of NC_1 is shown in Fig. 3.14 (a). It features two narrow and bright lines that stand on a very clean background. The line labelled QD_1 (QD_2) peaks at 907.5nm (920.5nm). Fig. 3.14 (b) shows their spectrally-integrated intensity I as a function of the excitation power P_{exc}. I is obtained by fitting each emission line to a Lorentzian spectral profile, and by summing the contributions of two spectra acquired for two angles of the $\lambda/2$ waveplate that differ by 45°. This procedure allows taking into account a weak polarisation of the nanocavity emission. More details on the polarisation analysis are given later. For low P_{exc}, both lines exhibit a linear power dependence. A close inspection of the emission spectrum for various polarisation analysis angle is next employed to check the presence of a fine structure splitting. QD_1 shows such splitting and is attributed to a neutral exciton, while QD_2 is associated with a charged exciton. Over the complete range of excitation powers, the measured integrated intensities are perfectly reproduced by,

$$I(P_{exc}) = I_{sat}\left[1 - exp\left(\frac{-P_{exc}}{P_{sat}}\right)\right], \tag{3.11}$$

with P_{sat} the saturation power and I_{sat} the integrated intensity at saturation. QD_1 and QD_2 feature similar I_{sat}, with I_{sat} = 64 kHz for QD_1, and I_{sat} = 77 kHz for QD_2: this constitutes a first evidence of the broad operation bandwidth of the device.

Table 3.2 Details on the 10 fastest excitonic lines measured. Under the column 'Exciton type', X represents a neutral exciton while X^* represents a charged exciton.

QD number	Wavelength (nm)	Exciton type	Nanocavity index	Diameter (nm)
1	907.5	X	NC_1	220
2	920.5	X^*	NC_1	220
3	922	X	NC_1	225
4	931	X	NC_2	240
5	909	X^*	NC_3	220
6	922	X	NC_4	240
7	930.5	X	NC_4	240
8	927	X^*	NC_5	220
9	912.5	X	NC_6	230
10	920	X	NC_6	230

3.4.2 Time-resolved measurement of exciton lifetime

In this section, we determine the acceleration of SE provided by the nanocavity. Since the nanocavity presents a very large cavity mode linewidth, it is not possible to tune the same emitter on- and off-resonance using e.g. temperature. Thus to quantify the Purcell acceleration provided by the nanocavity, we compare the radiative rate of nanocavity QDs to the one of similar QDs embedded in bulk GaAs. This reference rate Γ_0 is determined as follows.

3.4.2.a. Reference decay time of bulk InAs QDs

To measure a reference value for the excitonic recombination rate we excite an ensemble of QDs located within large 20 μm × 20 μm squares that were etched on the nanocavity sample. We present a scanning electron microscope (SEM) image of such a square in Fig. 3.15 (a). The interest for measuring QDs situated in these squares is to measure QDs that are very similar to the ones that are embedded in nanocavities. However, the QDs that we excite are chosen close to the centre of the square to additionally exclude the remote possibility of having undesirable influences on the QD properties due to reflections from sidewalls. Fig. 3.15 (b) shows a PL spectrum of a square obtained for a low pumping power.

At first glance, even though the laser excitation spot area ($\sim$1 μm) should excite hundreds of QDs producing an ensemble luminescence spectrum, the actual PL spectrum

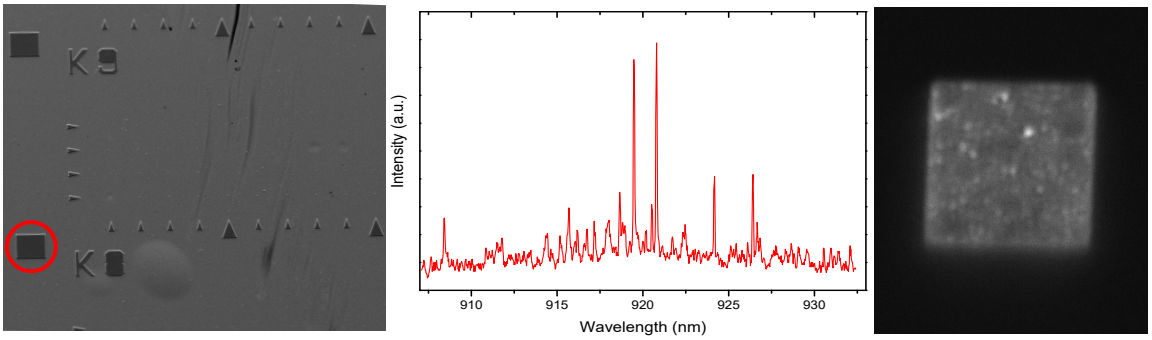

(a) **(b)** **(c)**

Fig. 3.15 (a) SEM image of the sample featuring a 20 μm $\times$ 20 μm square slab, on the bottom left corner of the image, used to measure exciton lifetime in bulk. (b) Micro-PL spectrum obtain from a square slab, under low power pulsed excitation, at T = 4 K. (c) Image of a square slab under IR LED illumination. The bright spots are the PL signal from individual QDs.

obtained from it is rather unexpected. We intend to find an inhomogeneous distribution characteristic of an ensemble emission, instead we obtain a spectrum of discrete lines much like the ones from QDs in nanostructures. More remarkably upon illuminating the squares with the IR LED (Fig. 3.15 (c)), used to navigate on the sample, we can distinguish individual bright spots which correspond to the PL of individual QDs. This is a new phenomenon that we observed on this sample which still needs to be probed in order to understand its origins. For now, we estimate the behaviour may be attributed to a preferential excitation mechanism in the squares that leads to a somewhat selective carrier trapping by some QDs making them light up at lower power than others.

We spectrally isolate a zone that doesn't contain any well-defined and intense emission lines and carry out the time-resolved decay time distribution measurements. The distributions are measured over an integration of 5 min. A representative measurement shown in Fig. 3.16 reveals a bi-exponential decay, which is typical of inter-conversions between the bright and dark excitons hosted by neutral QDs. We must establish a model of the system, taking into account the spin-flip transition between bright and dark exciton states, to interpret our experimental data and to extract from it an accurate estimation of the radiative decay time of the exciton.

Population decay rates in a three-level system. Since we excite the QDs with powers far lower than the saturation power, we assume that the population of the biexciton state is negligible. Furthermore, we suppose that the radiative recombination rates of the two bright exciton states are equal, therefore we simplify our system to only the ground state $|G\rangle$, the bright and dark exciton states $|X\rangle$ and $|D\rangle$ respectively, as shown in Fig. 3.17. Γ_{rad} is the radiative recombination of the exciton. $\gamma_{\uparrow}$ is the spin-flip rate from dark to bright and $\gamma_{\downarrow}$ is the spin-flip rate from bright to dark levels.

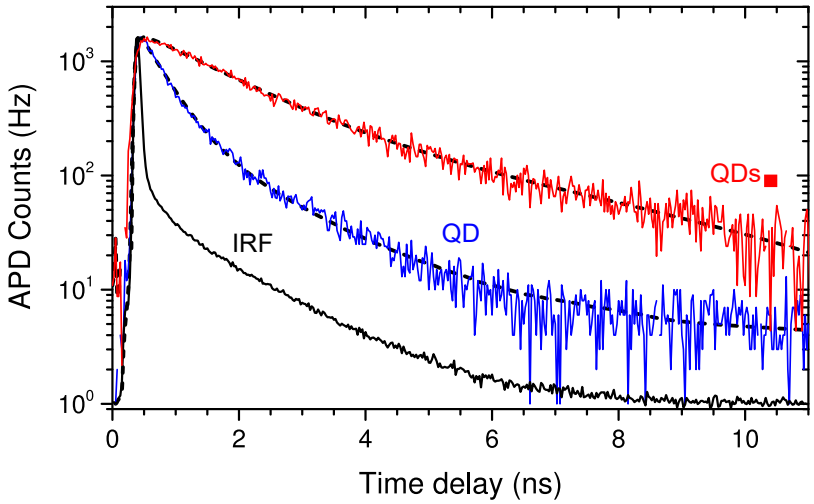

Fig. 3.16 Time-resolved measurements. 'IRF': measured instrument response function. 'QD': individual emission line from a QD in a nanocavity,(solid blue line: experimental data, dashed line: fit to a single exponential decay convoluted with the IRF). 'QDs■': ensemble of QDs embedded in a large square (20×20 mm^2) (solid red line: experimental data, dashed line: fit to a bi-exponential decay convoluted with the IRF). This measurement is used to determine the reference rate Γ_0.

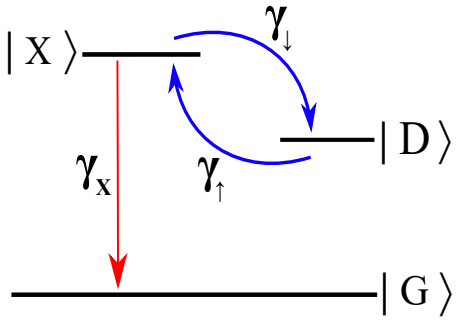

Fig. 3.17 Simplified exciton state diagram assuming equivalent radiative recombination rates for both bright exciton states. $|G\rangle$ represents the ground state, $|X\rangle$ is the bright exciton state, and $|D\rangle$ is the dark exciton state. Γ_{rad} is the radiative recombination rate, $\gamma_\uparrow$ and $\gamma_\downarrow$ are respectively the up and down conversion of population between $|X\rangle$ and $|D\rangle$.

The population of the bright state is $p_X(t)$ and the one of the dark state is $p_D(t)$. The dynamics of population in the two exciton states may be expressed as,

$$\text{or } \frac{d}{dt}\begin{pmatrix} p_X \\ p_D \end{pmatrix} = \begin{pmatrix} -(\Gamma_{rad}+\gamma_\downarrow) & \gamma_\uparrow \\ \gamma_\downarrow & -\gamma_\uparrow \end{pmatrix}\begin{pmatrix} p_X(t) \\ P_D(t) \end{pmatrix} \tag{3.12}$$

We can then compute the eigenvalues of the recombination-rate matrix $\mathbf{M}$ by solving the equation $(\mathbf{M}-\lambda\mathbf{I})\mathbf{X}=0$, where λ is the eigenvalues, and $\mathbf{X}$ is the eigenvectors. In our case, we obtain the following eigenvalues,

$$\lambda_{\pm} = \frac{1}{2}\left[-(\Gamma_{rad} + \gamma_{\uparrow} + \gamma_{\downarrow}) \pm \sqrt{\Gamma_{rad}^2 + (\gamma_{\uparrow} + \gamma_{\downarrow})^2 + 2\Gamma_{rad}(\gamma_{\downarrow} - \gamma_{\uparrow})}\right]. \tag{3.13}$$

Let's consider two limit cases, namely the case of slow spin-flips ($\Gamma_{rad} \gg (\gamma_{\uparrow}, \gamma_{\downarrow})$) and the one of fast spin-flips ($\Gamma_{rad} \ll (\gamma_{\uparrow}, \gamma_{\downarrow})$). For $\Gamma_{rad} \gg (\gamma_{\uparrow}, \gamma_{\downarrow})$ we approximate the term under the square root from Eqn. 3.13 as, $\sqrt{\Delta} = \Gamma_{rad} + \gamma_{\downarrow} - \gamma_{\uparrow}$.

Replacing this value in Eqn. 3.13 we obtain,

$$\lambda_{-} = -(\Gamma_{rad} + \gamma_{\downarrow}) = -\Gamma_1 \tag{3.14}$$

$$\lambda_{+} = -\gamma_{\uparrow} = -\Gamma_2, \tag{3.15}$$

where Γ_1 and Γ_2 are the parameters used to fit experimental data, as described in 3.3.3.c.. Under non-resonant excitation, the initial populations of states $|X\rangle$ and $|D\rangle$ are equal. In the presence of slow spin-flips $|X\rangle$ decays at two rates. We observe a quick rate Γ_1, which is dominated by the radiative recombination rate Γ_{rad}, with the contribution of loss of population to $|D\rangle$. We also observe a slower rate Γ_2, which represents the population of $|D\rangle$ which is first converted to $|X\rangle$ before decaying via a radiative process.

Conversely when $\Gamma_{rad} \ll (\gamma_{\uparrow}, \gamma_{\downarrow})$ we have, $\sqrt{\Delta} \approx (\gamma_{\downarrow} + \gamma_{\uparrow}) + \Gamma_{rad}[(\gamma_{\downarrow} - \gamma_{\uparrow})/(\gamma_{\downarrow} + \gamma_{\uparrow})]$, which then leads to

$$\lambda_{-} = -\left(\gamma_{\downarrow} + \gamma_{\uparrow} + \Gamma_{rad}\frac{\gamma_{\downarrow}}{\gamma_{\downarrow} + \gamma_{\uparrow}}\right) = -\Gamma_1 \tag{3.16}$$

$$\lambda_{+} = -\Gamma_{rad}\frac{\gamma_{\uparrow}}{\gamma_{\downarrow} + \gamma_{\uparrow}} = -\Gamma_2. \tag{3.17}$$

Γ_1 is dominated by $(\gamma_{\downarrow} + \gamma_{\uparrow})$, which represents the rate at which an equilibrium between the populations of $|X\rangle$ and $|D\rangle$ is reached. The equilibrium populations are governed by the ratio between $\gamma_{\uparrow}$ and $\gamma_{\downarrow}$. Γ_2 on the other hand, is the radiative recombination rate Γ_{rad}, weighted by $\frac{\gamma_{\uparrow}}{\gamma_{\downarrow}+\gamma_{\uparrow}}$, which is the fraction of time when the system occupies $|X\rangle$, once the stationary regime is attained.

In practice we set $\lambda_{-} = -\Gamma_1$ and $\lambda_{+} = -\Gamma_2$, where Γ_1 and Γ_2 are the parameters used to fit the experimental decay time measurement data, as described in 3.3.3.c.. Then we solve Eqn. 3.13 in order to extract the values of $\gamma_{\downarrow}, \gamma_{\uparrow}$, and Γ_{rad}. We make the assumption $\gamma_{\downarrow} = \gamma_{\uparrow}$, which is reasonable given the typical bright-dark energy separation is on the order of 200 μeV for our QDs, and the operation temperature is between 5 K and 10 K, which is elevated enough to have acoustic phonons with adequate energy to induced spin-flips.

Mean radiative recombination rate. We performed twenty time-resolved measurements over three different squares, integrating a spectral window of ~1 nm centred at 915 nm

and 918 nm, at different pumping powers. Each set of experimental data is fitted and the radiative recombination rate is computed following the method outline in the previous section. Fig. 3.18 summarises the values of Γ_{rad}, from which we extract the mean decay rate $\Gamma_{rad} = 0.8$ ns^{-1} (with a standard deviation of 0.07).

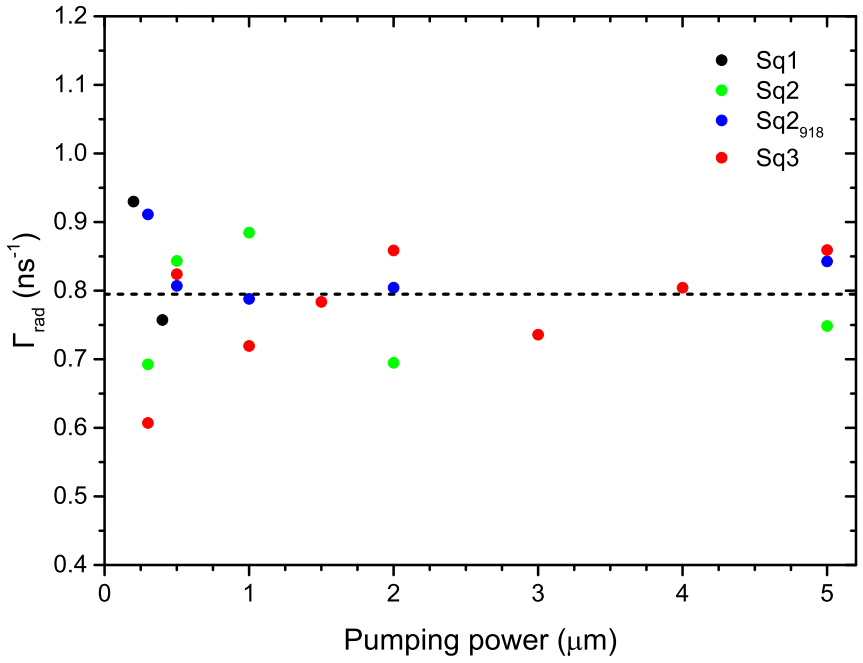

Fig. 3.18 Γ_{rad} deduced from time-resolved measurements of QDs in 20 μm $\times$ 20 μm squares, as a function of pumping power. The dotted line delineates the mean value of Γ_{rad}.

Correction of interface effects. Even though we picked QDs situated close to the centre of the squares to eliminate the possibility of reflections from sidewalls, we have no means to get rid of the reflected light at the top facet and the bottom mirror. The light that is reflected from the top facet and the bottom mirror interact again with the emitter, which slightly accelerates the spontaneous emission rate of the dipole. In a pure bulk medium, the emitter doesn't interact with the emitted light, and therefore a correction must be made to the measured decay rate in squares to obtain the desirable reference value for bulk.

The corrective factor was calculated using FDTD simulations performed by Jean-Michel Gérard. FDTD methods don't offer the possibility of calculating the spontaneous emission rates of an emitter. However since the Purcell effect is defined by the retroaction of the environment on the emitter, the acceleration of SE can be estimated by computing the ratio between the power emitted by a QD in a square and the power emitted by a QD in bulk. In practice, the simulation is carried out on a dipole with its dipole moment oriented in the horizontal plane. The dipole is embedded in a slab of GaAs that sits on a SiO_2-Au mirror. The total power exiting a small volume around the dipole is evaluated. The same measurement is performed on a dipole embedded in bulk GaAs, replicated by a block of

GaAs, with perfectly absorbing facets (perfectly matched layers). Following this technique, Jean-Michel determined that for a dipole emitting at $\lambda = 920$ nm, and situated in a GaAs square, the recombination rate is enhanced by a factor 1.32, which leads to a radiative decay rate in the bulk of $\Gamma_0 = 0.61$ ns^{-1} (standard deviation of 0.05 ns^{-1}), a value in good agreement with measurements on similar self-assembled InAs QDs [52].

3.4.2.b. Decay time of QD embedded in nanocavities

Single QDs embedded in nanocavities systematically exhibit much faster SE dynamics. Fig. 3.19 shows time-resolved data associated with QD_1 and QD_2. As expected for a charged exciton, QD_2 features a single-exponential decay. A fit of the data to $Aexp(-\Gamma_{rad}t)$ directly yields the radiative decay rate $\Gamma_{rad} = 3.0$ ns^{-1}, a value that exceeds Γ_{bulk} by a factor of 5 (charged and neutral excitons feature similar oscillator strength [193]). The decay curve of QD_1 is bi-exponential. As mentioned earlier, this feature is characteristic of the inter-conversion between the bright and dark exciton states hosted by a neutral QD. We use again a fit to a bi-exponential decay function and the simple three-level model to determine $\Gamma_{rad} = 2.4$ ns^{-1}, which exceeds Γ_{bulk} by a factor of 4. Despite their vastly different emission wavelengths, QD_1 and QD_2 display a pronounced SE acceleration: this directly evidences the broadband Purcell effect provided by the nanocavity.

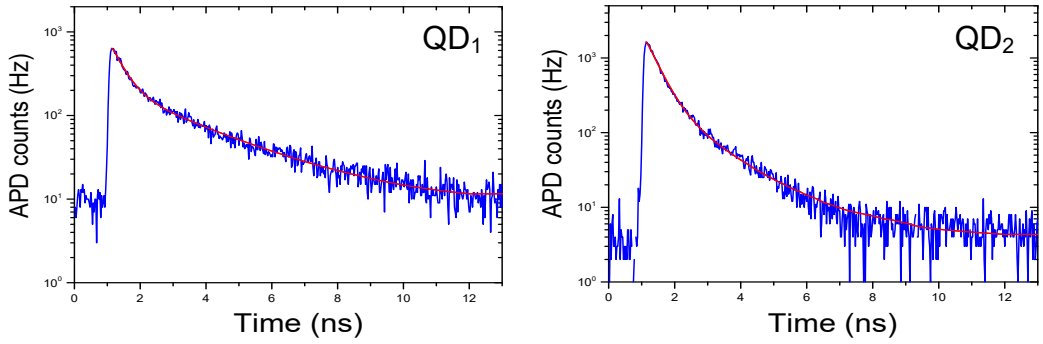

Fig. 3.19 Time-resolved PL measurements of QD_1 and QD_2. The respective excitonic radiative recombination rate was found to be, $\Gamma_{rad}^{QD_1} = 2.4$ ns^{-1}, and $\Gamma_{rad}^{QD_2} = 3.0$ ns^{-1}.

I carried out time-resolved excitonic lifetime measurements on 70 emission peaks between 895 nm and 930 nm, obtained from 15 different nanocavities with a diameter ranging from 200 nm to 240 nm. The fastest measured line (QD_4 from NC_2) features $\Gamma_{rad} = 3.4$ ns^{-1}, which results in $\Gamma_{rad}/\Gamma_{bulk} = 5.6$, thus approaching the predicted maximum radiative rate of 6.3. Fig. 3.20 summarises results obtained on 10 of the fastest excitonic lines (3 charged and 7 neutral excitons) measured in similar devices. I routinely observed large SE acceleration across the sample.

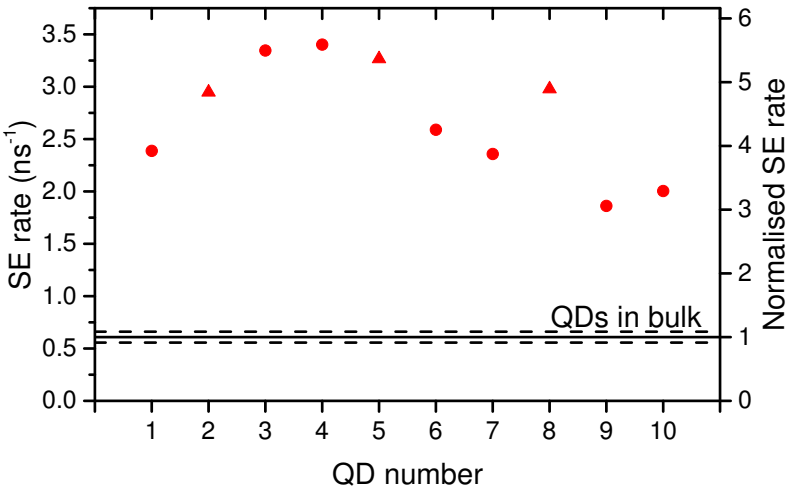

Fig. 3.20 SE rate of individual QDs embedded in nanocavities. Disks (triangles) correspond to neutral (charged) excitons. The SE rate of similar QDs embedded in bulk GaAs serves as a reference (horizontal solid line represents a mean value, and the dashed lines delineate $\pm$ 1 standard deviation).

3.4.3 Collection efficiency

Having studied the excitonic lifetimes of QDs and the Purcell acceleration of their radiative rate in nanocavities, the figure of merit that remains to be explored is the extraction efficiency of the source. To determine the source brightness, we compare the saturation intensities I_{sat} of the QDs referenced in Table 3.2 to the one of a QD embedded in an unprocessed environment. The following sections detail the procedure for determining this reference saturation intensity, I_{sat}^{ref} of QDs in an unprocessed sample.

3.4.3.a. Intensity at saturation of reference QDs

In order to estimate the extraction efficiency (ε) of our nanocavities, we first perform pumping power-dependent micro-PL measurements on QDs embedded under 120 nm of unprocessed GaAs. It features a calculated collection efficiency $\varepsilon_{ref} = 1.2 \times 10^{-2}$ for a first lens with NA = 0.75 [77]. The reference sample was grown by molecular beam epitaxy (sample ref. 374Y) and belongs to a "border zone" [94], where the QD areal density is low enough to ensure that single emitters can be isolated under the microscope excitation spot.

The photons emitted from QDs from the unprocessed sample we use, feature a preferential polarisation. This polarisation-dependent behaviour is illustrated in Fig. 3.21, where we see that the integrated intensity of a spectral line, arising from the excitonic recombination, is modulated as a function of the polariser angle. The signal in red represents a QD in a nanocavity and the one in black belonging to a QD in an unprocessed GaAs. Both the curves are obtained by integrating signals from QDs for $P > P_{sat}$.

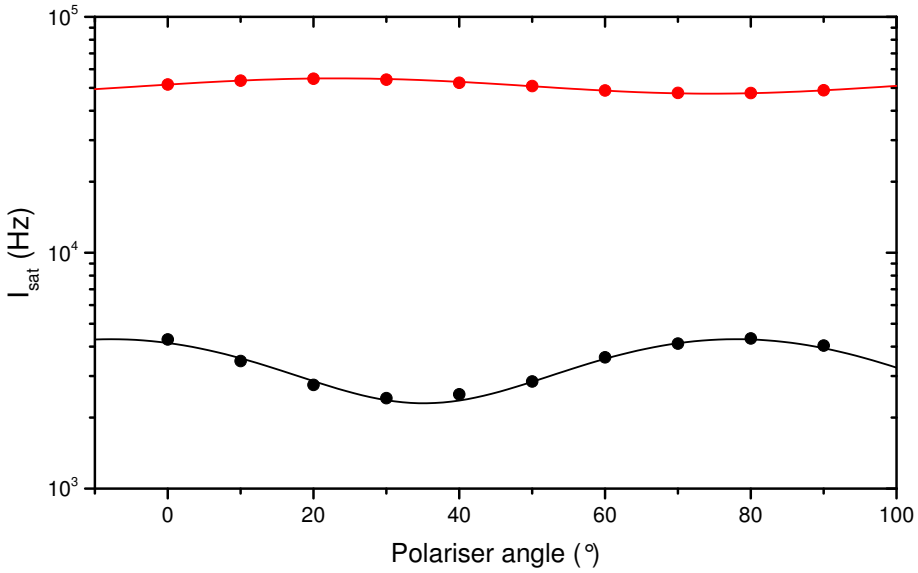

Fig. 3.21 Polarisation dependence, due to diffraction grating, of measured integrated intensity on CCD. The integrated intensity of emission for a saturated QD in bulk (black) and in a nanocavity (red), was recorded by varying the polarisation angle of the signal incoming on the grating.

We then perform two sets of pumping-power-dependent micro-PL spectral measurement, one set with the polariser fixed at the angle that gives the minimum intensity, and the second set with the polariser oriented at the angle producing the maximum intensity. The difference in polariser angle between the two sets of measurements is 45°. The final integrated intensity is obtained as the sum of the results corresponding to each of the two polariser configurations. We study the trend in integrated intensity of the QD emission lines to identify the intensity at saturation of these QDs. This forms a reference value for the amount of signal we can collect with our experimental setup. We determine an average CCD intensity at saturation of I_{sat}^{ref} = 3.0 kHz (standard deviation 0.9 kHz), from the measurements of five individual excitonic emission lines as recorded in Table 3.3.

Table 3.3 Saturation intensities I_{sat} of 5 QDs embedded in an unprocessed sample.

QD index	Wavelength (nm)	I_{sat} (kHz)
i	896	4.2
ii	892	3.4
iii	890	3.4
iv	892.6	2.2
v	912	2.0

3.4.3.b. Source brightness measurements

The method described for measuring the intensity at saturation of QDs in bulk is repeated maintaining the same setup conditions on QDs within nanocavities. As described in Sec. 3.4.1, for QD_1 (QD_2), we measured I_{sat} = 64 kHz (I_{sat} = 77 kHz). This corresponds to a brightness improvement by a factor of 20 (24) and yields a collection efficiency of 0.24 (0.29) for a first lens with NA = 0.75. Fig. 3.22 summarises brightness measurements conducted on the same 10 excitonic emission lines presented in Table 3.2. The brightest line (QD_{10}) features a collection efficiency as high as 0.35. This figure of merit could be further improved to approach the theoretical limit by stabilising the QD charge state [193] and by employing a deterministic fabrication technique [179, 180].

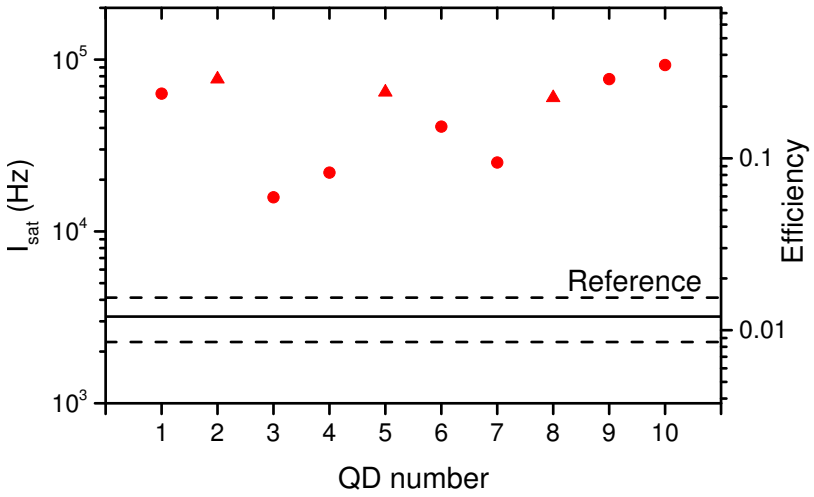

Fig. 3.22 Spectrally-integrated counts at saturation of individual QDs embedded in nanocavities. The reference is measured on individual dots embedded in a low-density unprocessed sample (horizontal solid line represents a mean value, and the dashed lines delineate ± 1 standard deviation).

3.4.4 Towards the emission of entangled photon pairs

A major application of the proposed nanocavity is the realisation of sources of polarisation-entangled photon pairs. Such entangled photon pairs can be emitted by the radiative cascade of the biexciton state hosted by a sufficiently symmetric QD. A broad operation bandwidth is necessary to collect the photons emitted by the $|XX\rangle \rightarrow |X\rangle$ and $|X\rangle \rightarrow |G\rangle$ transitions, which are generally detuned by a few nm. Besides, the Purcell acceleration is interesting, because it relaxes the constraint of the fine structure splitting which should be smaller than the radiative linewidth to ensure the emission photon pairs with a good entanglement fidelity.

We present here results of characterisation on an exciton-biexciton pair identified from nanocavity NC_6 (cf. Table 3.2). Fig. 3.23 (a), presents the polarisation dependent micro-PL

spectra of the pair measured with 10 μW excitation power. A constant offset is applied to each spectrum for better visibility. The peaks exhibit an extremely small fine structure splitting, which suggests QD_9 might be almost symmetrical, thus increasing the likelihood of having polarisation-entangled photon pairs. Next, we fit the two emission lines with Lorentzian profiles at varying pumping power, to compute the integrated intensity of each transition. The emission lines are respectively attributed to the exciton (QD_9^X at 912.5 nm) and biexciton (QD_9^{XX} at 911 nm) recombination. This identification is validated by the analysis of the integrated spectral intensity of each line, which we denote I_X and I_{XX}.

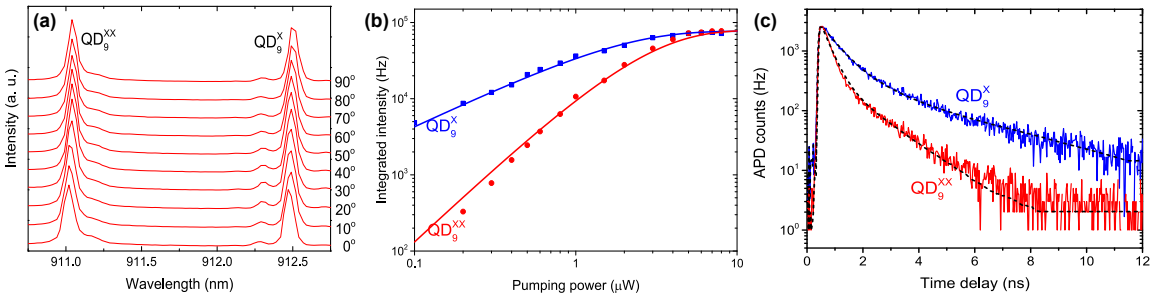

Fig. 3.23 (a) Micro-PL spectrum of an exciton-biexciton pair hosted by QD_9. The exciton QD_9^X emission line is positioned at 912.5 nm and the biexciton QD_9^{XX} at 911 nm. (b) Integrated intensity plots for QD_9^X (blue) and QD_9^{XX} (red) both saturating at 77 kHz. At low pumping power the data of QD_9^X (QD_9^{XX}) display a linear (quadratic) dependence. (c) Time-resolved measurement of decay time for QD_9^X (blue) and QD_9^{XX} (red) corresponding to radiative rates of $\Gamma^X_{rad} = 1.9\ \text{ns}^{-1}$ and $\Gamma^{XX}_{rad} = 3.8\ \text{ns}^{-1}$.

Fig. 3.23 (b) is a plot of experimental data for integrated intensity I_X in blue and I_{XX} in red as a function of pumping power. The data is fitted with functions (solid line) that represent the probability of creating n electron-hole pairs in a QD, governed by Poissonian statistics (cf. Appendix D). The fitting functions have the following form,

$$I_X(P_{exc}) = I_{sat}\left(1 - e^{-\frac{P_{exc}}{P_{sat}}}\right), \tag{3.18}$$

$$I_{XX}(P_{exc}) = I_{sat}\left(1 - e^{-\frac{P_{exc}}{P_{sat}}} - \frac{P_{exc}}{P_{sat}} e^{-\frac{P_{exc}}{P_{sat}}}\right), \tag{3.19}$$

where I_{sat} is the intensity at saturation and P_{sat} is the saturation power. For the two observed emission lines, at low pumping power we find I_X varies linearly as a function of pumping power while I_{XX} exhibits a quadratic evolution, which is characteristic behaviour of an exciton and a biexciton respectively. Both QD_9^X and QD_9^{XX} saturate at the same integrated intensity of I_{sat} = 77 kHz, which shows that the exciton and the biexciton emission couple equally well to the nanocavity. From these results, we obtain, in the first set $I_{sat} = 1.7\,\mu$W, with an excitonic wavelength of $\lambda_X = 912.5$ nm and the corresponding biexcitonic wavelength of $\lambda_{XX} = 911$ nm.

Additionally we measured the radiative recombination rate of QD_9^{XX} to be $\Gamma_{rad}^{XX} = 3.8$ ns^{-1}, which is two-fold faster than the rate of QD_9^{X} at $\Gamma_{rad}^{X} = 1.9$ ns^{-1} (Fig. 3.23 (c)). Finally, we observe a shift in wavelength of 1.5 nm between the two lines in our results which is in accordance with results, from literature, obtained on similar InAs QDs [194, 195], thus justifying our assumption of having indeed observed a set of exciton and biexciton hosted by the same QD.

We can conceive of applying mechanical stress on the QD with an integrated piezo actuator [196] in order to lift the fine structure splitting of the exciton, to generate polarisation-entangled photon pairs. Thus with the ability to simultaneously couple an exciton and biexciton the nanocavity emerges as a promising candidate for realising a source of pairs of polarisation-entangled and indistinguishable photons.

3.5 Conclusion

In this chapter, we have introduced a new and simple photonic structure (nanocavity) to achieve broadband Purcell enhancement of SE. The nanocavity is a truncated GaAs nanowire placed on a hybrid SiO_2-Au mirror with modal reflectivity, $|r_b|^2 \approx 0.9$. The semiconductor-air interface at the top facet forms a weakly reflecting mirror ($|r_t|^2 \approx 0.43$) which defines a low-Q (and thus spectrally broad) optical cavity. The numerical simulations done to establish the design and dimensions of the device were presented, and its optimal figures of merit were estimated. The ultra-small mode volume enables to reach a large Purcell factor of 6.3. Despite the nanoscale lateral dimensions, we estimated a first-lens collection efficiency as high as 0.54.

Then we described the fabrication process that was elaborated in the team to develop the nanocavity sample. Finally, we detailed the optics experiments carried out to gauge the Purcell acceleration of the SE and the extraction efficiency of the nanocavities. We measure a maximal acceleration of spontaneous emission by a factor as large as 5.6 and a bright quantum dot emission (collection efficiency of 0.35 into NA = 0.75). In addition to the individual nanocavity that featured two emission lines 13 nm apart, with a Purcell acceleration of the radiative rate of over 4, about 30% of the excitonic decays recorded across the sample also presented SE rate enhancement greater than 3. The emission wavelength of these QDs ranged from 900nm to 930 nm, thus demonstrating the broadband enhancement of SE in the nanocavities.

Such nanostructures present key assets to realise a bright and widely-tunable source of indistinguishable single photons, for example by applying mechanical stress on the QD with an integrated piezo actuator [196]. We note that thanks to its nanoscale volume, the proposed nanocavity additionally features a small sensitivity to the QD spectral broadening associated with thermal vibrations [164]. In the future, elliptical nanocavities could provide full control over the polarisation of the emitted photons, in analogy with previous work on nanowire

antennas [197]. The proposed nanocavity is also promising for the emission of pairs of polarisation-entangled and indistinguishable photons. Beyond advanced quantum light sources, this broadband photonic structure could enhance optical nonlinearities involving several detuned QD transitions [85], or be used to explore subtle nonresonant couplings between distinct QDs [86].

Finally, from a technological point of view, the relative simplicity of the device makes it also very appealing for emergent material systems, which are not yet as technologically mature as III-As semiconductors. As a final note, we believe that there is still room for improvement in the design, especially for the collection efficiency. At present, the collection efficiency is limited by the divergence of the output beam. The latter depends on the scattering of light at the top facet (both forward and backward), as well as on the interference associated with the reflection at the bottom mirror. Also, simulations have shown that it is necessary to integrate modes other than HE_{11} for the design. The very narrow output beam obtained for detuned emitters (see Fig. 3.5) is not yet completely understood. It nevertheless suggests that by exploring the parameter space more thoroughly, it may be possible to find a design that simultaneously offers large Purcell acceleration and state-of-the-art collection efficiency. This direction is currently being explored in the team, in collaboration with Niels Gregersen and his team at DTU, Copenhagen.

Chapter 4

Towards electrostatically-tunable nanowire single-photon sources

As discussed in Chapter 1, self-assembled InAs QDs are formed by the relaxation of the mechanical strain which arises from the lattice mismatch between the QD material and the GaAs growth substrate. This fabrication process produces QDs with a random spatial distribution and of varying sizes. Such non-uniformity in sizes results in a spectral dispersion in QD emission wavelengths [68]. There exist several deterministic fabrication techniques to control the position of the QDs on the substrate [184, 198], as well as select desired QDs based on their positions and emission wavelengths [124, 130, 183, 185]. These methods have produced cavity-based single-photon sources (SPSs) with state-of-the-art performances. However, in order to conceive of any multi-source application with such sources based on a cavity, it would be necessary to carefully isolate multiple QDs emitting around a common wavelength. Depending on the areal density of the QDs on a given sample, the endeavour of locating QDs with matching emission wavelengths might well resemble the efforts of locating a needle in a haystack. A far more practical solution in this situation would be to have a broadband tuning mechanism, by which the wavelengths of any two or more sources could be adjusted to match.

A source based on a QD embedded in a monolithic high-Q microcavity is not compatible with broadband tuning. Indeed, the large collection efficiency is maintained only over the narrow bandwidth of the cavity, and it is difficult to tune the cavity resonance wavelength. One solution around this difficulty is offered by semi-open hybrid microcavities, as recently demonstrated in Ref. [199]. This solution offers state-of-the-art brightness and tunability, but one loses device integration, one of the main advantages of solid-state systems. Another strategy is to rely on a photonic structure with a broad operation bandwidth. Prime examples of such a system include, circular Bragg resonators on highly efficient broadband reflectors [187], nanowire nanocavities (Chapter 3), or tapered nanowire antennas [78]. Here we consider 'trumpet' photonic wire antennas, which are based on a waveguide approach. A

trumpet exhibits a first-lens external efficiency of 0.75 and a high coupling efficiency to a Gaussian beam, but above all, it sustains its performance over a wide spectral range of ∼100 nm [78].

There exist several methods to tune the emission wavelength of a QD. Temperature [200], electric fields [201, 202], and material strain [203–206] are all acceptable methods to shift the energy of an emitter. Temperature enables only fine-tuning, since raising temperature also introduces homogeneous spectral broadening and undesirable decoherence in the emitted photons. Electric fields allow tuning in the range of up to 25 meV, with specific barrier materials, in order to avoid the ionisation of the QD [207]. Finally, large-scale tuning is achievable with strain, with up to 500 meV shifts being demonstrated on diamond anvil cells [208]. Piezoelectric actuators have also been widely employed for both large [209] and fine-tuning QD transition energy with strain [80, 210]. A particular asset of strain tuning is the ability of broadband tuning, without losing the oscillator strength.

In this chapter, we will present the first steps towards the realisation of an integrated wavelength-tunable single-photon source (SPS) based on a photonic trumpet. A pair of on-chip electrodes are used to apply an electrostatic force on the top part of the structure. This bends the trumpet and generates stress at the QD location, which acts as a "*tuning knob*" for the QD emission wavelength. We introduce the design of the system along with some expected performance, obtained from simulations I performed with Yoann Curé. Then we describe the lithography mask design that I defined followed by the detailed fabrication process (flip-chip process, and ICP etching recipe) I developed with Alberto Artioli. We conclude this chapter with some results of preliminary measurements of the performance of the sample, carried out by Matteo Finazzer and Alberto Artioli with the help of Fabrice Donatini.

4.1 Bending a trumpet to tune the emission wavelength of an embedded QD

In Chapter 2 we explored the degradation in the optical properties of a QD due to its interaction with low-frequency phonons, arising from thermally induced mechanical vibration modes of the nanowire. These vibration modes make the wire stretch, contract, and flex, thus inducing strains on the embedded QDs. Through the deformation potentials, this induces changes in the bandgap of the QD material, and thus changes in the electron and hole energy levels. Here, we plan to use a static deformation of the trumpet, obtained by applying a force on its top facet to tune the emission wavelength of an embedded QD.

4.1.1 Stress field generated by trumpet bending

The stress field inside the trumpet is then very close to the one obtained for the first flexural mode. The deflection of the top facet causes a portion of the trumpet to compress while stretching the rest leaving a neutral axis in the middle, which translates at the QD plane into a strain field featuring a strong gradient across the cross-section. The size of the QDs we use is at least one order of magnitude smaller than the nanowire diameter, hence we consider the former point-like structures. Furthermore, the bending of the nanowire induces predominantly uniaxial stress on the QD, oriented along its growth axis.

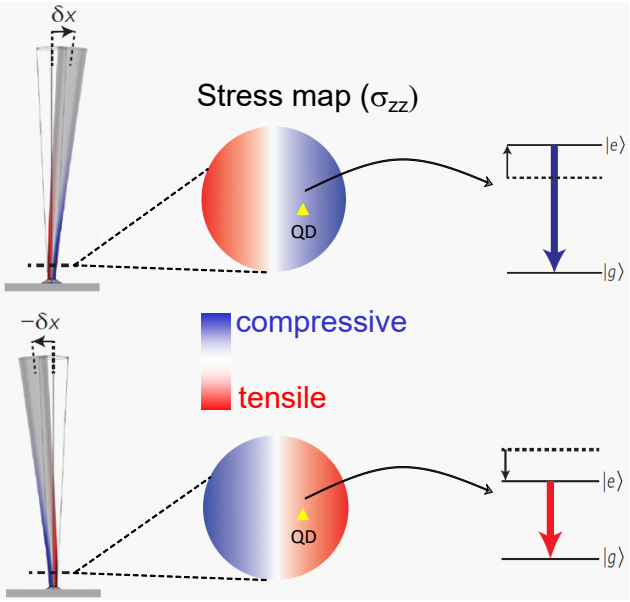

Fig. 4.1 Static strain tuning of QD emission energy. Bending a trumpet generates a stress field gradient on the QD plane. Half of the trumpet cross-section experiences a compressive stress (blue) and the other half undergoes a tensile stress (red) separated by a neutral axis (white). The emission energy of a QD that is compressed (stretched) exhibits a blue- (red-) shift.

The trumpet can be treated as a conical beam of height H, with a circular cross section of radius R_1 (R_2) at the base (top), that is clamped at its base. We assume a constant point force (F), perpendicular to the trumpet axis, is applied to the center of its top facet, displacing it by $\delta x(H)$, and bending the trumpet. Applying the Euler-Bernoulli beam theorem we can express $\delta x(H)$ as,

$$\delta x(H) = \frac{4H^3}{3\pi Y R_1^3 R_2} F, \tag{4.1}$$

where Y is the Young's modulus of the beam. The stress σ_{zz} generated at the base, attains its maximum value on the sidewall (see Fig. 4.1), which is written as,

$$\sigma_{zz}^{max}(0) = \frac{4H}{\pi R_1^3} F. \tag{4.2}$$

Thus we find that σ_{zz} scales with $\delta x(H)$ as,

$$\frac{\sigma_{zz}^{max}(0)}{\delta x(H)} = \frac{3YR_2}{H^2}. \tag{4.3}$$

The QD emission energy tuning slope obtained on self-assembled lens-shaped InAs QDs for a uniaxial stress along z is given by, $\delta E_{QD}/\delta\sigma_{zz} = 67$ μeV/MPa [88]. Therefore for the GaAs trumpet presented in Ref. [81], we obtain, $\sigma_{zz}^{max}(0)/\delta x(H) = 1.5$ GPa/μm with $H = 12$ μm, $R_2 = 0.845$ μm, and $Y = 85.9$ GPa for GaAs. From where, for a QD located on the edge of the trumpet cross-section, we anticipate a maximum energy tuning of the order of $\delta E_{QD}/\delta x(H) = 102$ meV/μm. This illustrates that a moderate top facet displacement may potentially enable a large shift in QD emission energy.

4.1.2 A proof-of-principle experiment

In this section, we take a closer look at the results of large-scale static strain tuning carried out on a photonic trumpet [81]. In this proof-of-principle experiment, a tip was employed to displace the top facet of the trumpet by close to 1 µm.

The GaAs photonic trumpet used was 12 μm tall, it had a top diameter of 1.69 μm, a base diameter of 0.35 μm, and it stood on a planar gold mirror. The trumpet embedded around 10 self-assembled InAs QDs, randomly distributed over a plane at 0.11 μm from the base of the trumpet. The QDs were excited with a continuous laser set to $\lambda = 830nm$. The experiment was carried out, at $T = 5K$, within a SEM from a modified cathodoluminescence setup (Fig. 4.2), the details of which can be found in Ref. [81]. The top facet of the trumpet was deflected using a tungsten tip mounted on a nanomanipulator. The total range of displacement of the nanomanipulator was 1 μm with shortest intervals of 1 nm.

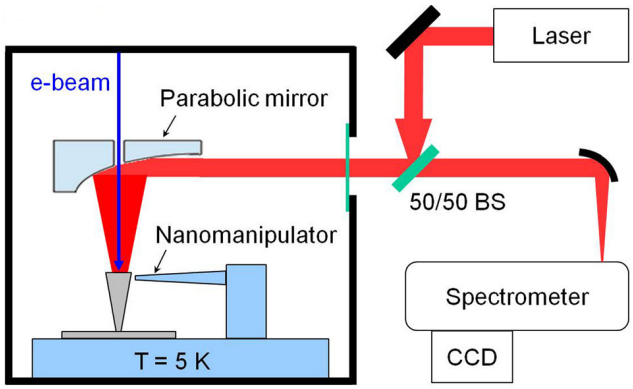

Fig. 4.2 Modified cathodoluminescence setup: the sample, nanomanipulator, and parabolic mirror, are placed within a SEM. The laser passes through an optical access before being focused onto the trumpet by the parabolic mirror, which also collects the PL signal from the QDs. The e-beam of the SEM allows to visualise the position of the nanomanipulator with respect to the trumpet top facet [81].

The shift in emission energy varies linearly with the top-facet displacement (Fig. 4.3). Additionally, for a given top-facet displacement, QDs further out from the trumpet axis bear higher stress which results in a larger energy shift. A maximum spectral shift of 25 meV was achieved on a QD at 70 nm from the axis, with a top-facet deflection of 0.8 μm. Although the trumpet could be bent further, the measurement was limited by the range of the nanomanipulator. This technique also made it possible to bring two QDs, in the same trumpet, whose initial emission energies differed by 2 meV, into resonance, with a top-facet displacement of 70 nm. Adding a second nanomanipulator pushing the trumpet along a different direction made it possible to bring three QDs into resonance [81].

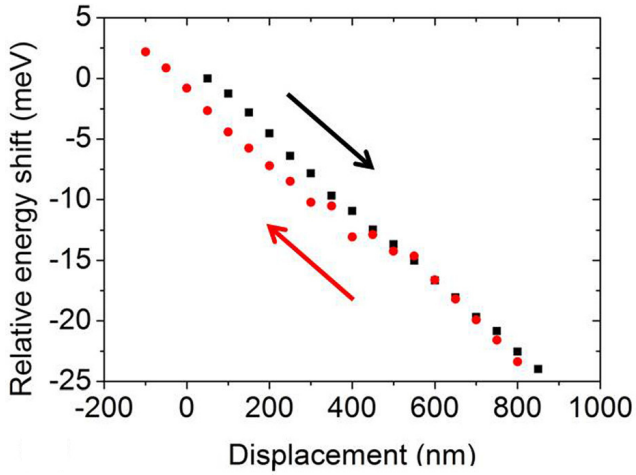

Fig. 4.3 Relative energy shift of the exciton as a function of trumpet top-facet displacement. The two sets of data represent measurements with increasing (decreasing) displacement in black (red). The slight shift in the red data set is caused by a slip in the nanomanipulator tip [81].

This study serves as proof-of-principle for using the deflection of a photonic trumpet as a QD emission tuning mechanism. However, such a system doesn't allow to have a SPS along with its tuning mechanism integrated on the same chip, which would complicate any effort to scale up the fabrication of multiple sources. Additionally, the physical contact between the nanomanipulator tip and the trumpet induces a redistribution of charge, which disrupts the emission spectrum of a QD. Finally, the nanomanipulator has a limitation in the range of maximum displacement and allows only movements in discrete steps.

4.1.3 Design of an integrated device based on electrostatic actuation

4.1.3.a. Principle

To overcome the limitations of the previous system we have taken this static tuning technique a step further. Instead of mechanically bending the trumpet we set out to deflect it using an electrostatic force. We introduce two gold-coated tapered electrodes positioned at a distance

from the trumpet and diametrically opposite from one another. By applying a potential difference across the tapered electrodes we generate an electric field with a strong gradient. This field causes the top-facet of the trumpet to be polarised. The polarised material in the electric field gradient, in turn generates a force that causes the top-facet of the trumpet to be deflected towards an electrode. This method enables the elaboration of a SPS and its tuning mechanism integrated on the same chip. It overcomes the charge redistribution and discrete and limited displacement problems by offering a *"contactless"* tuning through a continuous potential-tuning scale.

4.1.3.b. Design

Having introduced the principle we intend to exploit, in this section we present the design of the device that was established, with its basic expected performance, as obtained from finite element method simulations on COMSOL Multiphysics. As illustrated in Fig. 4.4 we have considered a trumpet of 20 μm in height, with a base diameter of 200 nm and a top diameter of 3.5 μm which corresponds to a total cone angle of 10°. The QD plane is situated at a height of 100 nm from the base. The separation d_1, between electrode E_1 and the trumpet top was set to 300 nm, a distance that was small yet wide enough to surely be able to etch each feature correctly without any degradation due to screening effects. The distance d_2 was variable in order to optimise the displacement. The electrodes and the trumpet rest on a 250 nm-thick Au mirror and are surrounded by air, the 9 nm-thick SiO_2 layer was omitted from the simulation to simplify the computation.

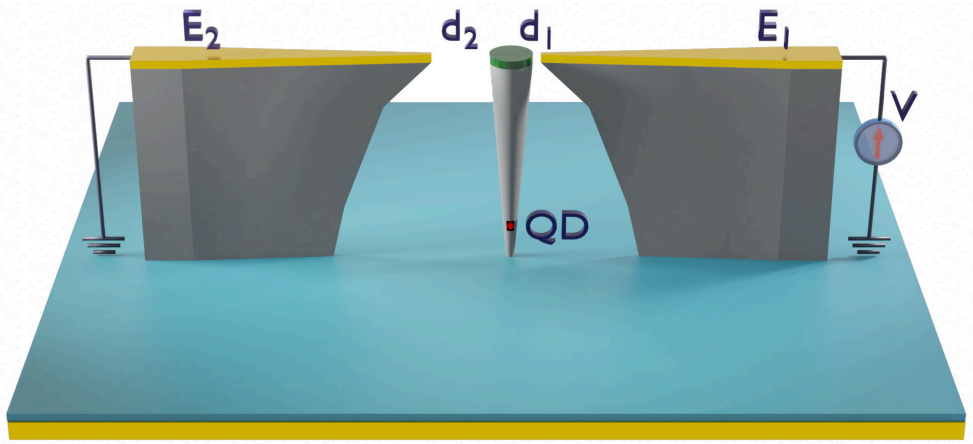

Fig. 4.4 Design of the electrostatically-tuned SPS. E_1 and E_2 represent the tuning electrodes with an Au coating indicated in yellow. The QD is housed near the base of the trumpet represented by the red triangle. The entire system sits on a SiO_2-Au mirror. The simulated design consists of a 20 μm-tall trumpet with a top diameter of 3.5 μm.

A potential difference of 50 V is applied across the two electrodes, which are tapered to a narrow tip as they approach the trumpet, in order to produce a non-uniform electric field.

Electrode E_2 is initially set to a separation $d_2 = d_1$. The separation between E_2 and the trumpet is then progressively increased such that $d_2 = d_1 + d_{shift}$. Plotting the component of electromagnetic force along the axis of the electrodes, measured at the top facet of the trumpet as a function of d_{shift} indicates a maximum around d_{shift} = 675 nm (Fig. 4.5).

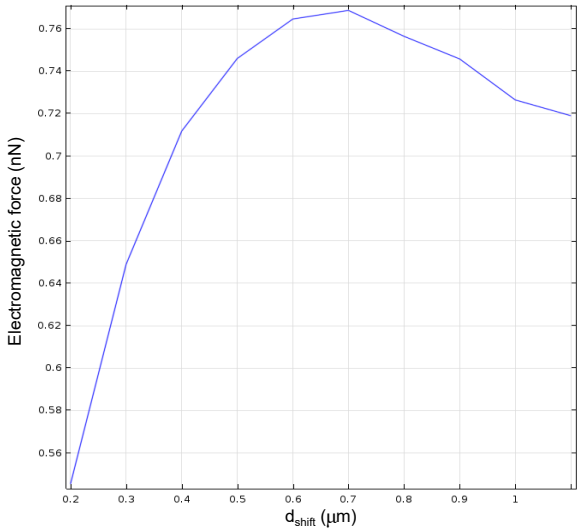

Fig. 4.5 The electrostatic force at the trumpet top facet as a function of separation offset $d_{shift} = d_2 - d_1$ between the electrodes and the trumpet. A potential difference of 50 V was applied across E_1 and E_2.

Next setting E_1 at d_1 = 300 nm and E_2 at d_2 = 975 nm, and applying a potential difference of 50 V, the displacement of the top facet of the trumpet is found to be 35 nm. A maximum QD emission energy shift of 2.6 meV is expected from the strain field produced by such a displacement. Since the electrostatic force scales as the square of the applied potential, for 100 V we anticipate a displacement of 140 nm which corresponds to 10.6 meV of energy shift.

4.2 Development of a new plasma-etching process at the PTA cleanroom

Plasma etching is one of the key steps of the fabrication process of photonic trumpets. Before the start of my PhD project, this etching was performed in a reactive ion etching (RIE) chamber located in the CEA-LETI industrial cleanroom. The process worked well but was slow, the etching of a 12 μm high trumpet typically took 3 hours. Furthermore, access to the cleanroom was not always possible for non-permanent researchers. Therefore we decided to develop a new recipe to etch trumpets on an ICP etching reactor located at the PTA academic cleanroom. After presenting the basics of plasma etching, we summarise here the main steps of the development of the process.

4.2.1 Basics of inductively coupled plasma etching

Inductively coupled plasma (ICP) etching is a form of dry RIE technique implementing a plasma. The successful etching of a material with a plasma involves three steps, which are, the transport of etchants to the surface of the material to be etched, the reaction between the etchants and the surface, and finally the removal of the volatile products created from the reaction [211].

An ICP etching chamber is schematised in Fig. 4.6. The chamber is maintained at low pressure, with the sample clamped on a temperature-controlled holder. The etchant gases are introduced into the chamber where a RF magnetic field across the ICP generator ionises them generating a plasma. The plasma is then accelerated towards the sample thanks to a RF bias applied through the CCP generator.

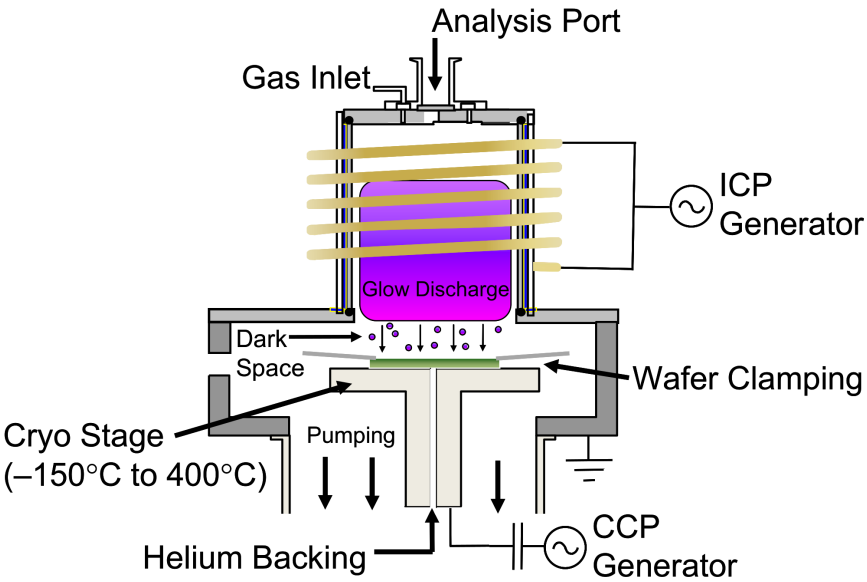

Fig. 4.6 Schematic diagram of an inductively coupled plasma etching chamber [212].

The etching process consists of three simultaneous processes as imaged in Fig. 4.7,

a. Ion sputtering, which primarily etches the material by physically removing it by bombardment. Additionally, sputtering can also help clean the sample surface from contaminants or local oxides, allowing better absorption of the gas etchant molecules. Ion sputtering is an anisotropic etching process (Fig. 4.7 (a)).

b. The ions consisting of reactive components can react with the surface material when it comes in direct contact with it, forming volatile compounds which escape the sample surface. Radicals of gas molecules can additionally move around on the sample surface before reacting, forming volatile compounds, and then being pumped away. The etching from surface chemical reaction tends to be isotropic (Fig. 4.7 (b)).

c. Radicals of the etchant gas molecules form a protective film on sidewalls, preventing chemical reactions on the lateral facets of features (Fig. 4.7 (c)).

In the following sections, we provide more details on some of the principal components of an ICP etching apparatus.

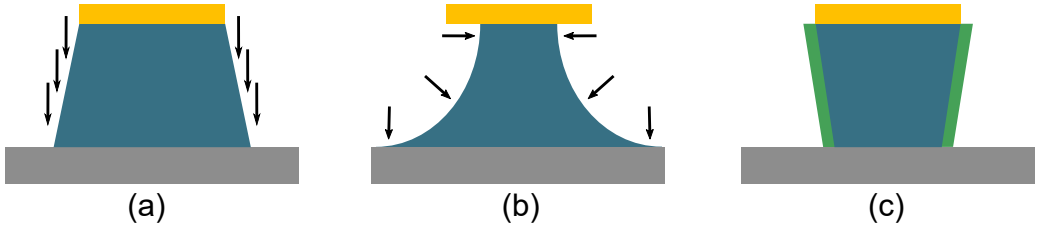

Fig. 4.7 Etch profiles associated to different types of etching. (a) Anisotropic physical etching. (b) Isotropic chemical etching. (c) Protective sidewall passivation.

4.2.1.a. Chamber pressure

The ICP chamber is maintained in a vacuum (pressure between 10^{-3} and 10^{-1} Torr), to increase the mean free path of electrons in the plasma. This allows the electrons to be accelerated more between collisions thus increasing the likelihood of ionisation. Lower pressure in the chamber reduces the gas density, and therefore also the number of collisions between ions and gas molecules, allowing the ions to move more directionally to achieve a higher anisotropy in etching. Conversely, higher chamber pressure increases the collision rate resulting in a more isotropic etch.

4.2.1.b. Sample clamping and temperature

The sample wafer is secured in place with a ring-like clamp pressing against the wafer edges. The temperature of the wafer is regulated with a flow of He on the back of the wafer. The sample tends to heat up as ions bombard its surface and a higher sample temperature increases the rates of chemical reactions on the surface. Therefore if the temperature of the wafer isn't maintained, the etch properties may vary in the course of the process.

4.2.1.c. Flow rate of reactive gasses

The reactive gases are introduced into the chamber through the gas inlet. The flow rates of the gases must be well calibrated for an optimal etch rate which depends on the rate of supply of reactive particles. However, for constant chamber pressure, the mere increase of gas flow rate produces a reduced reaction rate. With more gas being introduced the chamber would be pumped out faster in order to maintain a constant pressure, which would reduce the dwell time of the reactants. In this scenario, the plasma generation power must also be

boosted. Similarly, too low a flow of gas limits the amount of reactants present thus slowing down the etching as well.

4.2.1.d. Generation of plasma (ICP coil)

A plasma is generated inductively by applying a RF voltage across the magnetic coils. This voltage generates a RF current in the coil, which in turn results in a time-varying magnetic field $B(t)$ in the chamber oriented along the coil axis. According to Faraday's law, $B(t)$ induces an electric field $E(t)$ which rotates around the magnetic coil axis. Just after turning up the RF power, $E(t)$ provokes the ionisation of a few atoms/molecules. The fast-moving electrons enter into collisions with slower ions, leading to further ionisations and the formation of radicals [212]. This consistent cycling action increases the ionisation probability, enabling the generation of very high plasma density ($> 5 \times 10^{11}$ cm^{-3}) at low pressure [213].

In plasma etching, specific reactive gases (chosen depending on the material to be etched) are modified into etchant species in the plasma. These etchant species in the plasma comprise a mixture of ions, radicals, and electrons.

4.2.1.e. Generation of a self-biasing potential (CCP)

A separate RF power is applied to the sample stage, which draws ionised electrons out of the plasma. Electrons that hit the grounded walls of the ICP chamber are carried out of the chamber, but the ones that land on the sample plate remain trapped due to the DC isolation of the plate. Electrons accumulate on the sample stage leaving the edge of the plasma with a net positive charge due to ions, thus causing the emergence of a self-biasing potential. This potential accelerates ions towards the sample resulting in a directional and anisotropic etching.

4.2.1.f. Interferometric etch depth tracking

We track the progression of etching with the help of laser interferometry, in order to determine the etch-stop point. We first consider the simple case where the structure just consists of a top interface and a buried optical interface (difference in refractive index). The relative reflectance of the etching surface oscillates due to the interference between light reflected from the top and bottom facets. Concretely we can determine the etch endpoint by counting a specific number of oscillations which relates to the etched depth by, $\Delta d = N \times \lambda/2n$, where Δd is the thickness etched, N is the number of oscillations, λ is the laser wavelength, and n is the refractive index of the etched material. In practice, the sample to be etched may be a multi-layer heterostructure. In this case, the interferometric profile must be simulated using some kind of transfer matrix technique, prior to the etching.

4.2.2 Optimisation of the etching recipe

ICP etching is particularly efficient in producing high aspect ratio nanostructures, such as the photonic trumpets we intend to fabricate. However, in order to obtain the desired geometry of structures, it is necessary to strike a balance between the isotropic and anisotropic etching, as well as the sidewall passivation processes. Practically to achieve this balance, the control parameters at our disposal are, (i) the temperature of the sample, (ii) the RF power applied on the CCP generator, whereby the self-biasing potential, to accelerate the plasma to the sample, (iii) the RF power applied on the ICP generator, to control the plasma density (iv) the composition, and flow rate of the gases, and (v) the chamber pressure.

We set out to define a recipe to etch GaAs photonic trumpets, from an existing recipe, previously used in our team to fabricate cylindrical GaAs nanowires. The recipe we used is based on the following gases: silicon tetrachloride ($SiCl_4$), boron trichloride (BCl_3), and argon (Ar) gases. We performed a set of tests systematically exploring the reduced parameter set focusing on, the temperature of the sample, the RF power applied on the CCP generator, and the flow rate of the gases, in order to successfully etch photonic trumpets 15-20 μm tall, with a total angle at the base of 5-15°, and with smooth well-passivated sidewalls. We deposited a Ni hard mask on a matrix of discs whose diameters varied from 1-3 μm on 5 mm $\times$ 5 mm commercial GaAs wafer piece. We performed our etching tests by gluing one GaAs piece at a time, with a drop of Fomblin oil on a 4-inch SiO_2 carrier wafer, at the cleanroom of the PTA. The etching apparatus used was an Oxford Plasmalab 100 ICP etcher, with a plasma generation power of 50 W, and at a chamber pressure of 5 mTorr. After each run of etching, we imaged the sample observed at 45° in a SEM. In the following, we select some key results to highlight the impact the different parameters have on the etching outcome. We summarise the etching condition for each of these tests in Table 4.1 and illustrate an SEM image of each result in Fig. 4.8.

Table 4.1 ICP etching parameters of a few key tests that provide valuable insight on the impact each parameter has on the final outcome.

Fig. 4.8	Temperature (°C)	RF power (W)	Etch rate (nm/min)
(a)	50	120	141
(b)	134	120	226
(c)	50	90	316
(d)	50	82	336

Fig. 4.8 (a) illustrates the result of the recipe predefined to etch cylindrical nanowires. The etch is anisotropic with highly smooth sidewalls suggesting strong sidewall passivation. Such heavy sidewall passivation slows down the etching of the GaAs, resulting in a low etch rate. In this case, the etching has achieved an equilibrium between the chemical,

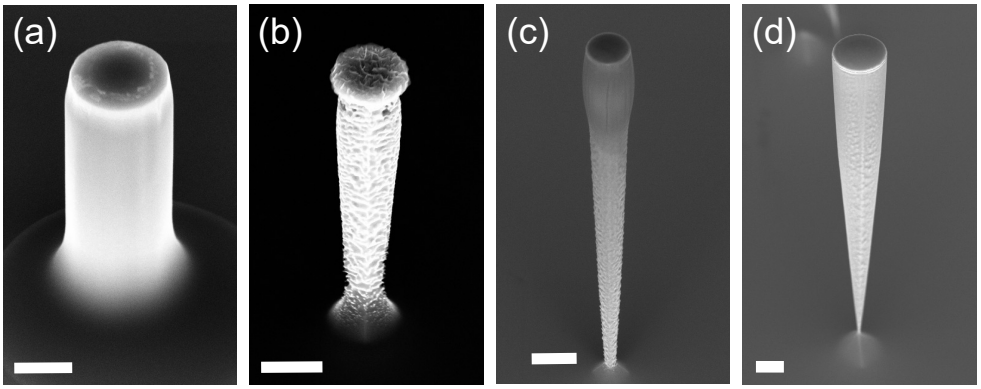

Fig. 4.8 A timeline of a few selected results leading to the definition of our recipe for ICP etching of GaAs trumpets. (a) The base recipe we picked served to etch cylindrical GaAs nanowires. This recipe was modified to etch trumpets. (b) Elevated sample temperature, T = 140°C. (c) Reduced RF power to 90 W. (d) Increased all gas flow rates. The scale bar on each image represents 1 μm.

physical, and sidewall passivation processes. We use this result as a reference to compare the following outcomes against.

Raising only the temperature of the sample in Fig. 4.8 (b), increases the rate of chemical etching by enhancing the surface chemical reactions, in comparison to Fig. 4.8 (a). This results in a more isotropic profile evidenced further by the deep undercuts beneath the Ni mask. The overall etch rate increases, however since there isn't as much sidewall passivation as in Fig. 4.8 (a), we end up with rough sidewalls.

By reducing the RF power on the CCP generator in Fig. 4.8 (c) we diminish the rate of physical etching, and in so doing also the sidewall passivation. In our process, we find that the SiO_2 carrier wafer contributes significantly to the sidewall passivation layer. Since the Cl-based etching gas mixture, like ours, has little impact on etching Si-based compounds, SiO_2 is predominantly etched through the physical pulverisation. By reducing the sidewall passivation rate, we achieve a higher etch rate and begin to produce the inverted taper of the trumpet.

Finally by decreasing RF power on the CCP generator further allows us to etch with a more prominent etch angle and gain an overall higher rate of etching. Fig. 4.8 (d) displays the product of our optimised etching recipe.

Overall we were able to reduce the etch duration with our recipe by a factor of three compared to the previous RIE recipes used in the team to fabricate trumpets, such as the ones in Ref. [78]. Our recipe is stable, producing consistent and reproducible results, however, the etch rate varied at times after the etcher was stopped for a long period due to maintenance. We adjusted for the reduction in etch rate by increasing the etch duration and/or by increasing the sample bias by a dozen volts.

4.3 Fabrication process of electrostatically-actuated photonic trumpets

Going from a finalised simulated design of a device to the realisation of a complete physical sample requires the following of an optimised fabrication process. In our case, the fabrication process consists of multiple steps summarised in Fig. 4.9. Some of the process steps have been briefly introduced in Chapter 3, and in subsequent sections, we will elaborate on each step in more detail.

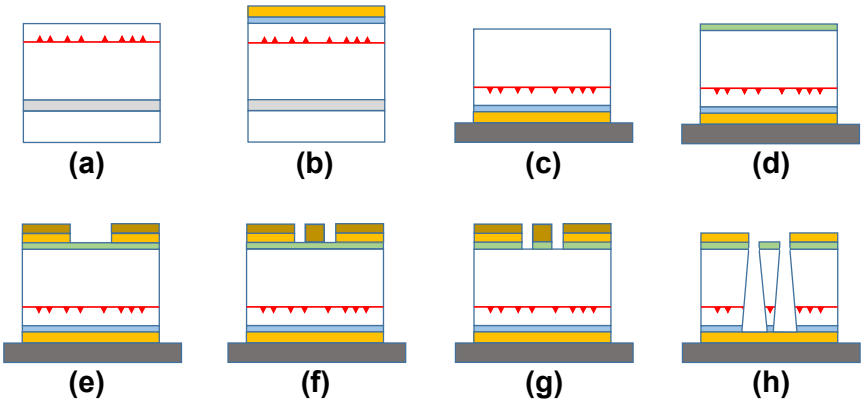

Fig. 4.9 Overview of the steps in our fabrication process. (a) MBE growth of a planar heterostructure. (b) Deposition of a SiO_2-Au mirror. (c) Flip-chip process. (d) Deposition of Si_3N_4 layer, which acts as an anti-reflection coating over the trumpets, and as electrical insulation between Au electrodes and GaAs. (e) EBL step 1 and deposition of Au to define the electrodes and alignment markers, and deposition of Ni hard mask. (f) EBL step 2 and deposition of Ni mask over trumpets (g) ICP etching of Si_3N_4. (h) ICP etching of GaAs and removal of Ni hard mask.

4.3.1 MBE growth

The MBE growth of the planar sample was carried out by Yann Genuist following the same technique described in Chapter 3. The recipe used, as well as the basic layer configuration, which is displayed in Fig. 4.10, were also unchanged. The layer thickness however differed from the nanocavity sample, and the growth parameters are given in Table 4.2.

4.3.2 Deposition of the hybrid SiO_2-Au bottom mirror

Once the growth is completed a SiO_2-Au hybrid mirror presenting a modal reflectivity of r = 0.9 for the fundamental HE_{11} guided mode is deposited. This deposition is carried out in two stages. First, a 9 nm layer of SiO_2 is deposited by electron-beam evaporation. The deposition is performed by Eric Delamadeleine (CEA-IRIG/SINAPS). This was followed by a 250 nm Au layer, deposited by electron-gun assisted metal evaporation. An additional

Table 4.2 Growth parameters used for planar heterostructures of the trumpet sample performed in an As-rich environment, where • indicates the shutter of respective cell is closed.

Growth step	Thickness (μm)	Temperature (°C)			
		Al	In	Ga	Substrate
GaAs buffer	0.5	•	•	952	630
$Al_{0.8}Ga_{0.2}As$	0.5	1088	•	852	630
GaAs body	18	•	•	952	630
InAs QDs		•	903	•	535
GaAs capping	0.95	•	•	920	630

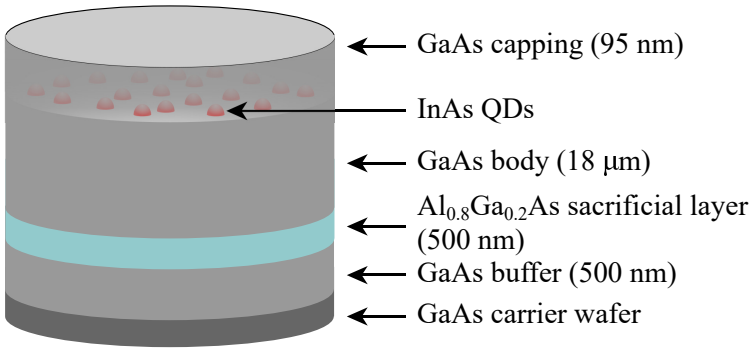

Fig. 4.10 Planar heterostructures used for the fabrication of trumpets.

Ti layer of 3 nm sandwiched between the SiO_2 and Au serves as an adherence layer for the Au. Having deposited the mirror, the sample is ready to be set right-side up by being transferred onto a new substrate using a flip-chip process, which will be elaborated in detail in the next section.

4.3.3 Flip-chip process

The flip-chip process consists of several steps as illustrated in Fig. 4.11.

4.3.3.a. Wafer bonding

In this step, the planar growth sample is reoriented "bottom-side up", by gluing the mirrored side to a new GaAs wafer substrate. The two wafers are indirectly bonded with SU-8 2005, which is an epoxy-based negative photoresist commonly used in nanofabrication processes to define high-resolution masks. The reasons that make an adhesive-based bonding of wafers desirable are that it allows sticking different material wafers together, it works irrespective of the topology of the surfaces to be glued, and it can be annealed at relatively low temperatures. It may be interesting to note that by using SU-8 2005 to bond our wafers we were able to make this step of the process more robust in comparison to the previously used M-Bond 610 epoxy glue technique. We were able to reduce the annealing time by about 6 times, and we successfully processed larger samples (12 mm × 12 mm over 5

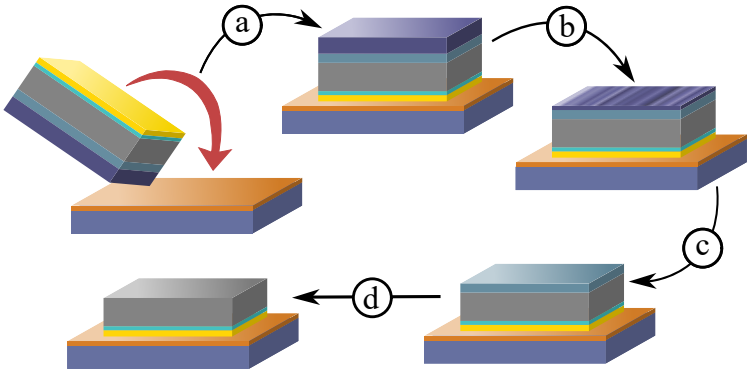

Fig. 4.11 Overview of the flip-chip process. (a) bonding planar sample mirror-side down on new GaAs substrate; (b) mechanical polishing to remove growth carrier wafer; (c) chemical etching to remove remainder of growth wafer exposing AlGaAs sacrificial layer; (d) removal of AlGaAs sacrificial layer using HF.

mm $\times$ 5 mm in the past), reproducibly without generating air bubbles in the glue during annealing a 100% of the times.

Preparation of bonding surfaces. Even though indirect bonding is insensitive to surface irregularities, it is always better to start with as clean bonding surfaces as possible. To do so, we first cleave the epitaxial growth sample into 5-6 mm square pieces. We wash the cleaved sample pieces as well the new carrier GaAs substrate (also cleaved into 8-10 mm squares) in a bath of acetone, followed by ethanol, and then IPA. While soaking in the different solvents we also expose the substrates to ultra-sound, which aids in better cleaning of surface impurities. Once washed we dry the wafers under a clean jet of nitrogen gas. We then place the wafers on a hotplate at 100°C for about a minute to ensure complete evaporation of all traces of solvent from the surface.

Attaching sample to substrate. Once the pieces of sample and host substrates are cleaned, we secure the host substrate on a spin coater and apply a small drop of SU-8 2005 in its centre. The amount of SU-8 2005 should be enough to coat the substrate forming a coat of about 5 μm thick. The substrate is then spun at 4000rpm, with an acceleration of 2000rpm for 60 sec to spread the SU-8 2005 evenly across the surface. We then place the coated substrate on a hotplate at 90°C for about 20 min to evaporate some of the solvent in the SU-8 2005. After the 20 min have elapsed we place the sample piece, mirrored side facing down, on the substrate still sitting on the hotplate. We gently press the sample down a bit to ensure a secure bond and remove the set quickly from the hotplate. It must be noted that if the substrate is withdrawn from the hotplate before placing the sample on it, the SU-8 2005 will no longer adhere to the sample and there will be no bond.

Curing of the glue with heat. The newly bonded sample is put through a heat treatment in order to cure the SU-8 2005 epoxy and to strengthen the bonded interface. We place the sample on a hotplate and place a set of metal dice (generating $\approx$ 160 kN/m^2 of pressure) on

the sample. We cure the epoxy for about 25 min at 100°C then we perform a post-cure bake at 210°C for about 30 min.

4.3.3.b. Removal of growth substrate

We remove the growth substrate by a combination of physical and chemical etching. We begin by attaching the sample to a metallic die. We ensure that the die used has a planar face with a maximum height variation within 20 μm. We use a transparent wax that is soluble in acetone to glue the sample on the die. We heat the die on a hotplate at 120°C, we then place a small bit of the wax at the centre of the die face. Once the wax has melted we place the sample on it and press it gently to ensure good adherence. Thereafter we remove the die and let it cool after which we check the planarity of the affixed sample (height variation should be within 20 μm).

The quantity of wax must be selected carefully so as to ensure a uniform spread under the entire sample but also avoid an excessive spill out from the sides. If there is an excess of wax on the sides of the sample, we remove it. Similarly, if there is any trace of wax on the sample we clean it carefully with some acetone.

Now that we have glued the sample on the metal die, we are ready to begin the mechanical grinding of the growth wafer, using abrasive discs. In this part, we make use of the thickness of the growth wafer we measured before the growth (Sec. 3.2.1). We grind the wafer in stages using abrasion discs of varying coarseness under an extraction hood and in the presence of a steady stream of water. These precautions are taken to minimise the amount of harmful ground GaAs debris that is released into the room.

We remove the first 200 μm with a p800 disc, the following 100 μm with a p1200, and the remainder with a p2400 disc. We finish the abrasion $\sim$ 30-35 μm before the AlGaAs sacrificial layer. We stop early to prevent physical surface damage from reaching close to the QD layer. After we have finished the polishing step we reheat the die on a hotplate at 120°C to melt the wax and detach the sample.

To remove all the GaAs (30-35 μm) from the growth substrate we implement chemical etching. To achieve a clean removal of GaAs we need a substance that selectively etches GaAs but has relatively little impact over AlGaAs. To achieve this kind of selectivity we employ a solution of citric acid ($C_6H_8O_7$) with H_2O_2. H_2O_2 oxidises the GaAs and $C_6H_8O_7$ dissolves the oxide at a desirable etch rate of $\approx$1.5μm/min. When the solution comes in contact with AlGaAs, aluminium oxide is formed which doesn't dissolve in $C_6H_8O_7$, thus the etching is practically stopped.

For the chemical etching step, we mount the sample on one extremity of a microscope glass slide with the help of the transparent acetone-soluble wax. We place the glass slide on a hotplate at 80°C and melt a small amount of wax placed near one extremity of the slide. Once the wax has melted we place the sample on it and gently press it down to ensure a flat

adherence. We take enough wax so that upon pressing the sample down there is some that spurts out the sides and covers the edges of the carrier wafer. This wax cover will protect the GaAs in the host wafer from being chemically etched. Any traces of wax on the sample must be carefully cleaned with acetone, otherwise they will hamper a clean removal of all the GaAs remaining from the growth carrier wafer.

After attaching the sample on a glass slide, we prepare the chemical solution by dissolving 40 g of $C_6H_8O_7$ into 40 ml of deionised water. We stir the mix on a hotplate at 35°C until all traces of cloudiness are gone and we are left with a transparent homogenised solution. To this we add 16 ml of H_2O_2 (30% in water) and stir to homogenise for about 5 min. We then plunge the sample into the solution at 35°C with continuous stirring until the shiny silver AlGaAs is exposed across the entire sample surface. At this point, we remove the sample from the solution and wash it under a jet of deionised water, before detaching the sample from the slide by heating it to 80°C and melting the wax. We clean away any excess wax under the sample with acetone. Alternatively, the entire detaching process can be done by plunging the glass slide with the sample in a bath of acetone, however the dissolution of wax takes a much longer time.

4.3.3.c. Chemical etching of AlGaAs sacrificial layer

The final step of the flip-chip process consists of chemically etching the AlGaAs sacrificial layer. This step should be performed, as soon as possible, after the etching of the growth substrate as possible. The interaction between the sacrificial layer and air must be minimised to prevent the oxidisation of AlGaAs.

The sacrificial layer is etched using 50% hydrofluoric acid (HF), due to its good selectivity for AlGaAs over GaAs. The sample is cleaned, in subsequent baths of acetone, ethanol, and IPA to remove any dust or wax residue, then dried under a jet of nitrogen gas. Following the cleaning, the sample is soaked in a 50% HF bath for about 1-2 min. A lower acid concentration may be used to slow down the rate of etching. Care must be taken not to let the sample soak too long because even though GaAs is practically unaffected by HF, the slim layer of SiO_2 is. The HF could therefore seep in, dissolving the SiO_2 and given enough time, could completely detach the sample from the carrier substrate.

Once the sacrificial layer is fully etched, the sample is removed and washed in deionised water, followed by a subsequent wash in acetone, ethanol, and IPA baths, before finally being dried under a jet of nitrogen gas. With that the flip-chip process is complete and the sample is ready to be processed.

4.3.4 Deposition of a Si_3N_4 anti-reflection coating

If the nanowire SPS were to be produced from the sample as is, the high contrast in refractive index between GaAs (n = 3.42) and air, would limit the extraction efficiency of photons

due to reflections at the interface. To reduce this effect an anti-reflection coating of Si_3N_4 ($n = 2.01$), that has a thickness of $\lambda/4n$ which for a QD emitting at $\lambda = 920$ nm leads to a thickness of 115 nm is added on the sample. This anti-reflection coating was deposited by Christelle Gomez at the PTA, using the physical vapour deposition (PVD) technique of sputtering.

4.3.5 Design of mask for electron-beam lithography

To be able to fabricate electrostatically-tuned photonic trumpets from a planar heterostructure using a top-down approach, we design a mask that consists of the entire sample design layout. The mask serves as a guide defining which areas must be exposed to electron beam lithography. The mask pattern is transferred onto the sample as a stencil pattern of unexposed photoresist, which covers the desired structures to be realised by etching. In this section, we address the process of designing the mask layout.

The basic layout of the sample consists of the motif illustrated in Fig. 4.12. A set of two rows of sixteen equiradial discs define the top facets of trumpets. Lined on either side of each trumpet are a set of two gradually tapering electrodes. The tips of the top row of electrodes are separated by 300 nm while the tips of the bottom row are separated by 975 nm from the edge of the discs. Each row of electrodes physically connect to a common bar which leads to one of two large 180 μm $\times$225 μm rectangles which will serve as contacting pads to apply a bias. Each electrode is composed of five separate sections, as illustrated in the close up in Fig. 4.12. Since the electrodes have strongly varying aspect ratio, it is divided into separate sections, in order to define a different dose to each during electron beam lithography. This ensures a more accurate transfer of the design.

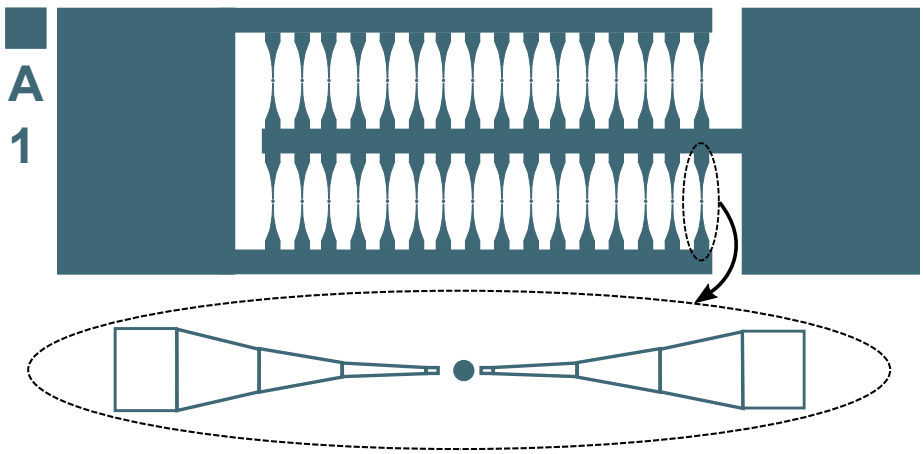

Fig. 4.12 Basic lithography mask motif for electrostatically-actuated trumpets. This motif is replicated over a 22 by 6 matrix to fill a 6 $\times$ 5.5 mm sample. (Close up) Electrode geometry, divided into five sections in order to define a dedicated dose to each.

The complete mask design consists of a matrix of replicas of the basic layout. The sample processed in the current work is 6 mm $\times$5.5 mm and comprises a 22 by 6 matrix. The basic layout in each element of the matrix is indexed with a letter of the alphabet enumerating its column followed by the number of its row. The trumpet diameter in each basic layout replica has a different diameter, varying in intervals of 20 nm, from 1 μm to 3.5 μm.

As illustrated in Fig. 4.13, the mask design also comprises six 200 μm $\times$200 μm markers in the shape of a '+', three on either side of the sample which will help align the sample precisely during the second lithography step, to match the coordinates with the first lithography step. The baseline is a 5.4 mm $\times$ 20 μm feature which is visible to the naked eye, meant to help orient the sample in the same way while mounting it into the lithography apparatus across both steps. Finally, the three right angles delineate the 500 μm $\times$500 μm writing field of the e-beam. Before the second lithography step, these markers will aid in calibrating the writing field such that it matches the parameter of the first stage. While designing a mask of such a large area, the writing field edges must not cut through crucial features such as trumpets and electrodes, to prevent damaging them due to eventual mismatch in alignment during stitching of individual writing fields. These points will be addressed in more detail in Sec. 4.3.6.

Fig. 4.13 Lithography mask design for e-actuated trumpets.

I developed the overall lithography mask in two stages. First I wrote a semi-automated programme on Matlab to determine the coordinates of all the points required to define every shape on the mask. I would need to input the basic layout parameters, such as the range of trumpet diameters, the diameter variation interval, the spacing between features on the

basic motif, and the total sample size, and the programme would fit the basic motif as many times as possible to optimally cover the complete sample area. Using the programme I could extract the coordinate data for each shape across the entire sample and export them into .tco data files.

In the second stage of the design, I used a mask editing software called L-Edit from Tanner Tools EDA to draw each unique shape, letter and number on individual cells. Then importing the coordinate data exported from the Matlab programme, I compiled instances of each shape to build the complete mask design on a new cell. Since the exposure of the mask will be done in two stages, I separated the trumpet, and numbering index character features in one layer, while putting all other features in a different layer. Separate layers will simplify selectively exposing some features during the first lithography step. Finally, I assigned a unique GDSII data type to each different category of shapes, which allows to associate individual doses to each type during lithography. I then exported the design in .gds format, which is readable by the lithography apparatus.

4.3.6 Pattern transfer by electron beam lithography

4.3.6.a. Description of the lithography system

Lithography serves as one of the most widespread techniques used for top-down nanofabrication. In particular electron-beam lithography (EBL) is a method of patterning that consists of exposing a photoresist by a focused beam of electrons, which is generated by thermal field emission from a filament. The electron stream passes through a series of apertures, electromagnetic lenses, electrodes, and coils that shape and direct the electrons into a focused beam onto the sample. The beam is electrostatically deflected to scan the surface of the sample to print the pattern on it by modifying its physical properties. Fig. 4.14 illustrates the various stages of beam manipulation used to obtain a precise electron beam for high-resolution patterning.

The EBL system we used for patterning at the PTA was the JEOL 6300 FS. It has a typical 20 nm spot size, with a minimum spot size of 4 nm for the highest accuracy, and presents well-calibrated writing fields. Electric and magnetic fields are used to deflect the beam to write relatively small surfaces. To avoid pronounced astigmatism in the beam spot large patterns are divided into smaller square fields of either 62.5 μm or 500 μm sides. The smaller fields are written separately and are then stitched together to form the complete pattern. A laser-interferometer ensures that the stage moves required to stitch individual fields are aligned precisely (stitching accuracy about 20 nm). Finally, to have a higher writing speed we use a beam current of 5 nA.

Electrons undergo both small angle (forward-) and large angle (back-) scattering in the resist and substrate. Collisions between primary electrons and atoms lead to several secondary effects (Fig. 4.15). These effects result in exposing areas larger than the beam

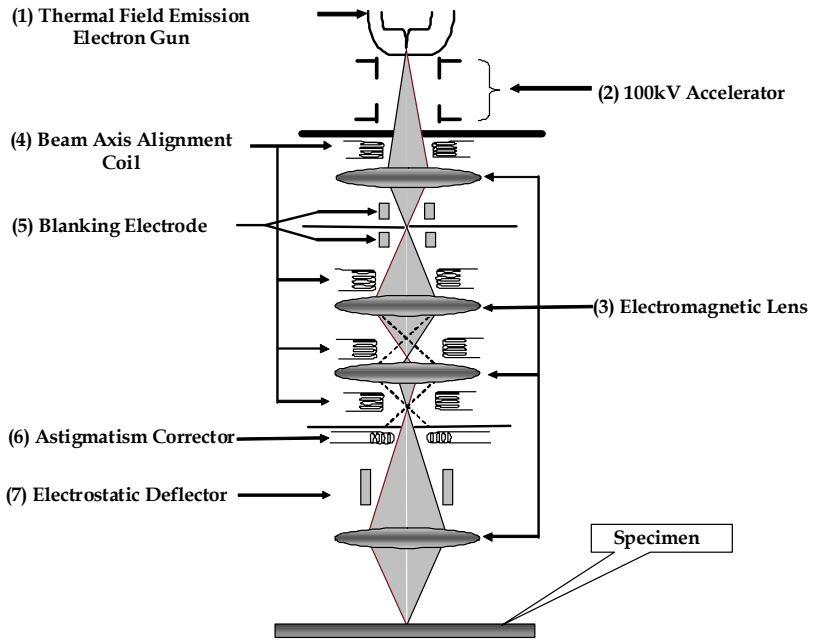

Fig. 4.14 Schematic representation of the electron optical column in an EBL system [214].

spot size which may produce zones of overlapping exposures, known as the *"proximity effect"*, leading to over-exposed sections. To achieve adequate exposure, the dose (number of charges per surface unit) is adjusted on every point depending on its position in the pattern.

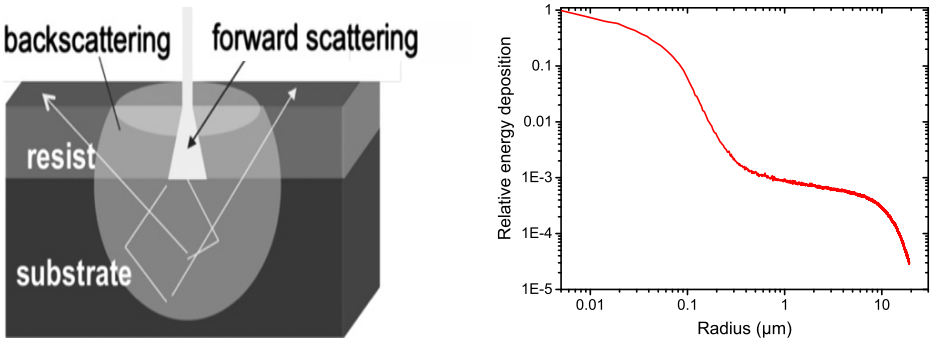

Fig. 4.15 (Left) Short and long range interactions of electrons [215]. (Right) Relative energy deposition point spread function for 100 kV electrons on GaAs [216].

The dose is a weight coefficient of exposure time that may be uniform for the entire pattern or may be position-dependent. It is evaluated in relation to the sensitivity of the resist used (required density of electrons for optimal exposure), as well as how much overlap a given point has from the proximity effect due to neighbouring points. The dose is reduced at a given spot if it will experience a proximity effect from many neighbouring points. The dose also depends on the geometry of individual elements in the pattern. The dose can be generally computed from,

$$D = \frac{I}{F_{exp} \times Grid^2} \tag{4.4}$$

where D = Dose, I = E-beam current, F_{exp} = Exposure frequency (number of pixels exposed per second), $Grid$ = Grid spacing (spacing between neighbouring exposure points).

4.3.6.b. The first lithography step

Before the sample can be exposed under EBL, it must first be coated with a photo-resist. The resist used was 4% poly(methyl methacrylate) (PMMA) which was spin-coated on the sample at 1500 rpm for 50 sec with an acceleration of 800 rpm/s, to form a ∼500 nm-thick layer. The sample was baked on a hot plate with the temperature ramped up from 90°C to 140°C over 5 min, then maintained at 140°C for 10 min. EBL was then performed on the sample with exposure doses in the range of 1000-3000 μC/cm^2. The exact dose varied based on the size of the sample feature that was being exposed. The doses were optimised by a few tests. Only the following regions are exposed in this step: the electrode surfaces, the electrical contact pads, and the markings that will serve as alignment guides for the second step of EBL (see Sec. 4.3.5).

After the PMMA was exposed under the electron beam it was developed in a 1:3 methyl isobutyl ketone (MIBK) and IPA solution for about 30 sec. The solution dissolves the PMMA that was exposed by the electron beam leaving behind a stencil of the desired pattern. The sample was submerged in IPA for about 30 sec to stop the development before being dried under a jet of nitrogen gas.

A layer of 150 nm Au, is deposited by electron-gun assisted metal evaporation on the sample. An additional Ti layer of 3 nm sandwiched between the Si_3N_4 and Au serves as an adherence layer for the Au. A layer of Ni with a thickness of 180 nm is deposited by the same method onto the Au layer. The Ni will act as a hard mask, protecting the material it covers, during the plasma etching step that will enable to define the nanostructures. The unexposed resin is then lifted off by submerging it in an acetone bath, removing also the excess metal, thus leaving only the electrodes, contact pads, and alignment markings coated in Au and covered under a Ni hard mask.

4.3.6.c. The second lithography step

We repeat the process of the first lithography step with some modifications. The PMMA is spin-coated at 4000 rpm for 60 sec with an acceleration of 2000 rpm/s to make a layer ∼270 nm-thick layer and baked. The sample is mounted in the EBL system in the same orientation as the first lithography stage. The e-beam and writing field coordinates are then programmed to precisely match the field positions of the first exposure step, with the help of the alignment markings defined around the sample. This alignment is done by noting the exact coordinates of the alignment features during the first lithography stage, and then ensuring that the features are again positioned at the same coordinates for the second lithography stage. Having ensured the optimal positioning of patterns, only the

discs that will form the trumpets and the alphanumeric pattern indices are exposed. After the development of the resist, a hard mask of Ni of a thickness of 180 nm is deposited. The lift-off of the unexposed resist with the excess Ni then leaves the sample ready for the plasma etching step.

4.3.7 ICP etching of the Si_3N_4 layer

We etched the Si_3N_4 anti-reflection coating first, with the sample temperature T = 30°C, and a chamber pressure of 5 mTorr. The gases used and their respective flow rates were the following: Ar - 40 Sccm, CH_2F_2 - 25 Sccm, and SF_6 - 5 Sccm. The plasma was generated with a power of 250 W on the ICP generator, and it was accelerated to the sample with a power of 50 W on the CCP generator. The etching was performed at a rate of 100 nm/min, and the etch-stop point was identified through interferometric etch depth tracking.

4.3.8 Deep ICP etching of the GaAs layer

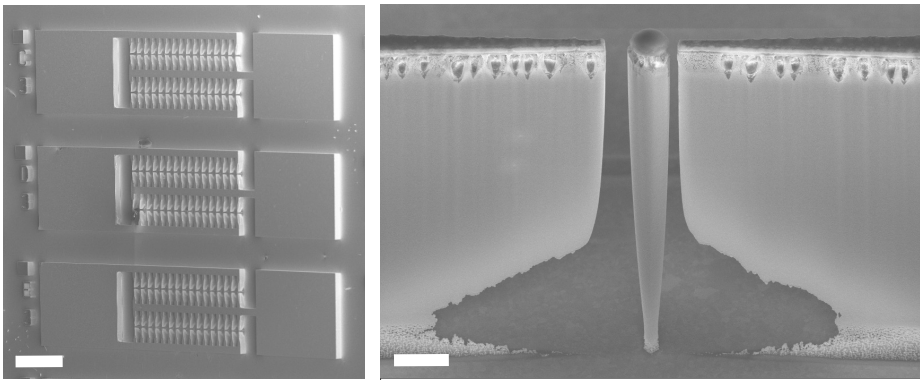

Fig. 4.16 SEM images of the complete electrostatically-actuated trumpet sample, embedding QDs expected to emit in the 880 nm to 930 nm range. The scale bars on the image on the left (right) represents 100 μm (2 μm).

The GaAs was etched with the optimised recipe we developed (see Sec. 4.2.2), at a rate of 180 nm/min producing trumpets $\sim$16 μm tall with an angle at the base of 8°. The last fabrication step before we can optically test our devices was to chemically etch the Ni hard mask by submerging the sample in a 10% HNO_3 solution for 90-120 s. The sample was washed with deionised water to stop the chemical reaction, then dried under a clean gaseous N_2 jet. The outcome of the complete electrostatically-actuated trumpet sample with embedded InAs QDs is pictured in Fig. 4.16. Thanks to our recipe, we were successful at cleanly defining the trumpets and the integrated electrodes, with a minimum separation of only $\sim$ 300 nm between the two. Although we see some small defects close to the GaAs-Si_3N_4 interface, most likely in the passivation layer, overall the Au layer remained well adhered to the Si_3N_4 layer and the device exhibits smooth and pristine sidewalls.

4.4 Preliminary device characterisations

Having successfully fabricated a complete sample, we performed some preliminary characterisation measurements, which will be presented in this section. An in-depth device characterisation and testing is currently in progress and is a major part of the PhD project of Matteo Finazzer. The early results discussed here consist of micro-PL spectra of the device, the mechanical response of a trumpet to a static potential bias across the electrodes, and the first signature of a spectral shift due to the electrostatic bending.

4.4.1 Micro-photoluminescence spectroscopy

We perform a micro-PL experiment on the trumpets to ensure we have the desired emission spectra expected from QDs. The growth parameters were set to generate QDs emitting at ~ 920 nm. The experimental setup used is the same as the one described in Sec. 3.3. The trumpets were excited using a continuous laser of wavelength $\lambda = 820$ nm, at a temperature T = 5 K. A lot of the trumpets with a top facet diameter between 1 μm and 1.66 μm did not survive. Their bases were too thin and snapped during the processing. Trumpets with a top facet diameter between 2.18 μm and 3.5 μm, on the other hand, are too wide at the base, thus leading to an emission spectrum resembling that of bulk material. Trumpets with a top facet diameter between 1.68 μm and 2.16 μm exhibit spectra with 10-20 isolated peaks, ranging between 880 nm to 930 nm, in each structure. Fig. 4.17 (a) displays the emission spectrum (integrated signal normalised to one second) of a trumpet with a top diameter of 1.84 μm pumped with a power of 2 μW. It appears to embed around twenty QDs.

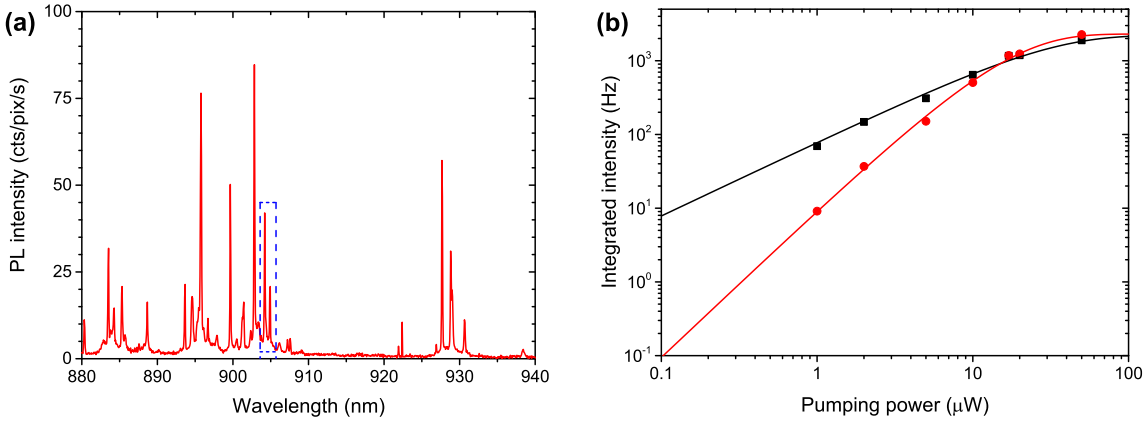

Fig. 4.17 (a) Micro-PL spectrum for QDs in a trumpet with a nominal top diameter of 1.84 μm pumped with a power of 2 μW at a temperature T = 5 K. (b) Plot of integrated intensity as a function of pumping power for spectral peaks at 904 nm (black) and 905 nm (red). The data are fitted with the function in Eqn. 3.18 for the exciton (black) and the function in Eqn. 3.19 for the biexciton (red).

We focus in particular on the peaks at 904 nm and 905 nm enclosed in the dotted rectangle. We plot the integrated intensities of these peaks as a function of pumping power for measurements made at a few different excitation powers, as seen in Fig. 4.17 (b). The plots can be fitted with the functions in Eqns. 3.18 and 3.19, which assume Poissonian statistics for the injected charges. From these fits it appears that the peak at 904 nm exhibiting a linear dependence to pumping power, may correspond to a neutral exciton, while the peak at 905 nm, with a quadratic dependence, belongs to its biexciton.

4.4.2 Electrostatic deflection of trumpets

Having ensured that our devices contain optically active QDs, we verify whether we can deflect the trumpets by applying a potential bias across the onboard electrodes. The experiment was carried out by Fabrice Donatini, and Matteo Finazzer, within the modified cathodoluminescence setup described in Sec. 4.1. The sample was placed in the SEM at a temperature of 4 K, and a bias potential was applied across the electrodes in the configuration pictured in Fig. 4.4, by connecting the contact pads with two nanomanipulators (Fig. 4.18 (a)). The potential difference is varied between -15 V to +18 V, and for each voltage applied a SEM image of the relative position between the trumpet and the electrodes is captured.

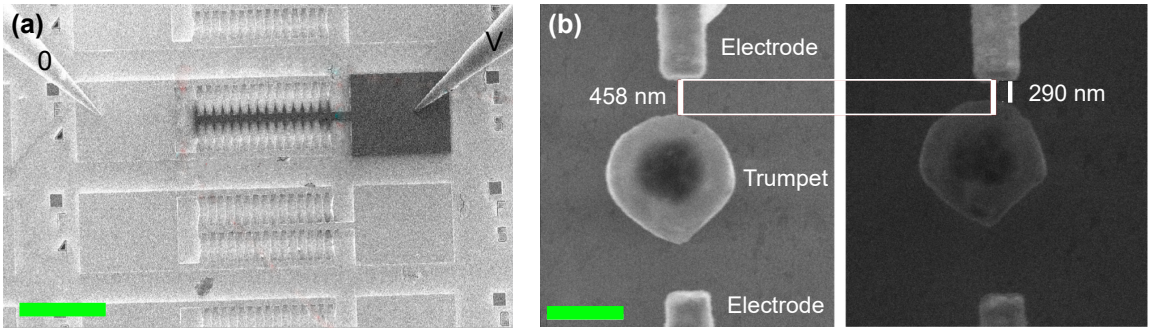

Fig. 4.18 SEM images of trumpet-top displacement due to applied potential bias. (a) A potential difference is generated by connecting two nanomanipulators to the contact pads. The pad on the left is grounded, while the pad on the right has a positive voltage. (b) Separation between the electrode tip and the trumpet edge before applying a voltage (left), and after a voltage is applied (right). A displacement of 168 nm was produced by applying V = 12 V. Scale bars: (a) 200 μm, (b) 1 μm.

The SEM image in Fig. 4.18 (a) is obtained with the detection of secondary electrons scattered from the sample. The zone electrically connected to the pad on which a positive voltage is applied becomes positively charged thus reducing the number of secondary electrons generated, which in turn results in a darkened area in the SEM image. As pictured in Fig. 4.18 (b) the trumpet is deflected by $\sim$168 nm with V = 12 V. The displacement is determined by measuring the separation between the trumpet edge and the electrode tip,

using the measuring tool provided in the SEM control software, which is accurate within a few tens of nm.

Finally, Fig. 4.19 represents a plot of trumpet and electrode separation as a function of applied potential difference. The measurements were performed on a trumpet having a top facet diameter of 1.56 μm.

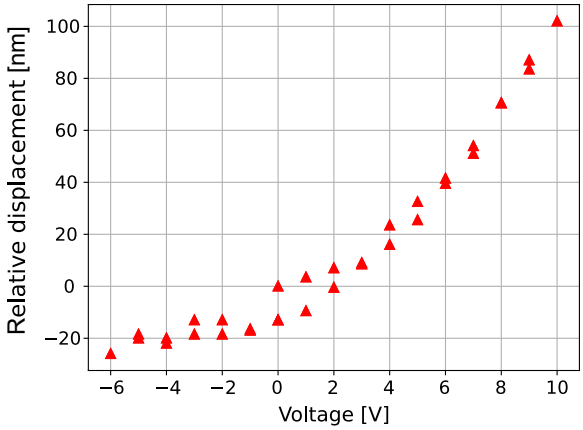

Fig. 4.19 Relative displacement of the top facet of a trumpet with respect to the tip of the electrode as a function of applied voltage across the electrodes. The measurements were performed on a trumpet having a top diameter of 1.56 μm.

While a negative bias has little to no impact on the relative position of the trumpet and electrode, the amplitude of deflection for a positive bias is much greater than originally simulated. The reason for the same might be in part due to the simultaneous observation under an electron beam that imparts charges on the structure. Besides, the structure may have been unintentionally negatively doped during fabrication which amplifies the electrostatic forces in the presence of a positive bias. More in-depth measurements and analyses are in progress, but from these preliminary results, we can realistically expect to demonstrate large-scale strain-tuning of QD emission energy.

4.4.3 Shifting QD emission wavelength with electrostatic actuation

Fig. 4.20 illustrates a first demonstration of tuning of the emission wavelength by electrostatic actuation of a trumpet. The measurement was carried out in the modified cathodoluminescence setup depicted in Fig 4.2, at T = 4 K, on a trumpet with a top diameter of 1.58 μm. The trumpet was driven under continuous excitation from a diode laser of wavelength λ = 830 nm. Micro-PL spectra were recorded for different applied voltages across the electrodes. The electron beam of the SEM was turned off while recording the PL signal. Fig. 4.20 tracks the emission of one excitonic line which exhibits a spectral shift of $\Delta\lambda \approx$ 0.15 nm for an applied voltage V = 10 V.

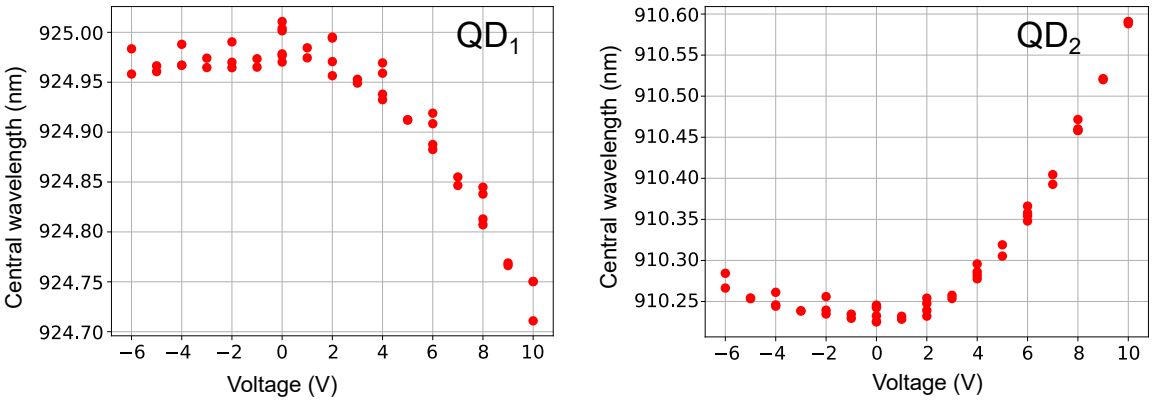

Fig. 4.20 Central wavelength of two excitonic emission line from two distinct QDs (QD_1 and QD_2) in a trumpet with a top diameter of 1.58 μm. The central wavelengths of QD_1 (left) and QD_2 (right) are measured as a function of different applied voltages across the actuation electrodes. The wavelength of QD_1 (QD_2) on the left (right) undergoes a blue-shift (red-shift) indicating that the QD is under compressive (tensile) stress. The two QDs are therefore of either sides of the neutral stress axis.

4.5 Conclusion

In this chapter, we propose a tunable single-photon source based on a QD inserted in a photonic trumpet that can be bent thanks to electrodes. Bending the trumpet generates a stress field at the QD level, which changes its bandgap and thus the colour of the emitted photons. We introduce two integrated electrodes on either sides of a trumpet and apply a potential difference across the electrodes. The electrodes generate an inhomogeneous electric field, and the top part of the trumpet is attracted towards the closest electrode. We designed a first device on COMSOL Multiphysics and our simulations showed that an asymmetric separation of electrodes (d_1 = 300 nm and d_2 = 975 nm) produced optimal shifts of a 20 μm-tall trumpet with a 3.5 μm-diameter top facet. We predicted a deflection of 35 nm, leading to a shift in emission energy of 1.5 meV, with an applied voltage of 50 V.

We then presented the entire fabrication process in detail. Our current flip-chip method using the photoresist SU-8 2005 instead of a previously used epoxy-based glue to bond the samples, allowed us to reduce glue-curing times by a factor of 6 (from over 6 hours to around 1 hour), and we are now able to process samples with 4-times larger surface area (from 5 mm $\times$ 5 mm to 10 mm $\times$ 10 mm). We also developed an ICP etching recipe to fabricate trumpets that allowed us not only to consistently define 20 μm trumpets with a base angle of over 10° but also the complete sample of trumpets with integrated electrostatic tuning electrodes. With this recipe we were able to achieve reproducible results by reducing processing times 3-folds (from over 3 hours to around 1 hour) compared to previously employed RIE techniques.

Finally, preliminary optical characterisation of the device show isolated peaks in the 880-940 nm wavelength range on the micro-PL spectra, corresponding to QD emission.

We are able to identify both exciton and biexciton transitions. Additionally, the trumpets were successfully deflected by applying a potential bias across the electrodes. We achieved around 170 nm of deflection with a bias of 12 V. As of now the electrostatic-deflection performance appears to vastly surpass our initial expectation, likely due to excess charges introduces either by the SEM or arising from the sample. It is too early to be able to conclude on what phenomenon is responsible for this behaviour and more rigorous measurements for a complete study of the sample are currently ongoing. We have also presented a first example of wavelength tuning

The few results presented here strongly suggest that our system is a promising one to achieve broad range QD emission tuning in an integrated device. This approach could be used to independently tune multiple SPS hosted on the same chip. Furthermore, beyond single QD devices, the strong stress gradients generated by a bending trumpet allows bringing two QDs, located on opposite sides of the neutral stress line, into resonance. Multiple electrodes would allow controlling the generated stress gradient more precisely enabling the resonance between three or more QDs at a time. Therefore this tuning strategy could be employed to explore collective effects, such as superradiance.

Conclusion and Perspectives

This work has aimed to control the spectral properties of photons that are emitted by a semiconductor QD embedded in a photonic nanowire antenna. In this respect, we have presented, in this thesis, three major studies concerning: (i) the understanding and control of QD emission decoherence due to interaction between the QD and the vibration modes of the nanowire; (ii) the development and characterisation of a nanowire nanocavity offering broadband SE acceleration; (iii) a strategy to tune the emission wavelength of a QD embedded in a nanowire antenna, which led to the fabrication of an integrated wavelength-tunable nanowire photon source and the presentation of a proof-of-principle experiment demonstrating electrostatically-induced wavelength tuning.

The first study evidenced the impact of mechanical vibration modes of nanowire antennas on the emission linewidth of an embedded QD. We considered two popular antenna designs: the needle-like top taper, widely used in top-down [77], and bottom-up [50, 83, 84] processes, and the inverted cone (trumpet) top taper [78]. Analysing the collective impact of only the longitudinal and flexural modes among the first 200 vibration modes supported by each structure we find the emission linewidth of an InAs QD being broadened as much as ten times over the radiative limit ($\sim 0.7\mu$eV). However, we noted that the impact of the thermally induced vibrations decreases with increasing mode frequency. We also remark that the QD emission broadening is strongly position-dependent, with QDs closer to the nanowire periphery being affected more than those at the wire axis. Nevertheless, we observed that the radiatively limited linewidth could be restored by quenching the influence of the first seven low-frequency vibration modes, from our analysis. To achieve this practically, we proposed nanomechanically engineered designs that suppress the impact of these low-frequency modes. The solutions we present set out to either: (i) make the nanowire less susceptible to vibrations by making it more rigid; (ii) reduce the coupling strength between the emitter and the vibration modes, for instance by positioning the QD on a stress node; (iii) shift all mechanical resonances to very large (GHz) values.

The second major result of this project was the development and characterisation of a nanowire nanocavity that offers broadband SE acceleration. The device was designed in collaboration with the team of Niels Gregersen (at DTU Fotonik, Copenhagen) using an open-Fourier modal method, predicting a Purcell factor of 6.3 that is maintained over a 30 nm bandwidth. In addition, the fraction of spontaneous emission funnelled into the

cavity mode reaches $\beta = 0.98$ at resonance, and exceeds $\beta = 0.95$ over a 100 nm spectral range. Close to optimal collection efficiency is maintained over an equivalent bandwidth and reaches a predicted value of 0.54 at resonance for a first lens with a NA = 0.75. We fabricated an Au-SiO_2-GaAs device embedding isolated InAs quantum dots. We measured a maximal acceleration of SE by a factor as large as 5.6 and a bright quantum dot emission with a recorded collection efficiency of 0.35 into a NA = 0.75 lens.

We believe the system still holds great potential to be further optimised to improve the source efficiency. Higher efficiency may be obtained by making the far-field emission more directional (see Figs 3.4 (b) and 3.5 (c)), for instance by controlling geometrical parameters to produce favourable interference effects between the direct-upward emission and the mode contribution that is back-scattered by the top facet and reflected by the bottom mirror. Such an optimisation of design requires an analysis that goes beyond the single-mode model, which is not sufficient to accurately describe the nanocavity. The latter is currently being explored in collaboration with the DTU Fotonik team in Copenhagen.

This nanowire cavity constitutes a promising building block to realise advanced sources of quantum light for a broad range of material systems. The small dimensions of the nanocavity result in high-frequency (GHz) vibration modes being supported. Thus QDs close to the nanocavity axis undergo almost no decoherence in emission due to vibration modes (Fig. 5.1 (a) and (c)). It can thus be seen as a first realisation of the strategies proposed in Chapter 2. Additionally, a significant Purcell factor makes the QD transition less sensitive to dephasing mechanisms. These attributes make the nanocavity a favourable platform for emitting indistinguishable photons. Hong-Ou-Mandel interference experiments, performed under resonant excitation, are planned with colleagues at Institut Néel, Grenoble, in order to evaluate the degree of photon-indistinguishability of our nanocavity sources.

Nanocavities are also suitable for emitting pairs of polarisation-entangled photons, through the radiative cascade associated with the recombination of a biexciton. In general, the morphological asymmetry of self-assembled QDs lifts the degeneracy of the bright excitonic states introducing a fine structure splitting (FSS), which prevents the emission of entangled photons. In this context, a higher Purcell factor leads to a broader radiatively-limited linewidth which relaxes the constraint on the FSS. Additionally, FSS can be controlled by external fields, in order to restore QD symmetry and hence the excitonic state degeneracy. QDs may be exposed to anisotropic in-plane strains [217] or electric fields [218]. The latter can be generated by applying electric fields with a system of electrodes positioned outside the nanowire. Such an approach is currently being explored in the team, in the context of two projects (under EU Innovative Training Network and Agence Nationale de la Recherche), and will constitute a major milestone in the PhD project of Matteo Finazzer.

The nanocavity device is also interesting in the context of hybrid nanomechanical systems. These rely on the coupling of an artificial atom (here the QD) to mechanical

vibration modes. The small physical dimension of the nanocavity, as briefly mentioned earlier, makes it a high-frequency resonator, having a fundamental flexural mode with a frequency of 578 MHz. The geometry also favours a clean spectrum, with isolated mechanical modes. For a QD away from the nanocavity axis, the coupling to such isolated high-frequency modes results in an emission spectrum featuring a ZPL flanked by spectrally resolved sideband peaks, as illustrated in Fig. 5.1 (b). These peaks correspond to Raman transitions, in which the emission of a photon is assisted by the emission or absorption of a phonon. Therefore, such a resolved spectrum would enable the manipulation of the population of mechanical modes with a laser, by exciting Raman transitions, thus allowing to cool down a mechanical mode or reversibly to increase its phonon population.

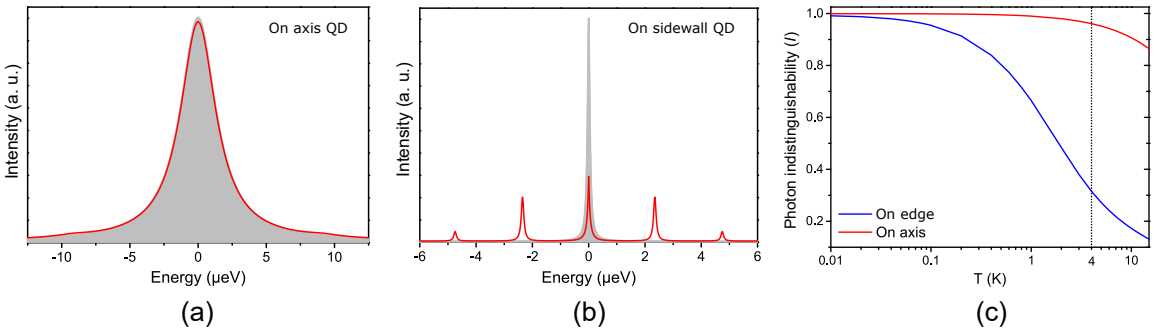

Fig. 5.1 (a) and (b) Solid line: Calculated QD emission profile, $S(\omega)$. Filled curve: Lorentzian, radiatively limited emission line, $S_{rad}(\omega)$. (a) on-axis QD; (b) on-sidewall QD. (c) Photon indistinguishability I as a function of the operation temperature T for a QD on-axis (red) and on-edge (blue) of a nanocavity.

The third significant outcome of this work is the design and development of a wavelength-tunable nanowire SPS. In this context, we proposed and designed a trumpet nanowire structure with integrated electrodes for electrostatically actuating the trumpets. We developed a new top-down ICP-RIE recipe for etching the trumpets and fabricated a complete nanowire sample with on-chip electrodes. During preliminary characterisations, we deflected the top facet of the trumpet by around 200 nm with a potential difference of 15 V across the electrodes. From such a displacement of the trumpet, we anticipate a shift in QD emission energy by around 8.5 meV (for a QD lying on the sidewall). Moreover, we have recorded a micro-PL spectrum of an excitonic emission line featuring a spectral drift as the voltage across the electrodes is varied. These early results prove that our electrostatic tuning mechanism works and that we are on track to successfully demonstrate a wavelength-tunable single-photon source. The first results in this direction have been obtained, and a complete characterisation of the current device is ongoing in the team. This complete study involves, for instance, a complete voltage-dependent energy shift study and single-photon purity ($g^{(2)}(0)$) measurements. This sample would also enable the investigation of collective photonic effects such as superradiance. For this, two QDs located on either side of the

neutral stress line of the bent trumpet could be brought into resonance as one of them would be compressed (stretched) experiencing a blue (red) shift in emission energy.

Finally, such an electrostatic actuation mechanism can be employed in a dynamic regime, to excite well defined mechanical modes. Applying a temporally oscillating voltage, a desired mechanical mode could be excited in the nanowire, which could be detected on the emission spectrum of the QD. Such a hybrid optomechanical system would allow to optically characterise individual modes, in particular the ones with high frequencies.

References

[1] N. Gisin and R. Thew, "Quantum communication," *Nature Photon.*, vol. 1, no. 3, pp. 165–171, 2007.

[2] C. L. Degen, F. Reinhard, and P. Cappellaro, "Quantum sensing," *Rev. Mod. Phys.*, vol. 89, no. 3, p. 035002, 2017.

[3] V. Giovannetti, S. Lloyd, and L. Maccone, "Quantum metrology," *Phys. Rev. Lett.*, vol. 96, no. 1, p. 010401, 2006.

[4] I. M. Georgescu, S. Ashhab, and F. Nori, "Quantum simulation," *Rev. Mod. Phys.*, vol. 86, no. 1, p. 153, 2014.

[5] A. Steane, "Quantum computing," *Reports on Progress in Physics*, vol. 61, no. 2, p. 117, 1998.

[6] J. J. Pla, K. Y. Tan, J. P. Dehollain, W. H. Lim, J. J. Morton, D. N. Jamieson, A. S. Dzurak, and A. Morello, "A single-atom electron spin qubit in silicon," *Nature*, vol. 489, no. 7417, pp. 541–545, 2012.

[7] C. D. Bruzewicz, J. Chiaverini, R. McConnell, and J. M. Sage, "Trapped-ion quantum computing: Progress and challenges," *Applied Physics Reviews*, vol. 6, no. 2, p. 021314, 2019.

[8] T. Xin, B.-X. Wang, K.-R. Li, X.-Y. Kong, S.-J. Wei, T. Wang, D. Ruan, and G.-L. Long, "Nuclear magnetic resonance for quantum computing: Techniques and recent achievements," *Chinese Physics B*, vol. 27, no. 2, p. 020308, 2018.

[9] J. M. Zadrozny, J. Niklas, O. G. Poluektov, and D. E. Freedman, "Millisecond coherence time in a tunable molecular electronic spin qubit," *ACS central science*, vol. 1, no. 9, pp. 488–492, 2015.

[10] M. H. Devoret, A. Wallraff, and J. M. Martinis, "Superconducting qubits: A short review," *arXiv preprint cond-mat/0411174*, 2004.

[11] C. Erven, C. Couteau, R. Laflamme, and G. Weihs, "Entangled quantum key distribution over two free-space optical links," *Optics express*, vol. 16, no. 21, pp. 16840–16853, 2008.

[12] S.-K. Liao, W.-Q. Cai, J. Handsteiner, B. Liu, J. Yin, L. Zhang, D. Rauch, M. Fink, J.-G. Ren, W.-Y. Liu, *et al.*, "Satellite-relayed intercontinental quantum network," *Phys. Rev. Lett.*, vol. 120, no. 3, p. 030501, 2018.

[13] B. J. Metcalf, J. B. Spring, P. C. Humphreys, N. Thomas-Peter, M. Barbieri, W. S. Kolthammer, X.-M. Jin, N. K. Langford, D. Kundys, J. C. Gates, *et al.*, "Quantum teleportation on a photonic chip," *Nature Photon.*, vol. 8, no. 10, pp. 770–774, 2014.

[14] J.-G. Ren, P. Xu, H.-L. Yong, L. Zhang, S.-K. Liao, J. Yin, W.-Y. Liu, W.-Q. Cai, M. Yang, L. Li, *et al.*, "Ground-to-satellite quantum teleportation," *Nature*, vol. 549, no. 7670, pp. 70–73, 2017.

[15] W. Gao, P. Fallahi, E. Togan, A. Delteil, Y. Chin, J. Miguel-Sanchez, and A. Imamoğlu, "Quantum teleportation from a propagating photon to a solid-state spin qubit," *Nature Commun.*, vol. 4, no. 1, pp. 1–8, 2013.

[16] W. Pfaff, B. J. Hensen, H. Bernien, S. B. van Dam, M. S. Blok, T. H. Taminiau, M. J. Tiggelman, R. N. Schouten, M. Markham, D. J. Twitchen, *et al.*, "Unconditional quantum teleportation between distant solid-state quantum bits," *Science*, vol. 345, no. 6196, pp. 532–535, 2014.

[17] V. Giovannetti, S. Lloyd, and L. Maccone, "Quantum-enhanced measurements: beating the standard quantum limit," *Science*, vol. 306, no. 5700, pp. 1330–1336, 2004.

[18] J. L. O'Brien, A. Furusawa, and J. Vučković, "Photonic quantum technologies," *Nature Photon.*, vol. 3, p. 687, 2009.

[19] T. Ono, R. Okamoto, and S. Takeuchi, "An entanglement-enhanced microscope," *Nature Commun.*, vol. 4, no. 1, pp. 1–7, 2013.

[20] F. Wolfgramm, C. Vitelli, F. A. Beduini, N. Godbout, and M. W. Mitchell, "Entanglement-enhanced probing of a delicate material system," *Nature Photon.*, vol. 7, no. 1, pp. 28–32, 2013.

[21] A. Crespi, M. Lobino, J. C. Matthews, A. Politi, C. R. Neal, R. Ramponi, R. Osellame, and J. L. O'Brien, "Measuring protein concentration with entangled photons," *Appl. Phys. Lett.*, vol. 100, no. 23, p. 233704, 2012.

[22] X.-Q. Zhou, T. C. Ralph, P. Kalasuwan, M. Zhang, A. Peruzzo, B. P. Lanyon, and J. L. O'brien, "Adding control to arbitrary unknown quantum operations," *Nature Commun.*, vol. 2, no. 1, pp. 1–8, 2011.

[23] B. P. Lanyon, M. Barbieri, M. P. Almeida, T. Jennewein, T. C. Ralph, K. J. Resch, G. J. Pryde, J. L. O'brien, A. Gilchrist, and A. G. White, "Simplifying quantum logic using higher-dimensional hilbert spaces," *Nature Physics*, vol. 5, no. 2, pp. 134–140, 2009.

[24] R. B. Patel, J. Ho, F. Ferreyrol, T. C. Ralph, and G. J. Pryde, "A quantum fredkin gate," *Science advances*, vol. 2, no. 3, p. e1501531, 2016.

[25] X.-D. Cai, C. Weedbrook, Z.-E. Su, M.-C. Chen, M. Gu, M.-J. Zhu, L. Li, N.-L. Liu, C.-Y. Lu, and J.-W. Pan, "Experimental quantum computing to solve systems of linear equations," *Phys. Rev. Lett.*, vol. 110, no. 23, p. 230501, 2013.

[26] E. Martin-Lopez, A. Laing, T. Lawson, R. Alvarez, X.-Q. Zhou, and J. L. O'brien, "Experimental realization of shor's quantum factoring algorithm using qubit recycling," *Nature Photon.*, vol. 6, no. 11, pp. 773–776, 2012.

[27] R. Santagati, J. Wang, A. A. Gentile, S. Paesani, N. Wiebe, J. R. McClean, S. Morley-Short, P. J. Shadbolt, D. Bonneau, J. W. Silverstone, *et al.*, "Witnessing eigenstates for quantum simulation of hamiltonian spectra," *Science advances*, vol. 4, no. 1, p. eaap9646, 2018.

[28] A. Aspuru-Guzik and P. Walther, "Photonic quantum simulators," *Nature physics*, vol. 8, no. 4, pp. 285–291, 2012.

[29] A. Peruzzo, J. McClean, P. Shadbolt, M.-H. Yung, X.-Q. Zhou, P. J. Love, A. Aspuru-Guzik, and J. L. O'brien, "A variational eigenvalue solver on a photonic quantum processor," *Nature Commun.*, vol. 5, no. 1, pp. 1–7, 2014.

[30] I. Pitsios, L. Banchi, A. S. Rab, M. Bentivegna, D. Caprara, A. Crespi, N. Spagnolo, S. Bose, P. Mataloni, R. Osellame, *et al.*, "Photonic simulation of entanglement growth and engineering after a spin chain quench," *Nature Commun.*, vol. 8, no. 1, pp. 1–8, 2017.

[31] J. Wang, S. Paesani, R. Santagati, S. Knauer, A. A. Gentile, N. Wiebe, M. Petruzzella, J. L. O'Brien, J. G. Rarity, A. Laing, *et al.*, "Experimental quantum hamiltonian learning," *Nature Physics*, vol. 13, no. 6, pp. 551–555, 2017.

[32] A. P. Lund, M. J. Bremner, and T. C. Ralph, "Quantum sampling problems, boson-sampling and quantum supremacy," *npj Quantum Information*, vol. 3, no. 1, pp. 1–8, 2017.

[33] R. Raussendorf and H. J. Briegel, "A one-way quantum computer," *Phys. Rev. Lett.*, vol. 86, no. 22, p. 5188, 2001.

[34] S. Slussarenko and G. J. Pryde, "Photonic quantum information processing: A concise review," *Applied Physics Reviews*, vol. 6, no. 4, p. 041303, 2019.

[35] E. Waks, E. Diamanti, and Y. Yamamoto, "Generation of photon number states," *New Journal of Physics*, vol. 8, no. 1, p. 4, 2006.

[36] A. B. U'Ren, C. Silberhorn, K. Banaszek, and I. A. Walmsley, "Efficient conditional preparation of high-fidelity single photon states for fiber-optic quantum networks," *Phys. Rev. Lett.*, vol. 93, no. 9, p. 093601, 2004.

[37] J. Fan and A. Migdall, "A broadband high spectral brightness fiber-based two-photon source," *Opt. Express*, vol. 15, no. 6, pp. 2915–2920, 2007.

[38] E. A. Goldschmidt, M. D. Eisaman, J. Fan, S. V. Polyakov, and A. Migdall, "Spectrally bright and broad fiber-based heralded single-photon source," *Phys. Rev. A*, vol. 78, no. 1, p. 013844, 2008.

[39] M. Hennrich, T. Legero, A. Kuhn, and G. Rempe, "Photon statistics of a non-stationary periodically driven single-photon source," *New Journal of Physics*, vol. 6, no. 1, p. 86, 2004.

[40] C. Maurer, C. Becher, C. Russo, J. Eschner, and R. Blatt, "A single-photon source based on a single Ca+ ion," *New journal of physics*, vol. 6, no. 1, p. 94, 2004.

[41] M. Steiner, A. Hartschuh, R. Korlacki, and A. J. Meixner, "Highly efficient, tunable single photon source based on single molecules," *Appl. Phys. Lett.*, vol. 90, no. 18, p. 183122, 2007.

[42] M. Nahra, D. Alshamaa, R. Deturche, V. Davydov, L. Kulikova, V. Agafonov, and C. Couteau, "Single germanium vacancy centers in nanodiamonds with bulk-like spectral stability," *AVS Quantum Science*, vol. 3, no. 1, p. 012001, 2021.

[43] A. Sipahigil, K. D. Jahnke, L. J. Rogers, T. Teraji, J. Isoya, A. S. Zibrov, F. Jelezko, and M. D. Lukin, "Indistinguishable photons from separated silicon-vacancy centers in diamond," *Phys. Rev. Lett.*, vol. 113, no. 11, p. 113602, 2014.

[44] A. Sipahigil, M. L. Goldman, E. Togan, Y. Chu, M. Markham, D. J. Twitchen, A. S. Zibrov, A. Kubanek, and M. D. Lukin, "Quantum interference of single photons from remote nitrogen-vacancy centers in diamond," *Phys. Rev. Lett.*, vol. 108, no. 14, p. 143601, 2012.

[45] A. J. Shields, "Semiconductor quantum light sources," *Nature Photon.*, vol. 1, p. 215, 2007.

[46] D. Bera, L. Qian, T.-K. Tseng, and P. H. Holloway, "Quantum dots and their multimodal applications: A review," *Materials*, vol. 3, no. 4, pp. 2260–2345, 2010.

[47] M. Z. Hu and T. Zhu, "Semiconductor nanocrystal quantum dot synthesis approaches towards large-scale industrial production for energy applications," *Nanoscale research letters*, vol. 10, no. 1, pp. 1–15, 2015.

[48] L. Goldstein, F. Glas, J. Marzin, M. Charasse, and G. Le Roux, "Growth by molecular beam epitaxy and characterization of InAs/GaAs strained-layer superlattices," *Appl. Phys. Lett.*, vol. 47, no. 10, pp. 1099–1101, 1985.

[49] M. Gurioli, Z. Wang, A. Rastelli, T. Kuroda, and S. Sanguinetti, "Droplet epitaxy of semiconductor nanostructures for quantum photonic devices," *Nature materials*, vol. 18, no. 8, pp. 799–810, 2019.

[50] M. E. Reimer, G. Bulgarini, N. Akopian, M. Hocevar, M. B. Bavinck, M. A. Verheijen, E. P. A. M. Bakkers, L. P. Kouwenhoven, and V. Zwiller, "Bright single-photon sources in bottom-up tailored nanowires," *Nature Comm.*, vol. 3, p. 737, 2012.

[51] P. Michler, *Quantum dots for quantum information technologies*, vol. 237. Springer, 2017.

[52] J. Bleuse, J. Claudon, M. Creasey, N. S. Malik, J.-M. Gérard, I. Maksymov, J.-P. Hugonin, and P. Lalanne, "Inhibition, Enhancement, and Control of Spontaneous Emission in Photonic Nanowires," *Phys. Rev. Lett.*, vol. 106, p. 103601, 2011.

[53] J. Johansen, S. Stobbe, I. S. Nikolaev, T. Lund-Hansen, P. T. Kristensen, J. M. Hvam, W. L. Vos, and P. Lodahl, "Size dependence of the wavefunction of self-assembled InAs quantum dots from time-resolved optical measurements," *Phys. Rev. B*, vol. 77, p. 073303, 2008.

[54] J.-M. Gérard and B. Gayral, "Strong purcell effect for inas quantum boxes in three-dimensional solid-state microcavities," *J. Lightwave Tech.*, vol. 17, p. 2089, 1999.

[55] P. Michler, A. Kiraz, C. Becher, W. V. Schoenfeld, P. M. Petroff, L. Zhang, E. Hu, and A. Imamoğlu, "A Quantum Dot Single-Photon Turnstile Device," *Science*, vol. 290, p. 2282, 2000.

[56] P. Senellart, G. Solomon, and A. White, "High-performance semiconductor quantum-dot single-photon sources," *Nature Nanotech.*, vol. 12, no. 11, p. 1026, 2017.

[57] N. Akopian, N. H. Lindner, E. Poem, Y. Berlatzky, J. Avron, D. Gershoni, B. D. Gerardot, and P. M. Petroff, "Entangled photon pairs from semiconductor quantum dots," *Phys. Rev. Lett.*, vol. 96, p. 130501, 2006.

[58] O. Benson, C. Santori, M. Pelton, and Y. Yamamoto, "Regulated and entangled photons from a single quantum dot," *Phys. Rev. Lett.*, vol. 84, no. 11, p. 2513, 2000.

[59] D. Huber, M. Reindl, J. Aberl, A. Rastelli, and R. Trotta, "Semiconductor quantum dots as an ideal source of polarization-entangled photon pairs on-demand: a review," *Journal of Optics*, vol. 20, p. 073002, 2018.

[60] I. Schwartz, D. Cogan, E. R. Schmidgall, Y. Don, L. Gantz, O. Kenneth, N. H. Lindner, and D. Gershoni, "Deterministic generation of a cluster state of entangled photons," *Science*, vol. 354, no. 6311, pp. 434–437, 2016.

[61] W. L. Barnes, G. Björk, J.-M. Gérard, P. Jonsson, J. A. E. Wasey, P. T. Worthing, and V. Zwiller, "Solid-state single photon sources: light collection strategies," *Eur. Phys. J. D*, vol. 18, p. 197, 2002.

[62] L. Besombes, K. Kheng, L. Marsal, and H. Mariette, "Acoustic phonon broadening mechanism in single quantum dot emission," *Phys. Rev. B*, vol. 63, p. 155307, 2001.

[63] I. Favero, G. Cassabois, R. Ferreira, D. Darson, C. Voisin, J. Tignon, C. Delalande, G. Bastard, P. Roussignol, and J.-M. Gérard, "Acoustic phonon sidebands in the emission line of single InAs/GaAs quantum dots," *Phys. Rev. B*, vol. 68, p. 233301, 2003.

[64] E. A. Muljarov and R. Zimmermann, "Dephasing in Quantum Dots: Quadratic Coupling to Acoustic Phonons," *Phys. Rev. Lett.*, vol. 93, p. 237401, 2004.

[65] P. Tighineanu, C. L. Dreessen, C. Flindt, P. Lodahl, and A. S. Sørensen, "Phonon Decoherence of Quantum Dots in Photonic Structures: Broadening of the Zero-Phonon Line and the Role of Dimensionality," *Phys. Rev. Lett.*, vol. 120, p. 257401, 2018.

[66] C. Arnold, V. Loo, A. Lemaître, I. Sagnes, O. Krebs, P. Voisin, P. Senellart, and L. Lanco, "Cavity-enhanced real-time monitoring of single-charge jumps at the microsecond time scale," *Phys. Rev. X*, vol. 4, no. 2, p. 021004, 2014.

[67] A. V. Kuhlmann, J. Houel, A. Ludwig, L. Greuter, D. Reuter, A. D. Wieck, M. Poggio, and R. J. Warburton, "Charge noise and spin noise in a semiconductor quantum device," *Nature Phys.*, vol. 9, p. 570, 2013.

[68] J.-Y. Marzin, J.-M. Gérard, A. Izraël, D. Barrier, and G. Bastard, "Photoluminescence of single InAs quantum dots obtained by self-organized growth on GaAs," *Phys. Rev. Lett.*, vol. 73, no. 5, p. 716, 1994.

[69] J.-M. Gérard, B. Sermage, B. Gayral, B. Legrand, E. Costard, and V. Thierry-Mieg, "Enhanced spontaneous emission by quantum boxes in a monolithic optical microcavity," *Phys. Rev. Lett.*, vol. 81, no. 5, p. 1110, 1998.

[70] S. Laurent, S. Varoutsis, L. Le Gratiet, A. Lemaître, I. Sagnes, F. Raineri, A. Levenson, I. Robert-Philip, and I. Abram, "Indistinguishable single photons from a single-quantum dot in a two-dimensional photonic crystal cavity," *Applied Physics Letters*, vol. 87, no. 16, p. 163107, 2005.

[71] C. Santori, D. Fattal, J. Vučković, G. S. Solomon, and Y. Yamamoto, "Indistinguishable photons from a single-photon device," *Nature*, vol. 419, p. 594, 2002.

[72] N. Somaschi, V. Giesz, L. De Santis, J. C. Loredo, M. P. Almeida, G. Hornecker, S. L. Portalupi, T. Grange, C. Antón, J. Demory, C. Gómez, I. Sagnes, N. D. Lanzillotti-Kimura, A. Lemaître, A. Auffèves, A. G. White, L. Lanco, and P. Senellart, "Near-optimal single-photon sources in the solid state," *Nature Photon.*, vol. 10, pp. 340–345, 2016.

[73] S. Varoutsis, S. Laurent, P. Kramper, A. Lemaître, I. Sagnes, I. Robert-Philip, and I. Abram, "Restoration of photon indistinguishability in the emission of a semiconductor quantum dot," *Physical Review B*, vol. 72, no. 4, p. 041303, 2005.

[74] M. Arcari, I. Söllner, A. Javadi, S. Lindskov Hansen, S. Mahmoodian, J. Liu, H. Thyrrestrup, E. Lee, J. Song, S. Stobbe, and P. Lodahl, "Near-Unity Coupling Efficiency of a Quantum Emitter to a Photonic Crystal Waveguide," *Phys. Rev. Lett.*, vol. 113, p. 093603, 2014.

[75] J. Claudon, N. Gregersen, P. Lalanne, and J.-M. Gérard, "Harnessing Light with Photonic Nanowires: Fundamentals and Applications to Quantum Optics," *ChemPhysChem*, vol. 14, pp. 2393–2402, 2013.

[76] J. P. Zhang, D. Y. Chu, S. L. Wu, S. T. Ho, W. G. Bi, C. W. Tu, and R. C. Tiberio, "Photonic-Wire Laser," *Phys. Rev. Lett.*, vol. 75, p. 2678, 1995.

[77] J. Claudon, J. Bleuse, N. S. Malik, M. Bazin, P. Jaffrennou, N. Gregersen, C. Sauvan, P. Lalanne, and J.-M. Gérard, "A highly efficient single-photon source based on a quantum dot in a photonic nanowire," *Nature Photon.*, vol. 4, pp. 174–177, 2010.

[78] M. Munsch, N. S. Malik, E. Dupuy, A. Delga, J. Bleuse, J.-M. Gérard, J. Claudon, N. Gregersen, and J. Mørk, "Dielectric GaAs-antenna ensuring an efficient broadband coupling between an InAs quantum dot and a Gaussian optical beam," *Phys. Rev. Lett.*, vol. 110, p. 177402, 2013.

[79] A. Jaffal, W. Redjem, P. Regreny, H. S. Nguyen, S. Cueff, X. Letartre, G. Patriarche, E. Rousseau, G. Cassabois, M. Gendry, *et al.*, "InAs quantum dot in a needlelike tapered InP nanowire: a telecom band single photon source monolithically grown on silicon," *Nanoscale*, vol. 11, no. 45, pp. 21847–21855, 2019.

[80] P. E. Kremer, A. C. Dada, P. Kumar, Y. Ma, S. Kumar, E. Clarke, and B. D. Gerardot, "A strain-tunable quantum dot embedded in a nanowire antenna," *Phys. Rev. B*, vol. 90, p. 201408, 2014.

[81] D. Tumanov, N. Vaish, H. Nguyen, Y. Curé, J.-M. Gérard, J. Claudon, F. Donatini, and J.-P. Poizat, "Static strain tuning of quantum dots embedded in a photonic wire," *Appl. Phys. Lett.*, vol. 112, no. 12, p. 123102, 2018.

[82] T. Huber, A. Predojević, M. Khoshnegar, D. Dalacu, P. J. Poole, H. Majedi, and G. Weihs, "Polarization entangled photons from quantum dots embedded in nanowires," *Nano Lett.*, vol. 14, pp. 7107–7114, 2014.

[83] M. A. M. Versteegh, M. E. Reimer, K. D. Jöns, D. Dalacu, P. J. Poole, A. Gulinatti, A. Giudice, and V. Zwiller, "Observation of strongly entangled photon pairs from a nanowire quantum dot," *Nature Comm.*, vol. 5, p. 5298, 2014.

[84] M. Khoshnegar, T. Huber, A. Predojević, D. Dalacu, M. Prilmüller, J. Lapointe, X. Wu, P. Tamarat, B. Lounis, P. Poole, G. Weihs, and H. Majedi, "A solid state source of photon triplets based on quantum dot molecules," *Nature Commun.*, vol. 8, p. 15716, 2017.

[85] H. A. Nguyen, T. Grange, B. Reznychenko, I. Yeo, P.-L. de Assis, D. Tumanov, F. Fratini, N. S. Malik, E. Dupuy, N. Gregersen, A. Auffèves, J.-M. Gérard, J. Claudon, and J.-P. Poizat, "Giant non-linear interaction between two optical beams via a quantum dot embedded in a photonic wire," *Phys. Rev. B*, vol. 97, p. 201106(R), 2018.

[86] Q. Mermillod, T. Jakubczyk, V. Delmonte, A. Delga, E. Peinke, J.-M. Gérard, J. Claudon, and J. Kasprzak, "Harvesting, Coupling, and Control of Single-Exciton Coherences in Photonic Waveguide Antennas," *Phys. Rev. Lett.*, vol. 116, p. 163903, 2016.

[87] M. Munsch, A. V. Kuhlmann, D. Cadeddu, J.-M. Gérard, J. Claudon, M. Poggio, and R. J. Warburton, "Resonant driving of a single photon emitter embedded in a mechanical oscillator," *Nature Commun.*, vol. 8, p. 76, 2017.

[88] P.-L. de Assis, I. Yeo, A. Gloppe, H. A. Nguyen, D. Tumanov, E. Dupont-Ferrier, N. S. Malik, E. Dupuy, J. Claudon, J.-M. Gérard, A. Auffèves, O. Arcizet, M. Richard, and J.-P. Poizat, "Strain-Gradient Position Mapping of Semiconductor Quantum Dots," *Phys. Rev. Lett.*, vol. 118, p. 117401, 2017.

[89] J. Kettler, N. Vaish, L. M. de Lépinay, B. Besga, P.-L. de Assis, O. Bourgeois, A. Auffèves, M. Richard, J. Claudon, J.-M. Gérard, B. Pigeau, O. Arcizet, P. Verlot, and J.-P. Poizat, "Inducing micromechanical motion by optical excitation of a single quantum dot," *Nature nanotechnology*, vol. 16, no. 3, pp. 283–287, 2021.

[90] I. Yeo, P.-L. de Assis, A. Gloppe, E. Dupont-Ferrier, P. Verlot, N. S. Malik, E. Dupuy, J. Claudon, J.-M. Gérard, A. Auffèves, G. Nogues, S. Seidelin, J.-P. Poizat, O. Arcizet, and M. Richard, "Strain-mediated coupling in a quantum dot-mechanical oscillator hybrid system," *Nature Nanotech.*, vol. 9, p. 106, 2014.

[91] S. Adachi, *Physical properties of III-V semiconductor compounds*. John Wiley & Sons, 1992.

[92] I. Stranski and L. Krastanov, "Theory of orientation separation of ionic crystals," *Ber. Akad. Wiss. Wien*, vol. 146, p. 797, 1938.

[93] K. Eberl, M. Lipinski, Y. Manz, W. Winter, N. Jin-Phillipp, and O. Schmidt, "Self-assembling quantum dots for optoelectronic devices on Si and GaAs," *Physica E: Low-dimensional Systems and Nanostructures*, vol. 9, no. 1, pp. 164–174, 2001.

[94] J.-M. Gérard, J. Genin, J. Lefebvre, J.-M. Moison, N. Lebouche, and F. Barthe, "Optical investigation of the self-organized growth of InAs/GaAs quantum boxes," *Journal of crystal growth*, vol. 150, pp. 351–356, 1995.

[95] C. Hamaguchi and C. Hamaguchi, *Basic semiconductor physics*, vol. 9, ch. 1. Springer, 2010.

[96] Y. Peter and M. Cardona, *Fundamentals of semiconductors: physics and materials properties*, ch. 2. Springer Science & Business Media, 2010.

[97] J.-Y. Marzin, J.-M. Gérard, P. Voisin, and J. Brumt, "Optical studies of strained iii-v heterolayers," in *Semiconductors and Semimetals*, vol. 32, pp. 55–118, Elsevier, 1990.

[98] J.-Y. Marzin and G. Bastard, "Calculation of the energy levels in inasgaas quantum dots," *Solid state communications*, vol. 92, no. 5, pp. 437–442, 1994.

[99] G. Cassabois, *Origines et limites du modèle de l'atome artificiel pour une boîte quantique de semiconducteurs*. Université Paris VI, 2006.

[100] D. Bimberg, M. Grundmann, and N. N. Ledentsov, *Quantum dot heterostructures*. John Wiley & Sons, 1999.

[101] R. Fons, *Propriétés optiques de boîtes quantiques semiconductrices intégrées dans des antennes à fil photonique*. PhD thesis, Université Grenoble Alpes, 2020.

[102] B. Grandidier, Y. Niquet, B. Legrand, J. Nys, C. Priester, D. Stiévenard, J. Gérard, and V. Thierry-Mieg, "Imaging the wave-function amplitudes in cleaved semiconductor quantum boxes," *Phys. Rev. Lett.*, vol. 85, no. 5, p. 1068, 2000.

[103] S. Hameau, Y. Guldner, O. Verzelen, R. Ferreira, G. Bastard, J. Zeman, A. Lemaitre, and J. Gérard, "Strong electron-phonon coupling regime in quantum dots: Evidence for everlasting resonant polarons," *Phys. Rev. Lett.*, vol. 83, no. 20, p. 4152, 1999.

[104] S. Sauvage, P. Boucaud, F. Julien, J.-M. Gerard, and J.-Y. Marzin, "Infrared spectroscopy of intraband transitions in self-organized inas/gaas quantum dots," *J. Appl. Phys.*, vol. 82, no. 7, pp. 3396–3401, 1997.

[105] C. Santori, M. Pelton, G. Solomon, Y. Dale, and Y. Yamamoto, "Triggered single photons from a quantum dot," *Phys. Rev. Lett.*, vol. 86, no. 8, p. 1502, 2001.

[106] A. Kiraz, S. Fälth, C. Becher, B. Gayral, W. Schoenfeld, P. Petroff, L. Zhang, E. Hu, and A. Imamoğlu, "Photon correlation spectroscopy of a single quantum dot," *Phys. Rev. B*, vol. 65, no. 16, p. 161303, 2002.

[107] A. Babinski, S. Awirothananon, J. Lapointe, Z. Wasilewski, S. Raymond, and M. Potemski, "Single-dot spectroscopy in high magnetic fields," *Physica E: Low-dimensional Systems and Nanostructures*, vol. 26, no. 1-4, pp. 190–193, 2005.

[108] Y.-M. He, Y. He, Y.-J. Wei, D. Wu, M. Atatüre, C. Schneider, S. Höfling, M. Kamp, C.-Y. Lu, and J.-W. Pan, "On-demand semiconductor single-photon source with near-unity indistinguishability," *Nature Nanotech.*, vol. 8, p. 213, 2013.

[109] P. Michler, *Single quantum dots: Fundamentals, applications and new concepts*, vol. 90, ch. 2. Springer Science & Business Media, 2003.

[110] M. Bayer, G. Ortner, O. Stern, A. Kuther, A. Gorbunov, A. Forchel, P. Hawrylak, S. Fafard, K. Hinzer, T. Reinecke, *et al.*, "Fine structure of neutral and charged excitons in self-assembled In (Ga) As/(Al) GaAs quantum dots," *Phys. Rev. B*, vol. 65, no. 19, p. 195315, 2002.

[111] P. Lodahl, S. Mahmoodian, and S. Stobbe, "Interfacing single photons and single quantum dots with photonic nanostructures," *Rev. Mod. Phys.*, vol. 87, pp. 347–400, 2015.

[112] M. Migliorato, D. Powell, E. Zibik, L. Wilson, M. Fearn, J. Jefferson, M. Steer, M. Hopkinson, and A. Cullis, "Anisotropy of the electron energy levels in $In_xGa_{1-x}As$/GaAs quantum dots with non uniform composition," *Physica E: Low-dimensional Systems and Nanostructures*, vol. 26, no. 1-4, pp. 436–440, 2005.

[113] F. Patella, S. Nufris, F. Arciprete, M. Fanfoni, E. Placidi, A. Sgarlata, and A. Balzarotti, "Tracing the two-to three-dimensional transition in the InAs/GaAs (001) heteroepitaxial growth," *Phys. Rev. B*, vol. 67, no. 20, p. 205308, 2003.

[114] A. Bennett, y. M. Pooley, n. R. Stevenson, M. Ward, R. Patel, A. B. de La Giroday, N. Sköld, I. Farrer, C. Nicoll, D. Ritchie, *et al.*, "Electric-field-induced coherent coupling of the exciton states in a single quantum dot," *Nature Physics*, vol. 6, no. 12, pp. 947–950, 2010.

[115] R. Trotta, E. Zallo, C. Ortix, P. Atkinson, J. Plumhof, J. Van den Brink, A. Rastelli, and O. Schmidt, "Universal recovery of the energy-level degeneracy of bright excitons in InGaAs quantum dots without a structure symmetry," *Phys. Rev. Lett.*, vol. 109, no. 14, p. 147401, 2012.

[116] T. Kuroda, T. Mano, N. Ha, H. Nakajima, H. Kumano, B. Urbaszek, M. Jo, M. Abbarchi, Y. Sakuma, K. Sakoda, *et al.*, "Symmetric quantum dots as efficient sources of highly entangled photons: Violation of bell's inequality without spectral and temporal filtering," *Phys. Rev. B*, vol. 88, no. 4, p. 041306, 2013.

[117] H. A. Kramers, "Théorie générale de la rotation paramagnétique dans les cristaux," *Proc. Acad. Amst*, vol. 33, no. 6, 1930.

[118] A. Berthelot, I. Favero, G. Cassabois, C. Voisin, C. Delalande, P. Roussignol, R. Ferreira, and J.-M. Gérard, "Unconventional motional narrowing in the optical spectrum of a semiconductor quantum dot," *Nature Physics*, vol. 2, no. 11, pp. 759–764, 2006.

[119] O. Gazzano, S. M. De Vasconcellos, C. Arnold, A. Nowak, E. Galopin, I. Sagnes, L. Lanco, A. Lemaître, and P. Senellart, "Bright solid-state sources of indistinguishable single photons," *Nature Commun.*, vol. 4, no. 1, pp. 1–6, 2013.

[120] V. Loo, L. Lanco, A. Lemaître, I. Sagnes, O. Krebs, P. Voisin, and P. Senellart, "Quantum dot-cavity strong-coupling regime measured through coherent reflection spectroscopy in a very high-q micropillar," *Appl. Phys. Lett.*, vol. 97, no. 24, p. 241110, 2010.

[121] S. Reitzenstein, C. Hofmann, A. Gorbunov, M. Strauß, S. Kwon, C. Schneider, A. Löffler, S. Höfling, M. Kamp, and A. Forchel, "Al as/ ga as micropillar cavities with quality factors exceeding 150.000," *Appl. Phys. Lett.*, vol. 90, no. 25, p. 251109, 2007.

[122] D. Englund, D. Fattal, E. Waks, G. Solomon, B. Zhang, T. Nakaoka, Y. Arakawa, Y. Yamamoto, and J. Vučković, "Controlling the spontaneous emission rate of single quantum dots in a two-dimensional photonic crystal," *Phys. Rev. Lett.*, vol. 95, no. 1, p. 013904, 2005.

[123] Y. Akahane, T. Asano, B.-S. Song, and S. Noda, "High-Q photonic nanocavity in a two-dimensional photonic crystal," *Nature*, vol. 425, no. 6961, pp. 944–947, 2003.

[124] K. Hennessy, A. Badolato, M. Winger, D. Gerace, M. Atatüre, S. Gulde, S. Fält, E. L. Hu, and A. Imamoğlu, "Quantum nature of a strongly coupled single quantum dot–cavity system," *Nature*, vol. 445, no. 7130, pp. 896–899, 2007.

[125] Y. Lai, S. Pirotta, G. Urbinati, D. Gerace, M. Minkov, V. Savona, A. Badolato, and M. Galli, "Genetically designed l3 photonic crystal nanocavities with measured quality factor exceeding one million," *Appl. Phys. Lett.*, vol. 104, no. 24, p. 241101, 2014.

[126] B. Gayral, J.-M. Gérard, B. Sermage, A. Lemaître, and C. Dupuis, "Time-resolved probing of the Purcell effect for InAs quantum boxes in GaAs microdisks," *Appl. Phys. Lett.*, vol. 78, no. 19, pp. 2828–2830, 2001.

[127] K. Srinivasan and O. Painter, "Linear and nonlinear optical spectroscopy of a strongly coupled microdisk–quantum dot system," *Nature*, vol. 450, no. 7171, pp. 862–865, 2007.

[128] M. Borselli, T. J. Johnson, and O. Painter, "Beyond the rayleigh scattering limit in high-q silicon microdisks: theory and experiment," *Opt. Express*, vol. 13, no. 5, pp. 1515–1530, 2005.

[129] L. Sapienza, H. Thyrrestrup, S. Stobbe, P. D. Garcia, S. Smolka, and P. Lodahl, "Cavity quantum electrodynamics with anderson-localized modes," *Science*, vol. 327, no. 5971, pp. 1352–1355, 2010.

[130] A. Dousse, L. Lanco, J. Suffczyński, E. Semenova, A. Miard, A. Lemaître, I. Sagnes, C. Roblin, J. Bloch, and P. Senellart, "Controlled light-matter coupling for a single quantum dot embedded in a pillar microcavity using far-field optical lithography," *Phys. Rev. Lett.*, vol. 101, no. 26, p. 267404, 2008.

[131] D. Chang, A. S. Sørensen, P. Hemmer, and M. Lukin, "Quantum optics with surface plasmons," *Phys. Rev. Lett.*, vol. 97, no. 5, p. 053002, 2006.

[132] A. Akimov, A. Mukherjee, C. Yu, D. Chang, A. Zibrov, P. Hemmer, H. Park, and M. Lukin, "Generation of single optical plasmons in metallic nanowires coupled to quantum dots," *Nature*, vol. 450, no. 7168, pp. 402–406, 2007.

[133] C. H. Gan, J.-P. Hugonin, and P. Lalanne, "Proposal for compact solid-state iii-v single-plasmon sources," *Phys. Rev. X*, vol. 2, no. 2, p. 021008, 2012.

[134] Q. Quan, I. Bulu, and M. Lončar, "Broadband waveguide qed system on a chip," *Phys. Rev. A*, vol. 80, no. 1, p. 011810, 2009.

[135] E. Yablonovitch, "Photonic band-gap structures," *JOSA B*, vol. 10, no. 2, pp. 283–295, 1993.

[136] G. Lecamp, P. Lalanne, and J. Hugonin, "Very large spontaneous-emission β factors in photonic-crystal waveguides," *Phys. Rev. Lett.*, vol. 99, no. 2, p. 023902, 2007.

[137] V. M. Rao and S. Hughes, "Single quantum-dot purcell factor and β factor in a photonic crystal waveguide," *Phys. Rev. B*, vol. 75, no. 20, p. 205437, 2007.

[138] P. Walther, K. J. Resch, T. Rudolph, E. Schenck, H. Weinfurter, V. Vedral, M. Aspelmeyer, and A. Zeilinger, "Experimental one-way quantum computing," *Nature*, vol. 434, no. 7030, pp. 169–176, 2005.

[139] S. Mazoyer, J.-P. Hugonin, and P. Lalanne, "Disorder-induced multiple scattering in photonic-crystal waveguides," *Phys. Rev. Lett.*, vol. 103, no. 6, p. 063903, 2009.

[140] P. García, A. Javadi, H. Thyrrestrup, and P. Lodahl, "Quantifying the intrinsic amount of fabrication disorder in photonic-crystal waveguides from optical far-field intensity measurements," *Appl. Phys. Lett.*, vol. 102, no. 3, p. 031101, 2013.

[141] G. Bulgarini, M. E. Reimer, M. Bouwes Bavinck, K. D. Jöns, D. Dalacu, P. J. Poole, E. P. Bakkers, and V. Zwiller, "Nanowire waveguides launching single photons in a gaussian mode for ideal fiber coupling," *Nano Lett.*, vol. 14, no. 7, pp. 4102–4106, 2014.

[142] I. Friedler, C. Sauvan, J. P. Hugonin, P. Lalanne, J. Claudon, and J.-M. Gérard, "Solid-state single photon sources: the nanowire antenna," *Opt. Express*, vol. 17, p. 2095, 2009.

[143] E. Snitzer, "Cylindrical dielectric waveguide modes," *JOSA*, vol. 51, no. 5, pp. 491–498, 1961.

[144] J. Claudon, *Antennes optiques à base de fils photoniques : concepts fondamentaux et applications à l'optique quantique*. Université Joseph Fourier - Grenoble I, 2014.

[145] E. Yablonovitch, T. Gmitter, and R. Bhat, "Inhibited and enhanced spontaneous emission from optically thin AlGaAs/GaAs double heterostructures," *Phys. Rev. Lett.*, vol. 61, no. 22, p. 2546, 1988.

[146] A. Maslov, M. Bakunov, and C.-Z. Ning, "Distribution of optical emission between guided modes and free space in a semiconductor nanowire," *Journal of applied physics*, vol. 99, no. 2, p. 024314, 2006.

[147] S.-T. Ho, S. McCall, and R. E. Slusher, "Spontaneous emission from excitons in thin dielectric layers," *Optics letters*, vol. 18, no. 11, pp. 909–911, 1993.

[148] A. Maslov and C.-Z. Ning, "Far-field emission of a semiconductor nanowire laser," *Optics letters*, vol. 29, no. 6, pp. 572–574, 2004.

[149] I. Friedler, P. Lalanne, J.-P. Hugonin, J. Claudon, J.-M. Gérard, A. Beveratos, and I. Robert-Philip, "Efficient photonic mirrors for semiconductor nanowires," *Optics letters*, vol. 33, no. 22, pp. 2635–2637, 2008.

[150] N. Gregersen, T. R. Nielsen, J. Claudon, J.-M. Gérard, and J. Mørk, "Controlling the emission profile of a nanowire with a conical taper," *Optics letters*, vol. 33, no. 15, pp. 1693–1695, 2008.

[151] N. Gregersen, T. R. Nielsen, J. Mørk, J. Claudon, and J.-M. Gérard, "Designs for high-efficiency electrically pumped photonic nanowire single-photon sources," *Opt. Express*, vol. 18, no. 20, pp. 21204–21218, 2010.

[152] D. Cadeddu, J. Teissier, F. Braakman, N. Gregersen, P. Stepanov, J.-M. Gérard, J. Claudon, R. J. Warburton, M. Poggio, and M. Munsch, "A fiber-coupled quantum-dot on a photonic tip," *Appl. Phys. Lett.*, vol. 108, p. 011112, 2016.

[153] X. Ding, Y. He, Z.-C. Duan, N. Gregersen, M.-C. Chen, S. Unsleber, S. Maier, C. Schneider, M. Kamp, S. Höfling, C.-Y. Lu, and J.-W. Pan, "On-Demand Single Photons with High Extraction Efficiency and Near-Unity Indistinguishability from a Resonantly Driven Quantum Dot in a Micropillar," *Phys. Rev. Lett.*, vol. 116, p. 020401, 2016.

[154] A. V. Kuhlmann, J. H. Prechtel, J. Houel, A. Ludwig, D. Reuter, A. D. Wieck, and R. J. Warburton, "Transform-limited single photons from a single quantum dot," *Nature Commun.*, vol. 6, p. 8204, 2015.

[155] F. Liu, A. J. Brash, J. O'Hara, L. M. Martins, C. L. Phillips, R. J. Coles, B. Royall, E. Clarke, C. Bentham, N. Prtljaga, *et al.*, "High purcell factor generation of indistinguishable on-chip single photons," *Nature Nanotech.*, vol. 13, no. 9, pp. 835–840, 2018.

[156] H. Thyrrestrup, G. Kiršanskė, H. Le Jeannic, T. Pregnolato, L. Zhai, L. Raahauge, L. Midolo, N. Rotenberg, A. Javadi, R. Schott, A. D. Wieck, A. Ludwig, M. C. Löbl, I. Söllner, R. J. Warburton, and P. Lodahl, "Quantum Optics with Near-Lifetime-Limited Quantum-Dot Transitions in a Nanophotonic Waveguide," *Nano Lett.*, vol. 18, pp. 1801–1806, 2018.

[157] P. Borri, W. Langbein, U. Woggon, V. Stavarache, D. Reuter, and A. D. Wieck, "Exciton dephasing via phonon interactions in InAs quantum dots: Dependence on quantum confinement," *Phys. Rev. B*, vol. 71, p. 115328, 2005.

[158] T. Grange, N. Somaschi, C. Antón, L. De Santis, G. Coppola, V. Giesz, A. Lemaître, I. Sagnes, A. Auffèves, and P. Senellart, "Reducing Phonon-Induced Decoherence in Solid-State Single-Photon Sources with Cavity Quantum Electrodynamics," *Phys. Rev. Lett.*, vol. 118, p. 253602, 2017.

[159] J. Iles-Smith, D. P. S. McCutcheon, A. Nazir, and J. Mørk, "Phonon scattering inhibits simultaneous near-unity efficiency and indistinguishability in semiconductor single-photon sources," *Nature Photon.*, vol. 11, pp. 521–527, 2017.

[160] T. Jakubczyk, V. Delmonte, S. Fischbach, D. Wigger, D. E. Reiter, Q. Mermillod, P. Schnauber, A. Kaganskiy, J.-H. Schulze, A. Strittmatter, S. Rodt, W. Langbein, T. Kuhn, S. Reitzenstein, and J. Kasprzak, "Impact of Phonons on Dephasing of Individual Excitons in Deterministic Quantum Dot Microlenses," *ACS Photonics*, vol. 3, pp. 2461–2466, 2016.

[161] A. J. Ramsay, A. V. Gopal, E. M. Gauger, A. Nazir, B. W. Lovett, A. M. Fox, and M. S. Skolnick, "Damping of Exciton Rabi Rotations by Acoustic Phonons in Optically Excited InGaAs/GaAs Quantum Dots," *Phys. Rev. Lett.*, vol. 104, p. 017402, 2010.

[162] A. Reigue, J. Iles-Smith, F. Lux, L. Monniello, M. Bernard, F. Margaillan, A. Lemaitre, A. Martinez, D. P. McCutcheon, J. Mørk, R. Hostein, and V. Voliotis, "Probing Electron-Phonon Interaction through Two-Photon Interference in Resonantly Driven Semiconductor Quantum Dots," *Phys. Rev. Lett.*, vol. 118, p. 233602, 2017.

[163] G. Lindwall, A. Wacker, C. Weber, and A. Knorr, "Zero-Phonon Linewidth and Phonon Satellites in the Optical Absorption of Nanowire-Based Quantum Dots," *Phys. Rev. Lett.*, vol. 99, p. 087401, 2007.

[164] A. Artioli, S. Kotal, N. Gregersen, P. Verlot, J.-M. Gérard, and J. Claudon, "Design of Quantum Dot-Nanowire Single-Photon Sources that are Immune to Thermomechanical Decoherence," *Phys. Rev. Lett.*, vol. 123, p. 247403, 2019.

[165] E. Peter, P. Senellart, D. Martrou, A. Lemaître, J. Hours, J.-M. Gérard, and J. Bloch, "Exciton-Photon Strong-Coupling Regime for a Single Quantum Dot Embedded in a Microcavity," *Phys. Rev. Lett.*, vol. 95, p. 067401, 2005.

[166] J. Garayt, J. Gerard, F. Enjalbert, L. Ferlazzo, S. Founta, E. Martinez-Guerrero, F. Rol, D. Araujo, R. Cox, B. Daudin, *et al.*, "Study of isolated cubic gan quantum dots by low-temperature cathodoluminescence," *Physica E: Low-dimensional Systems and Nanostructures*, vol. 26, no. 1-4, pp. 203–206, 2005.

[167] G. D. Mahan, *Many-particle physics*. Springer Science & Business Media, 2013.

[168] P. Tighineanu, C. L. Dreessen, C. Flindt, P. Lodahl, and A. S. Sørensen, "Supplemental material of phonon decoherence of quantum dots in photonic structures: Broadening of the zero-phonon line and the role of dimensionality." http://link.aps.org/supplemental/10.1103/PhysRevLett.120.257401, 2018.

[169] C. L. Dreeßen, C. Ouellet-Plamondon, P. Tighineanu, X. Zhou, L. Midolo, A. S. Sørensen, and P. Lodahl, "Suppressing phonon decoherence of high performance single-photon sources in nanophotonic waveguides," *Quantum Science and Technology*, vol. 4, no. 1, p. 015003, 2018.

[170] D. P. S. McCutcheon and A. Nazir, "Supplemental material of model of the optical emission of a driven semiconductor quantum dot: Phonon-enhanced coherent scattering and off-resonant sideband narrowing." http://link.aps.org/supplemental/10.1103/PhysRevLett.110.217401, 2019.

[171] I. Favero, *Décohérence, symétries et relaxation de spin dans les boîtes quantiques de semiconducteurs*. PhD thesis, Université Paris VI, 2005.

[172] P. Stepanov, M. Elzo-Aizarna, J. Bleuse, N. S. Malik, Y. Curé, E. Gautier, V. Favre-Nicolin, J.-M. Gérard, and J. Claudon, "Large and Uniform Optical Emission Shifts in Quantum Dots Strained along Their Growth Axis," *Nano Lett.*, vol. 16, p. 3215, 2016.

[173] D. Cadeddu, F. R. Braakman, G. Tütüncüoglu, F. Matteini, D. Rüffer, A. Fontcuberta i Morral, and M. Poggio, "Time-Resolved Nonlinear Coupling between Orthogonal Flexural Modes of a Pristine GaAs Nanowire," *Nano Lett.*, vol. 16, pp. 926–931, 2016.

[174] I. Wilson-Rae, P. Zoller, and A. Imamoğlu, "Laser cooling of a nanomechanical resonator mode to its quantum ground state," *Phys. Rev. Lett.*, vol. 92, p. 075507, 2004.

[175] I. Vurgaftman, J. R. Meyer, and L. R. Ram-Mohan, "Band parameters for III–V compound semiconductors and their alloys," *J. Appl. Phys.*, vol. 89, p. 5815, 2001.

[176] K. Roy-Choudhury and S. Hughes, "Spontaneous emission from a quantum dot in a structured photonic reservoir: phonon-mediated breakdown of fermi's golden rule," *Optica*, vol. 2, p. 434, 2015.

[177] A. Kiraz, M. Atatüre, and A. Imamoğlu, "Quantum-dot single-photon sources: Prospects for applications in linear optics quantum-information processing," *Phys. Rev. A*, vol. 69, p. 032305, 2004.

[178] A. K. Nowak, S. L. Portalupi, V. Giesz, O. Gazzano, C. Dal Savio, P.-F. Braun, K. Karrai, C. Arnold, L. Lanco, I. Sagnes, A. Lemaître, and P. Senellart, "Deterministic and electrically tunable bright single-photon source," *Nature Commun.*, vol. 5, p. 3240, 2014.

[179] M. Gschrey, A. Thoma, P. Schnauber, M. Seifried, R. Schmidt, B. Wohlfeil, L. Krüger, J. H. Schulze, T. Heindel, S. Burger, F. Schmidt, A. Strittmatter, S. Rodt, and S. Reitzenstein, "Highly indistinguishable photons from deterministic quantum-dot microlenses utilizing three-dimensional *in situ* electron-beam lithography," *Nature Commun.*, vol. 6, p. 7662, 2015.

[180] L. Sapienza, M. Davanço, A. Badolato, and K. Srinivasan, "Nanoscale optical positioning of single quantum dots for bright and pure single-photon emission," *Nature Commun.*, vol. 6, p. 7833, 2015.

[181] T. Heindel, C. Schneider, M. Lermer, S. H. Kwon, T. Braun, S. Reitzenstein, S. Höfling, M. Kamp, and A. Forchel, "Electrically driven quantum dot-micropillar single photon source with 34% overall efficiency," *Appl. Phys. Lett.*, vol. 96, p. 011107, 2010.

[182] M. N. Makhonin, J. E. Dixon, R. J. Coles, B. Royall, E. Clarke, M. S. Skolnick, and A. M. Fox, "On-chip resonantly-driven quantum emitter with enhanced coherence," *Nano Lett.*, vol. 14, p. 6997, 2014.

[183] A. Badolato, K. Hennessy, M. Atatüre, J. Dreiser, E. Hu, P. M. Petroff, and A. Imamoğlu, "Deterministic coupling of single quantum dots to single nanocavity modes," *Science*, vol. 308, no. 5725, pp. 1158–1161, 2005.

[184] D. Dalacu, K. Mnaymneh, V. Sazonova, P. J. Poole, G. C. Aers, J. Lapointe, R. Cheriton, A. J. SpringThorpe, and R. Williams, "Deterministic emitter-cavity coupling using a single-site controlled quantum dot," *Phys. Rev. B*, vol. 82, no. 3, p. 033301, 2010.

[185] P. Gallo, M. Felici, B. Dwir, K. Atlasov, K. Karlsson, A. Rudra, A. Mohan, G. Biasiol, L. Sorba, and E. Kapon, "Integration of site-controlled pyramidal quantum dots and photonic crystal membrane cavities," *Appl. Phys. Lett.*, vol. 92, no. 26, p. 263101, 2008.

[186] A. D. Osterkryger, J. Claudon, J.-M. Gérard, and N. Gregersen, "Photonic "hourglass" design for efficient quantum light emission," *Optics Letters*, vol. 44, no. 11, pp. 2617–2620, 2019.

[187] J. Liu, R. Su, Y. Wei, B. Yao, S. F. C. da Silva, Y. Yu, J. Iles-Smith, K. Srinivasan, A. Rastelli, J. Li, *et al.*, "A solid-state source of strongly entangled photon pairs with high brightness and indistinguishability," *Nature Nanotech.*, vol. 14, no. 6, pp. 586–593, 2019.

[188] H. Wang, H. Hu, T.-H. Chung, J. Qin, X. Yang, J.-P. Li, R.-Z. Liu, H.-S. Zhong, Y.-M. He, X. Ding, *et al.*, "On-demand semiconductor source of entangled photons which simultaneously has high fidelity, efficiency, and indistinguishability," *Phys. Rev. Lett.*, vol. 122, no. 11, p. 113602, 2019.

[189] T. Häyrynen, J. R. de Lasson, and N. Gregersen, "Open-geometry fourier modal method: modeling nanophotonic structures in infinite domains," *JOSA A*, vol. 33, no. 7, pp. 1298–1306, 2016.

[190] N. Gregersen, D. P. McCutcheon, J. Mørk, J.-M. Gérard, and J. Claudon, "A broadband tapered nanocavity for efficient nonclassical light emission," *Opt. Express*, vol. 24, no. 18, pp. 20904–20924, 2016.

[191] A. V. Lavrinenko, J. Lægsgaard, N. Gregersen, F. Schmidt, and T. Søndergaard, *Numerical Methods in Photonics*, ch. 6, pp. 139–195. CRC Press, 2014.

[192] A. D. Østerkryger, *Engineering of nanophotonic structures for quantum information applications*. PhD thesis, DTU-Department of Photonics Engineering, 2018.

[193] P. A. Dalgarno, J. M. Smith, J. McFarlane, B. D. Gerardot, K. Karrai, A. Badolato, P. M. Petroff, and R. J. Warburton, "Coulomb interactions in single charged self-assembled quantum dots: Radiative lifetime and recombination energy," *Phys. Rev. B*, vol. 77, no. 24, p. 245311, 2008.

[194] E. Moreau, I. Robert, L. Manin, V. Thierry-Mieg, J.-M. Gérard, and I. Abram, "Quantum cascade of photons in semiconductor quantum dots," *Phys. Rev. Lett.*, vol. 87, no. 18, p. 183601, 2001.

[195] J. Suffczyński, A. Dousse, K. Gauthron, A. Lemaître, I. Sagnes, L. Lanco, J. Bloch, P. Voisin, and P. Senellart, "Origin of the optical emission within the cavity mode of coupled quantum dot-cavity systems," *Phys. Rev. Lett.*, vol. 103, no. 2, p. 027401, 2009.

[196] J. Martín-Sánchez, R. Trotta, A. Mariscal, R. Serna, G. Piredda, S. Stroj, J. Edlinger, C. Schimpf, J. Aberl, T. Lettner, *et al.*, "Strain-tuning of the optical properties of semiconductor nanomaterials by integration onto piezoelectric actuators," *Semiconductor Science and Technology*, vol. 33, no. 1, p. 013001, 2017.

[197] M. Munsch, J. Claudon, J. Bleuse, N. S. Malik, E. Dupuy, J.-M. Gérard, Y. Chen, N. Gregersen, and J. Mørk, "Linearly Polarized, Single-Mode Spontaneous Emission in a Photonic Nanowire," *Phys. Rev. Lett.*, vol. 108, p. 077405, 2012.

[198] M. Felici, P. Gallo, A. Mohan, B. Dwir, A. Rudra, and E. Kapon, "Site-controlled ingaas quantum dots with tunable emission energy," *Small*, vol. 5, no. 8, pp. 938–943, 2009.

[199] N. Tomm, A. Javadi, N. O. Antoniadis, D. Najer, M. C. Löbl, A. R. Korsch, R. Schott, S. R. Valentin, A. D. Wieck, A. Ludwig, *et al.*, "A bright and fast source of coherent single photons," *Nature Nanotech.*, pp. 1–5, 2021.

[200] P. Gold, A. Thoma, S. Maier, S. Reitzenstein, C. Schneider, S. Höfling, and M. Kamp, "Two-photon interference from remote quantum dots with inhomogeneously broadened linewidths," *Phys. Rev. B*, vol. 89, no. 3, p. 035313, 2014.

[201] J. Finley, M. Sabathil, P. Vogl, G. Abstreiter, R. Oulton, A. Tartakovskii, D. Mowbray, M. Skolnick, S. Liew, A. Cullis, *et al.*, "Quantum-confined stark shifts of charged exciton complexes in quantum dots," *Phys. Rev. B*, vol. 70, no. 20, p. 201308, 2004.

[202] R. B. Patel, A. J. Bennett, I. Farrer, C. A. Nicoll, D. A. Ritchie, and A. J. Shields, "Two-photon interference of the emission from electrically tunable remote quantum dots," *Nature Photon.*, vol. 4, no. 9, pp. 632–635, 2010.

[203] E. B. Flagg, A. Muller, S. V. Polyakov, A. Ling, A. Migdall, and G. S. Solomon, "Interference of single photons from two separate semiconductor quantum dots," *Phys. Rev. Lett.*, vol. 104, no. 13, p. 137401, 2010.

[204] L. Rigutti, L. Venturi, J. Houard, A. Normand, E. Silaeva, M. Borz, S. Malykhin, A. Obraztsov, and A. Vella, "Optical contactless measurement of electric field-induced tensile stress in diamond nanoscale needles," *Nano letters*, vol. 17, no. 12, pp. 7401–7409, 2017.

[205] S. Seidl, M. Kroner, A. Högele, K. Karrai, R. J. Warburton, A. Badolato, and P. M. Petroff, "Effect of uniaxial stress on excitons in a self-assembled quantum dot," *Appl. Phys. Lett.*, vol. 88, no. 20, p. 203113, 2006.

[206] L. Venturi, L. Rigutti, J. Houard, I. Blum, S. Malykhin, A. Obraztsov, and A. Vella, "Strain sensitivity and symmetry of 2.65 ev color center in diamond nanoscale needles," *Applied Physics Letters*, vol. 114, no. 14, p. 143104, 2019.

[207] A. J. Bennett, R. B. Patel, J. Skiba-Szymanska, C. A. Nicoll, I. Farrer, D. A. Ritchie, and A. J. Shields, "Giant stark effect in the emission of single semiconductor quantum dots," *Appl. Phys. Lett.*, vol. 97, no. 3, p. 031104, 2010.

[208] X. Wu, X. Dou, K. Ding, P. Zhou, H. Ni, Z. Niu, D. Jiang, and B. Sun, "In situ tuning the single photon emission from single quantum dots through hydrostatic pressure," *Appl. Phys. Lett.*, vol. 103, no. 25, p. 252108, 2013.

[209] X. Yuan, F. Weyhausen-Brinkmann, J. Martín-Sánchez, G. Piredda, V. Křápek, Y. Huo, H. Huang, C. Schimpf, O. G. Schmidt, J. Edlinger, *et al.*, "Uniaxial stress flips the natural quantization axis of a quantum dot for integrated quantum photonics," *Nature Commun.*, vol. 9, no. 1, pp. 1–8, 2018.

[210] R. Trotta, J. Martín-Sánchez, I. Daruka, C. Ortix, and A. Rastelli, "Energy-tunable sources of entangled photons: A viable concept for solid-state-based quantum relays," *Phys. Rev. Lett.*, vol. 114, no. 15, p. 150502, 2015.

[211] S. Franssila, *Introduction to microfabrication*. John Wiley & Sons, 2004.

[212] M. Shearn, X. Sun, M. D. Henry, A. Yariv, and A. Scherer, "Advanced plasma processing: etching, deposition, and wafer bonding techniques for semiconductor applications," *Semiconductor technologies*, pp. 79–104, 2010.

[213] Z. Cui, *Nanofabrication: Principles, Capabilities and Limits: Second*. Springer, 2008.

[214] C. S. Wu, Y. Makiuchi, and C. Chen, *High-energy electron beam lithography for nanoscale fabrication*. InTech Europe: Rijeka, Croatia, 2010.

[215] G. Wiederrecht, *Handbook of nanofabrication*. Academic Press, 2010.

[216] Data obtained from the Yale Institute for Nanoscience and Quantum Engineering tutorial website named, *Using "point spread functions" in Beamer*, https://nano.yale.edu/using-point-spread-functions-beamer.

[217] D. Huber, M. Reindl, S. F. C. Da Silva, C. Schimpf, J. Martín-Sánchez, H. Huang, G. Piredda, J. Edlinger, A. Rastelli, and R. Trotta, "Strain-tunable GaAs quantum dot: A nearly dephasing-free source of entangled photon pairs on demand," *Phys. Rev. Lett.*, vol. 121, no. 3, p. 033902, 2018.

[218] M. E. Reimer, M. P. van Kouwen, A. W. Hidma, M. H. van Weert, E. P. Bakkers, L. P. Kouwenhoven, and V. Zwiller, "Electric field induced removal of the biexciton binding energy in a single quantum dot," *Nano Lett.*, vol. 11, no. 2, pp. 645–650, 2011.

Appendix A

List of publications

1. Artioli, A.,† **Kotal, S.,**† Gregersen, N., Verlot, P., Gérard, J.-M. and Claudon, J. [2019], 'Design of Quantum Dot-Nanowire Single-Photon Sources that are Immune to Thermomechanical Decoherence', *Phys. Rev. Lett.* **123**, 247403.

2. **Kotal, S.**, Artioli, A., Yujing Wang, Osterkryger, A. D., Finazzer, M., Fons, R., Genuist, Y., Bleuse, J., Gérard, J.-M., Gregersen, N., and Claudon, J. [2021], 'Design of Quantum Dot-Nanowire Single-Photon Sources that are Immune to Thermomechanical Decoherence', *Appl. Phys. Lett.* (In press).

3. Fons, R., **Kotal, S.**, Artioli, A., Bleuse, J., Gérard, J.-M. and Claudon, J. [2020], 'Unveiling spin-flip processes in a neutral quantum dot using an anisotropic photonic structure', *Phys. Rev. B* (Submitted).

Appendix B

Mechanical simulations

In this section we give some details on the mechanical simulations, which are performed with Comsol Multiphysics. For simplicity, we have used a common, mean diameter of 200 nm at the level of the QD for all the mechanical simulations. The exact geometry employed for mechanical simulations are shown in Figs. 2.7, 2.9, 2.10, and 2.11. For all the devices which employ a metallic-dielectric planar mirror, the bottom substrate is not included in the simulation (this facilitates the identification of the nanowire vibration modes). We impose a rigid clamping condition for the bottom facet of the nanowire. For the suspended photonic trumpet, the rigid clamping condition is imposed at the end of the anchoring arms (the remaining parts of the structure are free to move). The materials (GaAs and SiO_2) are considered to be mechanically-isotropic; the values of the Young modulus and Poisson coefficient are given in Table B.1.

Table B.1 Mechanical parameters used in the simulations.

	GaAs	SiO_2
Young modulus, Y (GPa)	85.9	70
Poisson coefficient, ν	0.31	0.17

As discussed in Sec. 2.3.1, the first vibration modes for a nanowire fall into three families (flexural, torsional and rotational). At higher frequencies, when the mechanical wavelength becomes comparable to the diameter, the nanowire also supports modes which do not fall in these categories. This is also the case when the structure aspect ratio (height/diameter) approaches one (needle covered with a shell, tiny nanowire section for the mechanically-decoupled taper). In that case, we preserve a distinction between the modes which feature a zero stress on the nanowire axis (in red in Figs. 2.9, 2.10, and 2.11), and the other ones (in blue).

Finally, Figs. 2.7, 2.9, 2.10, and 2.11, also show the values of θ_m^2 and η_m^2 (defined in Sec. 2.3.3) for all the structures, which support the calculation of the photon indistinguishability. For clarity, we do not represent the full spectral extension of the mechanical

Table B.2 Extension of the mechanical simulations.

	Standard needle	Standard trumpet	Needle + shell	Suspended trumpet	Decoupled top taper
Max. frequency (GHz)	8.1	1.8	4.1	1.6	18.8
Number of modes	90	100	100	412	50
Final θ_m^2	7.9×10^{-5}	1.6×10^{-3}	2.2×10^{-6}	1×10^{-5}	7.7×10^{-4}
Final η_m^2	2×10^{-6}	8.7×10^{-6}	2.8×10^{-8}	$5\text{x}10^{-8}$	4.9×10^{-5}

simulations. The latter is given in Table B.2, which also shows the typical values of θ_m^2 and η_m^2 for the last (high-frequency) considered modes.

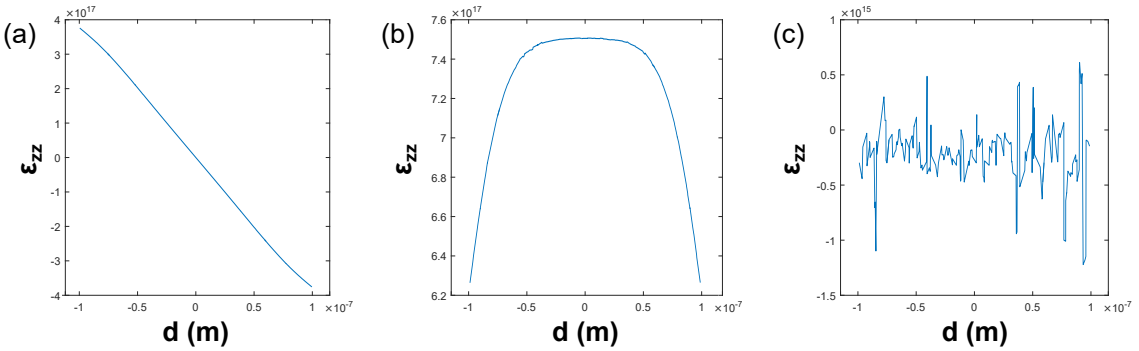

Fig. B.1 ε_{zz} as a function of position along the horizontal diameter of the cross-section of a nanowire antenna, used to classify vibration mode families. (a) Flexural modes. (b) Longitudinal modes. (c) Torsional modes.

To facilitate and accelerate the calculation of the impact of thermal vibrations on the QD emission, I programmed an interactive routine of code on MATLAB. The script takes as inputs the data exported (ω_m, u_m^{max}, and primary strain tensors ε_{xx}, ε_{yy}, and ε_{zz}) from simulations on COMSOL as well-tabulated text files. The strain tensors are extracted for points along the horizontal diameter across the nanowire cross-section at the height of the QD-plane from the base of the wire. The programme then requires the user to classify the modes into F, L, and T modes. This classification is done by evaluating the position-dependent plot of ε_{zz} across the cross-section. As seen in Fig. B.1, ε_{zz} is characterised by an odd function in F-modes, an even function in L-modes, and as numerical noise in T-modes. Every F-mode is doubly degenerate, each oscillating along mutually perpendicular axes. Only the one oscillating along the horizontal diameter of the wire cross-section is retained, since its partner exhibits a zero-stress axis along the horizontal diameter. This classification needs to be performed once for every simulated nanostructure. The algorithm then computes Eqns. 2.18 to 2.21, in order to extract for a given temperature the mode-specific coupling strength, the emission lineshape, and a temperature dependent indistinguishability, for a QD position on the wire axis, or on the wire edge, or at a specific radius from the wire centre.

Appendix C

Photonic properties

C.1 Single-mode model

To compute the total QD SE rate, we use the single-mode model presented in Ref. [142]. We start by considering an infinite nanowire and note $\Gamma^{\infty}_{\mathrm{HE}_{11}}$ the SE rate into the fundamental guided mode (HE_{11}) and γ^{∞} the SE rate into all the other modes. All devices feature a bottom mirror characterised by a modal reflectivity r_b (amplitude coefficient), and a top taper with a null modal reflection. When the QD stands on a (vertical) antinode of the interference pattern associated with the bottom reflection, the total SE rate can be expressed as,

$$\Gamma = (1+|r_b|)\Gamma^{\infty}_{\mathrm{HE}_{11}} + \gamma^{\infty}. \tag{C.1}$$

The fraction of SE funneled into the guided mode propagating upward is then maximal, and is defined as,

$$\beta_{\uparrow} = \frac{1}{2}\frac{\beta(1+|r_b|)^2}{1+\beta|r_b|}. \tag{C.2}$$

Here, $\beta = \Gamma^{\infty}_{\mathrm{HE}_{11}}/(\Gamma^{\infty}_{\mathrm{HE}_{11}} + \gamma^{\infty})$ is the fraction of SE coupled to the guided modes (propagating upward and downward) in an infinite wire. In the following, $\Gamma^{\infty}_{\mathrm{HE}_{11}}$, γ^{∞} and r_b are computed with a Fourier modal method [189]. $\Gamma^{\infty}_{\mathrm{HE}_{11}}$ and γ^{∞} strongly depend on the wire diameter and on the QD position within the nanowire section [75].

Table C.1 Photonic properties of the different designs. ($\star$) This value includes the 7 % transmission loss associated with a 10 nm gap.

	QD location	Standard antennas	Needle + shell	Suspended trumpet	Decoupled top taper
d/λ	–	0.23	0.24	0.25	0.20
$\lvert r_b\rvert^2$	–	0.91	0.91	0.41	0.91
$\Gamma/\Gamma_{\mathrm{bulk}}$	on-axis	1.74	1.65	1.47	1.13
$\Gamma/\Gamma_{\mathrm{bulk}}$	on-sidewall	0.33	0.37	0.33	0.24
$\beta_{\uparrow}$	on-axis	0.95	0.89	0.80	$0.85^{\star}$

C.2 Photonic properties of the devices

Considering a free-space operation wavelength $\lambda = 900\,\text{nm}$, Table C.1 summarises the main photonic properties of the five devices. It first shows the total SE rate normalised to the bulk reference value, $\Gamma/\Gamma_{\text{bulk}}$, for on-axis and on-sidewall QDs. Γ is used to compute the photon indistinguishability (we use a reference $\Gamma_{\text{bulk}} = 1\,\text{ns}^{-1}$). The table also shows $\beta_{\uparrow}$ for on-axis emitters. Importantly, the three last designs, which largely suppress the impact of nanowire vibrations, preserve large $\beta_{\uparrow}$ (> 0.8), and thus large collection efficiency.

Appendix D

Population dynamics of the exciton and biexciton

To be able to model the dynamics of QD emission we assume that the time taken to generate charges in the system is short in comparison to the radiative recombination time. We therefore set the initial condition of the system depending on the pumping power, and then leave the system to decay from the initial state.

We begin by making two hypotheses in order to define the charge state of the system as a function of pumping power. The hypotheses are, that the QD captures only electron-hole pairs (excitons) and not individual charge carriers, and that the carrier-capture process is random, which is independent of the presence of other charges, and the Coulomb interactions between charges is considered to be negligible. This entails that the number of generated excitons varies linearly with the pumping power. The probability that a QD will capture n excitons ensues from Poissonian statistics,

$$p(n) = \frac{\langle n \rangle^n}{n!} e^{-\langle n \rangle}, \tag{D.1}$$

where $\langle n \rangle$ is the average number of excitons generated, which depends on the exciting power, and may be written as the ratio (P/P_0) of the pumping power P over the power P_0 needed to inject one electron-hole pair into the QD. P_0, also referred to as the power required to saturate the QD, charaterises the absorption of the system.

We consider the QD to be a simplified 3-level system, that consists of a relaxed or ground state ($|G\rangle$), the exciton state ($|X\rangle$), and the biexciton state ($|XX\rangle$), as shown in Fig. D.1.

The initial population of the excitonic state as a function of pumping power, corresponding to the probability that a QD will trap at least one electron-hole pair, can be expressed as,

$$p_X^0 \propto p(1) = \frac{P}{P_0} e^{-\frac{P}{P_0}}. \tag{D.2}$$

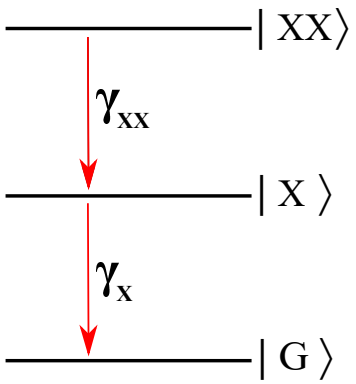

Fig. D.1 Representation of a QD as a simplified 3-level system, where $|G\rangle$ represents the ground state, $|X\rangle$ is the exciton state, and $|XX\rangle$ is the biexciton state. γ_X and γ_{XX} are respectively the recombination rates of the exciton and the biexciton.

Similarly the population for the biexcitonic state, which corresponds to the probability that the QD will trap at least two electron-hole pairs, can be written as,

$$p^0_{XX} \propto p(2) = \frac{1}{2}\left(\frac{P}{P_0}\right)^2 e^{-\frac{P}{P_0}}. \tag{D.3}$$

The dynamics of the system may be computed from the following system of equations,

$$\begin{aligned}
\frac{d}{dt}p_{XX}(t) &= -\gamma_{XX}\, p\, p_{XX}(t),\\
\frac{d}{dt}p_X(t) &= \gamma_{XX}\, p\, p_{XX}(t) - \gamma_X\, p_X(t),\\
\frac{d}{dt}p_G(t) &= \gamma_X\, p_X(t).
\end{aligned}$$

This system can be solved analytically and the expression for the temporal evolution of the population in the excitonic state as a function of the emission rate of excitons (γ_X) and biexcitons (γ_{XX}), may be expressed as follows,

$$p_X(t) = p^0_X e^{-\gamma_X t} + p^0_{XX}\frac{\gamma_{XX}}{\gamma_X - \gamma_{XX}}(e^{-\gamma_X t} - e^{-\gamma_{XX} t}). \tag{D.4}$$

From the equation above, we can deduce that, at low excitation power ($P << P_0$), the population of the biexcitonic state is negligible, in comparison to that of the excitonic state. The population decay is dictated by a mono-exponential trend. As the pumping power increases, so does the contribution of p^0_{XX} which gives rise to a leading rise time in the temporal distribution of a decay time measurement. This rise time corresponds to the time taken for the biexciton to exciton transition.